Universidad de Alcalá

Programa de Doctorado en
Tecnologías de la Información Geográfica

FOREST ATTRIBUTES MAPPING WITH SAR DATA IN THE ROMANIAN SOUTH-EASTERN CARPATHIANS

Requirements and outcomes

Tesis Doctoral presentada por
Ignacio Borlaf Mena

Directores
Dr. Mihai Andrei Tanase
Dr. Ovidiu Badea

Alcalá de Henares, 2022.

Table of Contents

List of figures

List of tables

Acknowledgements

Many people have supported the endeavor of writing this thesis, and I would like to thank all of them for their assistance. My supervisors, Mihai Andrei Tanase, Francisco Javier Salas and Ovidiu Badea provided the opportunity to enter the world of research. I am grateful for the independence they allowed when to exploring the data from a very challenging study area, and their patience letting me find an adequate answer to the issues I found. Special thanks to Javier for his aid while dealing with the administrative procedures, showing the patience of a saint.

Equally, I thank Maurizio Santoro, Juan García-Duro, Olivier Hagolle and Ludovic Villard who provided insight while writing this thesis and helped me understand many difficult topics. Many results would have been unreachable without their support. I am very grateful to the Biometry Research group at the INCDS "Marin Drăcea" and the Environmental Remote Sensing group at the university of Alcalá (UAH). Both institutions provided the resources to make this thesis possible and formed me through the years to tackle difficult technical problems. The seminars of the Environmental Remote Sensing research group at UAH have been a source of ideas, and a great opportunity to hone my own.

I have very fond memories of the time I shared with my colleagues at both, UAH and INCDS, the friendly working environment, and the fruitful discussions we have had. I would like praise Francisco Javier Salas and Francisco Javier Escobar Martínez for their terrific work in the in the UAH PhD program. Thanks to their effort there have been a large increase of courses for our doctorate program. Special thanks to my friends in the UAH who shared the good and bad times during these long years. I treasure the time we have shared together, and now that the journey is ending, I can only hope I can keep in touch with all of them.

I would never would have reached this point without the help of my family. The education my mother Pilar gave me motivated me to pursue a career in science, and I only reached this point thanks to the sacrifices my whole family has made. Thank you all for your help and patience: in many ways, you have shaped me into the person I am today. My friends kept me in company during the lonely days when I was in Romania, and I found them all when I came back to Spain. You are the best company anybody can wish for, the time we share is always a joy. I am also deeply grateful for my partner Elena, who made these years a lot more pleasant. You supported me through thick and thin, your smile makes any day shine brighter and any worry feel lighter.

Resumen

Esta tesis doctoral se centra en la estimación de variables forestales en la zona Sureste de los Cárpatos Rumanos a partir de imágenes de radar de apertura sintética. La investigación abarca parte del preprocesado de las imágenes, métodos de generación de mosaicos y la extracción de la cobertura de bosque, sus subtipos o su biomasa. La tesis se desarrolló en el Instituto Nacional de Investigación y Desarrollo Forestal Marín Dracea (INCDS) y la Universidad de Alcalá (UAH) gracias a varios proyectos: el proyecto EO-ROFORMON del INCDS (*Prototyping an Earth-Observation based monitoring and forecasting system for the Romanian forests*), y el proyecto EMAFOR de la UAH (*Synthetic Aperture Radar (SAR) enabled Analysis Ready Data (ARD) cubes for efficient monitoring of agricultural and forested landscapes*). El proyecto EO-ROFORMON fue financiado por la Autoridad Nacional para la Investigación Científica de Rumania y el Fondo Europeo de Desarrollo Regional. El proyecto EMAFOR fue financiado por la Comunidad Autónoma de Madrid (España).

El objetivo de esta tesis es el desarrollo de algoritmos para la extracción de variables forestales de uso general como la cobertura, el tipo o la biomasa del bosque a partir de imagen de radar de apertura sintética. Para alcanzar dicho propósito se analizaron posibles fuentes de sesgo sistemático que podrían aparecer en zonas de montaña (ej., normalización topográfica, generación de mosaicos), y se aplicaron técnicas de aprendizaje de máquina para tareas de clasificación y regresión. La tesis contiene ocho secciones: una introducción, cinco publicaciones en revistas o actas de congresos indexados, una pendiente de publicación (quinto capítulo) y las conclusiones.

La introducción contextualiza la importancia del bosque, cómo se recoge la información sobre su estado (ej., inventario forestal) y las iniciativas o marcos legislativos que requieren dicha información. A continuación, se describe cómo la teledetección puede complementar la información de inventario forestal, detallando el contexto histórico de las distintas tecnologías, su funcionamiento, y cómo pueden ser aplicadas para la extracción de información forestal. Por último, se describe la problemática y el monitoreo del bosque en Rumanía, detallando el objetivo de la tesis y su estructura.

El primer capítulo analiza la influencia del modelo digital de elevaciones (MDE) en la calidad de la normalización topográfica, analizando tres MDE globales (SRTM, AW3D y TanDEM-X DEM) y uno nacional (PNOA-LiDAR). Los experimentos se basan en la comparación entre órbitas, con un MDE de referencia, y la variación del acierto en la clasificación dependiendo del MDE empleado para la normalización. Los resultados muestran

una menor diferencia ente órbitas al utilizar un MDE con una mejor resolución (ej. TanDEM-X, PNOA-LIDAR), especialmente en el caso de zonas con fuertes pendientes o formas del terreno complejas, como pueden ser los valles.

En zonas de alta montaña las imágenes de radar de apertura sintética (SAR) sufren frecuentes distorsiones. Estas distorsiones dependen de la geometría de adquisición, por lo que es posible combinar imágenes adquiridas desde varias órbitas para que la cobertura sea lo más completa posible. El segundo capítulo evalúa dos metodologías para la clasificación de usos del suelo utilizando datos de Sentinel-1 adquiridos desde varias órbitas. El primer método crea clasificaciones por órbita y las combina, mientras que el segundo genera un mosaico con datos de múltiples órbitas y lo clasifica. El acierto obtenido mediante combinación de clasificaciones es ligeramente mayor, mientras que la clasificación de mosaicos tiene importantes omisiones de las zonas boscosas debido a problemas en la normalización topográfica y a los efectos direccionales.

El tercer capítulo se enfoca en separar la cobertura forestal de otras coberturas del suelo (urbano, vegetación baja, agua) analizando la utilidad de las variables basadas en la coherencia interferométrica. En él se realizan tres clasificaciones de máquina vector-soporte basadas en un conjunto concreto de variables. El primer conjunto contiene las estadísticas anuales de la retrodispersión (media y desviación típica anual), el segundo añade la coherencia a largo plazo (separación temporal mayor a un año), el tercero incluye las estadísticas de la coherencia a corto plazo (mínima separación temporal). Utilizar variables basadas en la coherencia aumenta el acierto de la clasificación hasta un 5% y reduce los errores de omisión de la cobertura forestal. El cuarto capítulo evalúa la posibilidad de detectar talas selectivas utilizando datos de Sentinel-1 y Sentinel-2. Sus resultados muestran que la detección resulta muy difícil debido a la saturación de los sensores y la confusión introducida por el efecto de la fenología.

El quinto capítulo se centra en la clasificación de tipos de bosque basado en una serie temporal de datos Sentinel-1. Se basa en la creación de un conjunto de modelos que describen la relación entre la retrodispersión y el ángulo local de incidencia para un determinado tipo de bosque y fecha concreta. Para cada píxel se calcula el residuo respecto al modelo de cada uno de los tipos de bosque, acumulando dichos residuos a lo largo de la serie temporal. Hecho esto, cada píxel es asignado al tipo de bosque que acumula un menor residuo. Los resultados son prometedores, mostrando que frondosas y coníferas tienen un comportamiento distintivo, y que es posible separar ambos tipos de bosque con un alto grado de acierto.

El sexto capítulo está dedicado a la estimación de biomasa utilizando datos Sentinel-1, ALOS PALSAR y regresión *Random Forest*. Se obtiene un error similar para ambos sensores a pesar de utilizar una banda diferente (band-C vs. -L), con poca reducción en el error

cuando ambas bandas se utilizan conjuntamente. Sin embargo, el ajuste de un estimador adaptado a las condiciones locales de Rumanía sí ofreció una reducción de del error al ser comparado con las estimaciones globales de biomasa.

Abstract

This doctoral thesis focuses on the estimation of forest variables in the Southeast area of the Romanian Carpathians using synthetic aperture radar images. The research covers image pre-processing and mosaicking methods as well as the extraction of the forest variables such as cover, type and above ground biomass. Research activities have been hosted by the Marin Dracea National Institute for Research and Development in Forestry (INCDS) and the university of Alcalá (UAH) thanks to several projects: the EO-ROFORMON project in the INCDS (Prototyping an Earth-Observation based monitoring and fore-casting system for the Romanian forests), and the EMAFOR project in the UAH (Synthetic Aperture Radar (SAR) enabled Analysis Ready Data (ARD) cubes for efficient monitoring of agricultural and forested landscapes). The EO-ROFORMON project was funded by the National Authority for Scientific Research of Romania and the European Regional Development Fund. The EMAFOR project was funded by the Autonomous Community of Madrid (Spain).

The objective of this thesis is the development of algorithms for the extraction of forest variables from synthetic aperture radar images. To this end, possible sources of systematic bias often encountered in mountain areas (e.g., topographic normalization, mosaic generation), were analyzed, and machine learning techniques were applied for classification and variable estimation tasks. The thesis contains eight sections: an introduction, six research chapters (five published and one pending publication) and the conclusions.

The introduction contextualizes the importance of the forest, how information on its status is collected (e.g., forest inventory) and the initiatives or legislative frameworks that require such information. Next, it is described how remote sensing can complement forest inventory information, detailing the historical context of the different technologies, their operation, and how they can be applied to extract forest information. Finally, forest monitoring activities in Romania are described, detailing the objective of the thesis and its structure.

The first chapter analyzes the influence of the digital elevation model (DEM) on the quality of topographic normalization, analyzing three global (SRTM, AW3D and TanDEM-X DEM) and one national (PNOA-LiDAR) DEMs. The experiments are based on the inter-orbit comparisons against a reference DEM and the classification accuracy depending on the DEM used for image normalization. The results show a smaller difference between orbits when using a DEM with a higher spatial resolution (e.g., TanDEM-X, PNOA-LIDAR), especially in areas with steep slopes or complex terrain forms, such as valleys.

In mountainous areas, synthetic aperture radar (SAR) images are frequently distorted. Distortions depend on the acquisition geometry, and thus, it is possible to combine images from several orbits so that the resulting spatial coverage is as complete as possible. To this end, the second chapter evaluates two methods for the classification of land uses using Sentinel-1 data acquired from different orbits. The first method creates by-orbit classifications and combines them, whereas the second generates a mosaic with data from different obits and classifies it. The accuracy obtained by combination of classifications is slightly higher, while the mosaic classification has important omissions of forested areas due to problems in topographic normalization and directional effects.

The third chapter focuses on separating forest cover from other land covers (urban, low vegetation, water) analyzing the usefulness of variables based on interferometric coherence. Three support vector machine classifications are compared each based on a specific set of variables. The first set contains the annual backscatter statistics (annual mean and standard deviation), the second adds the long-term coherence (time separation greater than one year), the third includes the short-term coherence statistics (minimum temporary separation). Using variables based on coherence increases the accuracy of the classification up to 5% and reduces errors of omission of forest cover. The fourth chapter evaluates the possibility of detecting selective logging using data from Sentinel-1 and Sentinel-2. The results show detection is very difficult due to the saturation of the sensors and the confusion introduced by the effect of phenology.

The fifth chapter focuses on the classification of forest types based on a time series of Sentinel-1 data. It creates a set of models, each of them describing the relationship between backscattering and the local angle of incidence for a given type of forest and a specific date. For each pixel, the residual is calculated with respect to the model of each of the forest types. By accumulating residuals throughout the time series each pixel is assigned to the type of forest with the least accumulated residuals. The results are promising, showing that broadleaf and needleleaf forest have a distinct behavior, and that it is possible to separate both forest types with a high degree of accuracy.

The sixth chapter is dedicated to biomass estimation using Sentinel-1 data, ALOS PALSAR and Random Forest regression. A similar error is obtained for both sensors despite using a different band (band-C vs. -L), with little reduction in error when both bands were used together. The adjustment of an estimator adapted to the local conditions of Romania offers a reduction in the estimation error when compared with estimates of biomass generated at global level.

Associated publications

Chapter 1: Borlaf-Mena, I., Santoro, M., Villard, L., Badea, O., Tanase, M.A., 2020. Investigating the Impact of Digital Elevation Models on Sentinel-1 Backscatter and Coherence Observations. Remote Sensing 12, 3016. https://doi.org/10.3390/rs12183016

Chapter 2: Borlaf-Mena, I., Badea, O., Tanase, M.A., 2021a. Influence of the Mosaicking Algorithm on Sentinel-1 Land Cover Classification Over Rough Terrain, in: 2021 IEEE International Geoscience and Remote Sensing Symposium IGARSS, Brussels, Belgium, 11–16 July 2021. Presented at the IGARSS 2021 - 2021 IEEE International Geoscience and Remote Sensing Symposium, Brussels, Belgium, 11–16 July 2021, IEEE, Brussels, Belgium, pp. 6646–6649. https://doi.org/10.1109/IGARSS47720.2021.9553648

Chapter 3: Borlaf-Mena, I., Badea, O., Tanase, M.A., 2021b. Assessing the Utility of Sentinel-1 Coherence Time Series for Temperate and Tropical Forest Mapping. Remote Sensing 13, 4814. https://doi.org/10.3390/rs13234814

Chapter 4: Tanase, M., Borlaf, I., Pascu, I., Pitar, Diana, Apostol, B., Petrila, M., Chivulescu, S., Leca, S., Pitar, Daniel, Ciceu, A., Dobre, A., Popescu, F., Badea, O., Aponte, C., 2020. Sentinel-1/2 Time Series for Selective Logging Monitoring in Temperate Forests, in: IGARSS 2020 - 2020 IEEE International Geoscience and Remote Sensing Symposium. Presented at the IGARSS 2020 - 2020 IEEE International Geoscience and Remote Sensing Symposium, IEEE, Waikoloa, HI, USA, pp. 2902–2905. https://doi.org/10.1109/IGARSS39084.2020.9323952

Chapter 5: Borlaf-Mena, I., Santoro, M., Villard, L., Badea, O. and Tanase, M.A. Seasonality and directionality are key to identify mountain forest types with Sentinel-1 data. [draft for publication]

Chapter 6: Tanase, M.A., Borlaf-Mena, I., Santoro, M., Aponte, C., Marin, G., Apostol, B., Badea, O., 2021. Growing Stock Volume Retrieval from Single and Multi-Frequency Radar Backscatter. Forests 12, 944. https://doi.org/10.3390/f12070944

Introduction

The importance of forests

The Food and Agriculture Organization (FAO) of the United Nations (UN) defines forests as areas occupied by trees taller than 5 meters covering over 10% of the ground, excluding agricultural or urban uses and small patches (< 0.5 hectares; Garzuglia et al., 2018). Forests occupy 25-31% of the world land area (Watson et al., 2018; FAO and UNEP, 2020) and host around 80% of the terrestrial biodiversity (FAO and UNEP, 2020). They play an essential role on the regulation of the water and carbon cycles: forest contribute ~50% of the terrestrial primary production (carbon sequestration), and they store ~40% of terrestrial carbon (Bonan, 2008). Besides their role in the Earth system, forests are an essential source of resources, such as food of timber. More than one billion people rely on forest for their livelihood, and hold a great cultural and emotional value for many communities (FAO and UNEP, 2020). In short, they provide all kinds of ecosystem services (regulation, supporting, provisioning, cultural) (Millennium Ecosystem Assessment, 2003).

Assessing forest resources: forest inventory

Ecosystem services are everlasting when management maintain the natural processes and biological diversity (United Nations, 1992a; Grumbine, 1994). In the case of forest this requires a careful assessment to avoid over-use:

> *"Forest inventory is the systematic collection of data on the forestry resources within a given area. It allows assessment of the current status and lays the ground for analysis and planning, constituting the basis for sustainable forest management."*
>
> (FAO, 2011)

Forest inventories were outlined in the last two centuries, with a very large influence of the German classical school of forestry (Morgenstern, 2007; Hölzl, 2010; Gschwantner et al., 2022) which introduced the concept of management units. The forest estates were divided in compartments which in turn were divided in forest stands, i.e., tree patches with uniform and distinct characteristics (Morgenstern, 2007; DIABOLO, 2021; Gschwantner et al., 2022). Initially, stand level assessments were based on visual estimates, transitioning to plot sampling of the tree measurements, using the advances in statistics (Tomppo et al., 2010; Gschwantner et al., 2022).

Some of the countries influenced by the German teachings were Norway, Finland and Sweden (Michelsen, 1995; Enander, 2007; Tomter, 2019). However, stand-based sampling was not a viable solution to survey their vast expanses of boreal forest (Gschwantner et al., 2022). This led to the development of large-area forest inventories by taking systematic samples of the target variables (COST action E43, 2009). After initial tests, Norway, Finland and Sweden started using such approaches for their national forest inventories, or NFIs (Norway, 1919; Finland, 1921; Sweden, 1923), making tree measurements along parallel belts (Korhonen, 2016; Gschwantner et al., 2022). The Finnish and German experience influenced the NFI of United States, started in 1928, which was based on a systematic grid of sampling plots (Lewis, 1999; LaBau et al., 2007; Shaw, 2008).

Many European countries stablished sample-based NFIs in the 1950-1980 decades, recognizing the need for periodic and representative information about forest resources (Vidal et al., 2016b). Both, these new NFIs and the preexisting ones (Northern European countries) employed plot sampling to take measurements of the tree population. At the same time re-measured permanent sampling plots were introduced as well, easing the observation of changes like tree felling and growth (Gschwantner et al., 2022). Currently many countries rely on permanent plots, sometimes in combination with temporary sampling plots (Alberdi et al., 2016; Gschwantner et al., 2016; Fridman and Westerlund, 2016; Lanz et al., 2016; Riedel et al., 2016; Tomter, 2016; Gschwantner et al., 2022). During the 1990s the scope of the NFIs broadened from wood production to ecosystem monitoring for sustainable management and international reporting, increasing the workload required from the NFIs (Vidal et al., 2016a).

International reporting at global level: United Nations programs

At global level the Organization of the United Nations (UN) is the main actor requesting information from NFIs. Several programs make use of forest information: the Food and Agriculture Organization (FAO), the UN Educational, Scientific and Cultural Organization (UNESCO) or the Intergovernmental Panel on Climate Change (IPCC). A timeline with their establishment is depicted in Figure 0.1.

Global Forest Resources Assessment (FRA) was started by the FAO just after the Second World War. It produces periodic reports about the status of the world forests based on the questionnaires filled by participating countries. This made necessary a harmonized definition for all kinds of forests, agreed upon and used within the 2000 FRA report. The reporting progressed as well, incorporating more sources of information (i.e., remote sensing), and broadening its scope from timber resources to forests environmental functions, especially after the UN convention on Environment and Development (UNCED) in year 1992 (Garzuglia et al., 2018).

Further, other international programs focused on combating anthropogenic climate change effects require forest related information. For example, the Villach Conference

(1985) sparked international action by founding several institutions with a pivotal role in the fight against climate change (Agrawala, 1998; Zillman, 2009; ICSU, 2018). The Intergovernmental Panel on Climate Change (IPCC), established in 1988 by the WHO and UNEP, has the task of preparing reports on climate change science (Zillman, 2009; IPCC, 2019). The Global Climate Observing System (GCOS) would follow in 1992 to support the IPCC and the upcoming legislation (i.e., UN Framework Convention on Climate Change, UNFCCC). GCOS provides recommendations for in-situ and space-based observations of the climate system components (Zillman, 2009; Bojinski et al., 2014). Both the IPCC and the GCOS underlined the importance of forests in Earth climate system since their first reports (IPCC et al., 1990; WMO et al., 1995, 1998).

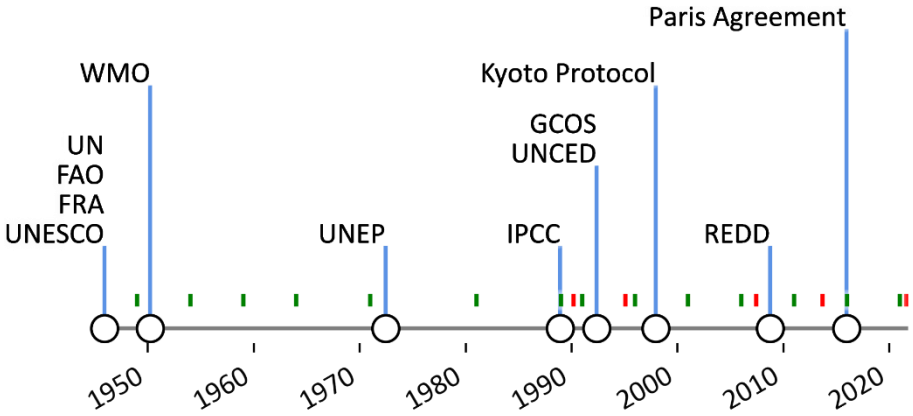

Figure 0.1 Timeline of the United Nations and its agencies, programs and agreements related to forest, or climate change. Acronyms: UN, United Nations; FAO, Food and agriculture Organization; FRA, Forest Resources Assessment; UNESCO, UN Educational, Scientific and Cultural Organization; WMO, World Meteorological Organization; UNEP, UN Environmental Program; IPCC, Intergovernmental Panel on Climate Change; GCOS, Global Climate Observing System; UNCED, UN Conference on Environment and Development. The green notches represent the FRA reports, the red notches mark the IPCC reports.

The UNCED, also known as the Rio de Janeiro "Earth Summit" laid down the foundations of our current understanding of sustainable development. It was outlined in three non-binding documents: the Rio Declaration on Environment and Development, Agenda 21 and the Forest Principles (United Nations, 1992b; Vidal et al., 2016b). Their ideas would be solidified in two legally binding agreements open for signature. One of them was the convention on biological diversity (CBD), which recognized forests as essential for maintaining economic development and biodiversity (United Nations, 1992a). The other was the UNFCCC, that laid out the basis to set binding limits on greenhouse gases (GHG) emissions (United Nations, 1992c).

The emission limits contemplated by UNFCCC were set through the Kyoto Protocol (United Nations, 1997). Kyoto protocol required the countries to monitor GHG emissions and removal based on IPCC guidelines (IPCC et al., 1996; United Nations, 1997). Forest management is one of the possible sink activities (IPCC, 2003, 2008; Vidal et al., 2016b).

In fact, IPCC assessments recognize deforestation reduction as the best short-term strategy to reduce carbon emissions (Metz and IPCC, 2007; Tomppo et al., 2010). This led to the approval of the program "Reducing emissions from deforestation and forest degradation" (REDD), with the objective of GHG emissions through sustainable forest management and conservation in developing countries (Tomppo et al., 2010). In 2015 the Kyoto protocol was succeeded by the Paris agreement, once again, underlining forest importance (United Nations, 2015a)

The role of the European Union in forest monitoring

European union does not have a legally binding forest policy, delegating such rules to member states (Baycheva et al., 2015; Elomina and Pülzl, 2021) but several sectorial policies affect forests such as the Habitat Directive or the Common Agricultural Policy (European Council, 1992; European Parliament and European Council, 2000, 2013, 2018). In this context, several initiatives focused on harmonizing forest information across Europe. The first pan-European forest monitoring initiative was the International Co-operative Program on Assessment and Monitoring of Air Pollution Effects on Forests (ICP-Forests), started in 1985 in the context of the forest decline caused by air pollution (Lorenz, 1995; Tomppo et al., 2010; Breidenbach et al., 2020). The ICP-Forests program was followed by regular Ministerial Conferences on Protection of Forest in Europe (MCPFE, renamed to "FOREST EUROPE" in 2009; Figure 0.2).

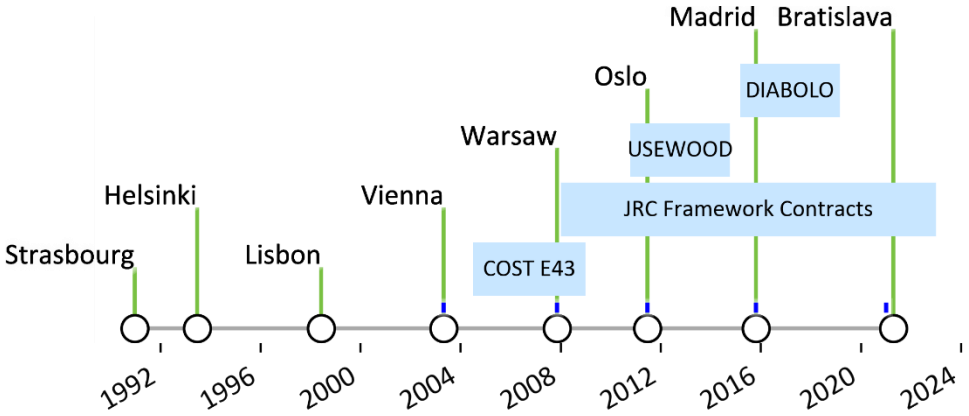

Figure 0.2. Ministerial Conferences on Protection of Forest in Europe (MCPFE/FOREST EUROPE) dates and locations (lines), European National Forest Inventory Network (EN-FIN) re-search activities. Blue notches represent the Status of European forest reports.

The first MCPFE (Strasbourg, 1990), had the objective of tackling forest decline, and cross-border forest protection. The second MCPFE (Helsinki, 1993) was heavily influenced by the UNCED. Its outcomes were two sets of guidelines, one for sustainable forest management and another for biodiversity conservation (Linser, 2005; Vidal et al., 2016b). These guidelines called for a series of criteria and indicators (C&I) for assessing forest status, that would be set in 1998 (Lisbon), and refined until 2015 (Madrid), when the final C&I list was accepted (Linser, 2005; Vidal et al., 2016b; MCPFE, 2015). Since 1998 these indicators have been reflected in the EU forest strategy and are employed

to report forest status (European Commission, 1998, 2013, 2021),.There are six groups of such criteria related to 1) resources and global carbon cycles, encompassing forest area, growth and carbon stock; 2) health and vitality, concerned with forest damage or defoliation; 3) production of woods and other products, considering the proportion of forests with a management plan; 4) conservation, regeneration, forest landscape patterns and protection; 5) protective functions for soil, and water; 6) socioeconomic functions, such as the forestry sector importance or occupational safety and forest cultural values (MCPFE, 2002, 2015).

It should be noted the activities of these ministerial conferences have been supported by European National Forest Inventory Network (ENFIN). Founded in 2003, it has the objective of enhancing comparability of forest information (Vidal et al., 2016b; Gschwantner et al., 2022). The network has pursued these objectives through several EU-funded projects, such as the COST actions E43 and FP1001 (Tomppo and Schadauer, 2004; Schadauer and Barreiro, 2010), the DIABOLO project (DIABOLO, 2019) or a series of contracts with the Joint Research Center (JRC). Some of the outcomes of these projects are tools for harmonization (i.e., reference definitions; COST action E43, 2009; DIABOLO, 2021) or improved knowledge of techniques that can reduce the cost of forest inventories, such as remote sensing (McRoberts and Tomppo, 2007; Barrett et al., 2016).

Remote sensing in forest inventories

Execution of forest inventories is time-consuming and expensive. There are many variables to retrieve and large expanses of land to survey, which may be difficult to traverse (i.e., mountains). NFIs seek low-cost solutions to produce timely information at affordable costs (McRoberts and Tomppo, 2007). One of them is remote sensing, techniques focused on obtaining information about physical targets with sensors mounted in satellites or aircrafts (Chuvieco, 2015; Gómez et al., 2019; NOAA 2021; NASA 2022; USGS 2022). This section briefly discusses some of the most used remote sensing technologies in the context of forest inventory, preceded by a short section describing their historical context.

Historical context of remote sensing

Remote sensing, developed largely during the XX century, as one of the many technological advancements made during military conflicts. An example is the first aerial camera, developed during World War I for aerial reconnaissance (Moore, 1979; Wakefield, 2014; Chuvieco, 2015, p. 21). Other examples is radar (radio detection and ranging), first employed for plane detection (chain home, the array of detectors built by England), and later to aid plane navigation (Woodhouse, 2006, pp. 14–18; Henderson and Lewis, 1998, pp. 3–5). After the war, there was some early research on the interpretation and modelling of ground return (i.e., Clapp, 1946). During the 1950s system design improved with Side-Looking airborne Radar (SLAR, real aperture or RAR), capable to take very fine resolution imagery. The same decade also brought forth processing techniques, such as

synthetic aperture radar (SAR), opening way for high-resolution spaceborne radar remote sensing (Henderson and Lewis, 1998; Ulaby and Long, 2014). Applications would start to emerge in the 1960s (i.e. Morain and Simonett, 1967), with imagery declassification (Henderson and Lewis, 1998; Ulaby and Long, 2014) and extensive RAR acquisition campaigns (Dellwig and Burchell, 1972; Woodhouse, 2006, p. 21).

The space race was another driver in the evolution of remote sensing, by developing the necessary capabilities for spaceflight. The U.S. National Aeronautics and Space Administration (NASA) was founded in this context (1958), as a response to the launch of Sputnik-1 by the Soviet Union. Many other countries founded space agencies over the following decades, for example France (*Centre national d'études spatiales*, CNES, in 1961), Germany (*Deutsches Zentrum für Luft- und Raumfahrt*, DLR, in 1969) or Japan (National Space Development Agency, NASDA, 1969, absorbed by Japan Aerospace Exploration Agency, JAXA in 2003). Joint European initiatives also grew during the 1960s, leading to the foundation of the European Space Agency (ESA) in 1975 (Krige et al., 2000), which became a major actor driving the development of remote sensing technologies. Since 1984 the work of these agencies has been coordinated and complimented by the Committee on Earth Observation Satellites (CEOS). CEOS was founded to facilitate the uptake of remote sensing data, with a strong focus in interoperability. Some tasks involved are an accurate inter-calibration of the sensors, common data formats or standardized processing and validation procedures (Lewis et al., 2018; CEOS, 2022).

The crew of the first NASA spaceflights took many photographs that picked the interest of the scientific community. This led the U.S. administration to plan a multi-spectral satellite mission to monitor earth resources. These plans came to fruition with the launch of the first member of the Landsat program in 1972 (Moore, 1979). However, multispectral sensors were limited by clouds. The SEASAT, demonstrated the all-weather capabilities of the spaceborne SAR technology. Experiments would continue during the 1980s with the Shuttle Imaging Radar (SIR). In 1990s many satellites carrying SAR systems were launched, such as ERS, JERS, or RADARSAT-1 (Henderson and Lewis, 1998, p. 5). Finally, LiDAR technology (light detection and ranging) appeared in the 1980s (laser profilers) and 1990s (aerial laser scanning, ALS; Beland et al., 2019), with its first spaceborne sensors launched in the 2003 (IceSAT GLAS), 2006 (IceSAT-2 ATLAS) and 2018 (Global Ecosystem Dynamics Investigation lidar, GEDI; Dubayah et al., 2020).

In 1995 GCOS recognized the possibilities of different remote sensing earth observation technologies to monitor essential climate variables, such as forest biomass (WMO et al., 1995). The 2000s were marked by the release of Landsat data under a free license in 2008 (Zhu et al., 2019), and the development of the Copernicus program by ESA. The program launched its first sensors in 2014 (Sentinel-1, SAR) and 2015 (Sentinel-2, multispectral), showing a huge promise for forest applications. Data generated by the Copernicus program is released under a free license (European Parliament and European Council, 2021), making Sentinel-1 the first SAR sensor whose data is distributed with

such a permissive license. ESA example led other agencies to reconsider their policies, and ease the access to data from older satellites (RADARSAT-1; Canadian Space Agency, 2019; ALOS PALSAR 1; JAXA and NASA, 2020). Alongside the launch of the successive Sentinel missions the European Space Agency has been developing the Climate Change initiative (ESA CCI), aimed to use remote sensing data to provide evidence necessary to tackle climate change (ESA, 2010; Bojinski and Fellous, 2013; Bojinski et al., 2014). Finally, CEOS Analysis Ready Data for Land (CARD4L) is another note-worthy initiative. CARD4L aims to make available data more accessible to non-expert users through a series of standards on the preparation of "analysis ready data" products (ARD products) with a suitable preprocessing for many land applications (Lewis et al., 2018).

Multi-spectral remote sensing

Optical remote sensing, a passive technology, recovers the sunlight reflected by the targets and records it on film (i.e., first aerial cameras), or an electronic media (i.e., recent aerial cameras, spaceborne sensors). Multispectral sensors record the amount of energy received for a specific section of the electromagnetic spectrum or "band", enabling analysis of phenomenon related to these sections (Figure 0.3 shows the bands of some widely used sensors). To make full use of multispectral images it is necessary to normalize the data recorded considering sun emission, atmospheric scattering, and interaction with the terrain. Part of the images may be masked if correction cannot be performed (i.e., cloud cover, terrain shadows). Once the normalization process has been completed the imagen can be considered "analysis ready" (ARD, Lewis et al., 2018). However, it should be noted some artifacts may remain (i.e., undetected cloud or cloud shadow), as multispectral data pre-processing remains an area of active research (Doxani et al., 2018; Skakun et al., 2022).

The uptake of optical data in forestry was fast, starting with the first aerial photographs. FAO FRA assessed the technology soon after World War II, stressing its usefulness for field sampling design (Spurr, 1948). The U.S. Forest survey would be the first incorporating the technology during the 1940s and 1950s. Aerial photography is frequently employed for sampling design and to describe forest attributes, such as forest presence, composition, canopy cover or development stage (Barrett et al., 2016). Satellite multispectral data only started to be used by NFIs with the launch of sensors with improved spatial resolution (i.e., Landsat Thematic mapper sensor, 30 m resolution). The Finnish NFI would be the first to make operational use of Landsat data (Barrett et al., 2016). Optical images are usually employed to generalize field data to a wall-to-wall coverage (Barrett et al., 2016; McRoberts and Tomppo, 2007).

Forest canopy reflectance largely depends on leaf chemical properties and structure, alongside with the shape and height of tree canopy, the disposition of the trees, and the total canopy cover (Jacquemoud et al., 2009; Ollinger, 2010; Homolová et al., 2013; Fassnacht et al., 2016). In this context optical data can provide information about forest area (Bartholomé and Belward, 2005), its layout (Newton et al., 2009; Sexton et al., 2013), its

losses and gains (Hansen et al., 2013; Viana-Soto et al., 2020), composition (Fassnacht et al., 2016), and health status (Hall et al., 2006; Torres et al., 2021). However, optical remote sensing has limitations related to changes in sun angle, atmospheric conditions, and cloud cover. Furthermore, optical sensibility to structural parameters saturates with increasing canopy closure (Nilson and Peterson, 1994; Puhr and Donoghue, 2000; Duncanson et al., 2010).

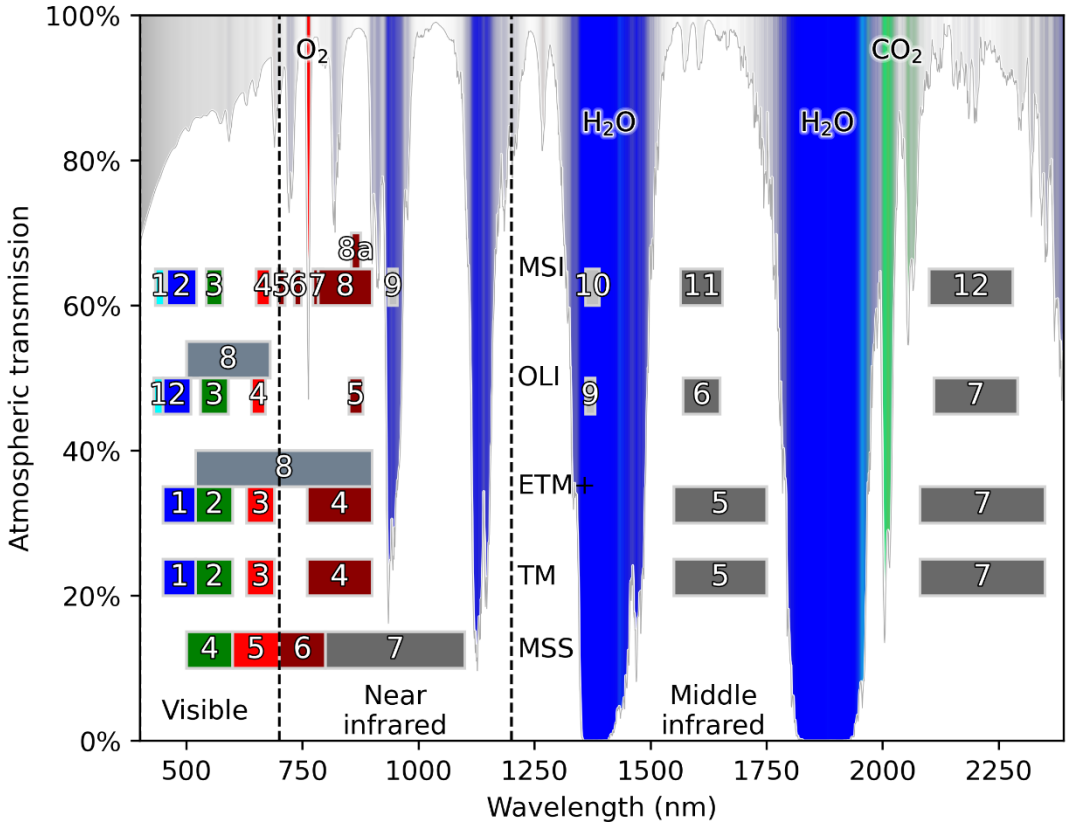

Figure 0.3 Atmospheric transmission (gray curve) and effect of some of the atmospheric gases (red, oxygen, green, carbon dioxide, blue, water vapor). Data simulated with Mid-latitude summer atmosphere template using NASA planetary spectrum generator (Villanueva et al., 2018). The bands of several sensors are depicted under the gray line (Landsat 1-5 Multispectral Scanner, MSS; Landsat 4-5 Thematic Mapper, TM; Landsat 7 Enhanced Thematic Mapper Plus, ETM+; Landsat 8-9 Operational Land Imager, OLI; Sentinel-2 Multispectral Instrument, MSI).

LiDAR

Light detection and ranging systems (LiDAR) generate laser pulses (active system) and record how long they take to bounce back to the sensor. This information is used alongside sensor motion data to determine the 3D position of surfaces. When pulses return, the instrument can register the complete profile (full waveform), or just the position of steep rises in the energy received (discrete return; Lefsky et al., 2002). The pulse recording employed varies depending on the platform. Spaceborne LiDAR sensors record the full waveform, whereas data from aerial laser scanners (ALS) usually is distributed as discrete-returns for data storage reasons. LiDAR system represent a powerful tool for

describing forest biomass and forest canopy structure (e.g., vertical distribution, fractional canopy cover, etc.; Lefsky et al., 2002). However, ALS discrete return systems have the disadvantage of needing costly scanning flight campaigns (Barrett et al., 2016; Beland et al., 2019), whereas spaceborne full-waveform systems have the disadvantages of having sparse sampling, and being sensitive to cloud coverage (Simard et al., 2011; Dubayah et al., 2020).

Synthetic Aperture Radar, SAR

Radar sensors use microwave pulse emission and echo reception to ascertain the position and characteristics of the objects. Most forestry applications use the specific subgroup of imaging radars. They emit coherent pulses (same wavelength and phase) at microwave wavelengths (Table 0.1), allowing day-and-night, and nearly all weather capabilities (heavy rain may alter the return; Doblas et al., 2020). Interaction with targets is conditioned by the wavelength and polarization of the wave (orientation of the electrical field with respect to direction of propagation). Shorter wavelengths interact more with smaller elements (leaves, twigs), whereas longer wavelengths interact more with larger elements (branches, trunks; Woodhouse, 2006; Brolly and Woodhouse, 2013). The wavelengths are regulated by a standard naming convention (Table 0.1; Flores et al., 2019; IEEE Radar Systems Panel, 2020).

Table 0.1. IEEE Standard Letter Designations for Radar-Frequency Bands. UHF also is commonly called P-band (Flores et al., 2019; IEEE Radar Systems Panel, 2020)

Band	X	C	S	L	UHF (P)
Wavelength (cm)	8 – 12	4 – 8	2 – 4	1 – 2	0.3 – 1
Frequency (GHz)	3.8 – 2.4	7.5 – 3.8	15 – 7.5	30 – 15	100 – 30

Pulses interact more with targets with the same orientation, for example, horizontally polarized waves interact more with horizontally oriented targets. Echoes may return with the same polarization of the generating pulse (co-polarized backscatter), or with a polarization perpendicular to the original one (cross-polarized backscatter). For example, Sentinel-1 sends pulses with vertical polarization, and can recover echoes with vertical (VV, co-polarized) or horizontal polarization (VH, cross-polarized, V sent, H received). Loss of polarization is frequently associated with multiple bounces within an array of scatterers, such as forest canopy (volume scattering).

Once the sensor receives the echoes it records their amplitude, phase, and return time for each polarization. This data is organized as a “echo table” and requires digital signal processing to become an image. Image generation (focusing) from the echo table is linked to sensor operation and works differently in the pointing direction of the sensor (range) and the sensor movement direction (azimuth). Position in range direction is determined based on echo return timing. This is the reason why both real and synthetic aperture radars have a side looking configuration. Looking from the nadir would cause similar return times at both sides of the beam, creating an ambiguity (Ulaby and Long,

2014). Side-looking solves this issue increasing the distance differences within the illuminated area. However, side-looking has the trade-off of increasing beam occlusion in mountainous areas, an effect called shadowing (Woodhouse, 2006). In range direction resolution depends on how well pulses can be separated. In this context shortening pulse length can increase resolution, albeit there is a limit imposed by power constraints. Another possible solution is to modulate the frequency of the outgoing pulses ("chirped" pulses), making them easier to identify, shortening effective pulse length (Woodhouse, 2006, pp. 217–231; Tanase, 2010, p. 9).

Position in azimuth direction (along-track) is based on sensor movement. In the case of real aperture radars (RAR) imaging in azimuth direction works by imaging 'slices' as thick as the beam width: two objects only can appear separately if the distance between them is larger than the beam width. Beam width depends on the wavelength employed, the distance to targets and the antenna size. Instruments with larger antennas have thinner beams and can generate images with a higher resolution. However, increasing distance to targets requires a proportional increase in antennas size to maintain high resolution. Thus, a spaceborne high-resolution RAR system would need an impossibly large antenna. Synthetic aperture radar systems (SAR) use a different approach. Instead of relying on thin 'slices' SAR systems use a wide beam and determine object azimuth position using the doppler shift caused by sensor movement. Successive pulses reaching a specific point will generate echoes with a different phase shift, information that can be used during focusing to improve azimuth resolution.

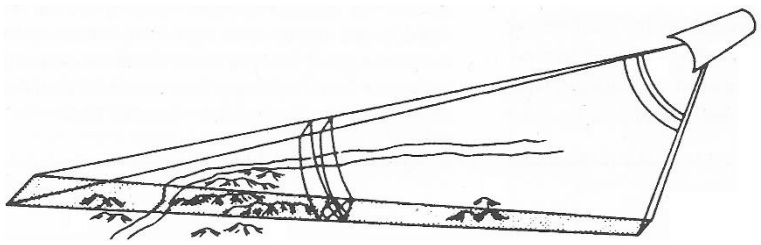

Real Aperture Radar (RAR)

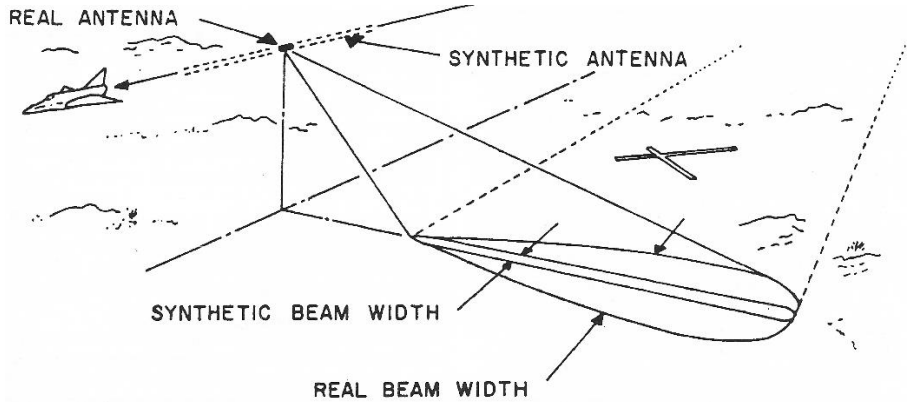

Synthetic aperture radar (SAR)

Figure 0.4. Sketch diagrams illustrating the operation of side-looking radar systems (Modified from Henderson and Lewis, 1998).

Image properties are linked to the acquisition and formation process which introduce some shortcomings, such as geometric distortions or a noise-like effect called speckle. Geometric distortions are caused by alterations in echo spacing caused by topography. Echoes return closer for slopes facing toward the sensor, causing these areas to appear compressed in the image, a distortion called foreshortening. In extreme cases echoes from the top of the mountains can be received earlier than those from the mountain-side, causing an extreme displacement called layover. Conversely, echo distancing increases for slopes facing away from the sensor, making them appear dilated in the focused images. These distortions need to be corrected using a detailed description of Earth surface, a digital elevation model, DEM. In the case of amplitude, correction also involves reducing radiometric distortions using a precise estimate of the scattering area (Small, 2011; Frey et al., 2013; Shiroma et al., 2022).

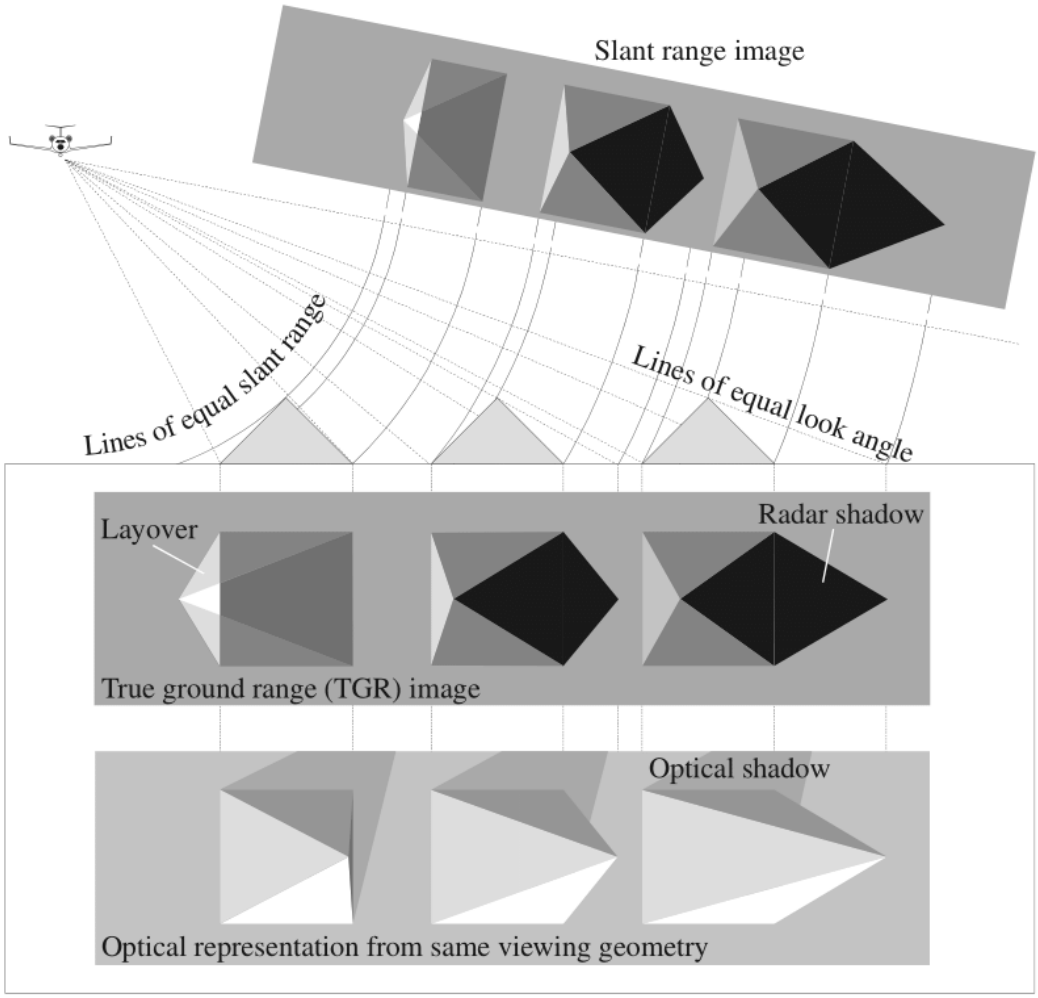

Figure 0.5. Distortions appearing in SAR images (Woodhouse, 2006, p. 283)

Speckle is a phenomenon caused by coherent illumination. Each interaction of the pulses with the scattering elements (physical objects within the illuminated area) generates its own echo. The sensor registers the coherent sum of the individual echoes, introducing a random component in both amplitude and phase. In the case of amplitude constructive or destructive interference result in very large or very low values, a noise-

like effect that hinders interpretation. Speckle amplitude is reduced by sample aggregation (i.e., multi-looking) or the use of sliding window methods (speckle filters). In the case of phase, speckle introduces a random component that can be removed by using several observations (images) acquired with some spatial separation (spatial baseline). These observations can be made simultaneously (single pass, i.e., Shuttle radar Topography Mission, SRTM; Farr et al., 2007; TanDEM-X, Rizzoli et al., 2017), or over time (multi-pass), the most common case for spaceborne SAR sensors. The result is an interferogram, a type of image containing 3D information about earth surface.

Focused images can include both amplitude and phase data for each polarization (the latter is not retained by some focusing procedures). Amplitude depends on target geometry and dielectric constant. In the case of forest, the geometry is affected by the spatial distribution of the trees (Lucas et al., 2006; Shimada et al., 2014a), their canopy architecture (shape, Dobson et al., 1996; height, Siqueira, 2019) and leaf dynamics (Ahern et al., 1993; Frison et al., 2018). Dielectric properties depend mainly on canopy water content and its status (liquid, ice), with temperature and salinity having some influence (Steele-Dunne et al., 2017; Pfeil et al., 2020). Forests tend to depolarize the incoming waves as they bounce several times within the canopy, making cross-polarized channels especially useful to identify forest cover (Shimada et al., 2014a; Ulaby and Long, 2014)

The phase describes the position of the wave vector within a cycle and is mainly related to the distance between the target and the sensor. An interferogram can be used to determine forest height, albeit errors usually are large due the degradation of phase information, a process called decorrelation. Decorrelation is caused, among other factors, by image misregistration between (spatial decorrelation) or changes in target properties between acquisitions (temporal decorrelation) (Martone et al., 2018). Decorrelation itself can be a source of information useful to estimate forest height or biomass using an estimator called interferometric coherence (Siqueira, 2019). In fact, forest produce volume decorrelation, a phase information loss due multiple bounces within the canopy. In the absence of other decorrelation factors the interferometric coherence has been employed to identify forest cover (Martone et al., 2018).

Albeit SAR data is not routinely employed by NFIs, it was proven to be useful in several large area studies (Barrett et al., 2016). Global forest maps of forest presence/absence have been generated using amplitude (Shimada et al., 2014a) and single-pass interferometric coherence (Martone et al., 2018). Relationship of radar return with forest aboveground biomass was determined early on (Attema and Ulaby, 1978) and has been employed by several large-area biomass mapping projects (Wagner, 2003; Reiche et al., 2010; Santoro et al., 2010; Schmullius et al., 2010). Recently, the CCI biomass initiative was launched with the objective of creating a global map of aboveground biomass (Santoro and Cartus, 2021). Regarding experimental applications, SAR data has been found to be sensitive to canopy closure (Lucas et al., 2006), structure (Dostalova et al., 2016),

forest loss and recovery (Tanase et al., 2011; Belenguer-Plomer et al., 2019) or forest health (Tanase et al., 2018).

Forest status and monitoring in Romania

The kingdom of Romania proclaimed its independence in 1877 (Encyclopedia Britannica, 2022), publishing its first forest code shortly after, in 1881 (Catrina and Giurgiu, 1983; Giurgiu, 2011; Lawrence, 2009). To meet the need of forestry professionals a specialized faculty opened in Bucharest (1883), staffed by French scholars (Stanescu and Negrutiu, 1983; Turnock, 1988). The forest code also stimulated scientific activity, with the first run of the *Revista pădurilor* (journal of forests) in 1882, and the foundation of the group *Progresul silvic* (silvicultural progress) in 1886, that would continue publishing the journal to this day (Turnock, 1988; Giurgiu, 2011).

The forest code was reformed in 1910 to prevent forest loss and 1923 to reflect the incorporation of Transylvania in greater Romania (Turnock, 1988; Lawrence, 2009; Roşculeţ, 2011). However, forest cover continued to decrease during the First World War due the high demand for timber (Munteanu et al., 2016; Turnock, 1988). In 1930 Romania set up the Autonomous House of State Forests (*Casa Autonoma a Padurilor Statului*, CAPS) to regulate forest exploitation (Catrina and Giurgiu, 1983). Said institution was directed by Marin Drăcea, an accomplished scholar influenced by the German and the American schools of forestry. Three years later he setup the Institute of forestry research and experimentation (*Institutul de Cercetari si Experimentari forestiere*, ICEF) (Catrina and Giurgiu, 1983; Turnock, 1988).

Clear-cutting continued during the Second World War, pressing the Romanian government to pass a law to reduce deforestation and enforce replanting (Turnock, 1988). After the war the country remained under the occupation of the red army, and the Romanian communist party seized power in 1947 (Encyclopedia Britannica, 2022). In 1948 all forest properties were nationalized; all forest were managed through central planning based on decadal management plans (Munteanu et al., 2016). After the war, the Soviet Union demanded large reparations for the participation of Romania on the German side. Part of said reparations were paid with timber, whose extraction cleared large areas of forest (Nita et al., 2018). Albeit reparations were paid in full in 1956, deforestation increased again in the period 1983-1985 to pay off loans from the International Monetary Fund (Ban, 2012; Munteanu et al., 2016). The communist regime imposed harsh austerity measures to pay said debts, impoverishing the population (Deletant and Ionescu, 2004; Ban, 2012).

After the fall of the communist regime in 1989 a series of laws were passed to restitute forest lands to their original owners. After each restitution law (passed in 1991, 2000 and 2005) a surge in deforestation has been observed (Griffiths et al., 2012). The reason for said increase can be attributed to several factors, such as the slow and chaotic way restitution was performed, uncertainty about its legal persistence, economic hardships

and lack of knowledge or attachment (Mantescu and Vasile, 2009; Griffiths et al., 2012). Tree felling decreased after a period of reforms, such as the implementation of private forest management structures or the legislative changes associated with the admission into the European Union (Griffiths et al., 2012)

Romania Forest Monitoring system started in 1990, when the country participated in the first MPFCE and became a member of the ICP – Forests network. Level I network implementation started the same year, whereas the Level II was implemented in 1994. Level I network (European grid) is a 16 x 16 km grid of permanent plots focused on general information about forest status. Level II network is non-systematic, and more focused on research, with intensive research plots placed in representative forest ecosystems (Badea et al., 2013)

Under communism, the forest inventory was based on aggregation of data recorded at stand level during management planning activities. Such inventories were completed at national level in 1965, 1973, 1980 and 1984 (Turnock, 1988; Marin et al., 2010). The large-scale national forest inventory of the Romanian forests started in 2006 and is managed by the successor of the ICEF, the Forest Research and Management Institute (*Institutului de Cercetări şi Amenajări Silvice*, ICAS; currently *Institutul Național de Cercetare-Dezvoltare în Silvicultură* "Marin Drăcea", INCDS). The NFI is based on repeated measurements of a grid of permanent and temporary plots with a 5-year inventory cycle (Marin et al., 2010). It assesses the forest based on both national and FAO definitions, retrieving the necessary information for carbon emission reporting, FAO FRA and FOREST EUROPE (Marin et al., 2016). The first cycle took place in the period 2008-2012, and the second in the period 2013-2018 (Marin et al., 2016; Ciceu et al., 2019).

Despite the hardships of its history, Romania is one of the European countries with the most diverse tree growing conditions (Veen et al., 2010), and the largest remnants of primary forests in Europe (Ioras et al., 2009; Veen et al., 2010; Knorn et al., 2012). These areas host large populations of brown bear, gray wolf, and lynx (Ioras et al., 2009; Knorn et al., 2012). Since the admission in the EU a large portion of these areas have been protected by the implementation of the Birds and Habitat EU directives (Iojă et al., 2010; Knorn et al., 2012). Currently, the Romanian forest management faces several challenges including risks associated wind-throws, snow breaks, drought associated stress, and insect outbreaks due the widespread presence of artificial spruce monocultures (Knorn et al., 2012; Griffiths et al., 2014; Nita et al., 2018). In many cases spruce was planted in areas formerly occupied by beech forests, where spruces have more difficulties growing, making trees vulnerable to windfall or diseases (Turnock, 1988; Anfodillo et al., 2008; Knorn et al., 2012; Griffiths et al., 2014). Furthermore, altering disturbance regimes associated with the climate change may increases the areas affected by natural hazards, (United Nations, 1992c). Apart of natural hazards, residual illegal logging affected the Romanian forests (Klawitter, 2015; Peter, 2015; Ilie, 2016; Walker, 2020). Such activities are difficult to track down due understaffing, the vast areas occupied by

forest and the location in difficult mountainous terrain (Anfodillo et al., 2008; Knorn et al., 2012).

Motivation, objectives, and content

Remote sensing data offers a cost-effective complement to field surveys, providing regular and systematic data over large areas. It can be employed to determine forest cover, its status, and to generalize forest variable measurements such as biomass. However, each remote sensing technique faces unique challenges over the Romanian territory. Optical and spaceborne LiDAR sensors are limited by the frequent cloud cover, affecting over 60% of observations and as high as 70 or 80% over specific regions (Figure 0.6). Furthermore, high-resolution sensors with frequent coverage had important limitations (Sentinel-2 Geolocation error; Clerc and MPC Team, 2018; limited performance of cloud masks; Skakun et al., 2022), reason why the thesis focuses on the use of SAR sensors. Therefore, **the objective of this thesis was to retrieve widely exploited forest variables such as cover, type and biomass by taking advantage of active remote sensing sensors.**

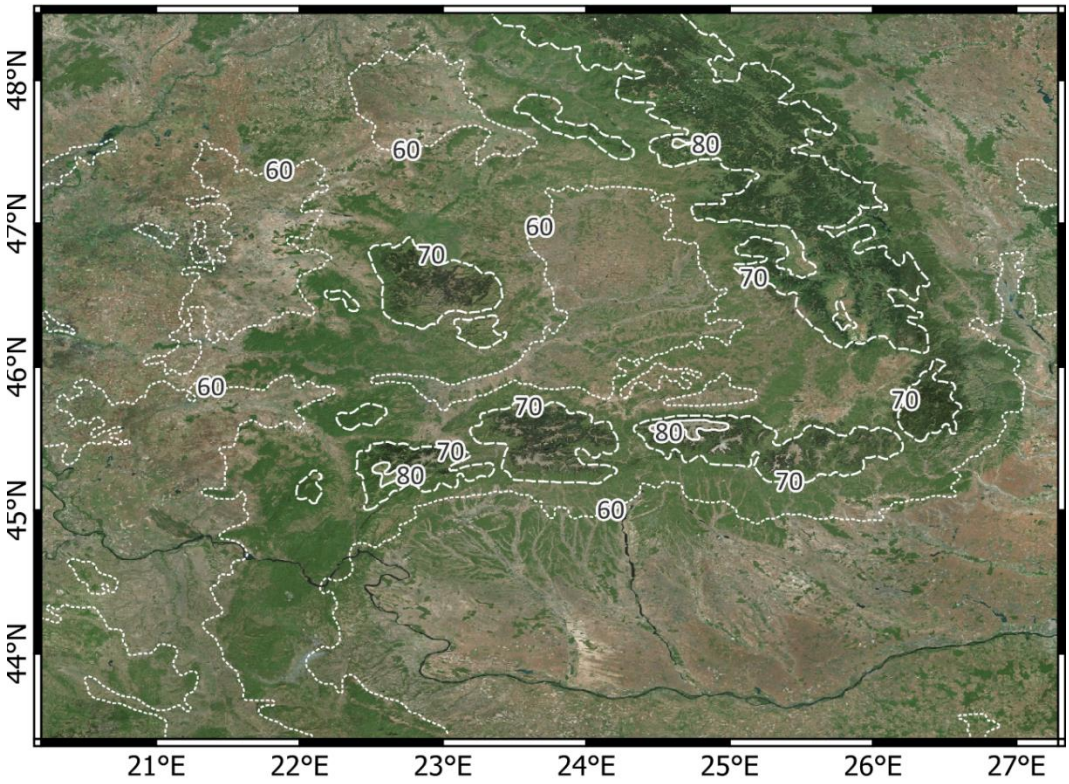

Figure 0.6 Simplified isolines of average cloud cover over the main forested areas of Romania with a 10% step. Cloud cover dataset was generated by Wilson and Jetz (2016) using 15 years of MODIS observations. Background imagery courtesy of Bing maps.

In the Southern Carpathians SAR sensors are limited by the ruggedness of the terrain, which results in image geometric and radiometric distortions. The **first part** of the thesis is, therefore, devoted to data preprocessing to ensure distortions are reduced and spatial coverage is maximized. **Chapter 1** analyzes the influence of the elevation model for

radiometric normalization and interferometric processing. As many slopes were distorted, masking large areas was a necessity. Reducing masked (no data) area through mosaicking was therefore crucial for wall-to-wall mapping, an aspect treated in **Chapter 2** where several methods for combining images acquired from different orbital tracks are tested together with their impact on the retrieval accuracy forest/non-forest classification.

The **second part** of the thesis is dedicated to the detection and mapping of forest presence. The **third chapter** assesses whether features based on interferometric coherence may improve the quality of forest cover classification. The **fourth chapter** assesses the possibility of monitoring selective logging using Sentinel-1 and -2 time series.

The **third part** is focused on forest variable extraction as in the **fifth chapter** a novel method that leverages backscatter coefficient directional effects is proposed for forest type classification while the **sixth chapter** focuses on above ground biomass estimation using synergies between Sentinel-1 and ALOS PALSAR**.**

Chapter 1: Investigating the impact of Digital Elevation Models on Sentinel-1 backscatter and coherence observations

Borlaf-Mena, I., Santoro, M., Villard, L., Badea, O., Tanase, M.A., 2020. Investigating the Impact of Digital Elevation Models on Sentinel-1 Backscatter and Coherence Observations. Remote Sensing 12, 3016. https://doi.org/10.3390/rs12183016

Abstract

Spaceborne remote sensing can track ecosystems changes thanks to continuous and systematic coverage at short revisit intervals. Active remote sensing from synthetic aperture radar (SAR) sensors allows day and night imaging as they are not affected by cloud cover and solar illumination and can capture unique information about its targets. However, SAR observations are affected by the coupled effect of viewing geometry and terrain topography. The study aims to assess the impact of global digital elevation models (DEMs) on the normalization of Sentinel-1 backscattered intensity and interferometric coherence. For each DEM, we analyzed the difference between orbit tracks, the difference with results obtained with a high-resolution local DEM, and the impact on land cover classification. Tests were carried out at two sites located in mountainous regions in Romania and Spain using the SRTM (Shuttle Radar Topography Mission, 30 m), AW3D (ALOS (Advanced Land Observation Satellite) World 3D, 30 m), TanDEM-X (12.5, 30, 90 m), and Spain national ALS (aerial laser scanning) based DEM (5 m resolution). The TanDEM-X DEM was the global DEM most suitable for topographic normalization, since it provided the smallest differences between orbital tracks, up to 3.5 dB smaller than with other DEMs for peak landform, and 1.4–1.9 dB for pit and valley landforms.

1.1 Introduction

Synthetic aperture radar (SAR) is an active imaging system with several advantages over optic sensors, such as Landsat OLI (Operational Land Imager) or Sentinel-2 MSI (MultiSpectral Imager). SARs are independent of solar illumination and use wavelengths that can penetrate cloud cover and have unique interactions with ground targets. Furthermore, the capability to transmit and receive signals enables the use of both phase and polarization information, to monitor, among others, landslides, avalanches, snowmelt, and forests (Ouchi, 2013). Terrain orientation affects the intensity of the backscattered signal based on lambert cosine law. The signal is further affected by the terrain scattering area. The SAR technique uses the return time to convert a table of recorded echoes into an image (focusing). These times are shortened in sensor-facing steep slopes, caus-

ing echoes to overlap and slopes to appear shortened in the focused image (a pixel represents more area). Both effects can be compensated for by using the acquisition geometry parameters and a digital elevation model (DEM). We refer to this compensation as topographic normalization. The backscattered intensity is normalized by accounting for the scattering area and the local incidence angle (Frey et al., 2013; Small, 2011). The coherence normalization is based on removing the topographic phase component from the interferogram before estimation (Askne et al., 1997). Normalization results are heavily dependent on the DEM characteristics and quality (Small, 2011; Frey et al., 2013) as they can be generated using different data sources, including remote sensing (optic, SAR, airborne laser scanning—ALS), and processing techniques (ALS point cloud, stereography, interferometry, and radargrammetry).

ALS uses the delay between emission and reception of light pulses to determine the 3D position of objects. When the pulses return, the instrument registers an intensity profile, which can be completely (full-waveform) or partially recorded (discrete return, i.e., the position of the leading edge before the peak) (Lefsky et al., 2002). Airborne discrete return systems have become the source of national elevation datasets for many countries (CNIG, Centro Nacional de Información Geográfica, 2014; ODP, 2019). Spaceborne full-waveform Light Detection and Ranging (space LiDAR, such as the ICESat, Ice, Cloud, and land Elevation Satellite) data have also been employed in the context of topographic mapping as a primary source for calibration or validation of global elevation datasets derived from other sensors (Shuman et al., 2006; Tadono et al., 2014). However, global topographic mapping from space based on LiDAR is difficult, due to the sparse sampling, and the sensitivity to cloud cover.

Stereoscopic techniques are based on differences in the line of sight to objects (parallax) for common points (tie-points) in an overlapping set of images. Results are dependent on tie-point quantity, image contrast, noise, and features (such as shadows and homogeneous surfaces), which may pose problems (Felicísimo, 1994; Aber et al., 2010; Purinton and Bookhagen, 2017). These techniques have been applied over aerial (Aber et al., 2010; CNIG, Centro Nacional de Información Geográfica, 2014) and satellite optical images (Tachikawa et al., 2011; Tadono et al., 2014), as well as SAR imagery (i.e., radargrammetry) (Felicísimo, 1994; Woodhouse, 2006). Stereoscopic processing of optical images was used to generate the ASTER global DEM (ASTER GDEM) and the ALOS (Advanced Land Observation Satellite) World 3D Digital Surface Model (ALOS AW3D DSM). The ASTER GDEM was created using imagery from the Advanced Spaceborne Thermal Emission and Reflection Radiometer (ASTER) onboard the Terra satellite. ASTER stereo pairs were formed from two near-infrared images (nadir, backward) with 15m resolution. The AW3D DEM was based on data from the Panchromatic Remote-sensing Instrument for Stereo Mapping (PRISM) onboard the ALOS. PRISM stereo acquisitions were formed with three panchromatic images (forward, nadir, backward) with 2.5 m resolution. In both cases, the most challenging task was masking clouds, snow, ice, or water

on every acquisition (Tadono et al., 2014) to avoid the introduction of outliers. Afterwards, images from each individual acquisition were matched, and elevation was calculated. All height estimates from individual acquisitions were stacked to ensure continuity and reduce noise (Tachikawa et al., 2011; Tadono et al., 2014). The AW3D was corrected for biases using preexisting data, such as ICESat shots and the preexisting Shuttle Radar Topography Mission (SRTM) DEM (see next paragraphs) (Tadono et al., 2014).

Even though the processing chains for ASTER GDEM and AW3D were similar, their accuracies are different. Studies comparing global DEMs based on ground control points (GCP) report that the ASTER GDEM has larger uncertainties and is affected by striping, hummock-like artifacts, and outliers (Purinton and Bookhagen, 2017; Hirt et al., 2010; Florinsky et al., 2018; Grohmann, 2018). These artifacts may stem from the tie point generation, the choice of band (NIR), its relatively low spatial resolution (Florinsky et al., 2018; Grohmann, 2018), or unremoved cloud patterns (Hirt et al., 2010). AW3D performed better, although hillslope and step-like artifacts (scene mismatch) have been found (Purinton and Bookhagen, 2017; Florinsky et al., 2018; Grohmann, 2018; Santillan and Makinano-Santillan, 2016; Courty et al., 2019).

SAR interferometry uses two co-registered SAR images acquired from close orbits. The interferogram (i.e., the phase difference between the two SAR images) relates to the 3D position of each target on the ground. Thereof, an interferogram reproduces the topographic information, which appears in the form of fringes as phase is measured between 0 and 2π. To obtain absolute phase values, from which elevation can be estimated, the interferogram is unwrapped. Unwrapping may be hindered in areas of steep topography or areas affected by the lack of coherence between images in consequence of changes between acquisitions (wind-induced motion, precipitation, etc.) (Ouchi, 2013; Woodhouse, 2006). SAR interferometry was used to generate two global DEMs, the SRTM DEM, and the TanDEM-X DEM.

The SRTM acquired data over 80% of the Earth's land surface (60°N–56°S) on an 11-day orbital flight in February 2000. SRTM operated two antennas physically separated in space by 60 m at C-band, as well as X-band. At C-band, a gap-free coverage was obtained with single-pass interferograms. The interferometric height was reconstructed (unwrapping) and re-gridded into map coordinates with variable-resolution smoothing. Data takes were combined using coincident tie points (Farr et al., 2007). The main artifacts of the SRTM dataset were related to striping from uncompensated movements of the mast, voids in correspondence of steep slopes or for low coherence areas, or coarser than nominal spatial detail from the re-gridding step (Grohmann, 2018; Farr et al., 2007; Smith, 2003; Guth, 2006). The global TanDEM-X DEM was generated using SAR data acquired during 2010–2015 by the TanDEM-X and TerraSAR-X satellites flying in formation. Individual scenes were focused, multi-looked (sample averaging) to 10–12 m pixel spacing and unwrapped. The DEM was generated in an iterative process with the first global coverage using data acquisition parameters (baseline) adequate for moderate terrain.

The second global coverage was shifted half a swath, and its unwrapping was aided by the data from the first coverage. Over some areas, further coverages were acquired from a different viewing geometry to avoid errors caused by topographic distortions or volumetric scattering (e.g., forest, desert) (Wessel, 2016; Rizzoli et al., 2017). Areas with height ambiguities were infilled using radargrammetric processing of the scenes. TanDEM-X DEM data are distributed with 12.5 m (0.4 arcsec, original), 30 m (1 arcsec), and 90 m resolution (3 arcsec). The latter was generated by the unweighted average of the overlapping 12.5 m pixels (Grohmann, 2018).

All DEMs are affected by contributions from elements covering the terrain, such as cities or vegetation, thus reporting elevations higher than those recorded for the ground control points (Hirt et al., 2010; Santillan and Makinano-Santillan, 2016). For this reason, elevation refers to surface elevation rather than terrain elevation. For the specific case of vegetation, the main reason for this is the different penetration of each wavelength. On the one hand, the nanometric-scale wavelengths employed for generating photogrammetric DEMs have limited penetration, and thus the tie points and the generated surface tend to reflect canopy surface height. On the other hand, the centimetric wavelengths employed by SAR sensors are able to penetrate further, albeit the scattering center height depends on the frequency employed and the vegetation structure (Farr et al., 2007; Izzawati et al., 2006; Santoro et al., 2005; Thirion-Lefevre and Colin-Koeniguer, 2007). Furthermore, the quality of InSAR-based DEM also depends on the spatial and temporal baselines, or unaccounted sensor movements.

Despite the rather large range of DEMs available, their effect on terrain normalization is poorly understood. Hoekman and Reiche (2015) suggested that the SRTM 90 m spacing may not be adequate for the radiometric normalization of the SAR backscatter in complex terrains. Recently Truckenbrodt et al. (2019) compared and tested the SRTM (30 and 90 m), AW3D (30 m), and TanDEM-X (90 m) DEMs in the context of radiometric terrain normalization of Sentinel-1 data. They analyzed the deviation of each DEM from the pixel-wise median of all DEMs and performed a regression analysis between terrain flattened γ^0 and the local incidence. The deviation analysis showed that the SRTM DEMs have the smallest difference from the median values, but the 30 m SRTM version had high deviation artifacts at one test site. The same errors were found for SRTM and AW3D, as the latter has been infilled with data from the former due persistent cloud cover. Both AW3D and TanDEM-X DEM contained outliers or noise over water areas. The 90 m TanDEM-X DEM was found to contain several large artifacts in mountainous areas. Regression analysis showed that all the analyzed DEMs largely removed the terrain influence, with complete removal (i.e., slope of 0) being observed in some experiments using higher resolution DEMs (SRTM 1 arcsec, AW3D) (Truckenbrodt et al., 2019).

The objective of this study was to investigate the impact of global DEMs on the normalization of SAR backscatter and coherence observations by Sentinel-1 at two sites characterized by complex topography. To build on previous literature (Truckenbrodt et al.,

2019), we analyzed the performance of 12.5 (resampled to 20 m, see Section 1.3), 30, and 90 m pixel Tandem-X DEMs, along with AW3D (30 m), SRTM (30 m). A very high-resolution (5m) ALS DEM was used to benchmark results. The impact of terrain normalization was assessed by investigating the inter-orbit variability of the observations by land cover and landforms. Then, we evaluated a land cover classification scheme based on the observations normalized for topography.

1.2 Study area and satellite data

The study area consisted of an N-S transect over the Romanian Carpathians (11,700 km^2) and the National Park of Sierra Nevada in Spain (2,360 km^2) (Figure 1.1). We could not add additional sites, due to TanDEM-X scientific proposal area limitations (DLR, 2020). The sites were selected to account for the different vegetation types and structures encountered in the temperate and Mediterranean climates. Due to the more humid climatic conditions, the vegetation in the Carpathians is characterized by denser, taller, and more diverse forest types (broadleaf, needleleaf, mixed) when compared to the sparser and shorter forests dominated by pine species encountered in Sierra Nevada.

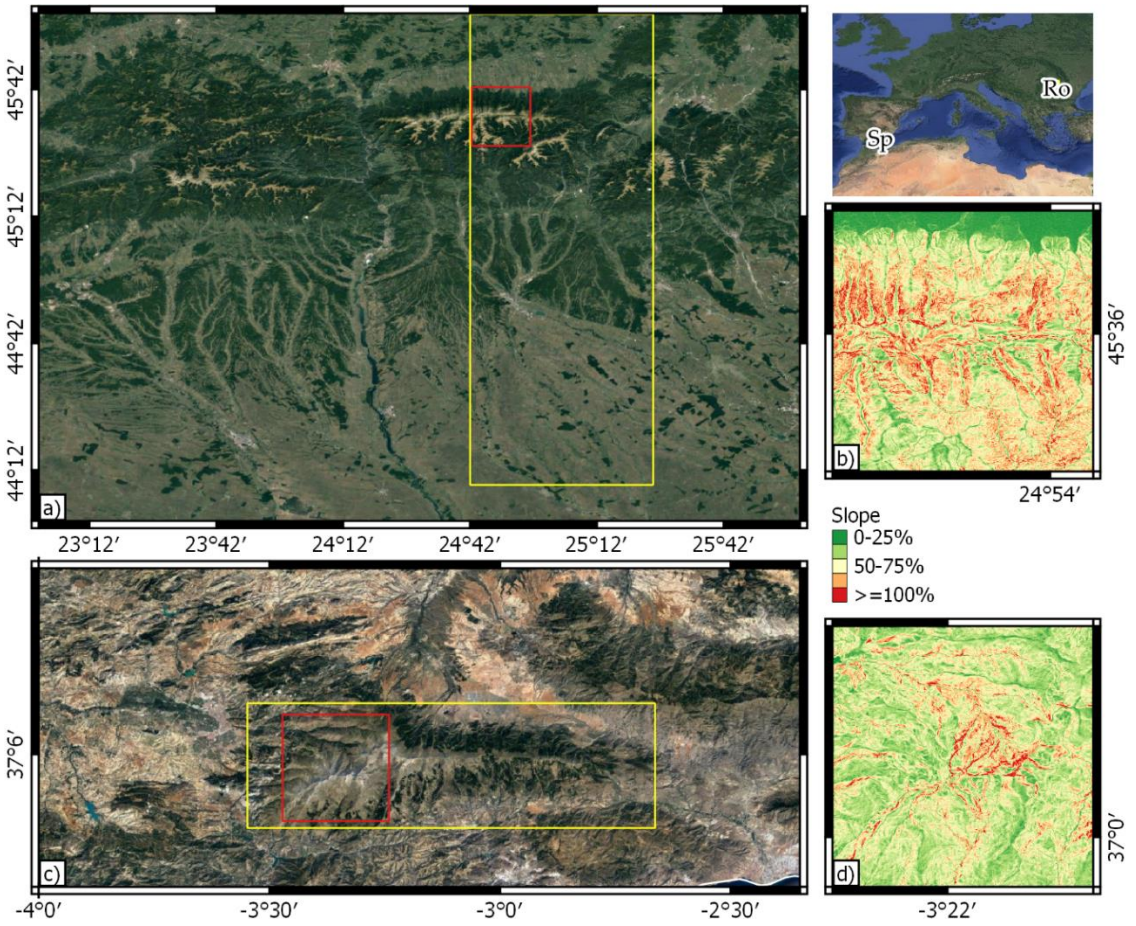

Figure 1.1 Extent of the study areas (a, Romania, Ro; c, Spain, Sp) and digital elevation models (DEMs) used for synthetic aperture radar (SAR) data processing. The yellow box indicates the location of the area covered by the Sentinel-1 dataset used for the analysis. The red box indicates the extent of the subset shown in the right-hand side panels (b, Romania; d, Spain).

Histograms of natural land covers for each site have been plotted to show their frequencies relative to the slopes they occupy (Figure 1.2). Needleleaf and mixed forests occupy steep slopes, whereas grasslands and broadleaf forests occupy moderate slopes at the Romanian site. At the Spanish site, bare and needleleaf forests occupy moderate slopes, although for the former, a significant fraction of the pixels occupy steep or very steep slopes.

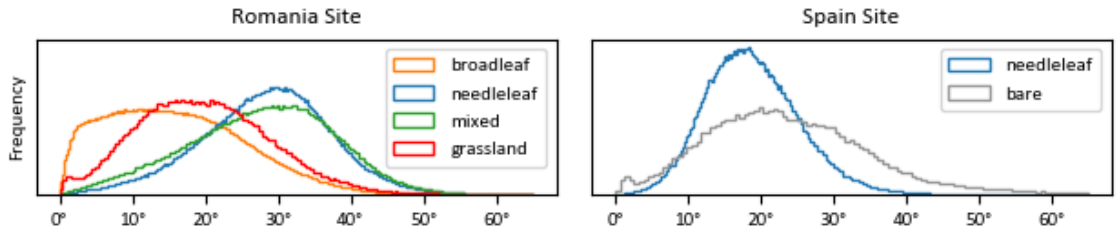

Figure 1.2 Distribution of the slopes for grassland, bare soils, and forest land. The latter has been separated according to leaf type.

For each site, we assembled the SRTM 1-arcsecond, i.e., 30 m, DEM (EROS, 2017) from the United States Geological Service (USGS) Earth Explorer (USGS, 2019), the AW3D 30 m DEM from the Japan Aerospace Exploration Agency (JAXA) Earth Observation Research Center (EORC) (JAXA, 2019) and the TanDEM-X DEM (©DLR 2019) with a pixel spacing of 12.5 m (original resolution), 30 m and 90 m (resampled) from the German Aerospace Agency (DLR, 2019). In addition, for the Spanish site, we used an ALS-based DEM to benchmark the results obtained from three global DEMs. The ALS DEM was available through the Spanish national plan of orthophotography (PNOA) from the National Center of Geographic Information of Spain (CNIG, Centro Nacional de Información Geográfica, 2019a, 2019b). The ALS DEM was created from ALS point clouds with a density of 0.5 returns/m^2. The ALS scan over our study area was performed in 2014 with the LEICA ALS60 sensor. The points were translated from ellipsoidal to ortho-metric heights, assigned color (RGB and near-infrared) from PNOA orthophotographs, and classified automatically using TerraScan (Lorite Martínez et al., 2019; Soininen, 2004). Classification eliminates returns considered noise and filters point to avoid oversampling due to flight strip overlap. Ground points classification is based on slope, rugosity, and return count. Vegetation and Buildings are classified based on height, separating both based on NDVI values. The DEM is generated by calculating the mean value of all ground returns within a 5m pixel (Lorite Martínez et al., 2017). The reported accuracies of the DEM products are presented in Table 1.1.

The SAR dataset consisted of a time series of Sentinel-1 dual-polarized (VV and VH) images acquired in the Interferometric Wide Swath (IWS) mode. The images were obtained in Single Look Complex format (SLC) with a pixel spacing of 14.1 m in azimuth and 2.3 m in range. All SAR images were resampled to a pixel size matching the different DEMs used (see Section 1.3.2). For the Romanian site, 21 images acquired between 2016/12/30 and 2017/02/06 from three relative orbits (7, 29, 131) were used. For the

Spanish site, 18 images acquired between 2018/08/21 and 2018/10/08 from relative orbits 1 and 81 were used.

Table 1.1. Reported accuracies of the DEM used in this study.

DEM Product	Pixel spacing	Accuracy horizontal	Accuracy vertical	Relative vertical Accuracy	Coverage	Reference
SRTM DEM	~30 m	≤ 12.6 m	≤ 9 m	≤ 9.8 m	Near-global (60°N–56°S)	(Rodríguez et al., 2006)
AW3D DSM	~30 m	-	< 7 m	> 3 m (slope ≤ 20%) > 5m (slope > 20%)	Global	(Takaku et al., 2016)
TanDEM-X DEM	~12.5 m	<10 m	<10 m	2 m (slope ≤ 20%) 4 m (slope > 20%)	Global	(Wessel, 2016)
PNOA LiDAR DEM	~5 m	≤ 0.5m	≤ 0.5 m	-	Spain	(IGN, 2016)

1.3 Methods

The following analyses and processes where carried away using the software GDAL/OGR (GDAL/OGR contributors, 2020), GAMMA software (Wegnüller et al., 2016), GRASS (Geographic Resources Analysis Support System) (GRASS Development Team, 2017), Python (Python Software Foundation, 2020), Rasterio (Gillies and others, 2013), Pandas (Pandas contributors, 2020), Geopandas (GeoPandas contributors, 2020), Numpy (van der Walt et al., 2011), Scipy (Jones et al., 2014), and Matplotlib (Hunter, 2007).

1.3.1 DEM assembly

The global DEMs were provided in equiangular geographic coordinates. The SRTM and the AW3D DEMs height reference had to be shifted from geoidal to ellipsoidal heights without resampling. The TanDEM-X (TDX) DEMs were provided as height above the ellipsoid. The Tandem-X DEM at 30 m (TDX30) was used as provided. The Tandem-X 12.5 m DEM was resampled (bilinear interpolation) to 20 m pixel spacing (TDX20) to reduce pixel size difference with respect to the multi-looked Sentinel-1 image. The 90 m resolution Tandem-X DEM (TDX90) was resampled to 30 m (bilinear interpolation). The ALS DEM, originally projected to ETRS89 UTM zone 30N coordinate system, was translated to a height above the ellipsoid and resampled to a 20 m pixel size (bilinear interpolation). As the ALS DEM has not been re-projected, all products geocoded with it (i.e., geocoded Sentinel-1 backscatter) share the same projection.

1.3.2 SAR data preparation

For each SAR image, the SLC sub-swathes were mosaicked, and the resulting image was multi-looked by a factor of 7 in range and 2 in azimuth. The objective was to reduce noise and obtain the SAR backscattered intensity at a pixel spacing close to the target 20 m used for the analysis. For a given orbit, the first acquired image was used as a master. All remaining SAR images from the same orbit were co-registered to the master image using an iterative process based on intensity matching and spectral diversity aided by each DEM (Wegmüller et al., 2002a). For each orbit, the master image was used to generate a lookup table (LUT) relating map and range doppler coordinates. The LUT was

used to orthorectify the master and the co-registered images (interferograms and SAR backscatter) from the same orbit.

Interferograms were generated for each consecutive image pair (a-b, b-c, c-d, etc.), and the DEM-estimated topographic phase was subtracted from each. The interferometric coherence was estimated in a two-step adaptive approach (Wegmüller and Werner, 1996; Werner et al., 2000). The first estimate of coherence was obtained with a 3-by-3 window. To reduce the estimation bias due to the small window size (Touzi et al., 1999), the coherence was then recomputed using a window size inversely proportional to the initial estimate of the coherence. As a trade-off between preserving spatial resolution and reducing the bias, the largest window size was set to 9-by-9 pixels. In addition, when the estimation window included scatterers with a coherence level different than the coherence of the target in the center of the window, the estimator masked out such features to preserve the true coherence of the latter target.

The backscatter coefficient was calibrated to terrain flattened γ^0, considering the scattering area on the ellipsoid and on DEM surfaces (A_{flat} and A_{slope}) (Frey et al., 2013) and the incidence angle on the ellipsoid and on DEM surfaces (θ_{ref} and θ_{loc}), as reported in equation 1 (Castel et al., 2001). The parameter n can be employed to account for volume effects (Castel et al., 2001). The parameter was set to 1, an adequate value for most land cover types, as dealing with volumetric effects was not the objective of this study. The backscatter intensity and coherence images were orthorectified using the LUT and an inverse distance resampling. LUT coordinates located more than two pixels (range) apart to its counterpart on the SAR image were masked as no data. To reduce speckle, the multi-temporal backscatter images were averaged, by polarization, in time. Seven images were averaged for each orbit for the Romanian site, while nine images were averaged for each orbit for the Spanish site. Similarly, the six and eight coherence images were averaged in time for each orbit and polarization for the Romanian and the Spanish site, respectively.

$$\gamma^0 = \sigma^0 \frac{A_{flat}}{A_{slope}} \left(\frac{\cos \theta_{ref}}{\cos \theta_{loc}} \right)^n \quad (1)$$

1.3.3 Auxiliary datasets

In support of the analysis, a land cover dataset was created for each site, based on the agreement between the ESA CCI land cover map (2015) (Kirches et al., 2017), the DLR`s global urban footprint (GUF) (2016) (Esch et al., 2011, 2017, 2018), the ALOS PALSAR forest map (ALOS FNF) (2017) (Shimada et al., 2014b), and either Corine land cover map 2012 (CLC) (Feranec et al., 2016) (Romanian Site) or Spanish information system on soil occupation (SIOSE, 2014) (Del Bosque González et al., 2005) (Spanish site, more detailed and recent) (Table 1.2). ESA CCI land cover maps are generated at 300 m resolution using optical imagery time series from AVHRR, MERIS, SPOT-VGT, and PROBA-V imagery, as well as GlobCover unsupervised classification chain and machine learning (Kirches et al.,

2017). GUF is generated from TanDEM-X imagery at 12 m resolution based on amplitude and texture (Esch et al., 2011, 2017, 2018). ALOS forest map is generated based on local thresholding of annual composites of ALOS PALSAR 1/2 amplitude images (25 m pixel side) (Shimada et al., 2014b). Both CLC and SIOSE are based on photointerpretation of satellite and aerial imagery, with minimum polygon surface of 25 Ha (Feranec et al., 2016) and 1 Ha (SIOSE, Sistema de Ocupación del Suelo de España, n.d.), respectively.

The ALOS FNF disagreed with the remaining data sets as part of the cities were classified as forest, and part of the water was classified as "other" (not water, nor forest). For cities, no ALOS FNF condition was applied, whereas the rest of the non-forest classes on other datasets were considered compatible with non-forest classes from ALOS FNF (non-forest, water). The polygons with the agreement were dissolved by the land cover to eliminate internal borders, and a negative buffer of 40 m was applied to avoid edge effects.

Table 1.2. Composition of the analyzed land covers based on preexisting datasets. When a higher level of Corine Land Cover or SIOSE has been employed (CLC (Corine land cover map) Lvl.1), the rest have been filled as "x". CCI LC forest types are further disaggregated by the fractional cover and were therefore aggregated. GUF, global urban footprint; ALOS FNF, Advanced Land Observation Satellite Forest map; SIOSE, Spanish information system on soil occupation; CODIIGE, Board of directors of the geographic information infrastructure of Spain.

	CLC 2012 (Feranec et al., 2016)	SIOSE 2014 (CODIIGE) (Del Bosque González et al., 2005)	CCI LC 2015 (Li et al., 2018)	GUF 2016 (Esch et al., 2017)	ALOS FNF 2017 (Shimada et al., 2014b)
Urban	1xx: Artificial surfaces	1xx: Artificial surfaces	190: Urban areas	Urban	-
Crops	21x: Arable land	210: Crops (herbaceous)	10, 20: Cropland, 11: Herbaceous cover	Other	Other
Pasture	23x: Pastures	320: Pastures	11: Herbaceous 130: Grassland	Other	Other
Grassland	321: Grassland	320: Pastures	11: Herbaceous 130: Grassland	Other	Other
Bare	33x: Open spaces	354: Bare	200: Bare areas	Other	Other
Broadleaf forest	311: Forest (broadleaf)	311: Forest (broadleaf)	50–62: Tree cover, broadleaved	Other	Forest
Needleleaf forest	312: Forest (needleleaf)	312: Forest (needleleaf)	70–82: Tree cover, needle leaved	Other	Forest
Mixed forest	313: Forest (mixed)	313: Forest (mixed)	90: Tree cover, mixed leaf type	Other	Forest
Water	5xx: Water bodies	5xx: Water bodies	210: Water	Other	Other

The analyses were undertaken in this study are also related to landforms (Figure 1.3), i.e., features of the terrain surface with a distinct and identifiable shape (MacMillan and Shary, 2009). Landforms were labeled using the GRASS GIS add-on "r.geomorphon" (Jasiewicz and Stepinski, 2013), with a search window of 25 pixels and a "flatness" threshold of 5 degrees applied to the highest spatial resolution DEMs available for each site, i.e., the TanDEM-X DEM at 30 m for the Romanian site and the PNOA DEM aggregated to 30 m for the Spanish site.

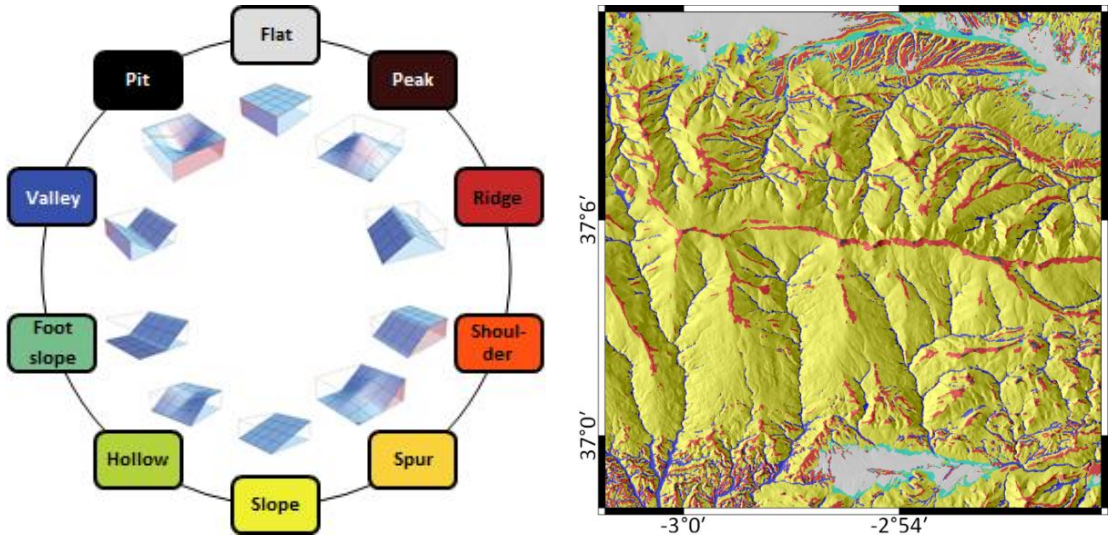

(**a**) (**b**)

Figure 1.3. Landform classification. The general shape of the landforms (a), modified from GRASS documentation, based on (Jasiewicz and Stepinski, 2013) and landforms over the shaded relief for a subset of the Spanish study area (b).

1.3.4 **Inter-orbital data analysis**

The topographic normalization (radiometric terrain normalization, topographic phase removal) and distortion masking (e.g., foreshortening, layover, shadows) of each SAR-derived variable (backscatter coefficients and coherence) were assessed using the inter-orbit range (IOR). IOR was calculated pixelwise for each SAR variable by subtracting the maximum and the minimum values available from all orbits. For example, for a pixel with data available from orbits a, b, and c, the IOR would be $max(a, b, c) - min(a, b, c)$. The inter-orbit range was plotted by land cover class (boxplots). The analysis was repeated by landforms for the needleleaf forest, the only common forest type between both sites, and classes appearing near the mountain tops (grassland, bare). Because the only difference in image processing is the DEM employed, low IOR values reflect improved topographic effects removal.

In addition, the scattering area estimates, backscatter coefficient, and the interferometric coherence obtained using the ALS DEM (the most detailed) were employed as a reference to assess the performance of the global DEMs at the Spanish site. Said assessment was based on the root mean square deviation (RMSD, eq. 2), relative RMSD (RMSDrel, eq. 3), mean absolute deviation (MAD, eq. 4), and Offset (eq. 5) for the products obtained from the global DEMs.

$$RMSD = \sqrt{\frac{1}{P}\sum_{p=1}^{P}\left(v_p - r_p\right)^2} \quad (2)$$

$$RMSDrel = \frac{RMSD}{\bar{r}} \quad (3)$$

$$MAD = \frac{1}{P}\sum_{p=1}^{P}|v_p - r_p| \quad (4)$$

$$Offset = \bar{v} - \bar{r} \quad (5)$$

where P is the total number of pixels, p is a specific pixel and v_n and r_n are the variable values (i.e., backscatter) obtained for said pixel using a global DEM (v) and the reference DEM (r), whereas $\bar{v}$ and $\bar{r}$ are the mean value for said variables.

1.3.5 Land cover classification

A Linear support vector machine (LinearSVM) classifier was selected for its robustness and short execution times. We employed the Scikit-Learn implementation (Buitinck et al., 2013) with default options with a regularization parameter of 1, primal problem optimization, 0.001 tolerance for stopping criteria, and 10.000 iterations maximum. The classifier was trained per orbit/DEM pair using 96,000 samples, using VV- and VH-polarized backscatter and co-pol coherence as features.

For each orbit and land cover class, 70% of the valid sample (foreshortened and shadowed pixels were masked during SAR processing) was used to calculate the median and the median absolute deviation (MAD) of each SAR variable. Median and MAD values were then employed to calculate the z-score for each predictor (VV- and VH-polarized backscatter and coherence) by land cover class. Only samples with an absolute z-score below three were retained. Depending on the land cover class, the number of pixels retained varied from several millions (forest and low vegetation) down to tens of thousands (urban and water). For each class, 12,000 pixels (the number of pixels available for the less extended class, i.e., water) were randomly selected and used for training (n). As low vegetation and forest classes were further split into three sub-classes each (crops, pastures, grasslands, and broadleaf, needleleaf, and mixed forests), the total numbers of training samples selected were thrice as much (3n) as for urban and water land cover classes.

The validation sample, formed by the remaining pixels (30%) of each class, was used to compute the confusion matrix and associated error metrics (i.e., user and producer accuracies, Cohen's Kappa, as described below). Error metrics for valleys were calculated after resampling (nearest neighbor) the landform layer to match the spatial resolution of the DEMs.

The confusion matrix C (equation 6) represents the occurrences of the predicted (rows) against the actual land cover class (columns) ($r \cdot r$ dimensions, where r is the number of classes). Diagonal cells (c_{ii}) count pixels with the same class in the classification and the reference dataset (True Positive, TP). Cells over the diagonal count pixels of class i that have received other class (False Negative, FN), whereas cells under the diagonal count pixels that have been classified as i, when they have other class in the reference dataset (False Positive, FP). Accuracies for a specific class i are the count of correctly classified pixels for the class (c_{ii}) divided by the number of pixels classified as i (count

across columns, c_{i+}), in the case of user accuracy (UA_i, also called 'precision' in machine learning literature, formula 7), or by the number actual i pixels (count across columns, c_{+i}), in the case of producer accuracy (PA_i, also called 'recall' in machine learning literature, formula 8).

$$C = \begin{bmatrix} c_{1,1} & c_{1,j} & c_{1,r} \\ c_{i,1} & c_{i,j} & c_{i,r} \\ c_{r,1} & c_{r,j} & c_{r,r} \end{bmatrix} \tag{6}$$

$$UA_i = precision_i = \sum_{i=1}^{r} \frac{c_{ii}}{c_{i+}} = \frac{TP}{TP + FP} \tag{7}$$

$$PA_i = recall_i = \sum_{i=1}^{r} \frac{c_{ii}}{c_{+i}} = \frac{TP}{TP + FN} \tag{8}$$

Cohen's Kappa (Cohen, 1960) is a measure of agreement between the predicted cover and the one appearing on the reference dataset.

$$\widehat{K} = \frac{N \sum_{i=1}^{r} c_{ii} - \sum_{i=1}^{r} (c_{i+} \cdot c_{+i})}{N^2 - \sum_{i=1}^{r} (c_{i+} \cdot c_{+i})} \tag{9}$$

where r is the number of rows, c_{ii} is the number of pixels where there is agreement between the classification and the reference dataset (cells on the diagonal, with row i and column i), c_{i+} and c_{+i} are the totals for row i (count of pixels classified as i) and column i (count of reference pixels with class i), and finally, N is the total number of observations (Congalton, 1991). A Kappa value of 1 represents the complete agreement between both, 0 represents a classifier performance similar to random guessing, and values under 0 indicate results worse than random guessing.

1.4 Results

In Sections 1.4.1 and 1.4.2, we show results of the IOR analysis by land cover and landform, respectively, Section 1.4.3 contains the ALS reference-based analysis, and Section 1.4.4 describes the results of the classification comparison. Through sections 1.4.1 to 1.4.3, coherence showed very small differences based on the DEM employed, under 0.01 for the IOR based analyses, and under 0.02 for ALS reference-based analysis. For this reason, these tables have been omitted, as they carried little to no information.

1.4.1 Inter-orbital range by land cover

The inter-orbit range (IOR, Table 1.3) was analyzed as an indicator of the residual terrain influence on the normalized SAR metrics (higher IOR, higher influence). The mean IOR for urban cover varied very little between DEMs, except for TDX90. Crops and broadleaf forests presented little difference (up to 0.3 dB) depending on the DEM employed, but increased for mixed forests (0.5 dB, Carpathians), and classes appearing near mountain peaks, such as grassland (0.6 dB) and bare soil (1 dB). Needleleaf forests had similarly high differences at the Romanian site (0.7 dB), whereas they were lower at the Spanish site (0.4 dB). TDX20/30 was the global DEM with the lowest IOR, whereas the highest IOR values were observed for the TDX90 DEM, followed by SRTM DEM. Results with

AW3D over natural covers (bare, grasslands, forest) varied depending on the site: At the Romanian site, its IOR was close to SRTM or TDX90 values; whereas at the Spanish site, it was closer to the values obtained with TDX20/30 DEMs. ALS-based PNOA DEM had the lowest IOR, with a large improvement over results with SRTM or TDX90 (up to 1.2 dB for bare areas, up to 0.5 for needleleaf forest), and a slight improvement over TDX20 results (0.2 dB for bare areas, and 0.1 dB for needleleaf forest). IOR values for PNOA and TDX20/30 DEMs showed less spread (Figure 1.4), concentrating around lower values, whereas the spread was larger for SRTM and TDX90. The main differences between sites were the lower spread of IOR at the Spanish site, and the behavior of AW3D IOR, which was closer to the TDX20/30 values at the Spanish site, but closer to SRTM/TDX90 values at the Romanian site.

Table 1.3. Backscatter Inter-orbit range (IOR) by polarization and land cover class at each study site (GL, grassland; BLF, NLF, and MLF, are broadleaf, needleleaf, and mixed forest). Cell color shows the gradient between the lowest (green) and the highest value (yellow). "M.D." column represents the maximum difference between global DEMs for each specific land cover.

	Romania						Spain						
	AW 3D	SR TM	TDX 20	TDX 30	TDX 90	M. D.	AW 3D	SR TM	TDX 20	TDX 30	TDX 90	ALS	M. D.
Urban	5.4	5.4	5.3	5.4	6.9	1.6							
Crops	2.3	2.3	2.2	2.2	2.3	0.1	1.3	1.4	1.3	1.3	1.5	1.2	0.2
GL	3.4	3.4	2.9	3.1	3.5	0.6							
Bare							3.1	3.5	2.9	3.1	3.9	2.7	1.0
BLF	2.0	2.0	1.7	1.8	2.0	0.3							
NLF	2.5	2.5	1.8	1.9	2.5	0.7	1.2	1.5	1.1	1.2	1.5	1.0	0.4
MLF	2.4	2.4	1.9	2.0	2.4	0.5							

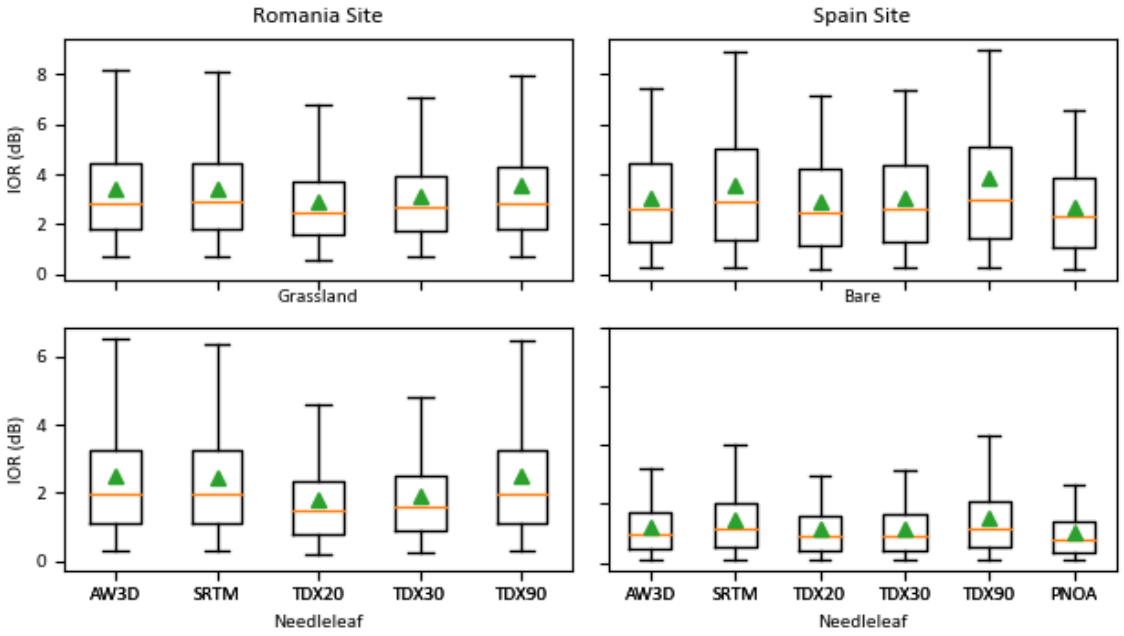

Figure 1.4. Boxplot representing the VV backscatter IOR for grassland, bare areas, and needleleaf forests at both sites: Mean and median values (green triangle, orange line) and inter quantile-ranges (whiskers) for 5–95%.

1.4.2 Inter-orbital ranges by landform

Analyzing IOR values by land cover may have dampened potential differences as all pixels, regardless of landform, were averaged by class. A more detailed analysis was conducted by disaggregating mean IOR values by landforms for the grassland, bare land, and needleleaf forests (Table 1.4 and Table 1.5). These classes were selected as they often occur on steep slopes (Figure 1.2). Only landforms with more than 1,000 pixels have been analyzed to limit spurious results, due to small sample size.

Table 1.4. IOR values disaggregated by landform for classes on mountain tops (grasslands, Romania; bare, Spain). Cell color shows the gradient between the lowest (green) and the highest value (yellow) for each row, which represents the IOR value for a specific landform when a certain was DEM employed. "M.D." column represents the maximum difference between global DEMs for each specific landform.

	Romania (grasslands)						Spain (bare)						
	AW3D	SRTM	TDX 20	TDX 30	TDX 90	M.D.	AW3D	SRTM	TDX 20	TDX 30	TDX 90	ALS	M.D..
peak	3.1	3.0	2.5	2.6	3.5	1.0	2.9	3.3	2.6	2.7	6.1	2.2	3.5
ridge	3.0	2.9	2.5	2.7	3.0	0.5	2.7	3.1	2.5	2.7	3.6	2.3	1.1
spur	3.2	3.2	2.7	2.9	3.1	0.5	3.1	3.4	2.9	3.0	3.9	2.7	1.0
slope	3.6	3.6	3.0	3.3	3.6	0.6	3.3	3.7	3.1	3.3	3.8	2.9	0.7
hollow	4.2	4.3	3.6	3.9	4.6	1.0	3.2	3.8	3.1	3.2	3.9	2.8	0.8
valley	4.5	4.7	4.1	4.4	5.5	1.4	3.0	3.4	2.9	3.1	4.7	2.6	1.8

Both grasslands and bare areas presented large differences between DEMs. In the case of grasslands, the landforms valley, hollow, and peak showed the largest differences between DEMs (1.0–1.4 dB). In the case of bare areas, peak and valley showed the largest differences (3.5 dB and 1.8 dB, respectively), followed by ridge and spur (1.1 and 1.0 dB). For needleleaf forest, the largest differences between DEMs were observed for concave landforms (Table 1.5): Hollow (0.8–0.9 dB at either site), valleys (up to 0.8 dB at the Spanish site, and up to 1.4 dB at the Romanian site) and pits (up to 1.9 dB at the Romanian site).

Table 1.5. IOR values disaggregated by landform for needleleaf forests. Cell color shows the gradient between the lowest (green) and the highest value (yellow) for each row, which represents the IOR value for a specific landform when a certain was DEM employed. "M.D." column represents the maximum difference between global DEMs for each specific landform.

	Romania						Spain						
	AW3D	SRTM	TDX 20	TDX 30	TDX 90	M.D.	AW3D	SRTM	TDX 20	TDX 30	TDX 90	ALS	M.D.
peak	2.3	2.2	2.0	2.1	2.3	0.3							
ridge	2.2	2.2	1.9	2.0	2.2	0.4	1.2	1.3	1.1	1.1	1.3	1.0	0.2
spur	2.2	2.2	1.7	1.8	2.2	0.5	1.2	1.3	1.1	1.1	1.4	1.0	0.3
slope	2.3	2.3	1.7	1.8	2.4	0.7	1.2	1.5	1.1	1.2	1.5	1.0	0.4
hollow	2.8	2.8	1.9	2.0	2.9	0.9	1.4	1.9	1.3	1.4	2.1	1.1	0.8
valley	3.7	3.5	2.4	2.5	3.8	1.4	1.6	2.1	1.5	1.6	2.3	1.2	0.8
pit	4.5	3.9	2.6	2.7	4.0	1.9							

Using the TDX20/30 generally yielded the lowest IOR among global DEMs, whereas using TDX90 yielded the highest. The absolute minimum was always observed when using the

ALS DEM (0.1–0.4 dB lower when compared to TDX20/30). IOR values obtained with the ALS DEM for bare areas were up to 3.9 dB lower when compared to the TDX90 DEM and up to 1.1 dB lower when compared with SRTM. For needleleaf forest, IOR values for valleys using ALS DEM were up to 1.1 dB lower than those obtained with TDX90.

1.4.3 Differences with and ALS-derived DEM

The PNOA ALS-derived DEM provided the lowest IOR in all previous analyses at the Spanish site and was used as a reference for quantitative analysis of the global DEMs (Table 1.6). For the scattering area, the highest deviation (RMSD) was observed for the TDX90, followed by the SRTM DEMs. The relative RMSD obtained with these DEMs was at least 10% higher when compared to the remaining DEMs (TDX20, TDX30, and AW3D). The lowest RMSD were observed for AW3D (orbit 1) and TDX20 (orbit81), followed by TDX30. The MAD for the scattering area was higher when using the SRTM or the TDX90 DEMs when compared to AW3D, TDX30, and TDX20. For both orbits, the SRTM-derived scattering area was the least biased when compared to the ALS DEM (–4 m^2 for orbit 1 and 0.4 m^2 for orbit 81), followed by TDX20 (–11 m^2 for orbit 1 and –12 m^2 for orbit 81).

Table 1.6. Quality assessment for needleleaf forests using PNOA as a reference. Cell color shows the gradient between the lowest (green) and the highest value (yellow).

		O001					O081				
	Statistic	**AW 3D**	**SR TM**	**TDX 20**	**TDX 30**	**TDX 90**	**AW 3D**	**SR TM**	**TDX 20**	**TDX 30**	**TDX 90**
Sc. area (m^2)	**Abs. RMSD**	97	188	102	109	213	115	214	113	123	245
	Rel. RMSD	11%	21%	11%	12%	24%	12%	22%	11%	12%	25%
	MAD	38	81	32	36	87	47	96	38	43	104
	Offset	18	–4	–11	14	–21	25	0.4	–12	20	–18
VV (dB)	**Abs. RMSD**	0.54	0.96	0.63	0.54	2.89	0.56	0.96	0.64	0.55	3.35
	Rel. RMSD	5%	10%	6%	5%	29%	6%	10%	7%	6%	34%
	MAD	0.38	0.64	0.41	0.36	0.74	0.38	0.63	0.41	0.35	0.75
	Offset	–0.19	–0.27	–0.27	–0.17	–0.35	–0.24	–0.30	–0.35	–0.23	–0.41

For both orbits (1 and 81), the use of AW3D, TDX30, and TDX20 DEMs resulted in backscatter coefficient (VV) values closest to those obtained using the ALS DEM, with relative RMSD under 8%. For both orbits, the smallest offset with respect to the ALS DEM was obtained using TDX30, followed by AW3D. In all cases, backscattering coefficient was underestimated when compared with ALS DEM results.

1.4.4 Land cover classification

The DEM used for radiometric terrain normalization and topographic phase removal showed little effect on the overall quality of the classification, regardless of the Sentinel-1 relative orbit (Annex 1-1). The Cohen's Kappa was between 0.94 and 0.96. Analyzing the confusion matrices and the associated error metrics (i.e., user accuracy, UE, producer accuracy, PE) showed that classes with a larger spatial extent (low vegetation or forest) had very high accuracies (>95%). However, most pixels misclassified as low vegetation (>85%) were, in fact, forest pixels according to the reference data. Water had a

reasonable accuracy (>80%). Depending on the DEM, the "source class" of pixels misclassified water pixels varied. When using TDX20 for normalization, 21–27% of misclassified water pixels were recorded as forest pixels on the validation dataset, 20–33% with TDX30, 33–50% with SRTM or AW3D, and 36–58% with TDX90. The urban class had relatively small omission errors (10–15%), but the commission error was high (around 40% for orbit 7, around 60% for orbit 29, and around 50% for obit 31), mostly due to the misclassification of forests (52–78% of the pixels misclassified as urban were forest pixels in the validation dataset).

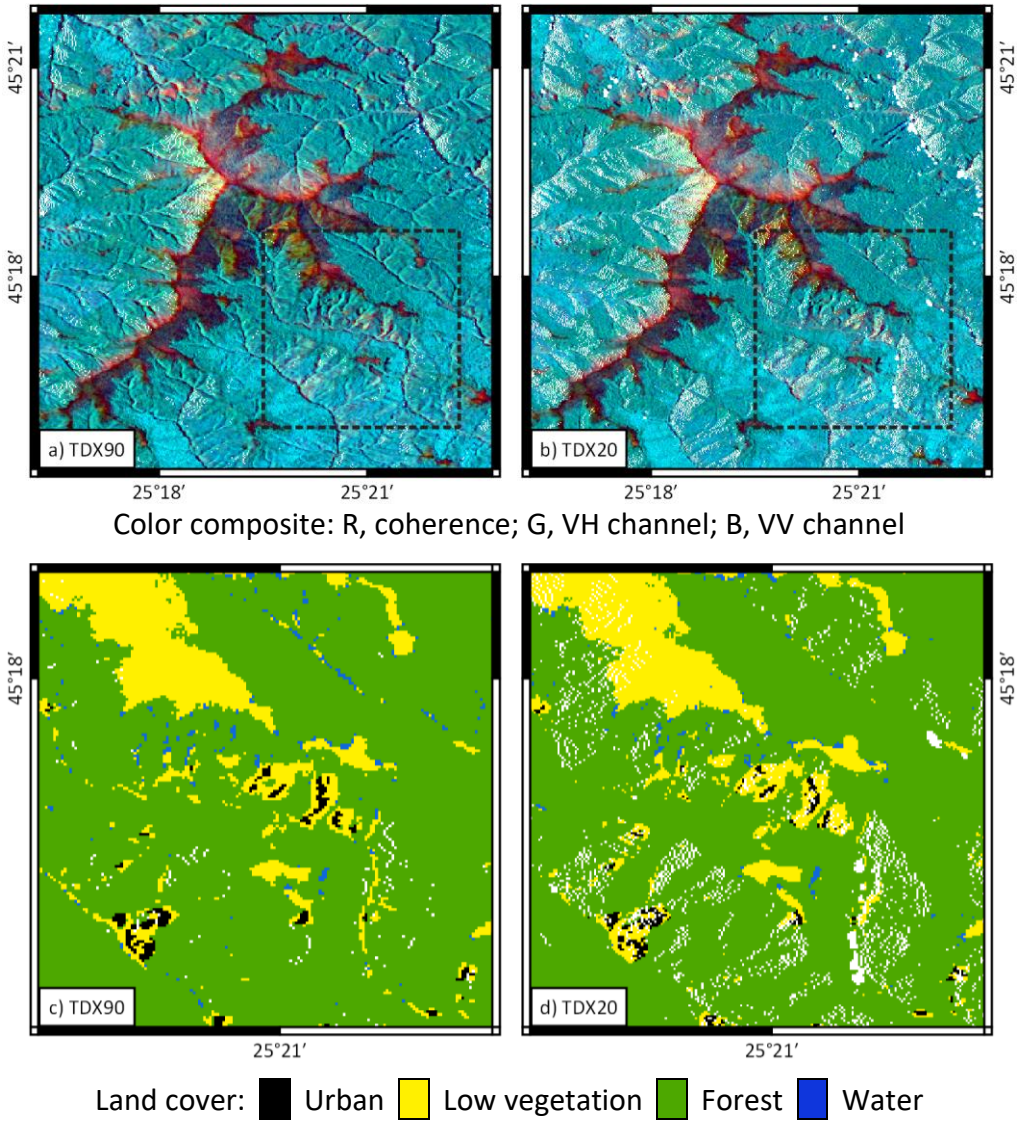

Figure 1.5. A small subset of the data around Leaota Peak. The first row shows the impact of terrain normalization on the imagery (a, b). The dotted box is the area shown for classification maps. The second row represents classified maps (b, c). White pixels indicate no data.

Classification results were also analyzed by landform (Annex 1-2), and in particular, for valleys. Valleys were selected as they showed the largest differences between DEMs in previous tests, and a reasonable number of samples were available (10 times more

when compared to the number of samples available for pit landform). When only valley pixels were considered, Cohen Kappa was low (0.57–0.70). Using the TDX20 DEM allows for a marginal increase of the Cohen Kappa values over the value obtained using the rest of the DEMs (0.05 for orbits 7, 0.03 for orbit 131, and 0.02 for orbit 29). For valleys, user accuracy for low vegetation class dropped. In this context, the use of the TDX20 DEM reduced commission errors up to 11% for low vegetation and up to 21.9% for water when compared to the remaining DEMs (Figure 1.5). Using the TDX20 DEM also reduced the number of forest pixels misclassified as water, representing a smaller percentage of the pixels misclassified as such (17–27% less, depending on the orbit). Commission errors for urban cover increased for valley landform, especially when terrain normalization is performed with any of the TDX DEMs.

The backscatter coefficient (VV) for forests located on valleys was examined to better understand the results obtained with the TDX DEMs (Figure 1.6). The boxplot showed that products normalized using lower resolution DEMs (AW3D, SRTM, TDX90) had an increased frequency of low values on the valley when compared to TDX20/30.

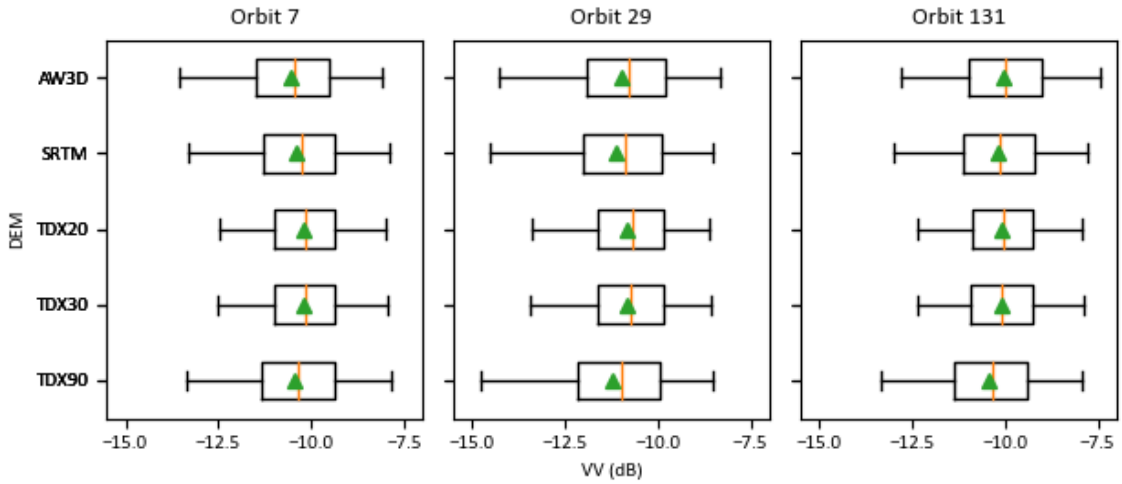

Figure 1.6. Boxplot representing the VV backscatter coefficient for forests located on valleys by Sentinel-1 relative orbit: Mean value (triangle) median value (orange) and inter quantile-ranges (whiskers) for 5–95%.

1.5 Discussion

The influence of the DEM employed for terrain normalization of backscatter and coherence data variability was analyzed in three ways: (a) Comparing several orbital tracks (inter-orbit range, IOR); (b) using the results obtained with an ALS-derived DEM as a reference; and (c) assessing land cover classification results after a specific DEM is employed for normalization. Coherence varied very little with the DEM employed, whereas the effect was larger on the backscatter coefficient.

Terrain normalization was better served by high-resolution DEMs (i.e., TDX20, ALS DEM, AW3D at Spanish site), in agreement with prior research (SRTM-1arcsec and AW3D outperformed SRTM-3arcsec and TanDEM-X 90m; Grohmann, 2018; Truckenbrodt et al.,

2019). Higher resolution DEMs have reduced vertical uncertainties (under 5 m over sloping terrain for TDX12.5 and AW3D) when compared to the SRTM DEM (Table 1.1), which may have contributed to reducing IOR values. Some DEMs (TDX20, TDX90, ALS) needed resampling prior, which may have impacted their performance. TDX20 and ALS DEMs, were down-sampled, which may have reduced the DEM detail with an associated increase of IOR values.

However, the IOR values obtained after resampling was still smaller than those observed for the lower resolution DEMs, underlining the importance of the vertical uncertainty of the original DEM. TDX90 was resampled to a finer resolution. However, as resampling is a destructive operation, the only expected impact was the smooth interpolation of the original data to a denser grid, which does not provide additional information over the original DEM. The advantage provided by high-resolution DEMs was dependent on the specific land cover, and the landform it occupies. For instance, IOR for urban and crops showed little difference, as they occupy near-flat areas.

Land cover classes occupying steeper slopes (i.e., forests, grasslands) received the largest benefits of using a more detailed DEM (minimum IOR). At the Romanian site, broadleaf forests showed smaller differences than mixed and needleleaf forest, as the latter grew on steeper slopes. Variability for needleleaf forests was smaller at the Spanish site, as it occupied milder slopes (Figure 1.2). Results were disaggregated by landform, as the "typical" slope of each land cover might obscure landform related effects. Peak, hollow, valley, and pit landforms showed the largest differences between the analyzed DEMs. Such differences can be attributed to the sensitivity of SAR to remote sensing artifacts, such as shadowing and foreshortening appearing with increasing slope. This affects DEM accuracy in sloped terrain, as shown in Table 1.4 and Table 1.5, propagating into any analysis based on pixel neighborhood, such as slope, orientation (Purinton and Bookhagen, 2017), or terrain normalization. On these landforms, TDX20/30 clearly outperformed the rest of the DEMs, as it provided an improved characterization of smaller terrain forms supporting results reported by Grohmann et al. (2018).

The use of an ALS-derived DEM resulted in the smallest IOR, pointing it as a suitable candidate to benchmark global DEMs at the Spanish site. Taking the ALS DEM as a reference, the lowest deviation and bias of the SAR metrics were observed for the AW3D and TDX20/30 DEMs. The results obtained by AW3D were explained by the combined effect of the resolution employed for its generation (5 m) and the low cover and height of Mediterranean forests. These factors may have eased the detection of vegetation-free pixels, "pushing" the reported data nearer to the true terrain surface once resampled to 30 m, as described by References (Grohmann, 2018; Santillan and Makinano-Santillan, 2016). TDX20/30 provided similar results thanks to the high spatial resolution of the X-band sensor employed for its creation. In addition, shorter wavelengths (X- as opposed to C-band) can capture finer spatial details (Ouchi, 2013; Woodhouse, 2006; Moreira et al., 2013). In some cases, better results were observed for the

TDX30 DEM when compared to the TDX20 DEM, pointing to a trade-off between the spatial detail and the effect of the DEM noise, with some improvement for slightly coarser resolutions (30 m instead of 20), but a high dispersion when resolution becomes too coarse (TDX 90). TDX90 and SRTM DEMs showed similar dispersion when compared to the ALS PNOA DEM reference values, possibly due to the variable-resolution smoothing (Farr et al., 2007) employed during the reprojection of SRTM to map coordinates, which may have decreased its detail, as shown in References (Grohmann, 2018; Smith, 2003; Guth, 2006).

DEM performance also varied across sites, with a larger inter-track variability being observed for needleleaf forests at the Romanian site. Such differences were explained by the steeper slopes this land cover class occupied in the Carpathians, as well as its characteristics (height and structure), which may have complicated DEM generation, due to volume decorrelation, as reported by References (Farr et al., 2007; Rizzoli et al., 2017): The Carpathians are covered by dense temperate forests, whereas Sierra Nevada is populated by Mediterranean forests with lower tree height and canopy density. Among all DEMs, AW3D IOR had a distinct behavior. While at the Romanian site, the AW3D results were close to those observed to the SRTM DEM, at the Spanish, the results were closer to those observed when using the TDX20/30 DEMs. The quality mask layer showed that, at the Romanian site, the AW3D DEM has a large strip where missing data (due persistent cloud cover) have been infilled with SRTM data, a problem mentioned by Truckenbrodt et al. (2019). For this reason, it is not possible to draw conclusions on the influence of canopy characteristics on the performance of AW3D.

The characteristics of each DEM propagated into the land cover classification results. Overall classification accuracy was similar regardless of the DEM, with reasonable accuracies for all classes except urban. The low accuracy of urban surfaces was attributed to (i) the prevalence of steep slopes, which difficult terrain normalization (not fully accounted scattering area) (Truckenbrodt et al., 2019) and may introduce DEM artifacts (mischaracterizing terrain surface) (Moreira et al., 2013; Purinton and Bookhagen, 2017; Woodhouse, 2006), and (ii) the prevalence of discontinuous urban fabric at the Romanian site, which may cause confusion with ornamental and fruit tree cover present around residential areas, and genuine forested lands.

When analyzing classification results for specific landforms (i.e., valleys), the AW3D, SRTM and TDX90 showed larger commission errors (CE), due to the misclassification of the forest as low vegetation or water. Such errors can be explained by the mischaracterization of the thin crevices of the drainage network on the DEMs (Purinton and Bookhagen, 2017). This is propagated to the lookup table and impacts both, the distortion masking process and the terrain normalization. Distortion masking is affected because the distance between the pixels in the range is altered. Therefore, such pixels are not marked as distorted or shadowed. Terrain normalization is affected as it uses the LUT, orientation, and slope layers to estimate the scattering area. In turn, the scattering

area is overestimated, under-compensating the radiometric effects, keeping a pseudo-shadow with lowered values (as opposed to true shadow, caused by occlusion, which cannot be compensated). Therefore, forests are misclassified due to the apparently low backscatter.

Using the TDX20 reduced commission error for low vegetation (11%) and water (12–22%) on valleys, as well as the percentage of forest pixels among all pixels misclassified as water (decrease of 17–27%). This was explained by reduced pseudo-shadows when using the TDX20/30 DEMs. However, the improvement came at the cost of a 3–6% increase of commission error for urban cover located on valleys, which was caused by a slight increase in backscatter values over forests (overcompensation), and the large size difference between the validation sample for urban and forest ($<10^3$ vs. $7.5 \cdot 10^4$ at valleys), as misclassification of a small subset of the latter would be much larger when compared with the sample size for the former. Even with this trade-off, classification results using TDX20 were marginally better (0.01–0.05 higher Cohen's Kappa). Furthermore, increased CE for urban cover on valleys did not affect the overall CE for the urban class, which was reduced by 2–3% when using the TDX20 DEM.

1.6 Conclusions

SAR observations are heavily affected by sensor-terrain geometry, which can be corrected using a DEM. Choosing a DEM for SAR data terrain normalization is not a trivial choice, as it affects backscattering coefficient variability, and mapping products generated downstream. High-resolution TanDEM-X DEM (20 or 30 m resolution) was the global DEM providing the largest reduction of terrain induced variability, followed by AW3D in sparse vegetation areas. Natural land covers (i.e., forest, bare areas, grasslands) occupying steeper slopes and complex landforms (i.e., peaks, pits, valleys) received the largest benefits. These benefits were felt on classification, where more forest pixels were classified correctly due to a better compensation of low values (valley pseudo-shadow). An ALS-based DEM was able to provide slightly better results (i.e., marginally reduced IOR) when compared to AW3D and TDX20/30 DEMs. However, AW3D and TDX20/30 DEMs seem suitable candidates to replace ALS-based local DEMs. However, AW3D should be checked for data infilling from older datasets (i.e., SRTM) as over such areas, its performance may be degraded.

This study showed the effect of several global DEMs on terrain normalization, highlighting their advantages and shortcomings when normalizing Sentinel-1 imagery. Further research should expand this analysis by including the recent NASADEM dataset (from re-processed SRTM) (NASA, USGS, 2020), using a reference ALS-based DEM for temperate forests, and studying the DEM-dependent normalization effects on SAR imagery acquired at different wavelengths. Finally, the effect of terrain normalization could be tested on downstream quantitative products, such as biomass estimates or canopy cover.

1.7 **Annexes**

Annex 1-1. Confusion matrices by DEM and orbit (Reference>columns; Classified>Rows) at overall level. (Ur, urban; LV, low vegetation; Fo, forest; Wa, water. UA, user accuracy, PA, producer accuracy).

		O007					O029					O131				
		Ur	LV	Fo	Wa	UA	Ur	LV	Fo	Wa	UA	Ur	LV	Fo	Wa	UA
AW3D	Ur	19147	6602	7310	43	57.84	18698	6465	19317	24	42.01	18749	5044	12423	44	51.71
	LV	2206	1548500	19344	271	98.61	2063	1544334	20493	321	98.54	2366	1545097	24852	358	98.25
	Fo	250	10075	811265	380	98.70	759	13244	787900	395	98.21	357	9861	739556	389	98.59
	Wa	0	506	506	5054	83.32	0	611	355	5007	83.83	0	688	468	4956	81.09
	PA	88.63	98.90	96.76	87.93		86.89	98.70	95.15	87.12		87.32	99.00	95.14	86.24	
SRTM	Ur	18868	6245	7204	40	58.31	18439	6055	19377	24	42.01	18725	5048	12952	48	50.92
	LV	2278	1540604	19090	262	98.62	2108	1537069	20272	318	98.54	2283	1538477	23950	340	98.30
	Fo	265	9900	806632	379	98.71	774	12931	782981	386	98.23	285	9564	735257	371	98.63
	Wa	0	546	549	4944	81.87	0	566	283	4895	85.22	0	618	358	4861	83.28
	PA	88.12	98.93	96.78	87.89		86.48	98.74	95.15	87.05		87.94	99.02	95.18	86.49	
TDX20	Ur	29990	9446	11850	73	58.39	28857	8597	30849	36	42.23	29327	7184	18985	73	52.78
	LV	3168	2411865	22525	363	98.93	3440	2410056	31421	475	98.55	3426	2407209	39924	475	98.21
	Fo	364	16915	1270072	619	98.61	1088	17561	1188573	552	98.41	439	12460	1060469	540	98.75
	Wa	1	1112	419	7772	83.53	0	960	251	7535	86.15	0	1063	311	7085	83.76
	PA	89.46	98.87	97.33	88.05		86.44	98.89	95.00	87.64		88.36	99.15	94.71	86.69	
TDX30	Ur	19156	6430	8530	42	56.08	18677	6280	21653	24	40.05	18793	4847	13386	46	50.69
	LV	2034	1540695	16591	239	98.79	2010	1538410	20705	301	98.53	2205	1539752	27089	303	98.11
	Fo	221	9505	808033	390	98.76	642	11234	773058	350	98.44	276	8255	712706	356	98.77
	Wa	0	665	321	4954	83.40	0	718	220	4867	83.84	0	680	171	4678	84.61
	PA	89.47	98.93	96.95	88.07		87.57	98.83	94.78	87.82		88.34	99.11	94.60	86.90	
TDX90	Ur	19027	6599	7449	46	57.45	18439	5990	18774	26	42.65	18727	5161	13647	53	49.82
	LV	2179	1542343	18571	245	98.66	2138	1538972	19112	309	98.62	2294	1540926	23537	344	98.33
	Fo	240	9780	808189	396	98.73	794	13421	789226	382	98.18	309	9608	743312	370	98.63
	Wa	9	666	921	4937	75.57	0	567	343	4905	84.35	0	641	357	4854	82.95
	PA	88.68	98.91	96.77	87.78		86.28	98.72	95.38	87.25		87.80	99.01	95.19	86.35	

Annex 1-2. Confusion matrices by DEM and orbit (Reference>columns; Classified>Rows) for valley. (Ur, urban; LV, low vegetation; Fo, forest; Wa, water. UA, user accuracy, PA, producer accuracy).

		O007					O029					O131				
		Ur	LV	Fo	Wa	UA	Ur	LV	Fo	Wa	UA	Ur	LV	Fo	Wa	UA
AW3D	Ur	304	188	827	2	23.01	305	225	2478	1	10.14	298	175	1292	2	16.86
	LV	25	5447	4117	26	56.65	20	5232	4292	30	54.65	27	5214	3984	33	56.32
	Fo	2	537	76000	19	99.27	1	697	73596	18	99.04	3	606	70952	20	99.12
	Wa	0	32	176	514	71.19	0	27	81	512	82.58	0	27	54	506	86.20
	PA	91.84	87.80	93.69	91.62		93.56	84.65	91.48	91.27		90.85	86.58	93.01	90.20	
SRTM	Ur	319	239	816	1	23.20	318	193	1974	2	12.79	318	177	949	1	22.01
	LV	29	5195	3821	18	57.32	30	5137	4540	28	52.77	29	5102	4404	28	53.35
	Fo	3	598	72313	17	99.15	0	689	70070	14	99.01	1	583	68204	15	99.13
	Wa	0	29	128	429	73.21	0	27	84	421	79.14	0	29	58	420	82.84
	PA	90.88	85.71	93.82	92.26		91.38	84.97	91.39	90.54		91.38	86.61	92.65	90.52	
TDX20	Ur	495	410	1795	1	18.33	492	371	4221	2	9.67	485	277	1923	1	18.06
	LV	35	8150	3874	29	67.42	35	8080	5511	47	59.09	33	7983	5496	44	58.89
	Fo	3	994	113029	34	99.10	1	1022	104714	21	99.01	4	844	95033	26	99.09
	Wa	0	38	108	724	83.22	0	31	36	673	90.95	0	27	48	596	88.82
	PA	92.87	84.97	95.14	91.88		93.18	85.02	91.47	90.58		92.91	87.43	92.72	89.36	
TDX30	Ur	329	274	1267	1	17.58	323	258	2910	1	9.25	324	205	1377	1	16.99
	LV	19	5160	2846	15	64.18	25	5091	3604	24	58.22	19	5068	3732	23	57.32
	Fo	3	594	72894	21	99.16	0	651	68921	12	99.05	1	553	64973	18	99.13
	Wa	0	33	71	428	80.45	0	29	51	411	83.71	0	29	33	378	85.91
	PA	93.73	85.13	94.57	92.04		92.82	84.44	91.30	91.74		94.19	86.56	92.67	90.00	
TDX90	Ur	305	258	1046	0	18.96	304	243	2341	0	10.53	309	187	1256	0	17.64
	LV	24	5299	3304	21	61.27	22	5183	3809	39	57.25	21	5216	3669	39	58.31
	Fo	3	606	70640	19	99.12	2	725	68702	14	98.93	2	610	67360	12	99.08
	Wa	0	26	259	451	61.28	0	28	116	437	75.22	0	25	106	439	77.02
	PA	91.87	85.62	93.88	91.85		92.68	83.88	91.64	89.18		93.07	86.39	93.05	89.59	

Chapter 2: Influence of the mosaicking algorithm on Sentinel-1 land cover classification over rough terrain

Borlaf-Mena, I., Badea, O., Tanase, M.A., 2021a. Influence of the Mosaicking Algorithm on Sentinel-1 Land Cover Classification Over Rough Terrain, in: 2021 IEEE International Geoscience and Remote Sensing Symposium IGARSS, Brussels, Belgium, 11–16 July 2021. Presented at the IGARSS 2021 - 2021 IEEE International Geoscience and Remote Sensing Symposium, Brussels, Belgium, 11–16 July 2021, IEEE, Brussels, Belgium, pp. 6646–6649. https://doi.org/10.1109/IGARSS47720.2021.9553648

Abstract

The aim of this study was to assess different strategies for wall to wall SAR-based (Sentinel-1) land cover mapping over mountainous areas. The first strategy was to classify by-orbit and combine the resulting classifications. The second strategy derived land cover from ascending-descending SAR mosaics. In both cases, the inverse of the scattering area was used for weighting. Slightly more accurate results were obtained using by-orbit classification, with larger omission errors for urban areas and forest being observed when classifying the SAR mosaics. Such errors were caused by mismatches between orbits caused by image normalization errors and/or directional effects.

2.1 Introduction

The use of local resolution weighted (LRW) mosaics (Small, 2012) was proposed to combine ascending and descending SAR data takes. LRW mosaics combine such data using the inverse of the scattering area as weight. Thus, each pixel in the mosaic is influenced by all available data takes, but data takes with smaller scattering area estimate (smaller resolution loss) have a larger influence. The mosaics were developed to optimize resolution and reduce speckle, by creating a weighted average of all acquisitions from a given period (i.e. 18 days; Rüetschi et al., 2017). When speckle from individual images is removed, one can calculate the weighted standard deviation (SD) over the target period, a useful feature to characterize the temporal behavior of land cover classes. For example, annual SD will be high for crops (due to tillage and harvest cycle), smaller for areas with little vegetation (due to soil moisture variations), and even smaller for forests (array of scatters always present) (Hansen et al., 2020).

The aim of this study was to find a suitable method for wall to wall SAR-based land cover mapping. In this context, we compared two methods leveraging backscattering intensity annual statistics. The first workflow (a) uses a similar strategy to (Hansen et al., 2020), classifying by-orbit and combining the results by vote weighting based on the inverse of

the scattering area. Workflow (b) builds on the ideas of (Small, 2012) and (Hansen et al., 2020), creating local resolution weighted mosaics for the annual statistics followed by land cover classification. We used each method to perform classifications over a steep mountainous area and assessed their strengths and limitations.

2.2 Study area and data sets

The study was carried out on a north-south transect in the southern Carpathians, Romania. The area is covered by broadleaf (oak, beech), needleleaf (spruce), and mixed forests. The SAR data consisted of three-year (2017-2019) dual-polarized (VV, VH) Sentinel-1 time series (relative orbits 7, 29 and 131). The images were acquired in interferometric wide swath mode (IWS) and were retrieved in single look complex format (SLC), with a pixel size of 14.1 m in azimuth and 2.3 m in range. The TanDEM-X DEM (Rizzoli et al., 2017) (©DLR, *Deutsches Zentrum für Luft- und Raumfahrt* 2019) was used for geometric and radiometric data normalization.

As ancillary data, we employed the 2015 ESA CCI land cover map (CCILC), the 2016 DLR's global urban footprint, the Tandem-X and ALOS PALSAR forest maps (TFNF, 2011-2015; AFNF, 2017), and the Corine land cover (CLC, 2018) (Esch et al., 2017; Feranec et al., 2016; Kirches et al., 2017; Martone et al., 2018; Shimada et al., 2014b). GEDI level 2B products (Dubayah et al., 2020) acquired between 2019-04-20 and 2020-04-15 were also employed to account for possible forest losses after the creation of the reference land cover datasets.

2.3 Methods

2.3.1 DEM assembly

The TanDEM-X DEM was received in ellipsoidal height and equiangular geographic coordinates, with a pixel size of 12.5 m. It was resampled (bilinear interpolation) to 20 m to match the resolution of the multi-looked Sentinel-1 imagery.

2.3.2 SAR data processing

2.3.2.1 Image normalization and geocoding

SAR images were assembled by combining the sub-swathes and multi-looked by a factor of 7 in range and 2 in azimuth to reduce speckle noise and to obtain a pixel spacing close to the analysis resolution (20 m). For each relative orbit, the first image served as master: the remaining acquisitions were co-registered to the master image using an iterative process based on intensity matching and spectral diversity aided by the DEM. The master image is employed alongside the DEM to generate the lookup-table (LUT) relating map and range doppler coordinates, as well as auxiliary files such as terrain slope and orientation, incidence angle, scattering area and layover and shadow masks. Backscatter intensity images were calibrated to terrain flattened γ^0, considering scattering area, the incidence angle and the DEM surface (Castel et al., 2001). Then, a multi-temporal speckle filter was applied. Once filtered, the images were orthorectified using the LUT.

2.3.2.2 Masking areas with radiometric distortions

For every orbit, layover and shadow areas were masked out using the auxiliary layers. Foreshortened areas were also masked based on: 1) pixels coordinates – pixels close (two pixels in range direction) to neighboring masked pixels were flagged for possible distortion and 2) VH z-score - pixels within 100 m distance to a flagged pixel and with a z-score > 3 in all years. The z-score was computed with respect to forest backscatter.

2.3.2.3 Generating the mosaics

We produced two sets of mosaics: by-orbit (BO) annual statistics (average and standard deviation, SD), and all-orbits LRW annual statistics (weighted average and weighted SD). By-orbit annual statistics were calculated as:

$$Average\ = \bar{x} = \frac{1}{n}\sum_{i=1}^{n} x_i \quad (1)$$

$$\mathrm{SD} = s = \sqrt{\frac{\sum_{i=1}^{n}(x_i - \bar{x})^2}{n-1}} \quad (2)$$

where x_i is an individual observation, and n, is the total number of observations. The all-orbit LRW statistics were based on the inverse of the scattering area, a_i. For a pixel of orbit i, the weight w_i would be:

$$Weight = w_i = \frac{1}{a_i} \quad (3)$$

Then, the weighted statistics are:

$$Weighted\ average = \bar{x}_w = \frac{\sum_{i=1}^{n} w_i x_i}{\sum_{i=1}^{n} w_i} \quad (4)$$

$$Weighted\ SD = s_w = \sqrt{\frac{\sum_{i=1}^{n} w_i (x_i - \bar{x}_w)^2}{\frac{(m-1)}{m}\sum_{i=1}^{n} w_i}} \quad (5)$$

m is the number of nonzero weights (i.e. the weight was zero if a pixel was masked).

2.3.3 **Land cover reference dataset**

A land cover layer was created using the agreement between the ancillary classification datasets (see section 2.2) as follows: 1) Urban when classified as such in all maps except for AFNF; 2) Low vegetation, when classified as non-urban in GUF and non-forest in AFNF and TFNF, further split into four sub-classes: a) Rainfed crops when classified as arable in CLC and crops or herbaceous cover in CCILC; b) Irrigated crops - manually digitized due to non-agreement of ancillary data; c) Pastures and d) grasslands when classified as such in CLC data and as grasslands or herbaceous in CCILC; 3) Forests when classified as non-urban in GUF, forest in both AFNF and TFNF, and when matching a forest subtype (broadleaf, needleleaf, mixed) in CCILC and CLC; and 4) Water when classified as non-urban in GUF, as water in both CCILC and CLC, and as non-forest in both AFNF and TFNF. Once the areas of interest for all land covers were defined, a 40 meters negative buffer was used for the extraction of training / validation data to avoid edge effects.

2.3.4 Training and validation data preparation

We separated the training and the validation pixels by exclusion: all candidates for the training sample were excluded from the validation sample. To be selected as part of the training sample, a pixel must be free of radiometric distortions in all three orbits. For each land cover, 25.000 random pixels were selected. For forests, pixels were selected from GEDI shots with fractional cover above 10% and forest height above 5 m (Global Forest Resources Assessment, 2000). The training sample was culled using local outlier factor algorithm (Breunig et al., 2000) and the yearly BO statistics as features. For the water class the median-based z-score of VH annual average was also employed, dropping any water sample with a median-based z-score larger than three. Finally, 5.000 random samples, evenly distributed between subclasses, were selected for each land cover.

2.3.5 Classification

The features employed for classification were the annual average and SD for VV and VH channel backscatter intensities. Each year was considered an independent sample. Thus, each classifier is trained with 60.000 samples, 15.000 per class. The samples were employed to train a linear support vector machine with a regularization parameter of 1, primal problem optimization, L1 penalty, 0.001 stopping tolerance, and 10,000 iterations maximum.

On BO classification, a classifier is fitted for each orbit. Then, for every pixel, all unmasked orbits cast a vote for a land cover class with weight w_i as defined in equation 3. The land cover receiving the largest total weight was the one reflected on the classified layer. A single classifier is trained and applied over LRW mosaics.

2.3.6 Validation

The accuracy assessment was performed using metrics derived from the confusion matrix: overall accuracy, Cohen's Kappa, and by-class commission and omission errors. Classification errors were also analyzed using alluvial diagrams to understand differences between classification strategies. The distributions of common misclassifications were compared to the distribution of correctly classified counterparts to understand if errors are related to the mosaicking process.

2.4 Results and Discussions

Accurate classification results were obtained regardless of the mosaicking strategy (Table 2.1), with a minimum overall accuracy of 93%, and a minimum kappa statistic of 0.83. Classifying individual orbits (BO) was slightly more accurate, reaching an overall accuracy of 95% and a kappa of 0.89 in two of the yearly classifications.

Table 2.1. General accuracy metrics for each classification

	By-orbit (BO)			Local Resolution Weighting (LRW)		
Metric	2017	2018	2019	2017	2018	2019
Overall accuracy	93	95	95	94	94	93
Kappa	0.85	0.89	0.89	0.85	0.84	0.83

When disaggregating the result by land cover class, water cover had similar omission errors (10-11%) being mislabeled as low vegetation for both mosaicking strategies (BO and LRW). Commission error differed slightly, 8-12% for BO and 7-15% LRW strategy.

No matter the strategy, most of the omitted low vegetation pixels were mislabeled as forest (Figure 2.1). This was attributed to the heterogeneity of the low vegetation class: agricultural areas usually display a large SD, but it may be lower for fallows, pastures, or grasslands (Figure 2.2). Misclassification of low vegetation as forest was more prevalent in BO classifications: low vegetation omission of 5-7% with BO, 2-3% with LRW and forest commission of 11-15% with BO, 6-8% with LRW. This was explained by the mosaicking strategy: an orbit may have the best resolution for a pixel but may not have the best separability for the land cover of said pixel. For example, in Figure 2.2 to Figure 2.4, values distribution for one orbit (29) shows displacement, most likely due to a higher nominal incidence angle (~41°) when compared to the remaining orbits (~37°).

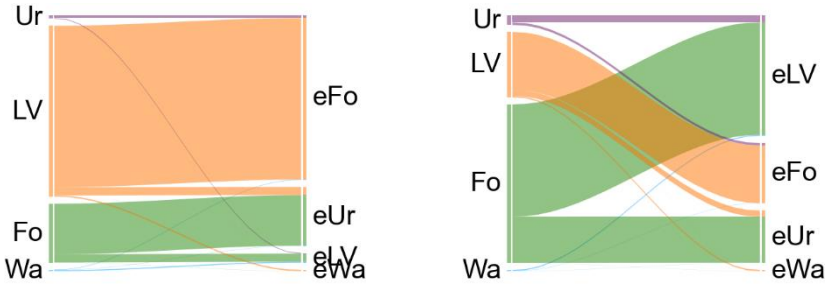

Figure 2.1. Alluvial diagrams of omission and commission errors (OE, CE) as a function of the mosaicking strategy. Left vertical axis and line color show the reference label (Ur, Urban, in purple; LV, low vegetation, in orange; Fo, forest, in green; Wa, water, in blue), right vertical axis shows the classified label for the mis-classified (error – 'e') pixels. The thickness of the lines indicates error frequency compared to the total error.

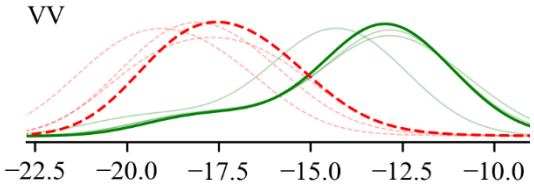

Figure 2.2. Correctly classified low vegetation pixels (solid green lines) and low vegetation pixels mislabeled as forest (dashed red lines) with the BO strategy. Thin lines - yearly SD for individual orbit images, and thick lines - yearly weighted SD (LRW mosaics) in dB scale. Solid green lines depict the value distribution for correctly labeled pixels (a classified as a), whereas dashed red lines depict the most common misclassification (a misclassified as b).

Low vegetation omission was lower in LRW classifications, but its commission error was higher (4-5% with LRW, <1% with BO) due the misclassification of urban (omission of 40-42% with LRW, 10-14% with BO) and forest (omission of 14-18% with LRW, 3-7% with BO). These errors may be explained by the displacement of the SD towards larger values

(Figure 2.3-Figure 2.4). In urban cover it may be caused by directional effects (double bounce scattering depends on street orientation). The VV channel showed little differences (Figure 2.3), between correctly and incorrectly classified pixels, whereas for the VH channel LRW SD was larger for pixels misclassified as low vegetation.

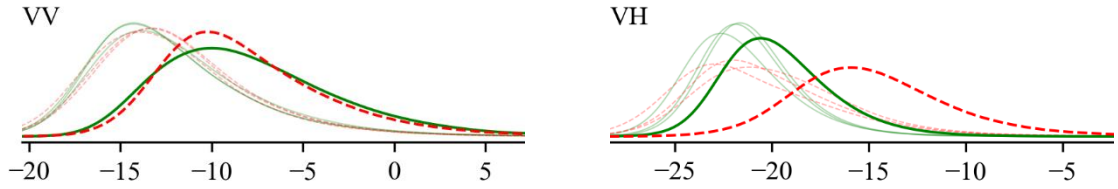

Figure 2.3. Urban pixels correctly classified (solid green lines) and misclassified as low vegetation (dashed red lines) with the LRW strategy. See Figure 2.2.

By-orbit SD distribution for mislabeled forest pixels had large spreads (Figure 2.4), and LRW SD was displaced towards higher values, indicating differences in the backscattering intensity of the different orbits. These may be caused by the acquisition geometry (nominal incidence angle), the presence of volume effects (differences in the distance traversed within the forest canopy) (Castel et al., 2001), or the mischaracterization of the terrain surface. Backscattering intensity is the product of three terms representing the backscatter coefficient of the land cover, the scattering area, and the incidence angle. Thus, variations on the land cover backscattering coefficient will be enlarged if the scattering area has been underestimated, whereas they will diminish for overestimated areas. Terrain mischaracterization is caused by the lack of detail of the DEM employed for scattering area normalization, and mainly appears in steep slopes and terrain crevices (Borlaf-Mena et al., 2020).

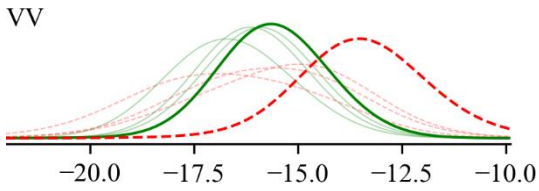

Figure 2.4. Correctly classified forest pixels (solid green lines) and forest pixels misclassified as low vegetation (dashed red lines) with the LRW strategy. See Figure 2.2.

2.5 Conclusions

The aim of this study was to assess radar-based land cover classification results as a function of the method employed to fuse the ascending and descending Sentinel-1 data. The by-orbit SAR image classification and the LRW mosaic-based classification strategies provided similar results, with slightly improved accuracy metrics for the former. However, there were large differences in the error source with LRW classification showing larger omission errors for urban and forest classes. These errors were attributed to an increase of the yearly SD caused by backscatter values mismatches between orbits due to image normalization, directional effects (street orientation affects double bounce, slope orientation alters traversed distance within the canopy), or differences induced by the acquisition parameters, such as a different nominal incidence angle.

These results indicate that land cover maps generated by combining ascending and descending SAR passes can provide high accuracies (>90%). However, user should use caution, as residual effects may remain (under-correction of scattering area and directional effects) particularly over steep areas. For this reason, by orbit products may provide better results as they are more resistant to the presence of residual effects, i.e., the annual SD is not swelled by combining multi-orbit data

Chapter 3: Assessing the Utility of Sentinel-1 Coherence Time Series for Temperate and Tropical Forest Mapping

Borlaf-Mena, I., Badea, O., Tanase, M.A., 2021b. Assessing the Utility of Sentinel-1 Coherence Time Series for Temperate and Tropical Forest Mapping. Remote Sensing 13, 4814. https://doi.org/10.3390/rs13234814

Abstract

This study tested the ability of Sentinel-1 C-band to separate forest from other common land use classes (i.e., urban, low vegetation and water) at two different sites. The first site is characterized by temperate forests and rough terrain while the second by tropical forest and near-flat terrain. We trained a support vector machine classifier using increasing feature sets starting from annual backscatter statistics (average, standard deviation) and adding long-term coherence (i.e., coherence estimate for two acquisitions with a large time difference), as well as short-term (six to twelve days) coherence statistics from annual time series. Classification accuracies using all feature sets was high (>92% overall accuracy). For temperate forests the overall accuracy improved by up to 5% when coherence features were added: long-term coherence reduced misclassification of forest as urban, whereas short-term coherence statistics reduced the misclassification of low vegetation as forest. Classification accuracy for tropical forests showed little differences across feature sets, as the annual backscatter statistics sufficed to separate forest from low vegetation, the other dominant land cover. Our results show the importance of coherence for forest classification over rough terrain, where forest omission error was reduced up to 11%.

3.1 Introduction

Forest ecosystems host a large portion of terrestrial biodiversity, and provide many ecosystem services, such as timber and food production, risk mitigation (i.e., flood, erosion), and climate regulation, as forests hold a large portion of terrestrial biomass, and its growth and degradation play an essential role on climate and atmospheric CO_2 dynamics. This has prompted several international agreements to preserve forest services and biodiversity, along with specific procedures to track forest cover and status. One of the earliest international efforts for tracking forest status was undertaken under the Food and Agriculture Organization (FAO) through the global Forest Resources Assessment (FRA), whose first report was published in 1948. FRA defines forest as areas with tree canopy cover above 10%, 5 m minimum tree height, and a minimum extent of 0.5 Ha (FAO FRA, 2000).

Forests' increasing importance is reflected by subsequent conventions such as the United Nations (UN) Rio Convention on Biological Diversity (United Nations, 1992a), and the UN Framework Convention on Climate Change (United Nations, 1992c), UNFCC. The UNFCC was extended by the Kyoto protocol and the Paris agreements (United Nations, 1997, 2015b) with the commitment of the signatory countries to reduce their greenhouse gasses emissions through, among other, reforestation programs. Further forest-related agreements include the Bonn Challenge (International Union for Conservation of Nature, 2011), a global effort for forest restoration, and the New York declaration of forests (United Nations, 2014), aimed at reducing the rate of deforestation. Agreements under the UNFCC use indicators considered critical to characterize Earth's climate, the so called essential climate variables (ECVs) (Bojinski et al., 2014) which are assessed and monitored through a range of programs and frameworks to track compliance. For example, between 2005 and 2015 the UN funded the REDD+ program, focused on "Reducing emissions from deforestation and forest degradation and the role of conservation, sustainable management of forests and enhancement of forest carbon stocks in developing countries" (Goetz et al., 2015). REDD+ requires the implementation of measurement, reporting and verification (MRV) systems as part of developing national forest monitoring systems. In the context of MRV systems, remote sensing technologies were used to keep track of forest status thanks to the short revisit times and consistent large-scale coverage.

Currently, most forest related ECVs are retrieved from earth observation satellites, with the European Space Agency (ESA) Climate Change Initiative (CCI) funding the extraction of many forest-related variables (i.e., land cover, above ground biomass, burned area) along with other ECVs (i.e., aerosols, sea surface temperature, snow cover, etc.). Remote sensing is the only technology able to provide the short revisit times and large-scale coverage needed for such tasks (Hansen et al., 2020). Recent approaches on forest/non-forest (FNF) classification leveraged optical imagery from AVHRR, MODIS, MERIS or Landsat, despite the cloud cover related problems of such sensors (Hansen et al., 2020; Shimada et al., 2014b; Baron and Erasmi, 2017; Martone et al., 2018; Sica et al., 2019). Active systems such as space-borne light detection and ranging (LiDAR) are sensitive to forest height and fractional cover, which are important indicators for separating forested areas (FAO FRA, 2000). However, the use of space-borne LiDAR is limited by its sparse coverage and cloud cover as is the case for the global ecosystem dynamics investigation (GEDI) instrument onboard the international space station (Dubayah et al., 2020). Active systems based on synthetic aperture radar (SAR), are not affected by cloud cover, provide continuous or near continuous coverage (due to distortions over rough terrain), and are sensitive to forest presence (Baron and Erasmi, 2017; Dostálová et al., 2018; Hansen et al., 2020) .

Over the past decades, the SAR backscatter coefficient has been employed for many forest-mapping studies (Quegan et al., 2000; Rüetschi et al., 2017; Shimada et al., 2014b;

Hansen et al., 2020). Forests tend to have higher backscatter coefficient than other land cover classes due to the multiple bounces of the signal within the canopy (volume scattering), allowing a larger amount of energy to return to the sensor. In general, longer wavelengths provide a larger contrast between forest and other classes (Mitchell et al., 2014; Shimada et al., 2014b) while cross-polarized channels are better suited at identifying forest cover since multiple bounces within the canopy cause the return to lose its original polarization (Woodhouse, 2006; Ulaby and Long, 2014). Recent mapping examples include the ALOS PALSAR forest/non-forest maps (Shimada et al., 2014b) which used L-band HV (horizontal (H) transmit—vertical (V) receive) backscatter to determine forest extent, while water bodies and non-forest areas are separated using the HH channel.

The utility of the backscatter coefficient for land cover mapping is often limited by unrelated factors such as dielectric (i.e., soil moisture) and geometric effects (i.e., roughness, tree stumps and debris left after forest clearing) as well as rain, snow, and freeze-thaw periods (Shimada et al., 2014b; Olesk et al., 2015; Dostálová et al., 2016, 2018; Martone et al., 2018; Hansen et al., 2020). For example, the backscatter coefficient may increase after forest clearing, as tree stumps and woody debris are left exposed (double bounce) and decrease with time as soil surface dries (Shimada et al., 2014b). Furthermore, some land cover classes may be misclassified due to their scattering properties' similarity to those of forest cover (i.e., vineyards, urban parks, and gardens). Nevertheless, changes in backscatter may be employed for detecting changes in the land cover (e.g., forest loss) (Canty et al., 2019; Doblas et al., 2020).

Phase information may be leveraged for land cover classification to avoid the shortcomings of backscattering intensity, albeit at the cost of increased data volumes and processing times. Single-pass interferometry has been successfully applied to generate a global forest map based on TanDEM-X HH interferometric coherence, i.e., the correlation between images acquired from different sensor positions acquired at the same time (single-pass) or at different time steps (repeat–pass) (Martone et al., 2018). Repeat–pass interferometric coherence has been also employed for land cover classification (Wegmuller and Werner, 1995; Bruzzone et al., 2004; Thiel et al., 2009; Sica et al., 2019; Jacob et al., 2020) with shorter temporal baselines improving the contrast between classes (Thiel et al., 2009; Jacob et al., 2020). Nevertheless, such contrast may be lost over some land cover classes (e.g., crops due to tillage) even for images acquired at very short intervals (Thiel et al., 2009; Jacob et al., 2020). Using dense time series (6–12 days) may overcome such limitations, but at a steep increase of data volume. Alternatively, adding coherence estimates from a few pairs with long temporal baselines can improve separating some classes, such as urban cover, (Sica et al., 2019) with a smaller computational cost.

Regardless of whether phase information has been employed, multitemporal datasets may inform classifiers on land cover temporal behavior. This information can be leveraged in several ways, such as using individual observations as features, or using the pixel-wise annual statistics (i.e., average, standard deviation). When both approaches were tested in the context of forest mapping, the latter approach obtained improved results (Hansen et al., 2020), as it reduces data dimensionality and it is less vulnerable to the influence of short-lived events such as precipitation (Hansen et al., 2020; Quegan et al., 2000; Sica et al., 2019). However, it is important to note that the usefulness of such statistics may be hampered by variability due to thawing/flooding events or infrequent image acquisition (Dostálová et al., 2018). Within annual statistics layers, SAR backscatter variations are usually lower over forested areas when compared to other land cover classes such as crops which are affected by cultivation cycles (Quegan et al., 2000; Hansen et al., 2020). Forest limited annual variation is related to scattering from tree canopy and the associated dampening of temporal variations in soil surface moisture. However, annual variations may not suffice when separating younger forests as the scattering is influenced by the underlying soil properties (Quegan et al., 2000), or in areas with pronounced seasonality (Hansen et al., 2020). Urban areas may also be misclassified as forests, as they have a similarly low variability. Hence, the annual backscatter average is also needed to separate forest from urban areas (infrastructure has a high backscatter coefficient; Quegan et al., 2000).

The objective of this study was to investigate the contribution of radar backscatter and coherence for forest cover mapping in temperate and tropical settings. Three increasingly richer feature sets were employed to assess the contribution of the variables that separate forest from other major land classes such as urban, low vegetation, and water. The first feature set was derived from annual backscatter statistics, the second set included long-term coherence (i.e., coherence estimate for two acquisitions with a large time difference) while for the last set short-term coherence statistics were added (i.e., average and standard deviation of coherence estimates with a short temporal baseline). The results were assessed using existing land cover datasets and spaceborne Lidar data.

3.2 Study Area and Data Employed

The first study area (Figure 3.1A) was a N-S transect over the Romanian Carpathians characterized by continuous and discontinuous urban areas, water courses and water bodies, croplands, tree and bush orchards, herbaceous cover (natural grasslands and pastures), as well as broadleaf, needleleaf and mixed temperate forest. Forests appear mainly on over-sloped terrain (Figure 3.2). It has an approximate area of 25,000 km^2. The second study area (Figure 3.1B) was in the Brazilian Amazon. It mainly contains broadleaf tropical forest and cropland mixed with natural vegetation (tree, shrub, herbaceous), with several water courses and small cities. At this site, forests appear mainly over gentle slopes (Figure 3.2). It has an approximate area of 43,000 km^2.

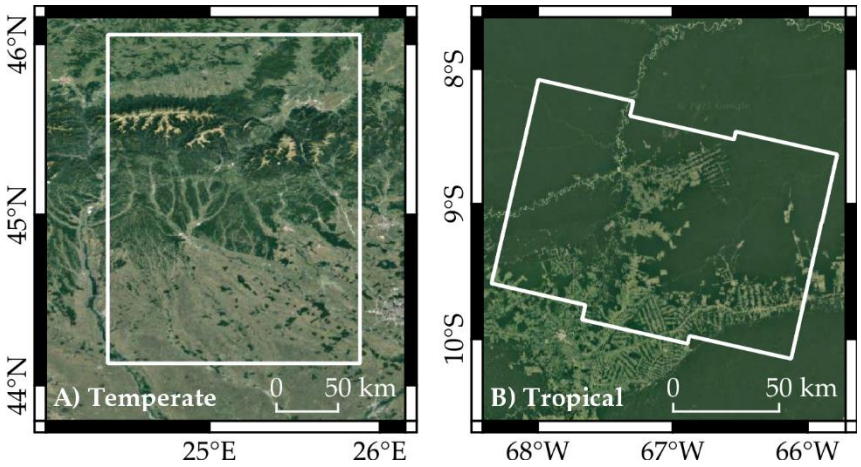

*Figure 3.1. Extent of the study areas ((**A**), temperate, Romania; (**B**), tropical, Brazil). the white outline represents the extent of the sites. Background imagery is courtesy of Google Satellite.*

Dual-polarized (VV, VH) single look complex (SLC) images acquired by Sentinel-1 A and B satellites (C-band) in interferometric wide swath mode (IWS) were used. The SLC images have a pixel spacing of 14.1 m in azimuth and 2.3 m in range. At the temperate site (Romania), we processed all overlapping acquisitions (6-day repeat interval) from both, ascending (29, 131) and descending (7) "orbital tracks" for years 2017–2019 to ensure complete coverage of the rough Carpathians terrain. Data from these three orbits were normalized (geometric, radiometric, interferometric) using the 12 m TanDEM-X digital elevation model (DEM) (Rizzoli et al., 2017) (©DLR, *Deutsches Zentrum für Luft- und Raumfahrt* 2019). For the tropical site (Brazil) we processed a time series for years 2018 and 2019, including only images from Sentinel-1A (12-day repeat interval) to ensure coherence observations with the same temporal baseline. Notice that Sentinel-1B satellite started to consistently acquire images over the area after May 2019. For the flatter terrain at the tropical site, the use of data from one relative orbit (54) was considered sufficient. SAR processing at this site was based on the NASADEM height data (Crippen et al., 2016; NASA and JPL, 2020).

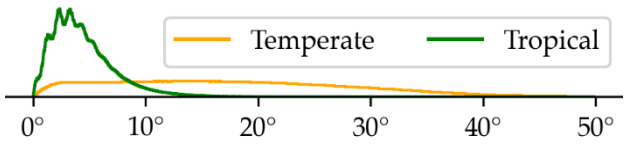

Figure 3.2. Frequency distribution of the slopes for forest pixels of both sites.

We used preexisting land cover maps as data sources to generate a consistent layer for training and validation purposes including:

- 2018 Corine land cover (CLC), generated by manual digitalization over satellite imagery with a minimum polygon area of 25 hectares (Büttner et al., 2017; Kosztra and Büttner, 2019), with an overall accuracy of 88.7% within the boundaries of Romania (Moiret-Guigand et al., 2021).

- 2015 European Space Agency Climate Change Initiative land cover dataset (ESA CCI LC, from here on CCILC), generated at 300 m resolution with a time series of optical data (AVHRR, MERIS, SPOT-VGT, PROBA-V) and machine learning (Kirches et al., 2017), with an accuracy of 75.1% (Achard et al., 2017).
- 2016 global urban footprint (GUF), generated at 12 m resolution with texture and intensity of TanDEM-X imagery, with an accuracy of 85–88% (Esch et al., 2017).
- 2011–2015 TanDEM-X forest non-forest map (TFNF), generated with 50 m resolution from TanDEM-X bistatic coherence data, with an estimated accuracy of 85–93% (Martone et al., 2018)
- 2017 Advanced land observing satellite phased array type L-band synthetic aperture radar forest/non-forest map (ALOS PALSAR FNF, shortened to AFNF) generated at 25 m resolution using backscatter data, with an accuracy of 85–95% (Shimada et al., 2014b)

To account for possible changes after the creation of the mentioned land cover datasets, we used the GEDI level 2B data from period 20/04/2019–15/04/2020 (both sites) and one Sentinel-2 image (tropical site, tiles 19LEK, 19LEL, 19LFK, 19LFL, 19LGK, 19LGL) acquired 24 August 2020.

3.3 Methods

3.3.1 SAR Data Processing

Before SAR data processing, the DEMs employed for SAR co-registration and radiometric/geometric corrections were mosaicked. Both the TanDEM-X DEM and the NASADEM tiles were received in equiangular coordinates. The TanDEM-X DEM, received as height above the ellipsoid with 12 m pixel spacing, was mosaiced and resampled to 20 m using bilinear interpolation. The NASADEM, received with a pixel size of 30 m and geoidal height reference, was mosaiced and shifted to ellipsoidal heights.

The Sentinel-1 SLC sub-swathes were assembled into a single image and multi-looked to a pixel spacing of approximately 25 m, using a factor of 7 in range, and 2 in azimuth. This allowed reducing the impact of speckle while bringing the pixel size closer to the resolution intended for analysis. The first image acquired in each relative orbit served as master. All remaining acquisitions were co-registered, by relative orbit, to the master image using an iterative process based on intensity matching and spectral diversity with the DEM as auxiliary dataset (Wegmüller et al., 2002b). The DEM was employed to generate a lookup-table (LUT), relating its own coordinates (map coordinates) and the SAR image coordinates (range-doppler coordinates), as well as auxiliary layers containing information on terrain slope and orientation, local incidence angle, scattering area and layover and shadowed areas. Interferograms were generated between subsequent image pairs as well as at yearly intervals starting with the master image acquisition date.

Two series of interferograms were thus obtained for each relative orbit: (1) the long-term series containing two to three yearly estimates, and (2) the short-term series containing near weekly (6 days) or bi-weekly (12 days) estimates depending on the study area. The topographic phase was subsequently removed and coherence was estimated for each interferogram using a two-step adaptive approach (Wegmüller and Werner, 1996; Werner et al., 2000).

The backscatter intensity was calibrated to terrain flattened γ^0, considering the incidence angle and the terrain scattering area estimate (Castel et al., 2001; Small, 2012; Frey et al., 2013). A multi-temporal speckle filter was applied to reduce speckle (Quegan et al., 2000). Coherence and backscattering intensity estimates were orthorectified using an inverse distance resampling and the yearly average and standard deviation (SD) were computed for each SAR metric (VV and VH backscatter and VV coherence) and converted to the decibel (dB) scale.

Notice that layover and shadow areas were masked using the DEM-derived auxiliary layers. Foreshortened areas were also masked, because scattering area may be underestimated, leaving them with anomalously high values. To determine when such anomalies appear, we characterized the distribution of the annual average of VH backscatter, calculating its median and median absolute deviation for all forest pixels (forest was expected to have the largest values over sloping terrain). A pixel was marked as distorted if the mean annual VH backscatter had a median-based z-score larger than 3 in all years and the pixel was within 100 m of any LUT-masked pixel (i.e., pixels where topographic normalization may still be problematic).

3.3.2 Land Cover Reference Dataset

We used two datasets for training and validation: a GEDI-derived point layer showing forest cover presence or absence, and a land cover raster layer. For the GEDI-based layer, shots (points) were labeled as presence when the fractional tree cover was above 10%, as estimated from both the GEDI shots and the Landsat-derived tree cover ancillary data included in the GEDI file; the canopy height (rh100) was above 5 m. If none of these thresholds was reached, the shot was considered as non-forest.

The land cover dataset was created by a Boolean combination of preexisting land cover maps. To combine them, we first resampled all data sources to a pixel grid matching the Sentinel-1 dataset. Nearest neighbor resampling was employed for qualitative datasets, bilinear resampling was employed for Sentinel-2 data, and mode resampling was employed for GUF, as its pixel size was smaller when compared to the processed Sentinel-1 data. The matching grids were combined based on the rules depicted on the Table 3.1 and Table 3.2: to receive a specific sub-class a pixel had to meet all conditions imposed for that specific subclass. The logic behind the specific ruleset is described in the following paragraphs, as different conditions were necessary for each site due to the land cover types present and the difference in available ancillary data.

At the temperate site, the AFNF was not used to determine urban cover because it disagreed with the remaining datasets (i.e., parts of the cities were classified as forest). For the rest of non-forest classes, the condition imposed on AFNF was "NOT forest", as open areas and water surfaces were sometimes misclassified as each other due to a similarly low backscatter. In the case of transitional woodland-shrub, it was necessary to remove AFNF or relax the condition (any natural cover of CCI land cover), as most of the plots from CLC were lost due to the large size of ESA CCI pixel size, or due to the object-based generalization of AFNF. For areas meeting the imposed conditions, a two-pixel negative buffer was applied to avoid edge effects.

Table 3.1. Temperate site classification scheme together with the ruleset employed to determine the membership based on the preexisting datasets. The subclasses are based on agreement between CLC and CCI LC. GUF had to be 255 (urban) for the homonymous class, and 0 (other) for the rest of classes. "!=" denotes the NOT operator, i.e. "! = 1" indicates not classified as forest in AFNF or TFNF.

Class	Subclass	CLC 2018	CCI LC 2015	AFNF 2017	TFNF 2018
Urban	Artificial	1xx: Artificial surfaces	190: Urban areas	-	0: Urban
Low vegetation	Crops	211: Non-irrigated Arable land	10: Cropland 11: Herbaceous	!=1: Other (not forest)	2: Not forest
	Pasture	231: Pastures	11: Herbaceous		
	Grassland	321: Grassland	130: Grassland		
	Permanent crops	222: orchards 242: agriculture mix	12: Tree or shrub		
	Transitional woodland-shrub	324: transitional Woodland-shrub	40–153: natural vegetation	-	
Forest	Broadleaf	311: broadleaf	50–62: broadleaf	1: Forest	1: Forest
	Needleleaf	312: needleleaf	70–82: needleleaf		
	Mixed	313: mixed	90: mixed		
Water	Water	-	210: Water	!=1: Other	!=1: Other

At the tropical site, Sentinel-1 annual averages (by polarization) were added to avoid the shortcomings of the preexisting datasets, together with normalized difference indices (ND) derived from one Sentinel-2 image (24 August 2020). In the case of low vegetation, large areas were covered by mixed land covers (forest and low vegetation appear together) in the CCI LC. To avoid including thin tree lines in the low vegetation sample, pixels with a backscattering intensity over −8 dB on the Sentinel-1 VV annual averages, a ND moisture index (NDMI, Gao, 1996) over 0.05, and ND vegetation index (NDVI, Tucker, 1979) over 0.6 in the Sentinel-2 image were masked out, as these characteristics indicate tree cover. Forest had to have an NDVI over 0.6 in the 2020 Sentinel-2 image to avoid including areas that may have been deforested after the creation of the land cover datasets. ND water index (NDWI, Xu, 2006) had to be negative for land classes, and positive for water. Water also needed to have an annual backscattering intensity average under −15 and −20 dB for VV and VH channels to avoid errors caused by changes in the water cover. Forest and low vegetation (dominant classes) received the two-pixel negative buffer. The few pixels available for urban areas precluded such a buffer. Similarly, the sample for water cover would have been greatly reduced by a negative buffer, as it appears as thin rivers.

Table 3.2. Tropical site classification scheme together with the ruleset employed to determine the membership based on the preexisting datasets. The subclasses are based on CCI LC. GUF had to be 255 (urban) for the homonymous class, and 0 (other) for the rest of classes. "!=" denotes the NOT operator.

Class	Subclass, CCI LC 2015	AFNF 2017	TFNF 2018	Sentinel-1 2018, 2019	Sentinel-2 2020
Urban	190: Urban areas	!=1: Other	0: Urban	-	NDVI < 0.6 NDWI < 0
Low vegetation	30: Mosaic of cropland with natural vegetation 40: Mosaic of natural vegetation with cropland 100: Mosaic tree/shrub and herbaceous 120: Shrubland		2: Not forest	VV < -8	NDMI < 0.05 NDVI < 0.6 NDWI < 0
Forest	50–62: broadleaf	1: Forest	1: Forest	-	NDVI > 0.6 NDWI < 0
Water	210: Water	!=1: Other	!=1: Other	VH < −20 dB VV < −15 dB	NDWI > 0

3.3.3 Training Data Preparation

The training sample was taken from unmasked SAR pixels (not affected by layover, shadow, or foreshortening) in all the relative orbits employed for the site. The training dataset was designed to withhold at least 30% of the sub-class samples for validation, taking up to 25.000 random samples from the pixels with said sub-class. In the specific case of forest sub-types, samples were taken from the GEDI-derived tree cover layer, selecting the shots overlapping with a pixel with the specific forest type.

The training data was culled by applying the local outlier factor algorithm to each individual sub-class, keeping all points that were considered inliers in all orbits and years. In the case of water cover, the median-based z-score was also employed by dropping any sample where the z-score for the VH channel was over three, cases where we assumed the pixel may be partially occupied by land and/or aquatic vegetation, thus reducing the separability with low vegetation classes. For each land cover, 5000 random points evenly distributed between its subclasses were selected. All sub-classes always had over 1000 training samples, with the lowest counts for the temperate site low vegetation sub-classes (1000 samples each), and tropical site urban (1891 samples as the single sub-class). Training data was employed to plot the distribution of the land cover classes.

3.3.4 Classification Scheme

Yearly classifications were created using an increasing number of features. The first set includes backscatter annual statistics, the second adds long-term interferometric coherence, and the third adds short-term coherence statistics. While training the classifier, each year was considered an independent sample, i.e., each classifier was trained with 20.000 samples per year. A "one-versus-rest" linear support vector machine classifier was fitted for every orbit, as anisotropic effects may remain even after performing radiometric terrain flattening (Castel et al., 2001). These classifiers were fit with a regularization parameter of 1, primal problem optimization, L1 penalty, 0.001 stopping tolerance, and 10.000 iterations maximum. At the temperate site, data from several relative

orbits were combined to maximize coverage as large areas were masked in each individual orbit due to the SAR related geometric distortions. For each pixel, every orbit casts a vote with a weight equal to the inverse of its scattering area, as pixels with large scattering suffer larger geometric and radiometric distortions (Small, 2012; Small et al., 2021). The pixel is classified as the land cover accumulating the largest weight. Detailed information about the methodology can be found in (Borlaf-Mena et al., 2021a).

3.3.5 Validation

The land cover validation set was created after discarding pixels overlapping the GEDI shots, those that have been masked as distorted in all orbits, and any pixel that has been considered for inclusion in the training sample. The GEDI validation set (forest and non-forest classes) was created using all shots, except for those considered as candidates for inclusion in the training sample (see 3.2 and 3.3).

Validation was performed directly for the land cover dataset (same classes), whereas, for comparison with the GEDI forest/non-forest validation set, the resulting classification was matched to the GEDI binary scheme, with forests being considered as forest presence and the remaining classes forest absence. We employed confusion matrices and its derived metrics, overall accuracy (OA), Kappa statistic (K), omission, and commission errors (OE, CE) to assess the results. Alluvial diagrams were employed to track OE and CE origin. Classification stability was assessed as the percentage of unchanged pixels between yearly classifications (i.e., 2018 vs. 2019) by separating pixels with known land cover (in the validation sample) and pixels not included in the validation sample. We analyzed the type of change by disaggregating into four groups: deforestation and "afforestation" (forest to low vegetation and vice versa), water related changes (water to low vegetation and vice versa), urbanization (forest or low vegetation to urban), and other changes. Note that these changes have not been independently verified.

3.4 Results

3.4.1 Data Distribution

At both sites, the pixel-wise annual backscatter average was larger over forests when compared to low vegetation, with a large overlap between both. Distribution of the urban class overlapped with the distribution of the forest class, as the former showed a large variability (Figure 3.3 and Figure 3.4).

Annual backscatter standard deviation (SD) displayed similar tendencies, with a large degree of overlap between forest, low vegetation, and urban classes. Long-term coherence helped separating forests from urban, as the former generally displays lower values, with little overlap between the two classes. Average short-term coherence showed the lowest value for forest, increasing for low vegetation and reaching maximum over the urban cover. The annual standard deviation helped separating forest from low vegetation, as it tends to be higher for the latter, albeit some overlap remained.

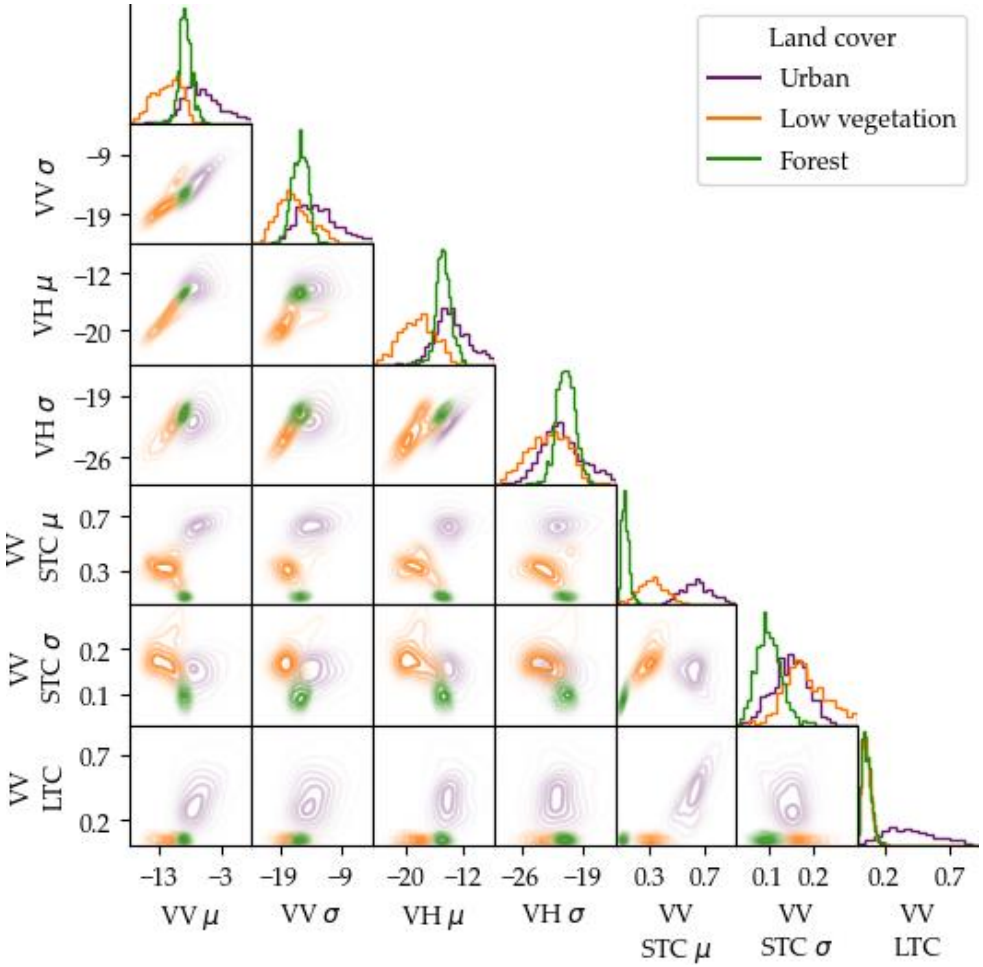

Figure 3.3. Value distribution of a subset of 1000 random pixels extracted from the training sample at the temperate site. The diagonal displays histograms, the remaining cells display the 2D kernel density estimate for each pair of variables. Water cover has been excluded to improve visibility for the remaining classes. STC stands for "short-term coherence" whereas LTC stands for "long term coherence". Note that backscattering intensity annual statistics were calculated in linear scale and then converted to decibel (dB).

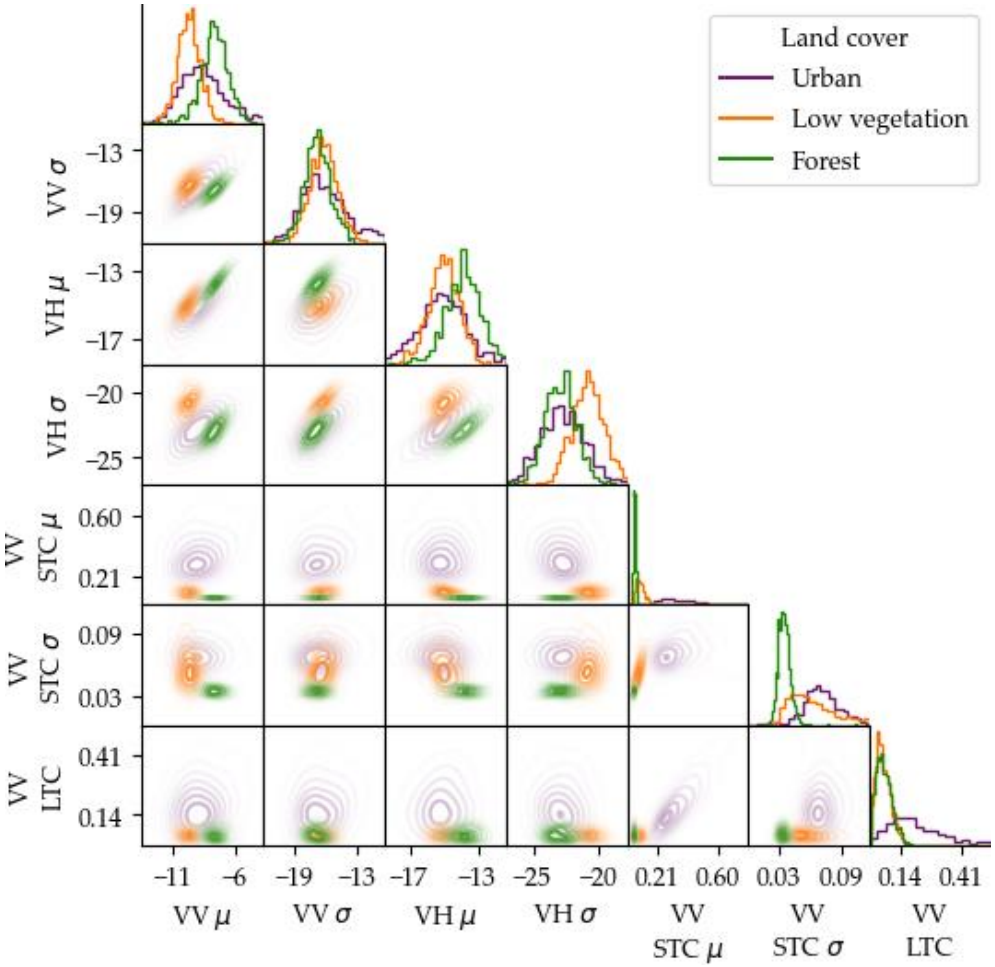

Figure 3.4. Value distribution of a subset of 1000 random pixels extracted from the training sample at the tropical site.

3.4.2 Classification with Feature Sets

All classifications attained accurate results (OA > 90%) and substantial agreement (K > 0.75; Landis and Koch, 1977) when assessed against the reference land cover (LC) and the GEDI-derived validation sets (Table 3.3). When only the backscatter annual statistics were used as predictors, the overall accuracy ranged between 94–99% (LC) and 92–97% (GEDI). At the temperate site, the Kappa statistic ranged within the 0.86–0.91 (LC) and 0.79–0.84 (GEDI) interval, whereas at the tropical site it ranged between 0.87–0.93 (LC) and 0.77–0.79 (GEDI). Adding long-term coherence data resulted in opposite results depending on the site. At the temperate site, the overall accuracy and K increased to 97% and 0.93, respectively. Conversely, at the tropical site the Kappa statistic decreased slightly, 0.85–0.91 (LC) and 0.76–0.79 (GEDI). Adding annual statistics from short-term coherence series increased the overall accuracy at both sites to 99% (using the land cover dataset as reference) and 96–97% (using the GEDI data set as reference). Similarly, the Kappa statistic increased at both sites. At the temperate site Kappa increased to 0.97–0.98 (LC), and 0.90–0.91 (GEDI), whereas at the tropical site it increased to 0.92–0.96 (LC), and 0.82–0.83 (GEDI).

Table 3.3. Overall accuracy (%) and kappa by classification. "LC" stands for land cover-based reference dataset. B00—classification using backscatter annual statistics, B0C—adding long-term coherence, and BCC—further adding short-term coherence statistics. Cells are shaded with a gradient between yellow and green, associated with lower, and higher metrics, respectively.

		Temperate						Tropical					
		Overall accuracy			Kappa statistic			Overall accuracy			Kappa statistic		
		B00	B0C	BCC	B00	B0C	BCC	B00	B0C	BCC	B00	B0C	BCC
LC	2017	94	97	99	0.86	0.93	0.98						
	2018	96	97	99	0.91	0.93	0.97	98	97	99	0.87	0.85	0.92
	2019	96	97	99	0.90	0.93	0.97	99	99	99	0.93	0.91	0.96
GEDI	2017	92	96	97	0.79	0.90	0.91						
	2018	93	95	96	0.84	0.89	0.91	95	95	96	0.77	0.76	0.82
	2019	93	96	96	0.82	0.89	0.90	95	95	97	0.79	0.79	0.83

At both sites, the prevalent land cover types (low vegetation and forest) were most affected by misclassification (Figure 3.5 and Figure 3.11). However, there were different tendencies between the two study sites.

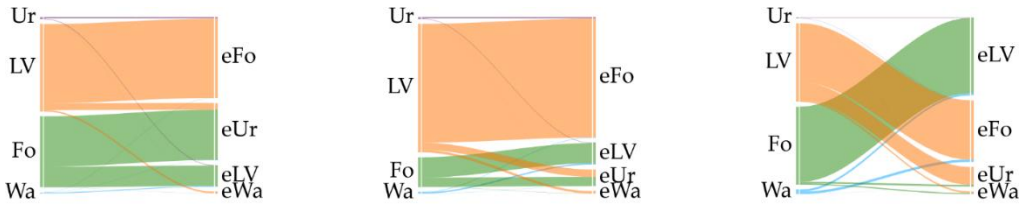

B00 (4–6% error) B0C (3% error) BCC (<1% error)

Figure 3.5. Alluvial diagrams of the errors (OE, CE) as a function of predictor variables used for classification at the temperate site. Left vertical axes show the reference label (Ur, Urban, in purple; LV, low vegetation, in orange; Fo, forest, in green; Wa, water, in blue), right vertical axes show classified label for the misclassified (error—'e') pixels. The thickness of the lines indicates error frequency compared to the total error.

At the temperate site, using only the backscatter annual statistics as predictor variables resulted in an omission error (OE) of 4–12% for the forest class, with most pixels being assigned to the urban class, which showed an 83% commission error for 2017, 60% for 2018 and 67% for 2019 (Table 3.4, Figure 3.5).

Table 3.4. Temperate site errors (%) disaggregated by land cover (Ur, Urban; LV, low vegetation; Fo, forest; Wa, water). B00—classification using backscatter annual statistics, B0C—adding long-term coherence, and BCC—further adding short-term coherence statistics. Complete matrices in Annex 3-1. Cells are shaded with a green-yellow gradient, indicating lower and higher errors.

		2017				2018				2019			
		Ur	LV	Fo	Wa	Ur	LV	Fo	Wa	Ur	LV	Fo	Wa
Commission error	B00	83	1	9	14	60	1	8	11	67	1	8	16
	B0C	37	1	7	14	30	1	7	10	28	1	7	14
	BCC	16	<1	1	6	13	1	1	5	17	1	1	5
Omission error	B00	7	4	12	9	14	4	4	9	11	4	6	9
	B0C	4	3	2	9	4	3	2	9	6	3	2	9
	BCC	1	1	1	8	1	1	2	8	1	1	2	9

There was a large variation on urban commission error across the yearly classification, with forest being the main contributor. To understand the source of this misclassification, we examined the prevalence of said error in the individual classifications generated for each orbit disaggregating by sub-swathes (Figure 3.6). For the by-orbit classification of year 2017, the misclassification of forest as urban was more prevalent within a particular sub-swath for both, 29 and 131 orbits.

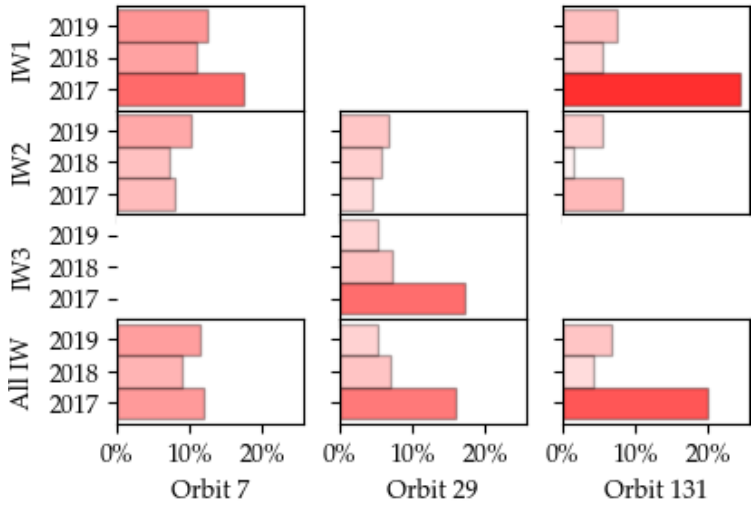

Figure 3.6. Percentage of forest pixels misclassified as urban, disaggregated by orbits and sub-swathes, at the temperate site.

When displaying the 2017 classifications there is a clear cutline, where misclassification becomes more prevalent (Figure 3.7). To understand the sub-swathes differences, we plotted the distribution of all pixels labeled as forest in the validation sample disaggregating by orbit, year, and sub-swath (Figure 3.8). VV and VH annual averages showed little difference between years and sub-swathes, with a near-complete match between the distributions of all years and sub-swathes. However, for year 2017 the VV annual SD

for ascending orbits (29, 131) had its distribution shifted compared to years 2018 and 2019. For orbit 29, the distributions for the sub-swathes were centered around different values, whereas both had a similarly high value for orbit 131. VH annual SD showed smaller shifts, with some mismatch between sub-swathes from orbit 131.

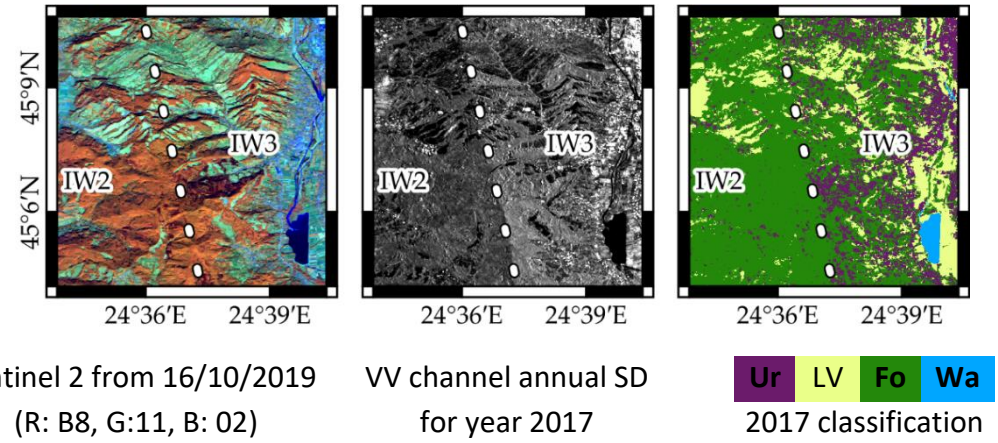

Sentinel 2 from 16/10/2019 (R: B8, G:11, B: 02) | VV channel annual SD for year 2017 | 2017 classification

Figure 3.7. Annual (2017) SD for VV polarization for orbit 29 (subset), and the derived classification for said orbit prior to classification merging. The dotted line represents the limit between both sub-swathes. From left to right: Sentinel-2 image shown as reference, annual SD (VV) and, classified land cover (Ur, urban; LV, low vegetation; Fo, forest; Wa, water).

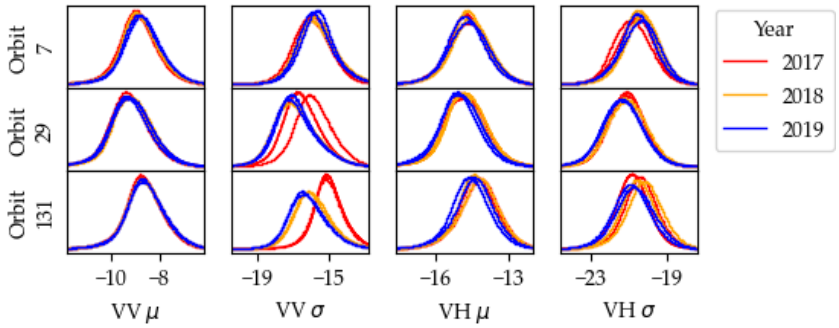

Figure 3.8. Statistical distribution for pixels labeled as forest in the validation sample disaggregated by year (color) and sub-swath (one line per sub-swath).

Omission errors for forest class were reduced when coherence information was included. Adding long-term coherence as predictor reduced forest OE to 2%, while urban CE decreased to 28–37%. Including coherence annual statistics further reduced the commission error for urban class (from 28–37% to 13–17%), forests (from 7% to 1%), and water (from 10–14% to 5–6%).

Evaluating forest cover presence with the GEDI-derived reference (Table 3.5) showed CE and OE for forest cover between 14–15% and 8–18%, respectively, when using backscatter annual statistics as predictor variables. CE and OE for non-forest ranged between 3 and 7%. Adding long term coherence reduced errors for both forest and non-forest classes whereas including coherence annual statistics further reduced CE for the forest class from 10–12% to 2–3%, while increasing OE omission from 4–5% to 11–13%. As expected,

the non-forest class showed opposite trends., i.e., decreasing OE from 4–5% to 1%, and increasing CE from 1–2% to 4–5%.

Table 3.5. Temperate site errors (%) based on GEDI forest presence/absence validation dataset. B00—classification using backscatter annual statistics, B0C—adding long-term coherence, and BCC—further adding short-term coherence statistics. Complete matrices in Annex 3-2. Cells are shaded with a green-yellow gradient, indicating lower and higher errors.

		2017			2018			2019		
		B00	B0C	BCC	B00	B0C	BCC	B00	B0C	BCC
Commission error	Forest	14	10	2	15	12	3	15	11	2
	Other	7	2	4	3	1	4	4	2	5
Omission error	Forest	18	5	11	8	4	11	10	4	13
	Other	5	4	1	6	5	1	6	5	1

Classifications using the full feature set had opposing trends on CE and OE, depending on the validation set employed for the assessment. Such trends were explained by examining the CCI/CLC cover over the GEDI shots where forest omission had happened. Most such shots were considered broadleaf forests (27–32% CCI, 19–27% CLC) followed by the CLC classes “Fruit tree and Berry plantations”, “Complex cultivation patterns”, and “Land mainly occupied by agriculture”. Combined, these agricultural areas represented a 35–41% of OE for forest class when using the GEDI-derived reference layer. Tree and shrub were the CCI land cover class with the second largest contribution to misclassification (18–23%). Notice that CCI tree and shrub class largely corresponds to CLC agricultural classes that can have a significant tree cover (Figure 3.9).

231, Hayfields with scattered woody vegetation in the Romanian Carpathian Mountains.

242, Complex cultivation pattern (arable land, orchards and hayfields) with scattered houses in the Ghimeș valley, Romania.

243, Land principally occupied by agriculture, with significant areas of natural vegetation (scattered trees), Romania

Figure 3.9. Example illustrations from Corine Land Cover nomenclature guidelines (Büttner et al., 2017; Kosztra and Büttner, 2019) for some mixed land covers appearing in the temperate site. Photographies by György Büttner (231) and Barbara Kosztra (242, 243). Copyright: European Environment Agency.

For the tropical site, the overall classification errors were similar no matter the feature set employed (Table 3.6), with slight differences for the majority classes (forest and low vegetation), which increased for the minority classes, especially urban, whose omission fell from 62–71% to 7–9%. The similar classification errors may stem from the adequate separability of forest and low vegetation based on backscatter statistics (Figure 3.4).

Table 3.6. Tropical site errors (%) disaggregated by land cover (Ur, Urban; LV, low vegetation; Fo, forest; Wa, water). B00—classification using backscatter annual statistics, B0C—adding long-term coherence, and BCC—further adding short-term coherence statistics. Complete matrices in Annex 3-3.

		2018				2019			
		Ur	LV	Fo	Wa	Ur	LV	Fo	Wa
Commission error	B00	99	17	<1	16	99	8	<1	16
	B0C	>99	15	<1	22	>99	6	<1	19
	BCC	89	11	<1	22	89	5	<1	17
Omission error	B00	71	4	2	1	62	4	1	1
	B0C	24	4	3	1	27	4	1	1
	BCC	7	4	1	1	9	3	<1	1

To check differences between sub-swathes on the backscatter-based classification, the percentage of forest validation pixels misclassified as low vegetation (most common misclassification of the forest class), was plotted by sub-swath (Figure 3.10). Indeed, a larger error (3%) was observed for sub-swath IW3 when compared to the remaining sub-swathes for year 2018. However, the differences in distribution were not as evident as at the temperate site.

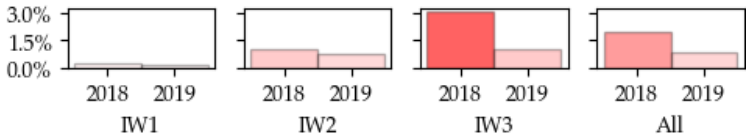

Figure 3.10. Tropical site percentage of forest pixels misclassified as low vegetation disaggregated by sub-swaths.

At the tropical site, adding the coherence-based variables resulted in under- or over-prediction of the minority classes (Table 3.6, Figure 3.11). Adding long-term coherence reduced forest omission, low vegetation commission and urban omission errors. When coherence annual statistics were included as well, CE for low vegetation dropped to 5–11%, forest OE dropped to 1% or less, and urban CE dropped to 89%.

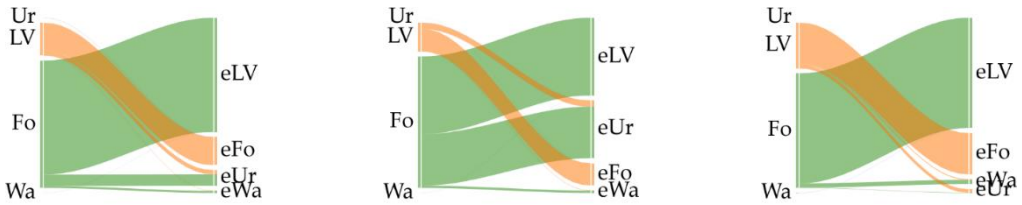

B00 (4–6% error) B0C (7% error) BCC (<1% error)

Figure 3.11. Alluvial diagrams of the errors as a function of predictor variables used for classification at the tropical site. Left vertical axes show the reference label (Ur, Urban, in purple; LV, low vegetation, in orange; Fo, forest, in green; Wa, water, in blue), right vertical axes show classified label for the misclassified (error—'e') pixels. The thickness of the lines indicates error frequency compared to the total error.

When assessing the tropical site classifications against the GEDI derived reference layer (Table 3.7), similar results were observed regardless of the input features. Differences appeared only when short-term coherence statistics were added, with CE for non-forest

dropping from 29–33% to 23–25%. In addition, the OE for both, forest and non-forest classes, were reduced by 1–2%.

Table 3.7. Tropical site errors (%) based on GEDI forest presence/absence validation dataset. B00—classification using backscatter annual statistics, B0C—adding long-term coherence, and BCC—further adding short-term coherence statistics. Complete matrices in Annex 3-4. Cells are shaded with a green-yellow gradient, indicating lower and higher errors.

		2018			2019		
		B00	B0C	BCC	B00	B0C	BCC
Commission error	Forest	1	1	1	<1	<1	<1
	Other	32	33	25	29	29	23
Omission error	Forest	5	5	4	5	5	3
	Other	5	5	4	4	4	4

3.4.3 Classification Stability

The stability between 2018 and 2019 yearly classifications was assessed. The year 2017 was excluded due to the SAR processing induced differences between sub-swaths and the lack of data over the tropical site. Over 85% of all unmasked pixels (not affected by SAR geometric distortions) were stable, i.e., did not change classes from year to year regardless of the site (Figure 3.12). In addition, pixels labeled as "forest" in the LC validation sample shows a particularly high stability (>95% in most cases).

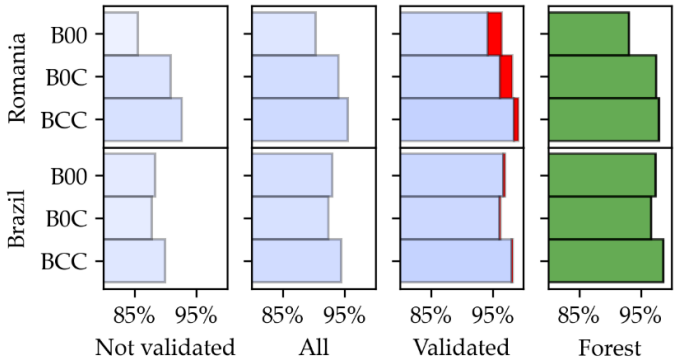

Figure 3.12. Percentage of pixels with no change between the 2018–2019 classifications segregated in: "Not validated"—pixels with no validation label, "all"—all pixels (with or without validation label), "validated"- pixels with validation labels, and "forest"—pixels whose validation label was forest (green). Blue bars denote stability. In the case of validated subset, the blue bar indicates accurate and stable pixels, whereas red indicates stable but misclassified pixels.

At the temperate site, the classification based on backscatter statistics features showed lower stability as well as slightly larger proportion of stable, but misclassified pixels when compared to classifications based on features taking advantage of the coherence information. Differences for the tropical site were smaller, with the largest stability appearing when using the full feature set, followed by the backscatter statistics set, and with little difference in the proportion of stable, but misclassified, pixels. Note that an unknown proportion of the changes detected may be actual land cover changes, as changes have not been validated.

Generally, changes between the yearly classifications (2018 vs. 2019) were caused by transitions between forest and low vegetation classes (Figure 3.13) which appeared frequently at class borders. At the temperate site, the apparent deforestation and afforestation increased when more coherence-based features were added, representing 41%, 58% and 70% of change as the feature set grows larger (backscatter annual statistics, long-term coherence, coherence annual statistics). These changes appeared near the mountain tops and in areas with a sparse tree cover (young forest, tree orchards). Changes from low vegetation/forest to urban accounted for 33% of the total changes. At the temperate site, unclassified changes accounted for up to 25% of all changes (using backscatter statistics), albeit most of them were eliminated by the morphological operator "opening".

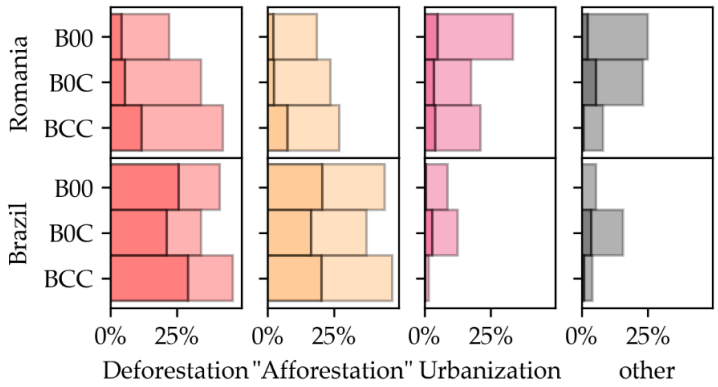

Figure 3.13. Contribution of each specific change type disaggregated by site. The paler bar indicates small-sized changes that would be lost after a single pass of the morphological operator "opening" (i.e., lone misclassified pixels). The darker bars indicate changes that were larger and would not be lost (i.e., bigger change patch).

Deforestation/afforestation followed a similar trend at the tropical site, accounting for 86% of the change in the yearly classifications when using the backscatter statistics feature set, 72% when adding long-term coherence and 93% when using the full feature set. Changes from vegetation to urban and unclassified changes had a larger representation when using the full feature set, reaching 12% (compared to 2–9%) and 16% (compared to 4–5%) respectively. Nevertheless, most patches were eliminated by the "opening" operator, indicating that they appear as small, thin areas (salt and pepper noise).

3.5 Discussion

Backscatter-based overall mapping accuracy was high regardless of the site (OA >92%). However, in temperate environments (i.e., Carpathians), classifications based on backscatter annual statistics frequently misclassified forest as urban, especially over steep slopes. The 2017 classification presented a particularly large tendency to misclassify forest as urban, prompting further analysis on the possible cause. The analysis showed that such misclassifications were prevalent in specific sub-swathes, where the statistical distribution of the pixel-wise annual standard deviation appears to be shifted compared to other sub-swathes and years. This phenomenon could be attributed to the

limited information provided by the Sentinel-1 noise lookup table prior to 13/03/2018, which only annotated noise in the range direction. Past this date, the Sentinel-1 instrument processing facility software (IPF), was upgraded to version 2.90, and started providing noise annotations in azimuth direction as well (ESA, 2018; Vincent et al., 2018, 2020). This conclusion is also supported by the marginal differences in distribution observed for years 2018 and 2019.

Backscatter-based classifications for years 2018 and 2019 displayed a smaller tendency to misclassify forest as urban. However, misclassifications were still observed and may be related to the inclusion of 2017 data (with the related noise problem) in the training sample. Other possible sources of error were the under-correction of slopes facing the sensor (Dostálová et al., 2016; Borlaf-Mena et al., 2020, 2021a) and the elongation of the path traversed within the forest canopy on backslopes (Castel et al., 2001). Such errors may be alleviated if topographic information is included (orientation, slope, incidence angle, etc.) (Mitchell et al., 2014). It is also important to consider that urban cover is mostly discontinuous, with a significant presence of gardens and trees that influence the urban radiometric signature (small settlements misclassified as forest), a problem that also has been encountered by (Santoro et al., 2007a). Furthermore, backscatter-based maps presented lower stabilities at the temperate site which may be related to differences in the meteorological conditions across the years such as the winter length (forest presents lower backscatter in freezing conditions; Ranson and Sun, 2000; Olesk et al., 2015), or rain frequency (less contrast between land covers; Sharma et al., 2005).

Adding long-term coherence reduced the misclassification of forest as urban up to 9%. Such reductions were possible because urban was the only land cover that retained higher coherence levels over long periods (Bruzzone et al., 2004; Sica et al., 2019). Errors for all land covers dropped when short-term coherence statistics were added. In particular, an important reduction of low vegetation to forest misclassification was observed, as the former has higher coherence values (i.e., pastures, grasslands), or higher variations (e.g., agriculture cropping cycle) than forests which are characterized by low coherence values (Wegmuller and Werner, 1995). Accompanying these gains in accuracy, there were successive increases in classification stability. The remaining apparent changes were mainly observed between forest and low vegetation. Apparent afforestation patches appeared close to the mountain tops and may be related to how long the stable winter conditions (i.e., increased coherence) lasted every specific year (Santoro et al., 2007b). Apparent deforestation generally appeared close to the edges of forest, and in areas with smaller tree cover and height. This may be related to the use of an adaptative estimator for coherence. Such estimators reduce the loss of resolution compared to a boxcar filter, albeit it may bias the coherence estimation (Jacob et al., 2020). The employed estimator combined several coherence estimates using a gaussian weighting function (Wegmüller and Werner, 1996; Werner et al., 2000). It is possible that in border areas (i.e., forest contact with pastures) the weighting may have been

modified depending on the meteorologic conditions (i.e., a coherence drop due intense precipitation), affecting the annual statistics and inducing instability.

When comparing with GEDI-derived forest presence/absence, including short-term, coherence statistics decreased the commission error for forest, but increased its omission. These opposing trends were explained by the presence of other land uses with tree presence (orchards, scattered trees, treed plot borders, Figure 3.9) considered as forest cover, according to the criteria set for the GEDI validation dataset, but not classified as such. This suggests that it may be possible to separate agricultural classes with significant tree cover from actual forests using the Sentinel-1 coherence temporal statistics (Wegmuller and Werner, 1995). Notice that such separation based solely on backscatter features is difficult, as is also shown in previous studies (Dostálová et al., 2018).

Over tropical areas, smaller differences between classifications were observed. The trends were also different when compared to temperate environments. Such differences were attributed to flatter terrain and improved Sentinel-1 processing at IPF which led to a reduced impact on the training sample. The use of C-band dual-pol backscatter annual statistics provided highly accurate results, in line with results in the recent literature (Hansen et al., 2020; Dostálová et al., 2016, 2018). This contrasts with older studies based on single-pol data from the active microwave instrument (SAR) on board of the European remote sensing missions (ERS AMI-SAR), where the C-band VV backscatter could not discriminate tropical forest from other land covers (Strozzi et al., 1999; Luckman et al., 2000; Gaboardi, 2003).

Including long-term coherence as a feature slightly decreased classification accuracy as well as its stability, due the over-prediction of urban (some near-bare areas also kept a high coherence). This had little impact on GEDI validation results, indicating the over-prediction of urban cover does not come from the misclassification of forest. Adding short-term coherence statistics increased accuracy, reducing the errors for most land cover classes, regardless of validation dataset. This is thanks to the improved contrast between forest, urban and low vegetation, as also shown in prior studies based on either ERS (Strozzi et al., 1999; Luckman et al., 2000; Gaboardi, 2003) or Sentinel-1 imagery (Diniz, 2019; Pulella et al., 2020).

Differences between sites could be related to the different land cover classes, terrain characteristics, land cover dataset generation, the changes in the Sentinel-1 IPF or the lower number of acquisitions at the tropical site, where the longer temporal baseline may have degraded the contrast between classes, and thus, the value of using coherence data (Thiel et al., 2009; Jacob et al., 2020).

3.6 Conclusions

The aim of this study was to evaluate how temporal features extracted from Sentinel-1 data affect forest/non-forest classification as well as to differentiate possible misclassification sources. Increasingly richer feature sets were tested starting with annual

backscatter statistics (average and standard deviation of VV and VH backscattering intensities) and adding long-term coherence as well as short-term coherence statistics. Using only backscatter derived features has advantages as they can be obtained from the ground range detected (GRD) products. Contrarily, coherence derived metrics require pairs of single-look complex images (SLC), with the associated increase in data volume and processing times. Validation was performed with a land cover dataset, and GEDI data binarized into forest presence and absence as per the FAO definitions (FAO FRA, 2000).

All three feature sets provided high overall accuracies, and acceptable omission (<19%) and commission (<16%) for forested areas with additional improvements in accuracy and classification stability being observed as more features were added. Accuracy of forest cover showed larger differences depending on the feature set used at the temperate site. Classifications based on backscatter annual statistics showed important omissions (up to 18%) for forested areas which were often misclassified as urban. Adding long-term coherence reduced forest omissions to 5%, while adding annual coherence statistics reduced forest commission errors.

Over the tropical site the results were highly accurate and stable from year to year, with small improvements being observed as more features were added. Classifications based on backscatter annual statistics tended to misclassify urban areas as forest. Adding long-term coherence greatly reduced such misclassifications. Annual coherence statistics had an overall positive effect, reducing forest omission and low vegetation commission error, as well as reducing the error for forest presence/absence when comparing with the GEDI dataset.

Our results show that it is possible to generate highly accurate (>92%) forest/non-forest maps based on backscatter annual statistics, with further gains being observed when adding coherence-based features, particularly over areas characterized by rough terrain. These results complement the study of (Jacob et al., 2020), by providing additional evidence on the use of dense temporal series of interferometric coherence for land classification in tropical areas, as well as over temperate regions characterized by very rough terrain.

3.7 **Annexes**

Annex 3-1. Romanian site confusion matrices by year and feature set (Reference>columns; Classified>Rows) compared to the land cover validation dataset.

		Backscatter statistics (B00)					**Backscatter statistics, long-term coherence (B0C)**					**Backscatter and short-term coherence statistics, long-term coherence (BCC)**				
		Ur, Urban	LV, Low vegetation	Fo, forest	Wa, Water	Commission error	Ur, Urban	LV, Low vegetation	Fo, forest	Wa, Water	Commission error	Ur, Urban	LV, Low vegetation	Fo, forest	Wa, Water	Commission error
2017	Urban	156219	55550	715668	658	83	162320	37453	55637	488	37	167829	29648	3342	130	16
	Low vegetation	3657	16924371	176319	5994	1	1439	17010367	78215	5904	1	605	17455162	71215	3200	0
	Forest	8643	592541	6284942	1474	9	4874	524324	7042834	1764	7	240	96711	7101180	3769	1
	Water	200	11807	774	80258	14	86	12125	1017	80228	14	45	2748	1966	81285	6
	Omission error	7	4	12	9		4	3	2	9		1	1	1	8	
2019	Urban	145629	46935	168236	1173	60	161350	33984	35227	723	30	167339	23224	2067	84	13
	Low vegetation	3767	16918692	145035	5343	1	1667	16981859	93019	5574	1	1072	17458751	146454	3239	1
	Forest	19092	609823	6863700	1502	8	5594	560937	7048591	1712	7	245	99990	7027733	4110	1
	Water	230	8826	732	80366	11	107	7496	866	80375	10	62	2311	1449	80951	5
	Omission error	14	4	4	9		4	3	2	9		1	1	2	8	
2019	Urban	149579	49470	258754	1242	67	158263	27764	34328	654	28	167557	32022	2929	106	17
	Low vegetation	3492	16927829	143335	5639	1	1972	17020180	103283	5730	1	887	17464510	140887	3525	1
	Forest	15427	592422	6774737	1371	8	8365	524202	7039024	1863	7	220	85246	7031885	3936	1
	Water	217	14549	874	80132	16	115	12124	1065	80137	14	51	2492	1999	80817	5
	Omission error	11	4	6	9		6	3	2	9		1	1	2	9	

Annex 3-2. Romanian site confusion matrices by year and feature set (Reference>columns; Classified>Rows) compared to the GEDI validation dataset.

		Backscatter statistics (B00)			**Backscatter statistics, long-term coherence (B0C)**			**Backscatter and short-term coherence statistics, long-term coherence (BCC)**		
		Forest	Other	Commission error	Forest	Other	Commission error	Forest	Other	Commission error
2017	Forest	132335	20733	14	153689	16252	10	144063	3162	2
	Other	28749	412269	7	7308	416645	2	16934	429735	4
	Omission error	18	5		5	4		11	1	
2018	Forest	148331	25887	15	155003	21617	12	143374	3911	3
	Other	12753	407116	3	5994	411281	1	17623	428987	4
	Omission error	8	6		4	5		11	1	
2019	Forest	144210	25552	15	154712	19966	11	140655	2581	2
	Other	16874	407451	4	6372	413037	2	20429	430422	5
	Omission error	10	6		4	5		13	1	

Annex 3-3. Brazilian site confusion matrices by year and feature set (Reference>columns; Classified>Rows) compared to the land cover validation dataset (comm. stands for commission).

		Backscatter statistics (B00)					**Backscatter statistics, long-term coherence (B0C)**					**Backscatter and short-term coherence statistics, long-term coherence (BCC)**				
		Ur, Urban	LV, Low vegetation	Fo, forest	Wa, Water	Comm. error	Ur, Urban	LV, Low vegetation	Fo, forest	Wa, Water	Comm. error	Ur, Urban	LV, Low vegetation	Fo, forest	Wa, Water	Comm. error
2018	Urban	238	8677	32889	0	99	634	18288	207037	15	>99	775	5743	618	14	89
	Low vegetation	248	2072595	437681	278	17	96	2069778	357844	313	15	57	2086317	247654	221	11
	Forest	345	84345	22139966	0	<1	103	75279	22041792	0	<1	2	71001	22357746	0	<1
	Water	4	770	5734	33914	16	2	1124	8265	33863	22	1	1356	8176	33924	22
	Omission error	71	4	2	1		24	4	3	1		7	4	1	1	
2019	Urban	316	15310	29671	0	99	606	22379	125915	9	>99	760	5903	372	12	89
	Low vegetation	219	2079824	187958	275	8	125	2074418	142987	311	6	72	2097155	106030	234	5
	Forest	293	70427	22393056	0	<1	97	68317	22336185	0	<1	0	61805	22499246	0	<1
	Water	5	826	5585	33917	16	5	1273	6785	33871	19	1	1472	5491	33913	17
	Omission error	62	4	1	1		27	4	1	1		9	3	<1	1	

Annex 3-4. Brazilian site confusion matrices by year and feature set (Reference>columns; Classified>Rows) compared to the GEDI validation dataset.

		Backscatter statistics (B00)			**Backscatter statistics, long-term coherence (B0C)**			**Backscatter and short-term coherence statistics, long-term coherence (BCC)**		
		Forest	Other	Commission error	Forest	Other	Commission error		Forest	Forest
2018	Forest	377770	2298	1	376550	2096	1	383515	1957	1
	Other	20381	43775	32	21548	43946	33	14572	44083	25
	Omission error	5	5		5	5		4	4	
2019	Forest	379793	1839	<1	379675	1842	<1	384333	1727	<1
	Other	18359	44236	29	18201	44219	29	13532	44332	23
	Omission error	5	4		5	4		3	4	

Chapter 4: Sentinel-1/2 time series for selective logging monitoring in temperate forests

Tanase, M., Borlaf, I., Pascu, I., Pitar, Diana, Apostol, B., Petrila, M., Chivulescu, S., Leca, S., Pitar, Daniel, Ciceu, A., Dobre, A., Popescu, F., Badea, O., Aponte, C., 2020. Sentinel-1/2 Time Series for Selective Logging Monitoring in Temperate Forests, in: IGARSS 2020 - 2020 IEEE International Geoscience and Remote Sensing Symposium. Presented at the IGARSS 2020 - 2020 IEEE International Geoscience and Remote Sensing Symposium, IEEE, Waikoloa, HI, USA, pp. 2902–2905.

https://doi.org/10.1109/IGARSS39084.2020.9323952

Abstract

The aim of this study was to evaluate the utility of Sentinel-1/2 time-series for monitoring selective logging in temperate forests. Ten stands were selectively logged with 5 to 28% of the existing growing stock volume being extracted. The analysis was focused on backscatter coefficient and surface reflectance changes for dates immediately prior and past the logging period. Monthly information on leaf area index (from terrestrial laser scanning) and vegetation water content (from destructive sampling) was used to support the analysis. The analysis suggested that monitoring selective logging using Sentinel-1/2 imagery is challenging in temperate montane forests due to a range of factors, including logging time and duration, saturation of C-band wavelength, and relatively small changes in canopy cover that cannot be reliably picked up by the optical sensor.

4.1 Introduction

Forests are a key element for carbon sequestration and thus a sensitive research topic since information on growing stock volume (GSV) is important for greenhouse gases flux estimation, and thus global policies monitoring (Gibbs et al., 2007). Over the past decade, the use of satellite datasets for forest monitoring have expanded significantly including the use of both active (radar) and passive (optic) sensors (Kennedy et al., 2010; Hansen et al., 2013; Tanase et al., 2015; Mermoz and Le Toan, 2016).

Passive sensors detect radiation emitted from other source (e.g., sun) and were commonly used for forest monitoring due to the wide range of spaceborne orbiting sensors and long-time archives. However, optical sensors are limited by cloud cover, low solar illumination angles and by sensitivity to mainly forest cover and plant phenology. The use of active sensors overcomes some of these limitations as they are independent of cloud cover and solar illumination and provide a measure of vegetation structure (Le Toan et al., 2011). Past passive missions allowed for the development of inter-annual

(Kennedy et al., 2010) and intra-annual algorithms to monitor forest degradation and in particular, selective logging (DeVries et al., 2015) despite relatively low revisit times. However, most such studies were carried out in tropical forests, less affected by phenological changes when compared to the deciduous temperate montane forests. The strong phenological changes typical for such forests coupled with selective logging duration (one to several months) and timing (often outside the vegetation season) limit the use of sparse active and passive time-series for monitoring activities.

The launch of Sentinel-1 and 2 satellite constellations characterized by high revisit times (5-6 days) and improved sensor characteristics (e.g., spatial resolution precise orbital information, increased spectral information channels) present new opportunities for the integration of active and passive dataset into operational forest monitoring. Therefore, this preliminary study evaluated the utility of was Sentinel-1 and Sentinel-2 datasets to monitor selective logging in temperate montane forests.

4.2 Study area and data sets

The studied forest sites, located in the Carpathian Mountains, include the four main forest types (Quercus petraea – QP, Fagus sylvatica – FS, Norway spruce - NS, and Mixed beech and coniferous stands - M) in Romania (Figure 4.1). The stands are part of the EO-ROFORMON permanent sampling areas (PSA) established in 2017 to monitor fast and slow changing forest parameters (Tanase et al., 2019). Six one-hectare PSAs were established in each forest type: two PSAs represent the reference (no silvicultural interventions) while four PSAs represent managed forests (i.e. two replicates for thinning - T and two for selective logging – SL). Reference PSAs were installed within the same forest stands (notice the same number in Figure 4.2) as for the corresponding managed PSAs thus minimizing differences (e.g., slope, orientation, species) to managed stands. In situ data collection provided ancillary information to understand intra-seasonal variations in radar scattering properties and surface reflectance of spaceborne sensors.

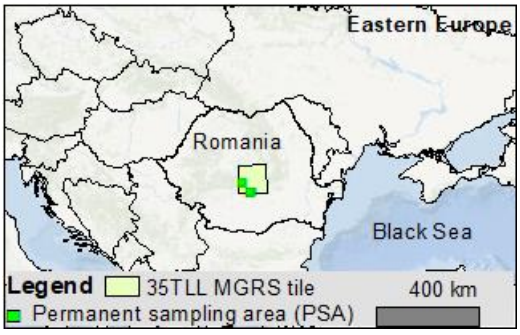

Figure 4.1. Study area and sites location position.

Fast-changing forest parameters (i.e., leaf area index - LAI, equivalent water thickness – EWT and trunk water content - TWC) were monitored monthly between April and October from 2017 to 2018 using terrestrial laser scanning (TLS), destructive sampling or ancillary sensors (e.g. soil moisture and temperature probes, girth bands). The time of field

sampling coincided (± 1 day) with Sentinel-1/2 overpasses. Ten managed and six corresponding reference PSAs were used as information on logging time, duration and intensity were not available for all PSAs (Table 4.1).

Table 4.1. Forest structural properties of the selectively logged (SL) and thinned (T) stands.

Site ID	GSV (m^3/ha)	% logged	Logging type	Difference post - pre	
				LAI	EWT kg/ m^2
QP1T	77	10.1	thinning	NA	NA
QP2T	105	9	thinning	-0.35	0
FS3T	252	14	thinning	-0.33	0
FS4T	250	4.8	thinning	-0.72	-0.02
FS9SL	420	20.8	selective	-5.21	0.03
FS10SL	541	24	selective	-0.84	0.01
QP11SL	352	28.4	selective	NA	NA
QP12SL	363	23.5	selective	NA	NA
NS8T	242	25	thinning	NA	NA
M13SL	641	15	selective	NA	NA

4.3 Methods

4.3.1 Data processing

Processing of Sentinel-1 Ground Range Detected (GRD) images included image calibration to gamma nought (γ°), orthorectification to the UTM reference system, tiling to the 100 x 100 km Military Reference System Military (MGRS) grid, and multi-temporal filtering to reduce speckle. All images (356 images) intersecting tile 35TLL, from both, ascending and descending passes, were processed.

Sentinel-2 imagery (191images) was processed with the MACCS-ATCOR Joint Algorithm (MAJA). For each image, MAJA estimates atmospheric absorption from Sentinel-2 band 9 using the Simplified Model for Atmospheric Correction (Rahman and Dedieu, 1994). Cloud and shadow detection and atmospheric optical thickness (AOT) estimation uses multispectral and multi-temporal information (Hagolle et al., 2015) nonlinear inversion as well as the dark pixel method to generate a lookup-table (LUT). Image atmospheric correction is based on the LUT and corrections for adjacency and topographic effects are also applied (Hagolle et al., 2015).

For each PSA the average of al pixels inside the perimeter was computed. To avoid spurious effects the SAR backscatter coefficient was computed independently for the ascending and descending passes as the average over one week, i.e., preceding and following the start and end of the logging period. Usually, two images were available within the one-week interval. Similarly, for the Sentinel-2 data the average reflectance, by band, was computed for the pixels falling inside the PSAs after masking out pixels affected by cloud and cloud shadows. As the region is often affected by orographic clouds the optical images were more difficult to match with the start/end of the logging periods. Therefore, the closest cloud-free optical images available prior/past the logging periods were used. As for the backscatter coefficient averages over one week were used when available.

In-situ data (LAI CWC, TWC) matched to the logging period were used as support. For logging periods outside the vegetation season in situ measurements were not available.

4.3.2 Data analysis

Scatterplots were used to evaluate the temporal trends for optical indices and backscatter coefficients (VV, VH and VV/VH ratio) together with logging effects and forest phenological cycles. Principal component (PCA) and correlation analyses were carried out to appraise spectral indices sensitivity to forest structural changes and their covariation while mixed linear models were used to evaluate differences in remote sensing indices between paired harvested and not harvested PSAs. Separate models were fitted for all plots (n=20), thinned (n=10) and selectively logged plots (n=10).

4.4 Results and discussions

For the studied PSAs, thinning of young oak and beech stands (QP1T, QP2T, FS3T, FS4T) was carried out at the beginning or during the growing season (Figure 4.2 and Figure 4.3) with post-harvest index values being larger when compared to pre-harvest values as foliage is added to the canopy. The trends suggested that low (5-15%) thinning intensities are compensated by canopy development in spring and that NDRE values increase less in thinned stands as also observed when monitoring chlorophyll content (Sun et al., 2018).

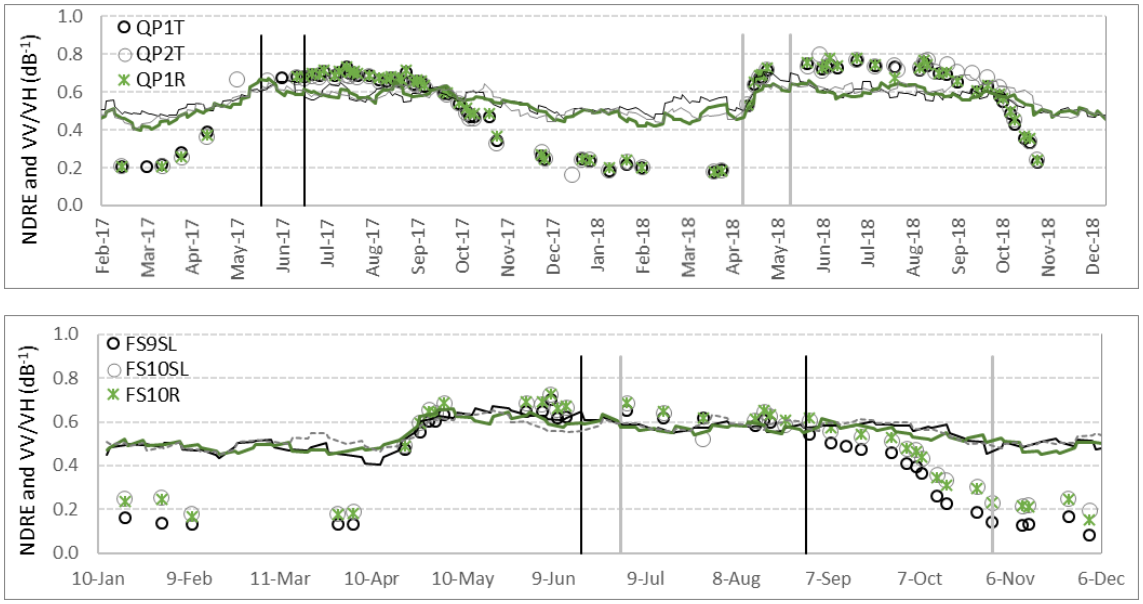

Figure 4.2. Temporal trends of NDRE (points) and VV/VH backscatter ratio (lines) for thinned oaks (QP1T, QP2T) and selectively logged beech stands (FS9SL, FS10 SL). Corresponding logging periods and reference stands (e.g. xxR) shown.

Selective logging of old stands coincided with leaf-fall in autumn phenology. Thus, the post-intervention spectral indices were lower for both reference and harvested plots. Logged old deciduous PSAs (FS9SL, FS10SL, QP11SL, QP12SL) had lower post-harvest reflectance values (less foliage) when compared to their paired counterparts. As expected,

logged coniferous and mixed stands (NS8T, M13SL) did not show such trends with index values being similar of their counterpart PSAs. However, even for PSAs where optical indices increased or decreased, the values for harvested stands were within 0.1 of the reference stands suggesting that phenology has a much larger role to play than partial harvest complicating monitoring activities in temperate mountainous forests from optical sensors. For the Sentinel-1 data the observed differences where related to the forest structure (old vs young stands) rather than harvesting activities.

A large degree of covariation ($r>0.8$) was observed among Sentinel-1 backscatter coefficients while covariation varied ($0.3<r<0.9$) among Sentinel-2 derived spectral indices. Significantly lower values ($p<0.05$) were found for the Normalized Red-Edge Indices (NDRE1 and NDRE2) for thinned when compared to the reference PSAs, suggesting that thinned PSA had gained a lower amount of foliage over the growing season, when the thinning took place, when compared to their reference counterparts. No further significant differences were otherwise observed between harvested and not harvested plots in any of the Sentinel-1 and Sentinel-2 indices examined (NDVI, EVI, Chlorophyll indices green and red-edge, NDWI, NBR, Tasseled cap indices greenness and wetness, and VH/VV backscatter ratio). The covariation between stand biomass, logging treatment, and logging timing was evident in Figure 4.3.

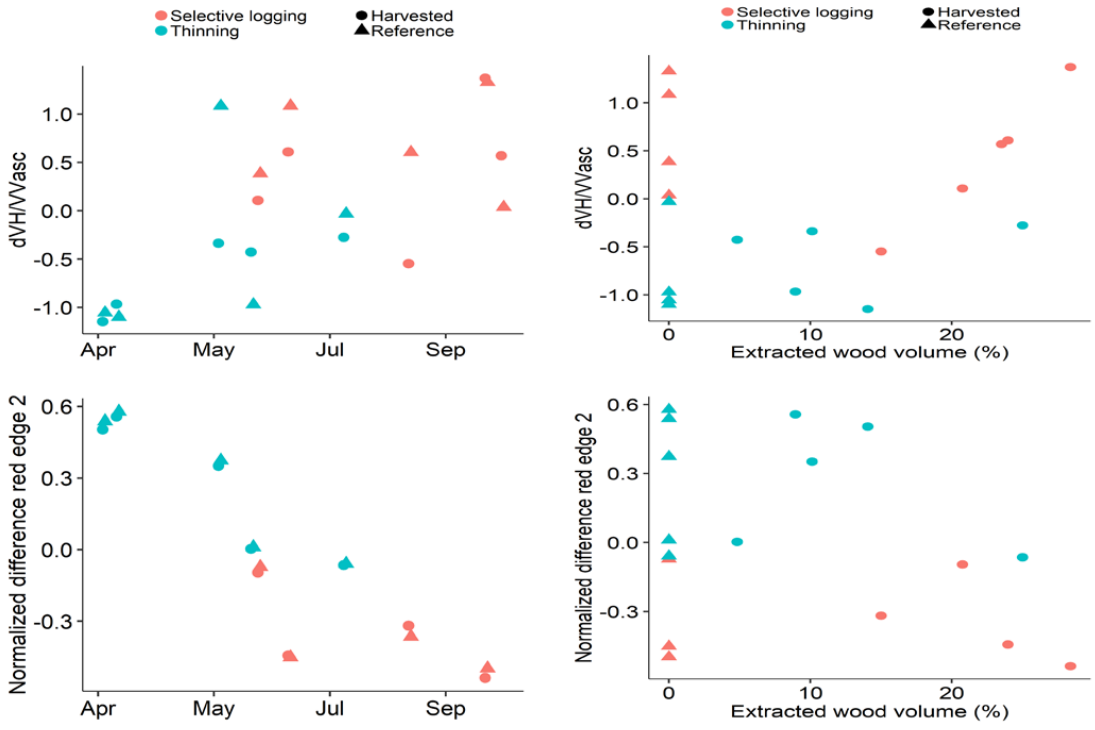

Figure 4.3. Comparison of VV/VH backscatter ratio (upper panels) and NDRE2 (lower panels) values between harvested and reference plots by plot type (selective logging and thinning). Data is shown in relationship to harvesting time (left panels) and extracted wood volume (right panels).

4.5 Conclusions

This study suggests that monitoring temperate montane forests past clear-cuts is challenging with Sentinel-1/2 imagery confirming previous simulation work at C-band (Tanase et al., 2019). Difficulties arise from a range of factors, including logging time and duration, C-band saturation, and relatively small changes in canopy cover that cannot be reliably picked up by optical sensors. Time series at longer SAR wavelengths (L- and P-band) may be needed to effectively monitor selective logging. Combining multifrequency SAR data may allow for key advancements towards the development of retrieval methods to characterize small-scale forest changes.

Chapter 5: Seasonality and directionality are key to identify mountain forest types with Sentinel-1 data

Borlaf-Mena, I., Santoro, M., Villard, L., Badea, O. and Tanase, M.A. Seasonality and directionality are key to identify mountain forest types with Sentinel-1 data. [To be published]

Abstract

Sentinel-1 systematic acquisitions provide a high-density high-resolution stream of data which allows to describe forest temporal dynamics in detail, a powerful tool for phenological studies and forest type classification. Several studies have explored the temporal variation of backscatter intensity in this context, but none considered that scattering directionality of canopies may vary. Said directionality is mainly related to target-sensor geometry (incidence angle), forest height, and optical depth, associated with leaf dynamics. This study explicitly models backscatter dependance on incidence angle by fitting a regression model per forest type/image pair and accumulating the by-type residuals across time series to allow differentiation of forest structure and thus type. Forest pixels are subsequently labeled as the type with the smallest accumulated residuals. This modelling and classification strategy has been applied over a tract of the Carpathian Mountains, performing increasingly detailed forest type classifications. Classification results were subsequently assessed against in-situ forest stand data as well as satellite-based land cover classification products (e.g., Copernicus Forest type layer). The results were promising, with high accuracies ($k > 0.88$, OA > 95%) being observed when separating broadleaf from needleleaf forest types. Classification accuracies decreased ($k > 0.61$, OA > 84%) when separating mixed forest types. Our results suggest that incorporating directional effects into classification models can improve SAR-based forest classification of temperate forest over mountainous terrain. Furthermore, models fitted between backscatter and incidence angle could be used to improve image normalization in regional studies devoted to forest quantitative variables retrieval, such as above ground biomass.

5.1 Introduction

Forests occupy up to 31% of Earth's land area (Watson et al., 2018; FAO and UNEP, 2020), hosting a large portion of terrestrial biodiversity (JRC, 2015; FAO and UNEP, 2020). They also provide services vital for humanity well-being, such as carbon cycle regulation (Bonan, 2008; FAO and UNEP, 2020), essential in the current context of climate change. Each forest type (i.e., broadleaf, needleleaf) provides ecosystem services at specific rates (i.e., depending on the harvest cycle) and have an unequal sensibility to

threats (i.e., pathogens, fire risk). Knowledge of forest type is thus essential for a sustainable forest management. Historically, such information was collected through costly field sampling campaigns (forest inventory) that may not capture all variations across forested landscapes. To overcome such shortcomings, remote sensing sensors were increasingly used to complement forest inventory design and generalize field sampled information into a continuous coverage (McRoberts and Tomppo, 2007).

The remote sensing sensors employed for forest type classification may be divided into optical (use sun illumination), LiDAR (light detection and ranging) and synthetic aperture radar (SAR) which use their own illumination. Multi- or hyper-spectral optical sensors have been widely used for forest species identification, accounting for most of the studies identified in systematic surveys (Fassnacht et al., 2016). They are sensitive to leaf structure and chemical make-up (i.e., pigment and water content; Ollinger, 2010; Homolová et al., 2013; Yang et al., 2017) and forest phenology (Yang et al., 2017; Zhu and Liu, 2014). They can also capture forest structure (Fassnacht et al., 2016), albeit this relationship saturates with increasing canopy closure (Nilson and Peterson, 1994; Puhr and Donoghue, 2000). Studies based on optical wavelengths frequently use additional information from aerial laser scanning (ALS, a type of LiDAR) to provide canopy structural information that multispectral data may miss, such as canopy height or closure (Fassnacht et al., 2016; Beland et al., 2019). ALS can provide high-resolution forest structure data, but requires costly scanning campaigns (Beland et al., 2019), and thus, few countries have a systematic wall-to-wall coverage. Although spaceborne LiDAR sensors exist (e.g., IceSat GLAS/ATLAS, GEDI) they only provide information on a sampling pattern as opposed to a continuous coverage (Simard et al., 2011; Dubayah et al., 2020).

SAR sensors use wavelengths that can penetrate clouds, and provide wall-to-wall coverage at high spatial and temporal resolutions, valuable characteristics to record a continuous description of forest phenology (Ling et al., 2022). The echoes received by the SAR sensor carry information about the dielectric constant and the geometry of the illuminated surfaces (Leckie and Ranson, 1998; Rüetschi et al., 2017). The dielectric constant depends on vegetation moisture, whether it is liquid or solid, and the presence of water droplets on surfaces (Way et al., 1994, 1997; Leckie and Ranson, 1998; Rüetschi et al., 2017; Proisy et al., 2000; Soudani et al., 2021). Forests geometry is related to canopy structure (height, closure) and leaf dynamics (Ahern et al., 1993; Proisy et al., 2000). In addition, the sensor- forest target geometry depends on the local incidence angle (θ), as it modifies the distance traversed within forest canopy and thus, the amount of scattered energy (Cimino et al., 1986; Saatchi and Rignot, 1997; Leckie and Ranson, 1998; Castel et al., 2001; Hoekman and Reiche, 2015).

Forest type classification using real- or synthetic aperture radar data was explored early on (Morain and Simonett, 1967), with studies on the influence of the sensor and acquisition characteristics (date, incidence angle) appearing later. Sensor wavelength (band) and polarization influence forest type separability, as each band and polarization have

unique interactions with canopy elements (Fung, 1994, pp. 483–516). Studies in boreal areas stressed the usefulness of cross-pol data, and debated the role of C-band (Rignot et al., 1994; Saatchi and Rignot, 1997; Udali et al., 2021) with some studies demonstrating a positive impact (Rignot et al., 1994) while some others suggesting little benefit from its use, possibly due calibration issues (Saatchi and Rignot, 1997). Regarding acquisition parameters, Ahern et al. (1993) investigated the impact of acquisition date, which controls forest status (i.e., leaf shedding), and found that backscatter data distribution for broadleaf and needleleaf forests overlaps, suggesting that classifications using imagery from multiple dates could attain higher accuracies, as confirmed by later studies (Saatchi and Rignot, 1997; Martinez et al., 1998; Maghsoudi et al., 2012, 2013). Finally, several studies showed that incidence angle plays a role on forest type classification as it modifies the interaction with the canopy (Cimino et al., 1986; Leckie and Ranson, 1998; Castel et al., 2001; Hoekman and Reiche, 2015).

Sentinel-1 C-band SAR data were successfully related to forest phenology (Frison et al., 2017; Rodionova, 2018; Dubois et al., 2020; Proietti et al., 2020; Soudani et al., 2021; Ling et al., 2022), and used to classify forest types (Rüetschi et al., 2017; Dostálová et al., 2018, 2021; Udali et al., 2021). Rüetschi (2017) and Dostálová (2018, 2021) separated broadleaf and needleleaf forests using temporal mosaics (18- and 12-days) whereas Udali et al. (2021) used the de-speckled and de-seasonalized original time series to the same end. Dostálová et al. (2018, 2021) used similarity (distance) to a "reference" time series whereas Rüetschi (2017) and Udali (2021) used random forest classification. These studies took advantage of the contrasting temporal behavior between broadleaf and needleleaf forests. Broadleaf forest had lower VH backscatter coefficient values during the summer months, associated with leaf growth, while needleleaf had a lower VH backscatter coefficient during winter which was associated to sub-zero temperatures. Such classification approaches quickly recognized the importance of removing the influence of the orography.

Sentinel-1 SAR images are provided in the ellipsoid-based sigma nought convention (σ_E^0) to account for scattering area variations caused by the distance to the sensor (range). However, such products do not account for target-dependent variations: the echoes returning from mountain ranges can overlap, causing slopes to appear as very bright "compressed" areas in the focused image. Terrain-flattened conventions remove or reduce target-dependent variations by using a precise estimate of the illuminated area based on digital elevation models (Small, 2011; Frey et al., 2013; Shiroma et al., 2022). In this context sigma-nought (σ_T^0) corrects for terrain scattering area, whereas gamma nought (γ_T^0), also corrects based on incidence angle, following the assumption-driven models developed by Clapp (1946).

Clapp (1946) models consider terrain to be formed by small spheric isotropic scatterers with specific arrangements based on the exponent n ($\gamma_T^0 = \sigma_T^0 / \cos(\theta)^n$). With $n = 0$ terrain is formed by a single layer of spheres that do not shield each other, resulting in

isotropic scattering. $n = 1$ represents the terrain as many layers of spheres, whose illuminated area projected onto the image plane depends on the incidence angle. This model corresponds to the typical γ_T^0 (Cosgriff et al., 1960; CEOS, 2021), widely used as it shows little dependance on the incidence angle (Raney, 1998, p. 33; Woodhouse, 2006, p. 108). $n = 2$ corresponds to Lambert's Law for optics (Cosgriff et al., 1960; Ulaby et al., 1982, pp. 833–837). Note that n does not need to be an integer, allowing for intermediate behaviors (Barrick, 1970). A similar formulation was reached by Castel et al. (2001) when adapting the radiative transfer model developed by Hsu (1996) for sloping terrain. Castel's model allows for reducing directional effects induced by the distance traversed within forest canopy.

Many of the previous studies assert that phenology affects the scattering directionality (i.e., forward scattering, transmission Ahern et al., 1993). However, they use backscatter conventions (σ^0, γ^0 with $n = 1$) that disregard such directionality which imply the existence of residual influence of the incidence angle due differences in the path length traversed within the canopy. Such residual effects can alter backscatter coefficients, reducing sensibility to seasonality and causing classification errors. This study contemplates that directional scattering may change with phenology, leveraging both to classify forest types on mountainous areas. We account for directionality using the semi-empirical model formulated by Castel et al. (2001), whereas phenology is considered through time series similarity to known values extracted from training samples (Dostálová et al., 2018). Results are then analyzed against in-situ stand data including the possible sources of misclassification. In addition, the results are compared to pre-existing forest type layers derived from remote sensing data (e.g., Copernicus Forest type) as a basis for comparison with prior studies (i.e., Dostálová et al., 2018, 2021).

5.2 Study area

A North-South transect over the Fagaraş Mountains (Romanian Southern Carpathians), covering about 25,000 km^2 was used as study area (Figure 5.1). The region hosts a diverse array of species (Table 5.1), including most tree species found in European forests. Broadleaf species occupy the lowlands in the south, characterized by average annual temperatures of 10.5 °C and annual precipitations of 700 mm. Needleleaf and mixed forest (mainly beech and conifer mixtures) occupy the highlands, characterized by average annual temperatures under 4 °C and annual precipitations around 1000 mm. Broadleaf forest usually occupies mild slopes, especially in the case of oak forest, whereas beech, mixed and needleleaf forest appear over increasingly steep slopes, as high as 50°. Over the entire area, minimum winter temperatures drop below zero °C. Most rainfall occur in May-July with a dry season between September and October (Micu et al., 2015; World Bank, 2020; García-Duro et al., 2021). Broadleaf forest usually occupies mild slopes, especially in the case of oak forest, whereas beech, mixed and needleleaf forest appear over increasingly steep slopes, as high as 50°.

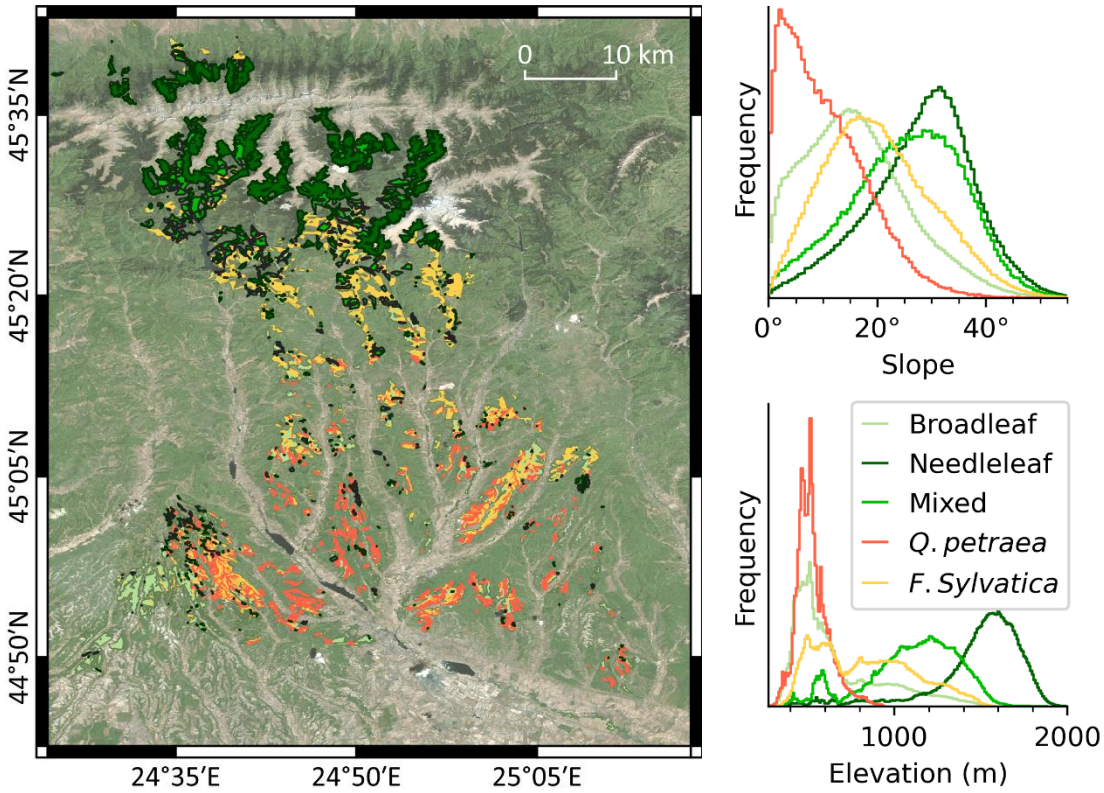

Figure 5.1. Forest stands mask overlaid on high spatial resolution satellite imagery (courtesy of Microsoft Bing, left) and frequency distribution, by slope and elevation, for the main forest species and types (right). Stands have been assigned as "Broadleaf" when they contain at least 80% of a single broadleaf species but they are neither oak (Quercus petraea) nor beech (Fagus sylvatica).

5.3 Methods

5.3.1 Preparation of the reference datasets

Available forest management plans were employed for training and validation (colored areas in figure 5.1; ICAS, 2013a, 2013b, 2014a, 2014b, 2014c, 2014d, 2015a, 2015b, 2016, 2017). The management plans contain information on forest stands, tree patches with uniform and distinct characteristics (DIABOLO, 2021) including boundaries, species composition, and fractional cover (reported in 10% intervals). Table 5.1 details the species that were mentioned in the forest stand management plans used. The forest management stands dataset (FMS) was created by filtering the forest management database based on fractional canopy cover (at least 50%) and species composition. Broadleaf and Needleleaf near-pure stands were defined as stands formed by at least 80% broadleaf and respectively needleleaf species. Near-pure stands, for the dominant broadleaf tree species in the study area (oak or beech) were defined using the same criteria, 80% of the specific tree species. Mixed stands were only used when a nearly even mix of species was present, i.e., the dominant leaf type did not represent more than 60% of the trees.

Three other datasets were employed as ancillary data: 1) a land cover classification layer from Borlaf-Mena et al. (2021b) was used to mask forested areas (forest mask from here

on). The layer was based on support-vector classification of annual backscatter and coherence statistics of year 2019 (full feature set), with an overall accuracy over 95%; 2) the high-resolution Copernicus Forest Type (CFT from here on; Langanke et al., 2013; CLMS 2021, with an overall accuracy of 96.64%) was used for cross-comparison with prior studies (i.e., Dostálová et al., 2018, 2021). CFT high-resolution dataset was resampled to match the resolution and projection of the Sentinel-1 data; and 3) a merged land cover dataset was also used for cross-comparison purposes. The merged land cover dataset (LCm from here on) was derived using the TanDEM-X SAR-based forest mask (for the interval 2011-2015; Martone et al., 2018), the ALOS PALSAR forest mask (year 2017; Shimada et al., 2014b), the global urban footprint (year 2016; Deutsches Zentrum für Luft- und Raumfahrt, DLR; Esch et al., 2017), the European Space Agency Climate Change Initiative land cover dataset (ESA CCI LC year 2015; Achard et al., 2017), and the Corine Land Cover layer (2018 CLC; Büttner et al., 2017; Kosztra and Büttner, 2019). These layers were combined to generate a unique map of main land cover classes as described in detail in Borlaf-Mena et al. (2021b). Briefly, pixels were considered a type of forest if all layers agreed (i.e., pixels classified as forest and Corine and CCI LC agreed on the forest type). The LCm dataset was employed as derived by Borlaf-Mena et al. (2021b; section 3.2), keeping areas labeled as different forest types (Broadleaf, Needleleaf, Mixed).

Table 5.1. Species reported in the forest management plans over the study region. Broadleaf mix and needleleaf mix classes are used to describe stands with many tree species.

	Scientific name	English name
Broadleaf	*Acer campestre*	Field maple
	Acer negundo	Boxelder Maple
	Acer platanoides	Norway Maple
	A. pseudoplatanus	Sycamore
	Alnus glutinosa	Black alder
	Alnus incana	Grey alder
	Betula pendula	Silver birch
	Carpinus betulus	Eur. hornbeam
	Fagus sylvatica	Eur. beech
	Fraxinus excelsior	Eur. ash
	Fraxinus ornus	Flowering ash
	F. pennsylvanica	Green/Red ash
	G. triacanthos	Honey-Locust
	Juglans nigra	Black walnut
	Juglans regia	Eur. walnut
	Morus alba	White mulberry
	Populus alba	Silver Poplar
	Populus nigra	Black Poplar
	Populus tremula	Eur. aspen
	P. x canescens	Grey Poplar
	Prunus avium	Wild cherry
	Quercus cerris	Turkey oak
	Quercus frainetto	Hungarian oak
	Quercus petraea	Sessile oak
	Quercus robur	Eur. Oak
	Quercus rubra	Red Oak
	R. pseudoacacia	Black Locust
	Salix alba	White Willow
	Salix caprea	Goat willow
	Sorbus aucuparia	Rowan
	Tilia tomentosa	Silver linden
	Ulmus glabra	Mountain elm
	Ulmus minor	Eur. field elm
	-	Broadleaf mix
Needleleaf	*Abies alba*	Silver fir
	Larix decidua	Eur. larch
	Picea abies	Eur. spruce
	Pinus nigra	Black pine
	Pinus strobus	White/soft pine
	Pinus sylvestris	Baltic pine
	P. menziesii	Douglas fir
	-	Needleleaf mix

5.3.2 SAR data processing

In total, 345 Sentinel-1 SLC images acquired between 2017 and 2019 were used in this study. The images were obtained in single look complex (SLC) format. The dataset consisted of images acquired along all relative orbits (i.e., 7, 29 and 131) overlapping the study area. The SLC images had a pixel spacing of 14.1 m in azimuth and 2.3 m in range

and carried both VV and VH polarizations. The DEM employed for normalization was using the 12.5 m TanDEM-X digital elevation model (©DLR, 2019; Rizzoli et al., 2017) resampled to a resolution of 20 m.

For each SLC image, a subset was generated by mosaicking only the sub-swathes overlapping the study area. The data was multilooked with factor of 7 in range and 2 in azimuth to reduce speckle and bring the pixel size closer to the resolution intended for analysis (20 m). The first image acquired for each orbit was used as reference. Each successive acquisition was co-registered to the reference using an iterative procedure based on intensity matching and spectral diversity aided by the TanDEM-X DEM (Wegmüller et al., 2002b).

The DEM was employed along with the Sentinel-1 state vectors to prepare a lookup table relating earth coordinates and SAR image coordinates, as well as auxiliary layers including the incidence angle (θ_E), the local incidence angle (θ_T), the pixel scattering area, and a layover-shadow mask. The backscatter intensity was calibrated to terrain flattened σ^0, or σ_T^0 (T, terrain-normalized), using the scattering area estimate (Castel et al., 2001; Small, 2011; Frey et al., 2013). A multi-temporal speckle filter with a window size of 5 pixels was applied to reduce speckle (Quegan et al., 2000). Backscatter intensity images were ortho-rectified using inverse distance resampling and converted to decibel scale (dB). Areas affected by radiometric and geometric distortions were masked using the layover and shadow masks derived from the DEM, as well as masking areas with anomalously high values as outlined in Borlaf-Mena et al., (2021b; areas not masked as layover or shadow where scattering area may have been underestimated).

5.3.3 Modelling backscatter dependance on the incidence angle

Castel (2001) proposed a simple semi-empirical model relating forest backscattering intensity and slope orientation, which has been employed in a multitude of SAR-based forest studies (i.e. Santoro et al., 2006; Thiel et al., 2009; Cartus et al., 2014). The complete model (eq. 1) considers the scattering area and the incidence angles respective to ellipsoid and terrain surfaces (ellipsoid, A_E and θ_E; terrain, A_T and θ_T, respectively), along with the crown optical depth of each polarization (τ_p, transmitted-pol; τ_q, received-pol) and the path length within the canopy (L_T) which depends on crown height, the local incidence angle (θ_T), and the terrain slope (α) (eq. 2).

$$\gamma_T^0 = \sigma_E^0 \frac{A_E}{A_T} \frac{\cos\theta_E \cdot \left(1 - e^{-(\tau_p + \tau_q) L_E}\right)}{\cos\theta_T \cdot \left(1 - e^{-(\tau_p + \tau_q) L_T}\right)} = \sigma_E^0 \frac{A_E}{A_T} \left(\frac{\cos\theta_E}{\cos\theta_T}\right)^n = \sigma_T^0 \left(\frac{\cos\theta_E}{\cos\theta_T}\right)^n \quad (1)$$

$$L_E = \cos 0 \sec\theta_E = \sec\theta_E; L_T = \cos\alpha \sec\theta_T \quad (2)$$

where: γ_T^0 is backscatter coefficient normalized for both the DEM-derived scattering area and the incidence angle; σ_E^0 is the backscatter coefficient normalized with an ellipsoid-derived scattering area; σ_T^0 is σ^0 corrected for local terrain surface scattering area (T, terrain-normalized). The model can be approximated as the ratio of the cosines of

the incidence angles raised to the power n, dependent on the sensor parameters (i.e., nominal incidence angle, wavelength) and forest parameters, such as canopy height and optical thickness (Castel et al., 2001). In turn, optical thickness depends on fractional canopy cover (more space filled by branches and leaves), and leaf area index, as it contributes to wave attenuation (Leckie and Ranson, 1998). If equation (1) is redistributed and linearized through decibel scale (eqs. 3-5) it becomes possible to estimate a common γ_T^0 (intercept) and n (slope) for a group of observations by using simple linear regression where $10 \cdot \log_{10}(x_\theta)$ ($x_\theta = \cos\theta_T / \cos\theta_E$) and $10 \cdot \log_{10}(\sigma_T^0)$ are the predictor and the predicted variables, respectively.

$$\sigma_T^0 = \gamma_T^0 \left(\frac{\cos\theta_T}{\cos\theta_E}\right)^n \quad (3)$$

$$10 \cdot \log_{10}(\sigma_T^0) = 10 \cdot \log_{10}(\gamma_T^0) + n \cdot 10 \cdot \log_{10}\left(\frac{\cos\theta_T}{\cos\theta_E}\right) \quad (4)$$

$$10 \cdot \log_{10}(\sigma_T^0) = 10 \cdot \log_{10}(\gamma_T^0) + n \cdot 10 \cdot \log_{10} x_\theta \quad (5)$$

5.3.4 Sample selection and model fitting

As the relationship (n) between backscatter intensity and incidence angle depends on forest characteristics, ideally a separate model should be fit to each forest species/structure (e.g., age class) combination. However, such modeling is not feasible with limited in situ data while also difficult to implement outside of the training/validation sample as additional information of forest characteristics (e.g., age) would be needed to assign a model to a certain pixel. Instead, we assume certain scattering homogeneity within the same forest species or forest types, as the relationship between backscatter and age or biomass saturates early at C-band.

To train the model (i.e., derive n and γ_T^0 as a function of forest species/type) a common frame of sampling (i.e., pixels selection) was needed to avoid large differences (orbit to orbit) in the location and the number of the sampled pixels. From the entire sample, 30% of the pixels were reserved for validation, using the rest as candidates for model fitting. For every orbit, the candidate sample was culled to 50.000 pixels per forest type while excluding areas prone to radiometric normalization errors (masked areas, $\theta_T < 10°$). Said sample was stratified in 50 intervals of x_θ, taking up to 1.000 random samples per interval. This approach ensured uncommon x_θ values (i.e., there are few forests in areas with slopes over 40°) were sampled while also ensuring a representative sample to fit the model. All pixels not selected during this process were added to the validation sample, to ensure classes with a smaller representation have a sufficient sample size. With sampling pixel locations selected, a model was fit for each image and forest type. Model fits were evaluated using their coefficients of determination (R^2).

5.3.5 Classification

For each image and forest type we modelled the expected backscatter intensity ($\widehat{\sigma_T^0}$) based on the cosine ratio (x_θ), both with decibel scaling. Subsequently we calculated

(eq. 6) the absolute residual (AR) for all forest pixels included in the forest mask. The residual value was accumulated across images by model (i.e., one for each forest type and image) as a weighted average of absolute residuals (WAAR). The weight was the inverse of the scattering area to give a larger importance to observations with smaller geometric distortions (Small et al., 2021) (eq. 7).

$$AR = \left|\sigma_T^0 - \widehat{\sigma_T^0}\right| \quad (6)$$

$$w_i = \frac{1}{a_i}; WAAR = \frac{\sum_{i=1}^{n} w_i AR}{\sum_{i=1}^{n} w_i} \quad (7)$$

Pixels were assigned to the forest type with the smallest WAAR under the assumption that it showed the largest similarity to the ensemble of models fitted for a given forest type. To avoid misclassifications caused by radiometric distortions we applied a circular majority filter with a diameter of 7 pixels, followed by a MMU (minimum mapping unit) filter reclassifying patches smaller than 25 pixels (1 ha).

We performed several classifications by varying the polarization employed for modelling, the time window employed to calculate the WAAR (yearly versus all three years together), and the detail of forest type classification: broadleaf/needleleaf (two classes), separating mixed as well (three classes), and separating broadleaf forest into beech and oak (four classes).

5.3.6 Validation and inter-comparison with pre-existing datasets

Classification runs were assessed based on the FMS dataset using metrics derived from confusion matrices: Kappa statistic (K), overall accuracy (OA) and commission and omission (CE, OE) errors. Classifications showing the largest accuracies were disaggregated based on management information, slope, and elevation to understand the drivers behind the errors. Classification results were further compared with CFT and LCm. These pre-existing datasets were also analyzed against the FMS field data to understand their utility as reference datasets.

5.4 Results

5.4.1 Modelling backscatter based on incidence angle

Models adjusted for broadleaf, needleleaf and mixed forests classification obtained moderate results in the percentile based R^2 summaries (Table 5.2): median R^2 of 0.5, a minimum 5th percentile of 0.32 and a largest 95th percentile of 0.69.

Table 5.2. Summary (percentiles) of the coefficients of determination for the linear models disaggregated by forest type and polarization.

	Broadleaf		Needleleaf		Mixed		Oak		Beech	
	VH	VV	VH	VV	VH	VV	VH	VV	VH	VV
Min	0.18	0.30	0.27	0.43	0.20	0.41	0.03	0.10	0.18	0.33
P05	0.32	0.39	0.39	0.57	0.39	0.47	0.10	0.21	0.34	0.40
P50	0.50	0.53	0.55	0.62	0.51	0.56	0.30	0.35	0.50	0.52
P95	0.59	0.63	0.63	0.68	0.59	0.64	0.42	0.49	0.58	0.61
Max	0.65	0.68	0.68	0.71	0.64	0.67	0.50	0.56	0.62	0.65

Fits for individual species varied: the fit for beech forest showed similarly moderate R^2 (min 5th perc. 0.34, median 0.5, max 95th perc. 0.61), whereas the fit for oak forest showed lower values (min 0.03, min 5th perc. 0.1, median 0.3, max 95th perc. .49). In all cases R^2 values were higher for VV, when compared to VH, polarization. Figure 5.2 represents a selected group of fits for orbit 7.

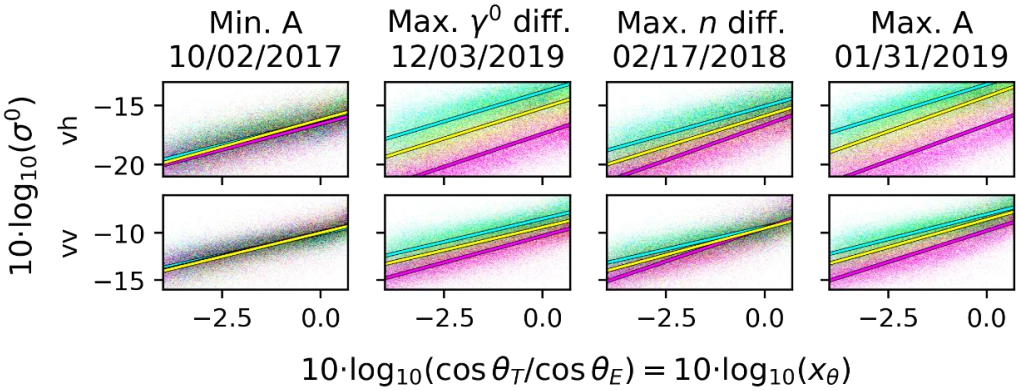

Figure 5.2. Some fits with R^2 > 0.5 from images of orbit 7. From left to right: fit with the least area enclosed between the lines of broadleaf (cyan) and needleleaf (magenta), cases with the largest γ^0 and n difference between broadleaf and needleleaf fits, and the fit with the largest enclosed area. Mixed forest was represented as yellow color. Points follow the same code, using subtractive color to represent overlaps between points (cases where points of all three forest types overlap are colored black). Note x_θ decreases with larger values of θ_T.

The smoothed time series of the n and γ^0 values (Figure 5.3) showed seasonal variations. For broadleaf forests the largest n_{VV} and γ^0_{VV} were observed in June-July, with the lowest values being observed around October-November. n_{VH} minima and maxima showed similar periodicity, albeit with larger inter-orbit differences. Peak values for γ^0_{VH} were observed in November-December and April while it reached minimum values in September-October. Needleleaf forest γ^0 displayed a clear yearly cycle with the highest values being recorded around July, and lowest values in January-February. n_{VV} showed weak cycles with the highest values being observed in February-March and lowest values around May and November. Similar cycles were observed for mixed forests with peak values in summer, half-peak in autumn, and minimums in January-February. Mixed forest γ^0_{VV} showed peak values in winter (as observed for broadleaf class) as well as summer (as observed for the needleleaf class) whereas γ^0_{VH} was high all over the year.

5.4.2 Classification results

All classifications presented at least a moderate agreement (K > 0.5; Landis and Koch, 1977) with the FMS validation dataset. Results varied little with the time interval used (one vs. three years, Table 5.3), with larger differences being observed as a function of polarization and number of classes. The highest OA were observed when using the VH channel. In particular, classification of two-classes showed a near-perfect agreement with the FMS (K > 0.8; OA > 95%) while separating three-classes resulted in slightly lower

accuracy (K > 0.7; OA > 85%; Figure 5.4). A moderate agreement with the reference data was observed when separating four classes (K > 0.4; OA > 68%).

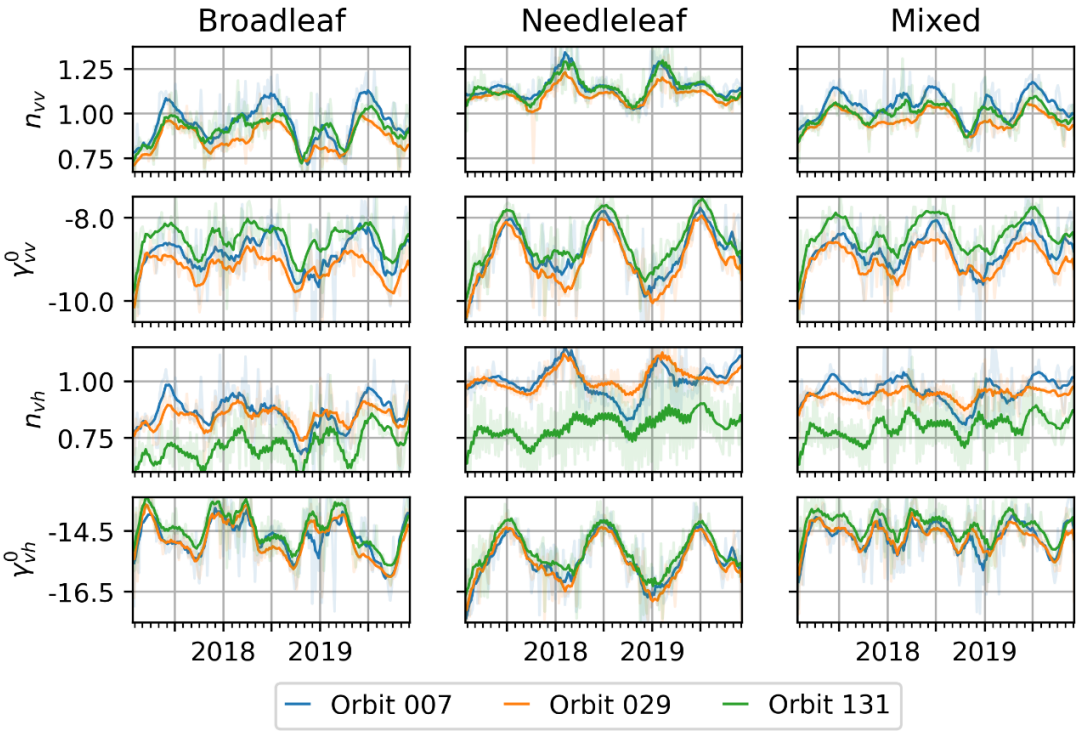

Figure 5.3. Results of the fitting process separated by forest type and orbit. Thick lines represent the 9-dat rolling average while pale lines represent the values obtained during the fitting process.

Table 5.3. Kappa and overall accuracy of the classifications as evaluated against the in-situ data. Cells are colored with a gradient between yellow and green to indicate lower to higher values.

Datasets used	# of classes	Kappa statistic				Overall accuracy			
		2017	2018	2019	all	2017	2018	2019	all
VH polarization	2	0.88	0.90	0.90	0.90	95.7	96.6	96.7	96.5
	3	0.72	0.72	0.70	0.72	87.2	87.0	85.6	86.9
	4	0.66	0.62	0.63	0.65	77.7	73.8	74.3	76.6
VV polarization	2	0.87	0.85	0.87	0.87	95.4	94.9	95.6	95.6
	3	0.62	0.63	0.62	0.63	81.7	81.6	81.1	82.0
	4	0.57	0.55	0.55	0.57	71.1	69.1	68.2	70.8

Considering the patterns found at overall level we decided to focus on the classifications performed with the whole time series and the VH channel, as the time window employed seemed to have little influence, and VH channel always had a larger kappa and overall accuracy. Furthermore, classifying several years together may help alleviate differences across years. The errors are depicted in the Table 5.4, and the Figure 5.5.

Table 5.4. Classification errors when using the entire time series of VH backscatter evaluated with FMS. Cells are colored with a gradient between green and yellow to indicate lower and higher values of error, respectively.

	Commission Error (CE)					Omission Error (OE)				
Classes	Broad leaf	Needle leaf	Mixed	Oak	Beech	Broad leaf	Needle leaf	Mixed	Oak	Beech
2	3.2	4.5				1.2	11.1			
3	4.3	10.1	61.9			9.2	15.6	39.7		
4		8.7	51.2	52.4	17.7		15.2	49.8	18.4	22.1

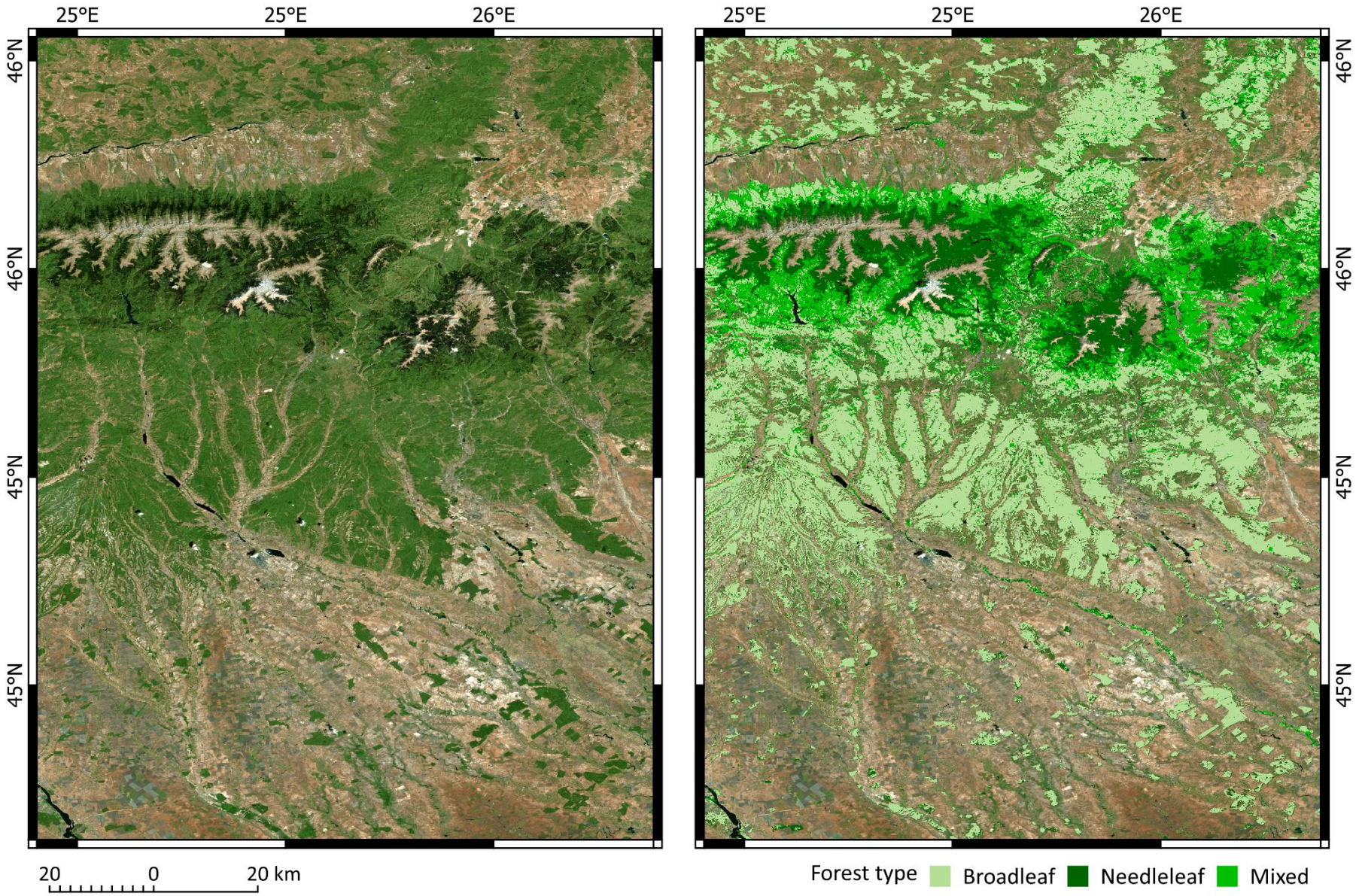

Figure 5.4. Bing maps imagery (left), classification in broadleaf, needleleaf and mixed based on the complete time series of VH data (right)

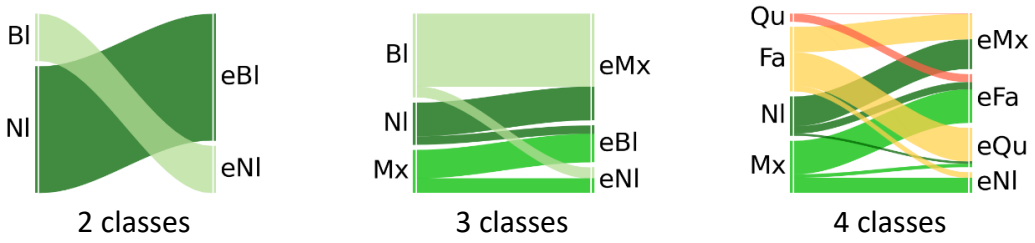

Figure 5.5. Alluvial diagrams of the omission and commission errors depending on the number of forest types classified. Left axis shows the reference label (Bl, Broadleaf, light green; Nl, Needleleaf, dark green; Mx, mixed forest, medium green; Qu, Quercus petraea, red; Fa, Fagus sylvatica, orange), right axes the label received by the misclassified pixels (error – 'e'). The thickness of the lines indicates the frequency of each error compared to the total error.

5.4.3 Factors affecting classification

Pure and near-pure stands were properly classified in most cases. When only broadleaf and needleleaf forests were separated (two-classes) the former type was over-predicted in stands with an even mix of species (Figure 5.6, left panel). When mixed forests were added (three-classes) the over-prediction of broadleaf forests decreased in a near-symmetric fashion (Figure 5.6, central panel).

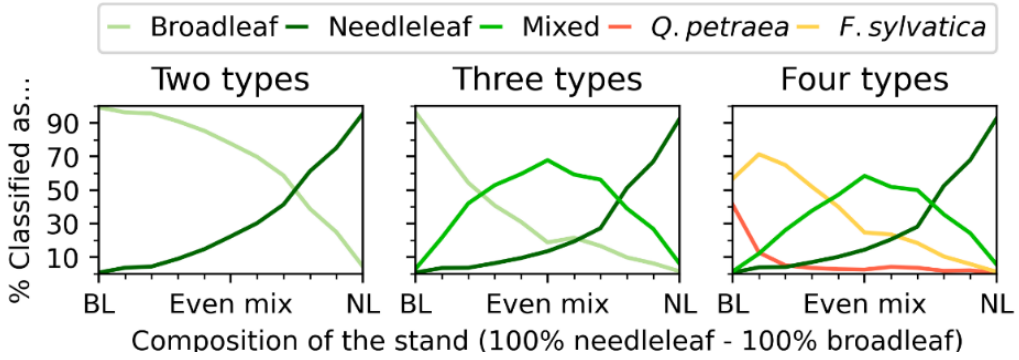

Figure 5.6. Percentage of pixels classified as each forest type (y-axis) with respect of the reported proportion of broadleaf and needleleaf species (x-axis). Classification based on the VH channel when using the entire time series and stand data as reference.

The proportion of pixels classified as mixed forest followed a symmetric distribution centered around the even mix. However, for evenly mixed stands over 30% of the pixels were assigned as pure broadleaf or needleleaf forest. In the four-type classification (Figure 5.6, right panel), mixed forest had a less symmetric distribution, and the overtake point between broadleaf and needleleaf was shifted. Oak stands were properly identified mainly in areas with pure stands (>80% broadleaf species).

Misclassification seemed not related to the fractional canopy cover (FCC) when only separating broadleaf and needleleaf forests (Figure 5.7). However, increasing FCC reduced the misclassifications as mixed forest, while increasing misclassifications as broadleaf forest in areas with high (>80%) FCC. When separating four classes, classification errors for oak forests seemed little related to FCC while beach forests misclassification increased dramatically in stands with FCC above 70%.

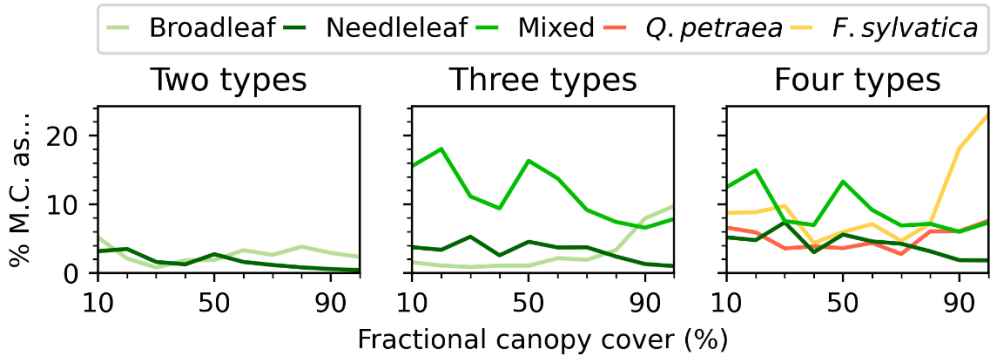

Figure 5.7. Percentage of all pixels within a fractional cover interval (FCC, x-axis) that have been pixels misclassified as a specific forest type (M.C., y-axis).

Analyzing classification results as a function of slope (Figure 5.8), showed that broadleaf forests were more often misclassified over steep slopes (>35°), whereas needleleaf forests misclassification were largely constant over the entire slope range although a small uptick was observed over nearly flat (<5°) areas. When separating three forest types, misclassification errors for needleleaf and mixed forest increased with increasing slope. The opposite trend was observed for oak and beech stands, four-classes, with classification errors decreasing with increasing slope. Mixed and needleleaf classes maintained the trends observed for the three-class run.

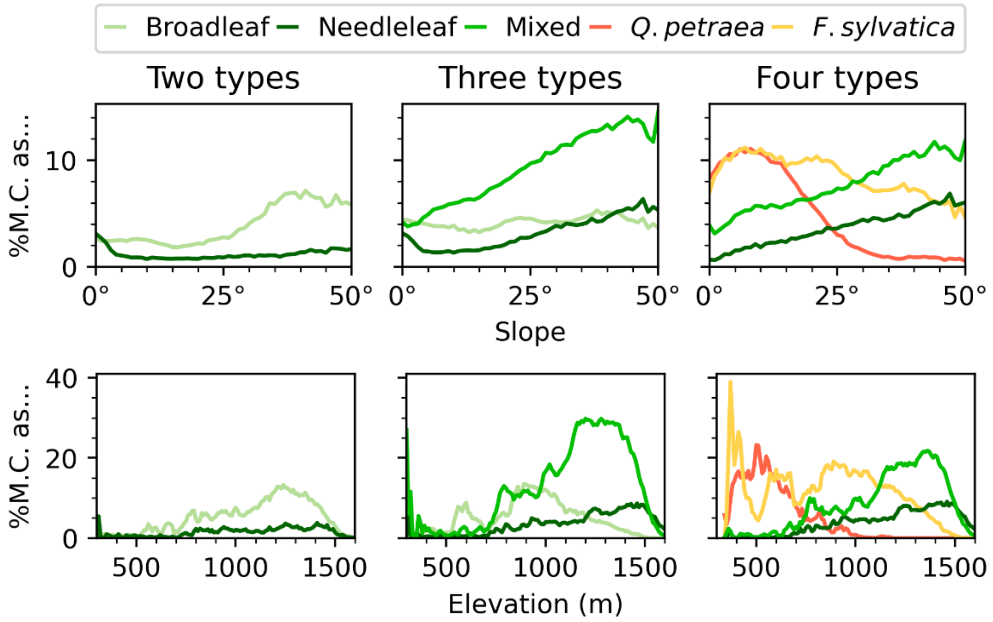

Figure 5.8. Percentage of all pixels within a 1º degree slope interval or 10-meter elevation interval (x-axis), that have been misclassified as a specific forest type (M.C., y-axis).

Analyzing misclassification errors as a function of elevation (Figure 5.8) revealed a common pattern for needleleaf forest with slightly increasing errors up to 1500 m above sea level (a.s.l.). Mixed forests were more often misclassified in the 1200-1400 m a.s.l. interval. Broadleaf forest classification errors appeared more frequently at 1200-1300 m a.s.l. when separating only two forest types and at 800-1000 m a.s.l. when separating three types. The largest misclassifications as oak or and beech appeared at low altitudes, albeit

the former decreased rapidly, while misclassification as beech was still substantial at 1000 m a.s.l.

5.4.4 Inter-comparison with pre-existing datasets

5.4.4.1 Assessment of the preexisting forest type datasets

Overall, the CFT and LCm reference layers showed high accuracies when compared to the FMS (Table 5.5, Figure 5.9). CFT (two classes) had a 94.6% overall accuracy (OA) when compared to FMS, a value similar to the reported accuracy (96.6%; CLMS 2021). Broadleaf forest class reached 95% accuracy whereas the needleleaf forest showed some tendency to be misclassified as the former (12.9% omission error). The LCm dataset (three classes) was less accurate (88.4% OA), with particularly large CE and OE for mixed forests (>47%).

Table 5.5. Confusion matrices comparing the stand data (reference, columns) and the datasets employed for validation (Copernicus Forest Tyle, Land Use/Land Cover, rows). K – Kappa, OA – overall accuracy, CE – commission error, OE – omission error.

	Copernicus forest type (CFT) (K=0.86; OA=94.57%)			**Merged land cover (LCm)** (K=0.71; OA=88.38%)			
	Broadleaf	Needleleaf	CE	Broadleaf	Needleleaf	Mixed	CE
Broadleaf	924882	47914	4.93	673217	10870	36278	6.55
Needleleaf	23778	324241	6.83	456	122763	5076	4.31
Mixed				45933	12087	45649	55.97
OE	2.51	12.87		6.45	15.75	47.53	

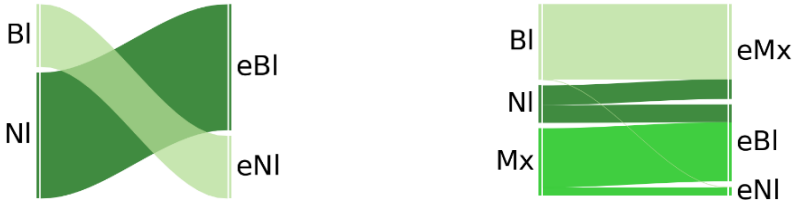

Copernicus forest type (CFT) Merged land cover (LCm)

Figure 5.9. Disagreement between the Copernicus Forest Type and the Land Use/Land Cover dataset with respect to the GIS forest stand layer. Left vertical axes show the label in the reference GIS forest stand layer, right vertical axes show the label in the evaluated ('e') dataset.

5.4.4.2 Agreement with pre-existing datasets

Two-type classification showed moderate agreement with CFT (Table 5.6, Figure 5.10, K = 0.7; OA = 91.1%), observing particularly large commission (26.4%) and omission errors (21.5%) for needleleaf forest. Agreement between the two-type classification and LCm was near-perfect (k ≈ 0.9; OA = 97.8%), with some commission error for needleleaf forest (14.1%) while for the three-type classification was moderate (K ≈ 0.6; OA = 86.5%), with most of the disagreement caused by misclassification of broadleaf as mixed or mixed as other forest type.

Table 5.6. Classification errors when comparing the entire time series of VH backscatter and pre-existing datasets. CFT stands for Copernicus Forest Type, LCm stands for merged land cover; CE and OE stands for commission and omission error, respectively. Cells are colored with a gradient between green and yellow to indicate lower and higher values of error, respectively.

	CFT (2 classes) (K=0.70; OA=91.1%)		**LCm (2 classes)** (K=0.89; OA=97.8%)		**LCm (3 classes)** (K=0.64, OA=86.5%)		
	Broadleaf	Needleleaf	Broadleaf	Needleleaf	Broadleaf	Needleleaf	Mixed
CE	4.8	26.4	0.5	14.1	2.1	24.7	62.2
OE	6.2	21.5	1.9	4.0	11.8	7.9	36.2

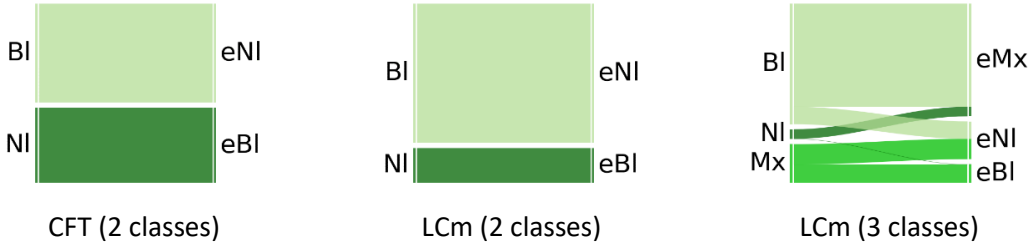

CFT (2 classes) LCm (2 classes) LCm (3 classes)

Figure 5.10. Disagreement between the Copernicus Forest Type and the Land Use/Land Cover dataset with respect to the GIS forest stand layer. Left vertical axes show the label in the reference GIS forest stand layer, right vertical axes show the label in the evaluated ('e') dataset.

5.5 Discussion

5.5.1 Modelling the backscatter based on incidence angle

The relationship between backscatter intensity and cosine ratio was relatively strong for all forest types (broadleaf, needleleaf and mixed) with median R^2 values around 0.5 and a maximum of 0.73 (Table 5.2). By species, different trends were observed with median R^2 values for beech forests reaching 0.5 while for oak forests the median value vas lower (0.3) as they generally occupy flatter areas (see Figure 5.1) which reduced the influence of topography on the backscatter coefficient. Such values suggest that incidence angle account for about 50% of backscatter variability in forested areas. The remaining variability could be attributed to soil moisture or forest structure (e.g., height, canopy cover) which are neglected in the model. Variation of the R^2 individual values around the median could be attributed to meteorological events such as rain and snow, which may alter the relationship between slope and scattering mechanisms.

By polarization, R^2 quantiles for VV channel were higher (Table 5.2), which may be explained by the model design, a first-order model (Castel et al., 2001) which only considers single interactions. This can be adequate for modelling co-polarized backscatter but insufficient for modelling the depolarization process characterized by multiple interactions. Thus, cross-polarized backscatter from vegetated surfaces may be mis-characterized, causing fits based on the model to capture less variability (Oh et al., 2002; Kweon and Oh, 2015).

Temporal patterns observed for γ^0 and n were attributed to broadleaf forest leaf dynamics (Figure 5.3). Broadleaf forest had an increased VH backscatter during winter (Rüetschi et al., 2017; Dostálová et al., 2018; Dubois et al., 2020), when the exposed woody elements act as a volume scatterer, depolarizing the incoming wave (Ahern et al., 1993; Proisy et al., 2000; Dubois et al., 2020; Soudani et al., 2021). As leaf area reaches its maximum, the canopy becomes more opaque (higher optical depth; Castel et al., 2001), masking woody components and decreasing γ^0_{VH} (Frison et al., 2017; Dubois et al., 2020; Pfeil et al., 2020; Soudani et al., 2021; Ling et al., 2022). In autumn, the canopy loses mass and water (Yang et al., 2017; Soudani et al., 2021) thus exposing the woody elements with the associated increase in γ^0_{VH} (Dubois et al., 2020; Proietti et al., 2020; Soudani et al., 2021; Ling et al., 2022).

γ^0_{VV} channel displayed a characteristic cycle over broadleaf forest, a contrasting result when compared with prior studies (Proisy et al., 2000; Frison et al., 2017; Dostálová et al., 2018; Soudani et al., 2021; Ling et al., 2022). A possible explanation is the use of a variable optical depth (n) in our study when compared to the use of a constant value, such as the "common" γ^0_T (Rüetschi et al., 2017; Proietti et al., 2020), or σ^0_E (Frison et al., 2017; Soudani et al., 2021; Dubois et al., 2020; Ling et al., 2022; Dostálová et al., 2018, 2021). Relationship between VV backscatter and incidence angle has been found to vary with vegetation water content over large scales, which also could be related to changes in forest optical depth (ASCAT C-band VV data with 12.5 km resolution; Pfeil et al., 2020). A second plausible explanation is related to scale, as prior studies extracted the backscatter time series over smaller areas (Proisy et al., 2000; Frison et al., 2017; Rüetschi et al., 2017; Soudani et al., 2021). Rüetschi et al. (2017) observe no cycle except for the largest beech stand (46 ha), where a small increase in VV backscatter during spring followed by a gradual decrease during summer was observed. It is possible that VV backscatter relationship with phenology is fainter, or it is affected by additional factors (i.e., soil moisture, double bounce) and only appears at larger scales. Indeed, scatterometer data showed cyclical differences similar to those reported by Rüetschi et al. (2017), that were attributed to variations in the woody vegetation water content (Pfeil et al., 2020).

γ^0 from needleleaf forests displayed a yearly cycle with the highest point during summer and the lowest during winter, usually associated to sub-zero temperatures (Ahern et al., 1993; Rüetschi et al., 2017; Dostálová et al., 2018; Rodionova, 2018; Dubois et al., 2020; Yu et al., 2020; Ling et al., 2022). This has been explained by frost resistance mechanisms in conifer species (Dubois et al., 2020). As days get shorter and colder conifer species stop growth, reduce metabolic activity, and increase solute concentrations (e.g., sucrose) to withstand frost. This prepares tissues to allow a large portion of the water to freeze (Havranek and Tranquillini, 1995; Chang et al., 2021). Both ice formation and so-

lute accumulation can decrease the dielectric constant, making the canopy more transparent and thus decreasing scattering (Ahern et al., 1993; Way et al., 1997; Santoro, 2003; Rodionova, 2018; Dubois et al., 2020; den Besten et al., 2021).

Mixed forests showed an intermediate behavior between broadleaf forest, with peaks characteristic of both forest types, in agreement with results shown by Dubois et al. (2020). Nevertheless, it should be noted that both soil moisture and weather events also may play a role in the behavior of γ^0 and n. For example, a larger moisture content or rain events may raise backscatter, whereas snow presence may reduce it (Proisy et al., 2000; Rodionova, 2018; Dubois et al., 2020).

5.5.2 Classification results

There was a large variability in the results attained for different classifications with K varying from 0.5 to 0.9, whereas overall accuracies (OA) ranged between 68 and 97% although results based on a single year of data and those using multiple years were similar (Table 5.3). More accurate classifications were obtained when using the VH channel, possibly because the spacing between the fitted lines is larger compared to VV channel (Figure 5.2). Udali et al. (2021) obtained similar results, where improved accuracies were observed when using the VH polarization when compared to VV or their joint use. This could be explained by the VH channel being more sensitive to tree structure and phenology, whereas the VV channels not only is less sensitive, but also is more affected by weather events, soil moisture or ground-trunk interactions (Proisy et al., 2000; Patel et al., 2006; Dostálová et al., 2016; Frison et al., 2017; Proietti et al., 2020; Soudani et al., 2021; Ling et al., 2022)

Separating broadleaf and needleleaf forest based on the VH channel resulted in high accuracies, K ≈ 0.9 and OA > 95% (Table 5.3), values significantly higher when compared to prior studies (Rüetschi et al., 2017, K=0.73, OA=86%; Udali et al., 2021, K=0.86, OA=94%). When mixed forest is separated as well the accuracy decreased (K > 0.7, OA > 85%, Table 5.4, Figure 5.5), with most errors being caused by confusion of mixed forests with either pure conifer or broadleaf forest stands as also suggested by (Ahern et al., 1993). Classification accuracies decreased further (K 0.62-0.66, OA 74-78%) when disaggregating at broadleaf species level. Beech forests were frequently misclassified as oak as mixed forests as beech trees are often one of the main species in such forest stands, (Ahern et al., 1993). Albeit not entirely comparable, classification at main species level suggest similar accuracies as those observed in previous studies (Rüetschi et al., 2017, K=0.58 and OA=72%; Udali et al., 2021, K=0.54 and OA=66%).

5.5.3 Factors affecting classification results

Classifications were assessed against forest management stand data to understand the relationship between the mutually exclusive classes, and species composition (mixture; Figure 5.6). Classifications separating just broadleaf and needleleaf forest classes showed a possible bias towards broadleaf class over areas with an even mix of the two

species groups. Such bias was related to the absence of a mixed forests class in the classification legend and the propensity of the algorithm to classify such stands as broadleaf forests. Indeed, such assumption was confirmed when mixed forests were added to the classification scheme, as misclassification of mixed forests as broadleaf or needleleaf becomes near-equally likely.

The number of classes considered influenced misclassification errors related to the forest fractional canopy cover, slope, or elevation, which could be attributed to the classifier design (Figure 5.7 and Figure 5.8). A pixel is classified as a specific class using the closest modelled line, i.e., similarity to the "expected" relationship between backscatter and incidence angle. However, introducing model lines for additional forest types may alter which is the closest line. For example, pixels whose scattering area has been undercompensated (high backscatter) will be classified as whichever class has the largest modelled backscatter among all classes considered. Furthermore "closest" does not necessarily mean "close": pixel values can fall well outside the area bound by the fitted lines, i.e., no matter how far they are, they are still assigned to a class.

The fractional canopy cover (FCC, Figure 5.7) had little influence on classification errors for broadleaf and needleleaf classes although it was related to variations in accuracy for the mixed, beech and oak forest classes. In general, for these classes, a larger FCC was tied to reduced classification errors. Confusions at low FCC levels were attributed to reduced differences between forest types due the increased influence of the underlying soil. At high FCC, broadleaf (beech) species may heavily influence pixel scattering. This would be consistent with the tendency to misclassify areas with an even mix of broadleaf and needleleaf species when separating just those classes. Increasing terrain slope usually resulted in lager errors for broadleaf in the two-type classification or for needleleaf and mixed forest in the remaining classifications (three and four classes; Figure 5.8). Patterns observed for elevation influence on classification were more difficult to explain and could be attributed to climatic conditions (i.e., longer periods with snow cover), or differences in forest structure at different altitudinal levels (Dostalova et al., 2016; Dostálová et al., 2018).

5.5.4 Inter-comparison with pre-existing datasets

The agreement of the classifications based on the full time series of VH data with CFT was moderate (K = 0.7, OA ≈ 91%; Table 5.6, Figure 5.10), similar to prior studies (Dostálová et al., 2018, K=0.69, OA=85%). Nevertheless, one should note that such values were obtained over a largely mountainous area where prior studies suggested decreased accuracies. Indeed, Dostálová (2018) suggested a drop in OA to 67-76% over mountainous regions. This could be explained by the assessment of CFT with FMS as reference, where CFT displayed some tendency to misclassify needleleaf of as broadleaf, with the former having an omission error of 13% (Table 5.5, Figure 5.7). Such limitation, described on CFT product manual, was explained by an overcorrection of Sentinel-2 imagery over mountainous areas which propagates into classification results (CLMS 2021,

pp. 45–49). Thus, areas misclassified in CFT dataset will cause a disagreement, artificially raising the commission error for needleleaf to up to 26%.

5.6 Conclusions

In this study we proposed a classification framework that leverages the relationship between radar scatter and the local incidence angle, as well as the temporal capabilities of Sentinel-1 A and B. For each image and forest type we fitted a regression line between the backscatter coefficient and the local incidence angle. Subsequently we calculated the absolute residuals between every forest pixel and each regression line. The absolute residuals were accumulated across dates for each forest type and the pixels were classified based on the smallest accumulated residuals. The framework was applied to classify temperate forests across a North-South transect in the Carpathian Mountains. Classification results were validated against in-situ stand data and cross-compared with the Copernicus high-resolution forest type data.

The classification framework was found to be sensitive to forest phenology regardless of the polarization used (VV or VH). Classification of broadleaf and needleleaf forest attained accurate results, with a similar or better performance when compared to prior studies. The improvement was especially relevant over areas with significant terrain slopes, where the performance of our model degraded less. Incorporating mixed forest into the classification scheme reduced the accuracy. As mixed forest retain some similarity to the individual species components it is believed that introducing a fuzzy approach may be beneficial. When separating broadleaf into oak and beech species the accuracy degraded further, with large misclassification of beech as oak, and a large confusion between beech and mixed forest, especially in pixels located at high altitudes or on steep slopes. Nevertheless, our results show that the proposed framework may generate highly accurate (>95%) maps separating broadleaf and needleleaf forest, and moderate accuracies (>84%) when separating mixed forest as well. Further, the forest optical depth related parameter n is estimated as a biproduct of the process and may be employed to reduce directional effects in regional studies focused on the retrieval of continuous variables (i.e., above ground biomass) although additional research would be needed to explain its variability.

Chapter 6: Growing Stock Volume Retrieval from Single and Multi-Frequency Radar Backscatter

Tanase, M.A., Borlaf-Mena, I., Santoro, M., Aponte, C., Marin, G., Apostol, B., Badea, O., 2021. Growing Stock Volume Retrieval from Single and Multi-Frequency Radar Backscatter. Forests 12, 944. https://doi.org/10.3390/f12070944

Abstract

While products generated at global levels provide easy access to information on forest growing stock volume (GSV), their use at regional to national levels is limited by temporal frequency, spatial resolution, or unknown local errors that may be overcome through locally calibrated products. This study assessed the need, and utility, of developing locally calibrated GSV products for the Romanian forests. To this end, we used national forest inventory (NFI) permanent sampling plots with largely concurrent SAR datasets acquired at C- and L-bands to train and validate a machine learning algorithm. Different configurations of independent variables were evaluated to assess potential synergies between C- and L-band. The results show that GSV estimation errors at C- and L-band were rather similar, relative root mean squared errors (RelRMSE) around 55% for forests averaging over 450 m^3 ha^{-1}, while synergies between the two wavelengths were limited. Locally calibrated models improved GSV estimation by 14% when compared to values obtained from global datasets. However, even the locally calibrated models showed particularly large errors over low GSV intervals. Aggregating the results over larger areas considerably reduced (down to 25%) the relative estimation errors.

6.1 Introduction

Forests are among the most biodiverse terrestrial ecosystems and a key element for carbon sequestration as they store large amounts of organic matter (i.e., biomass). Therefore, forest above ground biomass (AGB) estimation is a sensitive research topic, as information on AGB levels and dynamics is needed to estimate greenhouse gases flux and thus to shape policies development, implementation, and monitoring (Gibbs et al., 2007). This importance is highlighted by the countless forest inventory programs aimed at evaluating, monitoring, and reporting, among others, AGB or Growing Stock Volume (GSV) levels. Such programs use an array of data sources from in situ measurements to information acquired by earth observation (EO) platforms. In situ surveys, based on systematic sampling grids, are the backbone of traditional national forest inventory (NFI) programs sometimes stretching back centuries (Breidenbach et al., 2020). However, NFI programs are expensive and time consuming while not providing for a synoptic view across the landscape (Santoro and Cartus, 2018).

With the development of EO technologies, new avenues were open as the systematic data collection allowed for frequent, spatially resolved AGB or GSV estimates to be derived within a range of national and global initiatives, such as the Japan Aerospace Exploration Agency (JAXA) Kyoto and Carbon (KC) Initiative, the United Nation Collaborative Programme on Reducing Emissions from Deforestation and Forest Degradation (REDD), NASA's Carbon Monitoring System (CMS), and the European Space Agency (ESA) Climate Change Initiative (CCI). Forest AGB was estimated from optical, radar, and lidar sensors. Tracking forest properties with optical sensors is usually limited to the first decades of development (Tanase et al., 2011). Lidar sensors provide very accurate information on forest vertical structure (Hyde et al., 2007), but their use is limited by temporal (airborne) or spatial (space borne) coverage and cloud presence. As the radar signal is directly influenced by the vegetation structure, synthetic aperture radar (SAR) sensors are more sensitive to AGB levels when compared to optical data, and less limited by spatial and temporal availability when compared to Lidar data (Tanase et al., 2015). Therefore, over the past two decades SAR sensors have been widely used to retrieve forest biomass at a regional to global level due to constant improvements in coverage and temporal and spatial resolutions, as well as independence from cloud cover (Santoro et al., 2002; Sandberg et al., 2011; Mitchard et al., 2012; Neumann et al., 2012; Askne et al., 2013; Mihai A. Tanase et al., 2014a; Santoro et al., 2015). Such studies used a variety of modelling approaches, including empirical, semi-empirical, numerical, and non-parametric modelling. Regardless of the models used, the major limitation of spaceborne SAR observations is the sensitivity to forest unrelated variables which result in substantial uncertainties and AGB-dependent biases (Rodríguez-Veiga et al., 2019).

From the first prototype studies in the 1990s which evaluated the capability of a certain set of optical and SAR observations to estimate GSV or AGB, recent studies in the 2000s demonstrated that a combination of observations is beneficial to map biomass across extended landscapes. While most studies reported on estimating biomass at local to regional scale, a range of projects targeted biomass mapping at continental to a global scale (Baccini et al., 2008; Saatchi et al., 2011; Thurner et al., 2014; Santoro et al., 2015; Avitabile et al., 2016; Hu et al., 2016; Santoro et al., 2021a). However, such data products are of limited use at national level due to the (i) limited sensitivity to biomass, obtained through indirect relationship requiring inference with models and approximations, (ii) low temporal frequency (e.g., one off), (iii) generally low (>100 m) spatial resolution, (iv) unknown errors at national levels, (v) compromises in the retrieval algorithms which need to account for a wide range of conditions (e.g., boreal to tropical), and (v) the lack of calibration data over large tracts of forests with the in situ data used for algorithm development being sourced from relatively few countries. Such limitations translate into discrepancies between in situ and mapped biomass stocks. Indeed, many studies have shown differences between the global products specified accuracy and in situ samples over national to regional scales (Mitchard et al., 2011; Tropek et al., 2014;

Avitabile et al., 2016; Rodríguez-Veiga et al., 2016, 2019; Michelakis et al., 2014) with locally calibrated products providing significant improvements for the estimated forest parameters (Michelakis et al., 2014; Rodríguez-Veiga et al., 2016, 2019; Næsset et al., 2020).

Forests are under constant pressure due to anthropogenic factors related to clearing activities and changes in land use with approximately 4.5% of the Romanian forests being affected by at least one disturbance event (complete or nearly complete tree removal) over the past two decades. The high rate of forest disturbance, as estimated from remote sensing datasets (Knorn et al., 2012), suggest changes in Romanian forests growing stock volume as significant as those caused by climate changes alone (Schimel et al., 2000; Scheller and Mladenoff, 2005). However, spatially explicit GSV estimates are not available for the Romanian forests, as remote sensing technologies were mostly used to estimate forest cover rather than GSV (Griffiths et al., 2012; Knorn et al., 2012; Potapov et al., 2015). The hypothesis of this study was that SAR datasets may provide the means to derive spatially explicit estimates of GSV with higher frequency when compared to the five-year cycle of the National Forest Inventory (NFI) and lower errors when compared to globally derived GSV estimates (Santoro et al., 2015, 2021a). The aim of this study was to ascertain the utility of locally calibrated models, based on in situ NFI information and SAR datasets, for GSV estimation in the Romanian forests. The specific objectives were to (i) calibrate single- and multi-frequency SAR-based models for GSV retrieval in the Romanian forests, and (ii) ascertain the synergies of C- and L-band SAR datasets for GSV retrieval. The results were then compared against recent global GSV maps (Santoro et al., 2021a) to assess the potential utility of the locally calibrated models over global datasets.

6.2 Materials

6.2.1 Study Area and In Situ Data

The study was carried out in selected areas of the Romanian Carpathian Mountains (Figure 6.1). The Carpathians is third longest range within Europe, after the Urals and the Scandinavian Mountains, and stretches 1500 km across seven countries, although most of the range (54%) is located within the Romanian borders. The Carpathians are an eastward continuation of the Alps, but differ considerably from them as they are less compact and reach lower elevations. In contrast to the Alps, glaciation affected only the highest peaks, with the remaining areas being shaped by rivers. The climate is influenced by polar-continental air from east and northeast in winter and oceanic mases from the west during the rest of the year differentiating them from the much dryer surrounding plains. Precipitations range from 600 to 1800 mm. The vegetation is dominated by forests, mainly beech, spruce, and, to a lesser extent, oak species, which provide habitats for the largest European populations of brown bears, wolves, and lynxes. The Carpathians contains most of the European Union's remnant virgin forests. The selected areas

include some of the highest mountain peaks (exceeding 2500 m) as well as three of the six ecoregions present within the Romanian national territory (Olson et al., 2001).

The in-situ samples were collected within the second cycle (2013–2018) of the Romanian NFI. The NFI was established in 2008 using a 4 × 4 km grid, although a denser 2 × 2 km grid is used in plains where forest cover is low. The NFI is a two stage (aerial photography followed by in situ surveys) continuous forest inventory with a five-year cycle that covers the entire national territory. The field surveys comprise, at the end of the five-year cycle, about 24,000 permanent sample plots. To increase field work efficiency, the measurements are realized on four permanent sampling plots (PSP) at each grid node (Figure 6.1b).

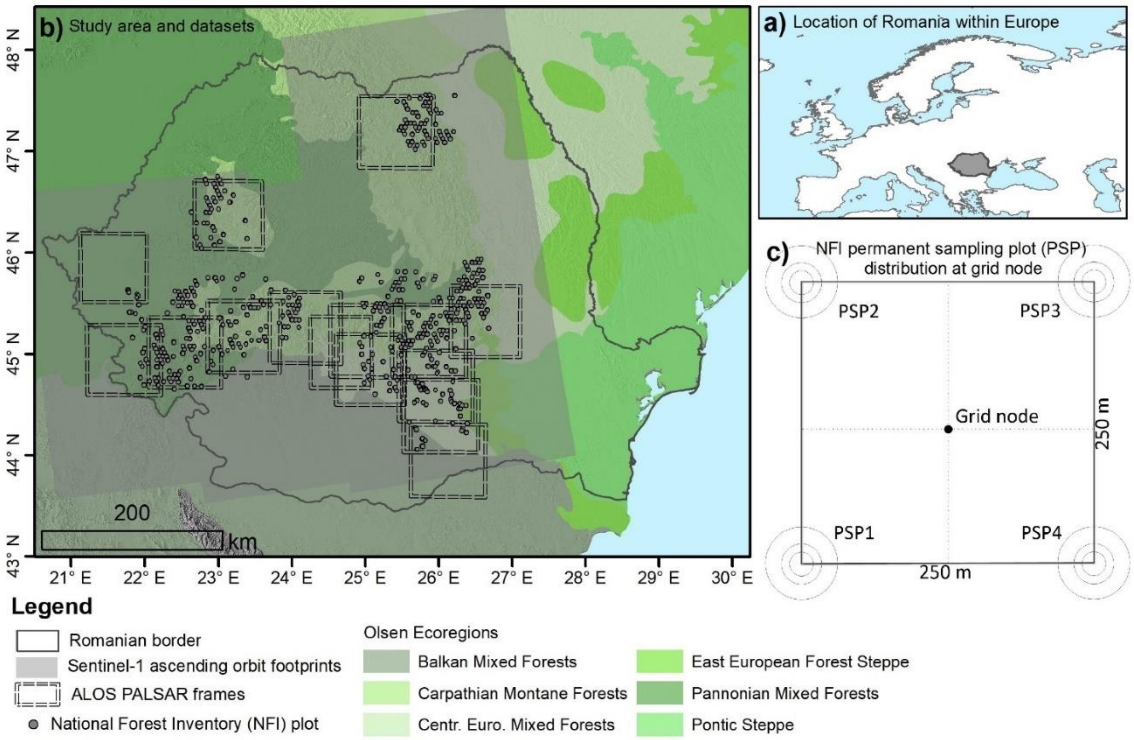

*Figure 6.1. Study area within the Romania borders (**a**) and the locations of the available national forest inventory (NFI) sample plots (**b**). Detail of NFI node (**c**). Each PSP is formed by concentric circles of 7.98 m, 12.62 m, and 25 m radius.*

Each PSP contains three concentric circles (7.98 m, 12.62 m, and 25 m in radius) where different forest characteristics are assessed, including forest type, tree species, diameter at breast height (DBH), height (H), lying deadwood, and ground vegetation. DBH and height are assessed in the first two circles, 7.98 m (5.6 cm ≤ DBH ≤ 28.5 cm) and 12.62 m (DBH ≥ 28.5 cm). The GSV estimation is based on species-specific (43 main species) allometry based on DBH and height. For conifers, the volume of branches (>5 cm diameter) was established through specific equations as percentage of stem volume and was added to the stem volume (Giurgiu et al., 2004). The volume measurements are scaled (by the circle area), aggregated, and reported per hectare. NFI estimates GSV with a sampling error of 1.79%, with target differences between measurements and control

surveys less than 1%. The NFI objective is to derive statistics of forest properties over the national territory. As such, individual plot measurements are not optimized to calibrate or evaluate remote sensing products due to the relatively small sampling area.

For each PSP, the data provided included the main forest species, forest inventory date, percentage forest cover, mean diameter at breast height, and height, as well as per hectare GSV. Of the 1815 PSPs available for this study, 1153 were inventoried between 2015 and 2016, coinciding with the EO data acquisition period. The remaining plots were inventoried in 2014. As forest stands in Romania consist of homogeneous tracts (species composition, age, and DBH classes), the NFI plots are representative of larger areas were not falling on stand border, as stands range between 6–10 ha in hilly and 10–15 ha in mountainous regions. The DBH, H, and GSV over the in-situ data, reached 96 cm, 50 m, and 1577 m^3 ha^{-1}, respectively, depending on the sample plot (Table 6.1). As small pockets of large trees influence average values, when relatively small areas are assessed, the PSP-wise GSV was high (>1000 m^3 ha^{-1}) for some plots (Figure 6.2).

Table 6.1. Range of plot-wise mean DBH and H and GSV. Values for all/modelling plots (see Section 6.3.1).

Main Species	DBH Range (cm)	H Range (m)	GSV Range (m^3 ha^{-1})
beech (n = 900/322)	7–157/8–96	3–50/8–50	5–1577/9–1577
oaks (n = 249/72)	11–80/11–52	9–36/11–32	13–742/22–731
coniferous (n = 560/238)	8–85/11–85	8–44/9–43	12–1470/22–1401
other species (n = 106/33)	10–66/10–59	9–39/12–39	15–1080/15–1080

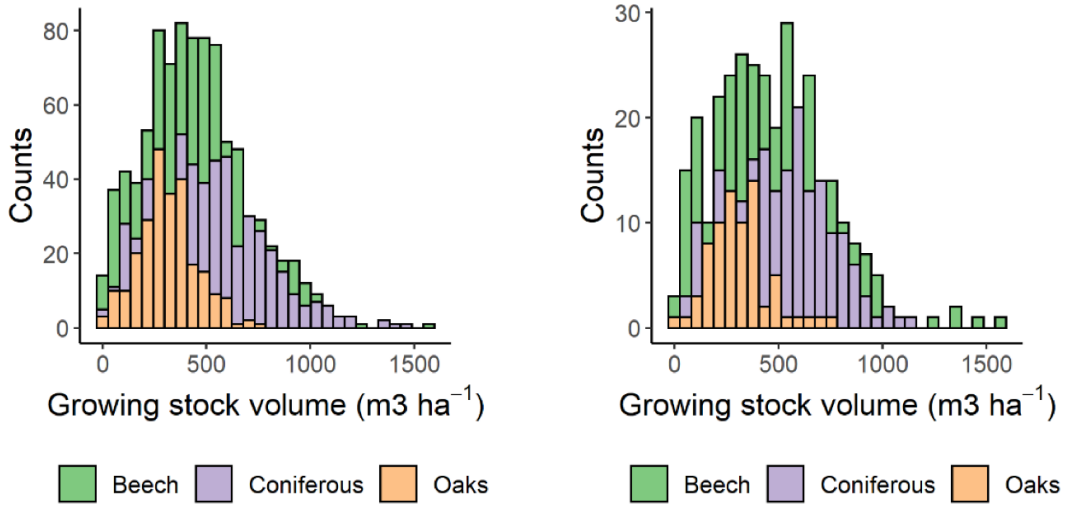

Figure 6.2. Growing stock volume distribution for all sample plots (left) and plots used for SAR-GSV modelling (right).

6.2.2 Earth Observation Data

The NFI plots used in this study were covered within 13 ALOS PALSAR-2 frames and six ascending and descending Sentinel-1 relative orbits (Figure 6.1). 104 L-band ALOS PALSAR-2 dual-polarized (HH and HV polarizations) datasets were provided by JAXA (2014–2017 period) as single look complex (SLC) images, while 1034 Sentinel-1 A and B granules were downloaded from open repositories for the years 2015–2016, the period when

most (83) ALOS PALSAR-2 datasets were acquired. Sentinel-1 ground range detected (GRD) dual polarized (VV and VH polarizations) C-band datasets (A and B satellites) were downloaded for the six relative orbits (29, 102, and 131 ascending and 7, 80, and 109 descending passes) covering the selected study areas.

6.3 Methods

6.3.1 SAR Data Processing and Extraction

The images acquired on the same orbit were first co-registered in the radar geometry. For Sentinel-1 products, the orbital state vectors were updated using the Precise Orbit Ephemerides, with the co-registration process being carried out by relative orbit after slice assembly (i.e., concatenation) as the Sentinel-1 image frames (i.e., slices) acquired from the same orbital path are provided in slices of variable ground footprints. For the ALOS PALSAR-2 data, the SAR processing was carried out on a path/frame basis. Image co-registration was based on a cross-correlation algorithm (Werner et al., 2005) with the first image of the temporal data series being used as reference. Each co-registered image was multi-looked to obtain a ground pixel spacing of approximately 30 m (4 × 8 pixels in range and azimuth for ALOS PALSAR-2 and 20 × 3 pixels in range and azimuth for Sentinel-1). The backscatter was converted to gamma0 using an ellipsoid-based area as reference, to account for the influence of topography (Small, 2011). The backscatter coefficient (γ°) was subsequently topographically normalized using the real scattering area, derived pixel-wise (Frey et al., 2013), from the one arc-second Shuttle Radar Topography Mission (SRTM) digital elevation model (DEM). Each image was then orthorectified to the Universal Transverse Mercator (UTM) coordinate system (zone 35 North, datum WGS84) using a look-up table that related the coordinates of each pixel in the radar geometry with the coordinates of the same pixel in the map geometry. The look-up table was generated using image orbital information and the digital elevation model (Wegmüller et al., 2002b).

At each PSP, the backscatter coefficient of all images acquired before the forest inventory date was extracted for the pixel containing the center coordinates. The backscatter values were averaged for all available dates by polarization and by relative orbit (Sentinel-1). The standard deviation of the backscatter temporal series (i.e., temporal stability) was also computed at each PSP location for every sensor, polarization, and relative orbit (Sentinel-1). Out of the 1815 available NFI samples, 704 (665 forest and 39 non-forest) were used for modelling and validation of the retrieved GSV. The reduced number of useful samples was determined by the intersection between ALOS PALSAR-2 and Sentinel-1 orbits, the correspondence between NFI inventory date and ALOS PALSAR-2 and Sentinel-1 image acquisition dates, and topography, as pixels affected by geometric distortions were masked out during SAR data processing. As both ascending and descending Sentinel-1 orbits were tested, the number of PSPs affected by layover and shadow was high.

6.3.2 Growing Stock Volume Retrieval

Several modeling approaches can be used to retrieve forest GSV (or AGB) from radar backscatter coefficients, including parametric and nonparametric models (Lucas et al., 2010; Englhart et al., 2011; Sandberg et al., 2011; Saatchi et al., 2011; Cartus et al., 2012; Mitchard et al., 2012; Neumann et al., 2012; Michelakis et al., 2014; Mermoz et al., 2015; Santoro et al., 2015; Villard et al., 2016; Santoro and Cartus, 2018). Within a previous study, some of these models were evaluated using the Romanian NFI and ALOS PALSAR-2 datasets (Tanase et al., 2020). The results suggested that non-parametric models provide the lowest errors and bias, regardless of polarization or forest species over the selected study area. Therefore, we used a non-parametric modelling approach, based on Random Forests (Breiman, 2001), to assess the synergies between the C- and L-band dataset for GSV retrieval. As non-parametric models offer the opportunity to include non-linearly related variables, and have no assumptions regarding the statistical properties of the data, such models are often preferred when a sufficiently large dataset of samples is available for model parameterization. The models use ensemble learning methods to improve the overall predictive power with respect to any of the constituent models by aggregating their predictions. In random forest regression, each tree is built using a deterministic algorithm by selecting a random set of variables and a random sample from the training dataset (Breiman, 2001). Although RF models provide high fit statistics there are known drawbacks, including difficulties in interpreting the results, potential overfitting, and high computational demands. A total of 85 RF models were trained and evaluated by gradually increasing the independent variables, starting from single polarized to multi-polarization multi-sensor data (see Section 6.4 and Annex 6-1 for detailed information of the predictor variables used). Each sensor was individually tested to generate a reference baseline and allow for cross-sensor comparisons. The use of additional variables (e.g., forest type, temporal backscatter variability, and local incidence angle) was also evaluated to ascertain the opportunity for GSV retrieval improvements. For each sensor, we increased the independent variables, starting with the average backscatter, temporal stability (i.e., the standard deviation of the time series, sd), local incidence angle (LIA), and the forest type (Ft). For the C-band we analyzed the ascending and descending passes separately, as well as their combination. The models were calibrated using the 704 PSP samples. In this study, TreeBagger from MATLAB® software package (v. 2020b) was used to construct the RF classifier. The number of decision trees was set to 200 and a curvature test was used to select the best split predictor and grow unbiased trees (Loh, 2002). The remaining parameters were kept as default, with surrogate splits being allowed to account for missing values in the data.

6.3.3 GSV Retrieval Accuracy

Model performance was evaluated at both pixel and grid levels. At pixel (i.e., plot) level, the retrieval was evaluated using repeat random sub-sampling with cross-validation for each individual sensor and polarization, as well as for dual polarized and dual frequency

configurations. To reduce variability due to random sampling effects, 100 rounds were performed by randomly splitting the 704 PSPs into training (75%) and validation (25%) samples. During each round, the models were calibrated using the training samples and subsequently used to estimate the GSV for the validation samples. The observed and predicted GSV for the validation samples was accumulated over the 100 rounds and used to compute four accuracy error metrics: the root mean squared error (RMSE, Equation (1)), the relative RMSE (RelRMSE, Equation (2)), the bias (Equation (3)), and the Pearson's correlation coefficient (r).

$$RMSE = \sqrt{\frac{1}{n}\sum_{j=1}^{n}\left(P_j - O_j\right)^2} \quad (2)$$

$$RelRMSE = RMSE/\tilde{O} \quad (3)$$

$$Bias = \tilde{P} - \tilde{O} \quad (5)$$

where: P_j = predicted values, O_j = in situ observed values, n = number of samples, and $\tilde{O}$ and $\tilde{P}$ = mean values for the observed and predicted values, respectively.

As GSV estimation errors are inherently large when using small NFI plots for SAR models calibration (Robinson et al., 2013; Mihai A. Tanase et al., 2014b), accuracy metrics (as per Equations (1)–(3)) were also derived over predefined grids of 10 × 10, 20 × 20, and 30 × 30 km. The grid size was a compromise between having enough samples in each tile to obtain a more reliable estimate of the NFI average stem volume and having enough tiles to compute the accuracy metrics by volume intervals. As the Sentinel-1 strips covered the 1815 available PSPs (Figure 6.1), the analysis was focused on the GSV maps derived from C-band VH polarized data (see Section 6.4.2) to maximize the number of tiles containing at least 4 in situ plots (i.e., one NFI grid node). The errors were estimated for both ascending and descending satellite passes. Models using the VH backscatter and its temporal standard deviation (see Table 6.2, in bold) were calibrated using the reduced set (704) of NFI for cross-comparison purposes. At each tile, the average NFI GSV was compared to the average GSV for the corresponding predicted pixels.

6.3.4 Local vs. Global GSV Retrieval

The GSV overall accuracy estimates were compared against values derived at continental to global levels. We used the GlobBiomass dataset (Santoro et al., 2021a), the only global product currently available at comparable pixel spacing (100 m) and derived from comparable remote sensing datasets (C- and L-band SAR data). The GlobBiomass product provides GSV estimates for the reference year 2010 based on the combined use of Envisat ASAR (C-band) and ALOS PALSAR (L-band) sensors and ancillary information from Landsat imagery. GSV values from the first NFI cycle (2008–2012) were used as reference to match the dates of the GlobBiomass product. As NFI data collection protocol and location did not change between the first and second NFI cycles and we have used the

same SAR wavelengths to derive the local product, input datasets influence on the results were minimized. Please note that Envisat ASAR and ALOS PALSAR sensors were decommissioned in 2012 and 2011, respectively while data from Sentinel-1 and ALOS PALSAR-2 were not available until 2014. The GlobBiomass GSV values were extracted at the location of the available NFI plots to compute the same error metrics.

6.4 Results and Discussions

The higher backscatter variability at L-band when compared to C-band, due to the limited number of multi-temporal datasets available is evident for all the main species in the Carpathians (Figure 6.3). Additionally, notice the different GSV ranges, significantly larger for beech forests when compared to the coniferous and oak forests. The backscatter coefficient shows the specific raise with GSV up to a SAR wavelength specific saturation point. By main species, the average backscatter values were slightly higher at L-band over the coniferous forests (Figure 6.3b). For display reasons, a logarithmic model was fitted to the data. The fit was very similar for both SAR wavelengths over the high biomass beech forests (Figure 6.3c). Different saturation points between the two wavelengths are apparent over the coniferous and oak forests (Figure 6.3b,d), suggesting changed sensitivity to GSV.

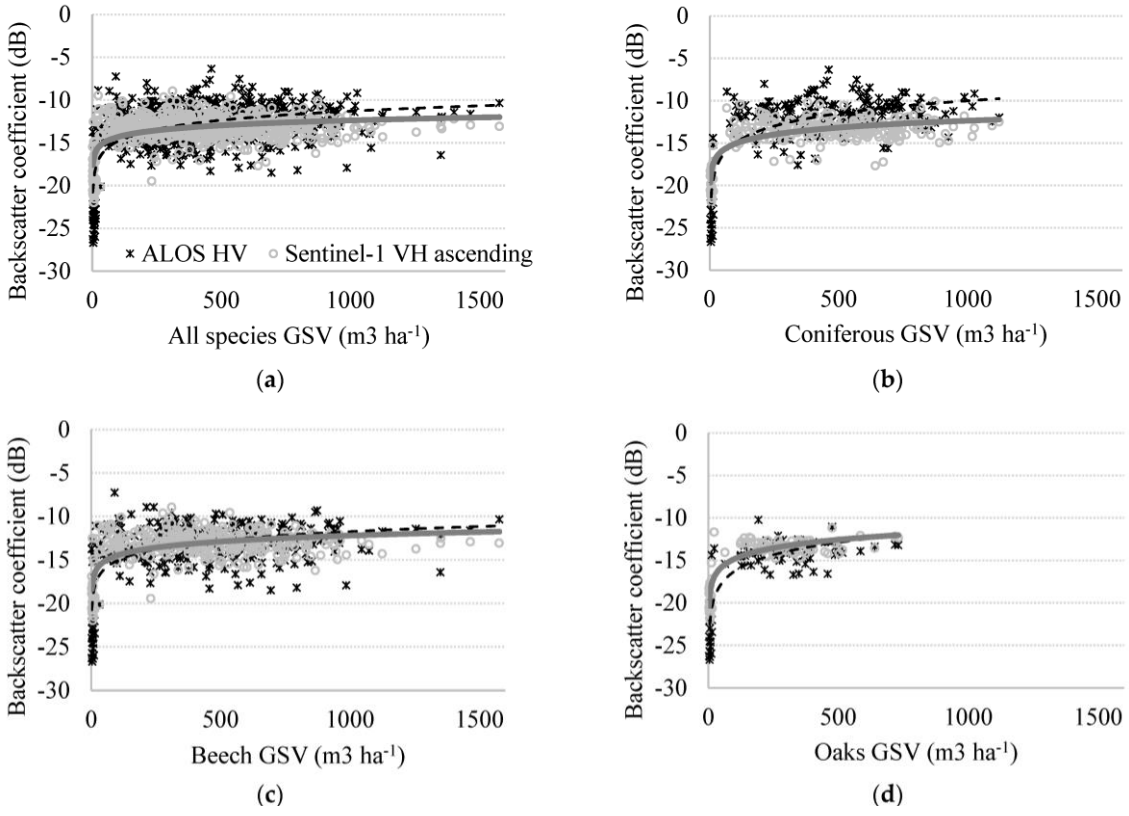

*Figure 6.3. Scatterplots of cross-polarized backscatter coefficient as a function of growing stock volume (GSV) for all samples and by main forest species (**a**–**d**). Values show multi-temporal averages. Grey and black (dashed) lines show logarithmic model fit.*

6.4.1 Pixel-Wise GSV Estimation

Over all sensors, polarizations, and predictor variables combinations, the RMSE, Rel RMSE, and r ranged between 238–278 m^3 ha^{-1}, 55–65%, −5–6 m^3 ha^{-1}, and 0.14–0.48, respectively (Table 6.2 and Annex 6-1). As showing results for all possible combinations of the predictor variables (19) is problematic, Table 6.2 shows the error metrics for a selection of models to understand their variations when expanding the number of predictor variables. Notice that adding more variables does not translate into more accurate predictions. Additional configurations were provided in Annex 6-1 for completeness. The data is presented by SAR wavelength, multi-frequency configurations and descending C-band passes combinations.

Table 6.2. GSV accuracy as a function of the independent variables used for the single polarized models. Bold numbers show overall results for the models analyzed by GSV intervals in Figure 6.4 and Figure 6.5. Abbreviations as follows: RMSE—root mean squared error, RelRMSE—relative RMSE, r—Pearson's correlation coefficient, L—stands for L-band, C—stands for C-band, H—horizontal, V—vertical, a—ascending pass, d—descending pass, sd—standard deviation, Ft—forest type, and LIA—local incidence angle.

Independent Variables	RMSE	Rel RMSE	Bias	r
L-HV	266.9	62.4	−1.4	0.30
L-HH	282.9	66.3	3.1	0.14
L-HV, L-HVsd	254.3	59.5	−1.4	0.35
L-HV, L-HH	253.0	58.9	0.2	0.36
L-HV, L-HVsd, Ft	244.0	57.1	0.02	0.41
L-HV, L-HH, L-HH/HV, LIA, Ft	241.9	56.1	−3.4	0.46
L-HV, L-HH/HV, Ca-VH, Ca-VV/VH, LIA	239.9	56.2	1.9	0.45
Ca-VH	274.0	63.9	−0.3	0.24
Ca-VV	275.0	63.9	−2.7	0.21
Ca-VH, Ca-VHsd	**263.4**	**62.6**	**−0.3**	**0.28**
Ca-VV, Ca-VH	267.0	62.4	0.7	0.25
Ca-VH, Ca-VHsd, Ft	249.0	59.2	2.1	0.38
Cd-VV, Cd-VH, Cd-VV/VH, LIA, Ft	245.7	57.0	−4.6	0.41
Ca-VH, Ca-VHsd, Cd-VH, Cd-VHsd, Ft, LIAa, LIAd	249.5	59.5	−0.6	0.40

Within the single sensor single polarization configuration, the L-band data provided similar relative RMSE errors when compared to the C-band data. The small difference was explained by the much denser C-band time series, and the use of average backscatter over 3 years prior to the forest inventory date. This allowed for a considerable reduction in the environmental induced noise (i.e., backscatter variation due to changes in soil and vegetation water content) at C-band, where over 150 images were averaged over each relative orbit. In contrast, fewer images (5–10) were available for the ALOS PALSAR-2 sensor over each acquisition frame. Improved GSV retrieval accuracy at C-band was observed when adding as an independent variable either the local incidence angle (LIA) or the forest type (FT). However, such improvements were marginal for all accuracy metrics. The RMSE, RelRMSE, and r improved, on average, by 15 m^3 ha^{-1}, 3%, and 0.1, respectively. Dual polarized models were slightly more accurate (2–5%) when compared to single polarized models at both C- and L-bands, while the addition of co- to cross-polarized backscatter ratios further decreased the estimation error, albeit marginally. Adding the time series standard deviation to backscatter and co- to cross-polarized ratios improved the accuracy metrics slightly, suggesting that some information can be added to that already contained in the backscatter coefficient.

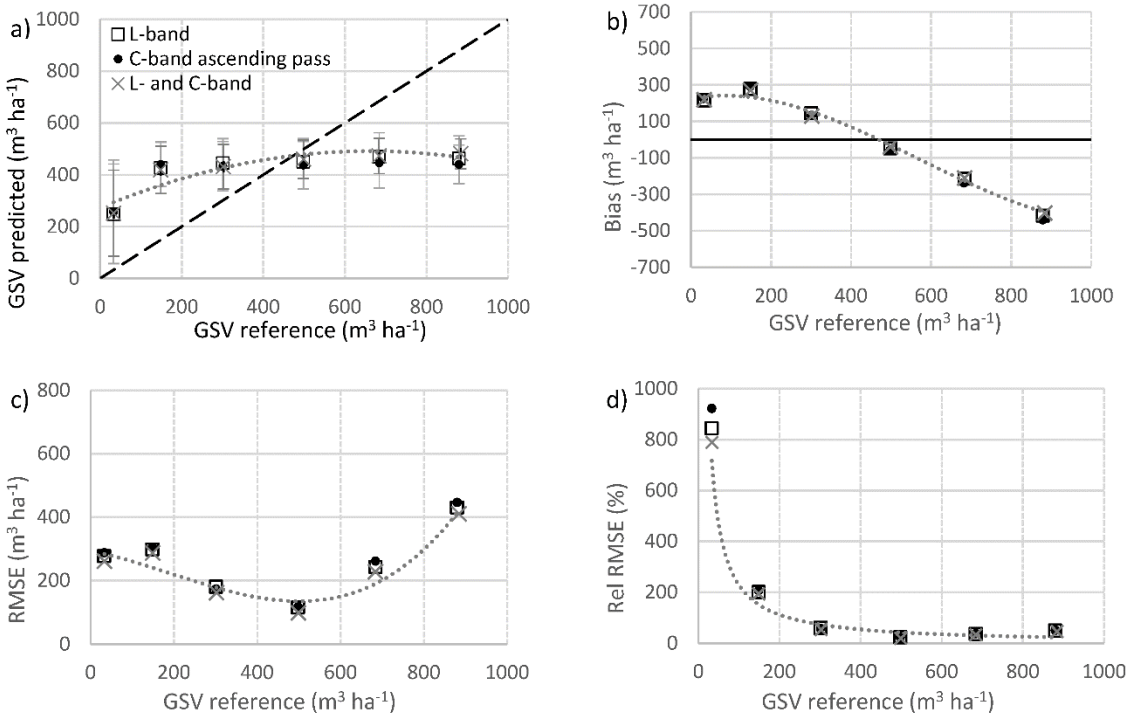

Figure 6.4. GSV retrieval metrics at pixel level for single polarization C- and L-band models, as well as the combined C- and L-band data: (a) GSV by range, error bars indicate standard deviation of the predicted values. (b) Distribution of bias, (c) root mean square error, and (d) relative root mean squared error. Dotted lines indicate fitting polynomial (a–c) and power (d) curve to the calculated points. The dashed line indicates identity line. Bins plotted at average bin value.

Similarly, adding LIA and/or FT to the models only resulted in marginal improvement, most likely being related to the increased number of variables available in the model. No synergies were observed in terms of retrieval accuracy, when combining information from both ascending and descending C-band passes with model performance not improving over the use of either pass. However, GSV estimation from both ascending and descending passes has merit over the rough Carpathian topography, as it limits the extent of 'not-observed' areas, i.e., areas with topographic distortion due to shadows and layover which are masked out during SAR processing. Further, the similar error level from both passes provides for a homogeneous GSV estimation over the entire landscape. Little synergy was also observed when simultaneously using C- and L-band for GSV retrieval. Improvements in the RMSE, RelRMSE, and r were noticed with respect to using single pass C-band data, but were marginal, i.e., 10 m^3/ha, 3%, and 0.05, respectively. In addition, such improvements were observed when adding the LIA to the various combinations of SAR frequencies, polarizations, and passes. The information provided by LIA and Ftype was largely interchangeable in all configurations (single, dual, multi-frequency, and multi-pass), as simultaneously using both variables did not improve the results. In fact, the opposite was observed for some of the tested combinations. It seems that LIA partitions data in a similar way to Ftype as oak forests are mostly

found on lesser slopes in the hilly region, with conifers being found towards the mountain tops on steep terrain. This explanation is further supported by the fact that adding the LIA from different sensors or satellite passes provided no tangible improvement of the accuracy metrics.

Error analysis by intervals (Figure 6.4 for models in bold in Table 6.2) shows much higher relative RMSE errors over forests supporting low (<100 m^3 ha^{-1}) GSV values at both C- and L-bands, which is consistent with previous findings (M. A. Tanase et al., 2014; Rodríguez-Veiga et al., 2019). The high relative RMSE are related to the high signal variability due to the influence of local surface conditions (i.e., soil surface roughness and moisture) as direct scattering from the ground dominates the signal in forests supporting low GSV levels (van Zyl, 1989). In addition, the relative RMSE metric is unstable at lower GSV values, as the denominator approaches zero the relative error approaches infinity. Over the remaining GSV intervals the relative RMSE decreased significantly at both wavelengths with the minimum values (around 20%) being observed for the 400–600 m^3 ha^{-1} GSV range. The estimation error was largely dominated by bias, as the coefficient of variation (CV) of the error was below one (data not shown), for most GSV intervals except the 400–600 m^3 ha^{-1} where the random error dominated, and the 0–100 m^3 ha^{-1} interval where bias and random error contribution was balanced ($0.8 < CV < 0.9$). Note that the bias was positive over low GSV ranges and negative over the high GSV ranges (Figure 6.5b), with a crossover at the GSV range with the lowest errors, 400–600 m^3 ha^{-1}. The standard deviation (SD) of the predicted values did not vary across GSV intervals (75–85 m^3 ha^{-1}) except for the first bin, where the SD was twice as much (Figure 6.5a). Similar values were observed over temperate forests in Poland in previous studies (Rodríguez-Veiga et al., 2019). Overall, the accuracy assessment shows that GSV is over- and under-estimated at low and high GSV values, respectively as the models fitting aims at the point defined by the average of the observed and predicted values (Rodríguez-Veiga et al., 2019).

The relatively large errors observed for all combinations of predictor variables may be related to potential mismatches between the Earth Observation data and the in situ samples, as the coordinates at each PSP were reconstructed from the node grid coordinates using the specified distance and azimuth. This may introduce displacements with respect to the real location of the NFI plot where field crews were not able to precisely measure the required azimuth and distance, or the exact location of the grid node (e.g., GPS location error under dense forest canopy may reach several meters). Such positioning errors coupled with the relatively small area inventoried may induce errors particularly for border stands. For the remaining NFI samples, the positioning errors should have limited effects as Romanian forests stands, averaging between 3.5 and 15 ha from plains to mountains, have homogeneous structure and species composition.

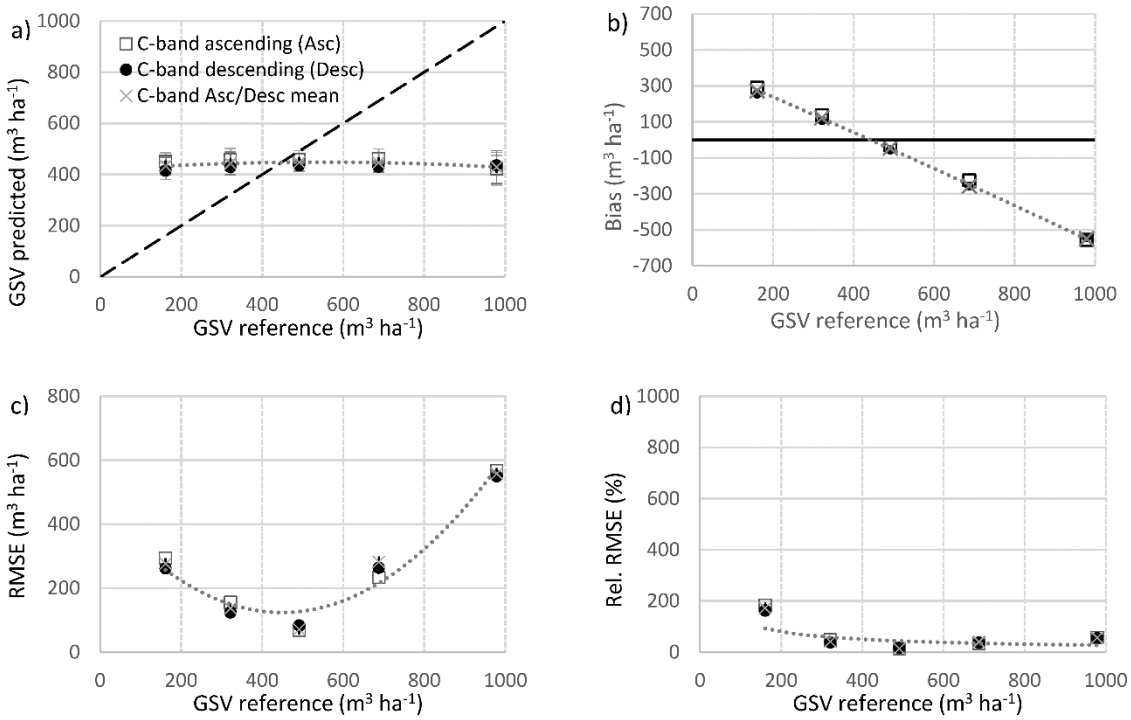

Figure 6.5. GSV retrieval metrics for 10 × 10 km grid cells for single polarization C-band models. Panels (a–d) show the same information as in Figure 6.4.

6.4.2 **Grid Based GSV Accuracy**

Over the 10 × 10 km grid (244 cells), the RMSE and RelRMSE decreased to 158 m^3 ha^{-1} and 35%, respectively (average values), with marginal differences being observed between values from ascending (35.2%) and descending (33.8%) satellite passes. Averaging GSV values from ascending and descending passes did not result in improved accuracy metrics. Further aggregation through the larger 20 × 20 (125 cells) and 30 × 30 km (78 cells) grids improved RMSE (119 and 105 m^3 ha^{-1}, respectively) and RelRMSE (29% and 25%, respectively) values, but also increased the bias from 13 to 30 and, 35 m^3 ha^{-1}, respectively, as only two or three bins were available. The RelRMSE for the 30 × 30 km aggregation level was similar to that observed over the Swedish forests (21.4%) at the same scale. However, our retrieval statistics indicate some residual bias, which was not the case in Sweden, where a longer wavelength (L-band) was used for retrieval and more samples were aggregated (Santoro et al., 2021b).

When compared to the pixel-based assessment, similar patterns were observed over all biomass intervals except for the 0–100 m^3 ha^{-1} range for which no grid cell was available (Figure 6.5 for models in bold in Table 6.2). The improvement in retrieval statistics seemed related to the absence of low GSV plots (<100 m^3 ha^{-1}) where large estimation errors were observed at pixel level (Figure 6.4 and Figure 6.5). Notice that the lower number of available cells at larger grids precluded a similar analysis for the 20 × 20 and 30 × 30 km grids.

6.4.3 Comparison to Global Products

Our results support previous findings which demonstrated increased retrieval accuracies for locally calibrated models (Michelakis et al., 2014; Tropek et al., 2014; Rodríguez-Veiga et al., 2019; Næsset et al., 2020). When compared to the GlobBiomass values (Figure 6.6), locally derived estimates showed potential to improve the RelRMSE by about 15% (55.4 vs. 70.5%), decrease the RMSE by about 54 m^3 ha^{-1} (236 vs. 290 m^3/ha), and increase the correlation between predicted and observe values from 0.2 to 0.5. Such improvements, although significant and at a higher (30 vs. 100 m) spatial resolution, are still far from the required accuracies needed for operational forest management which target 5–10% accuracies for GSV at stand level. Nevertheless, one should notice that aggregating the pixel wise GSV to lower spatial resolution (e.g., stand level) has the potential to significantly decrease the RMSE and RelRMSE values (Santoro et al., 2011, 2015) as also demonstrated by the improvements observed at grid level. The incentive in using SAR based GSV estimation from locally calibrate models resides in the opportunity to better fine tune the model to the local conditions when compared to using globally available estimate. In addition, SAR-based maps provide wall to wall cover, yearly updates, and the opportunity to derive regional statistics.

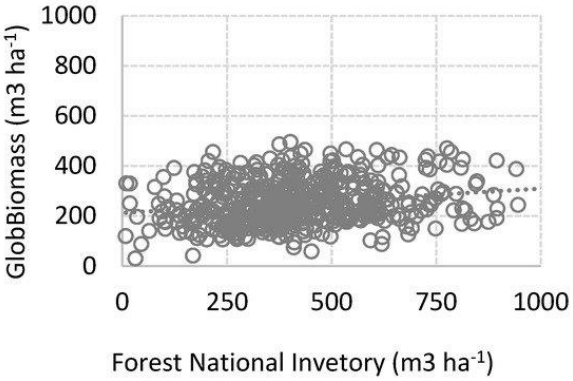

Figure 6.6. Growing stock volume estimated by GlobBiomass map at national forest inventory locations.

6.5 Conclusions

This study assessed the utility of C- and L-band data for GSV estimation over high growing stock volume forests in the Carpathians. The study included representative areas covering the three main forest species, oak, beech, and coniferous, making up the bulk of the Romanian forests. The in situ NFI data and the SAR imagery were acquired between 2015 and 2016. GSV retrieval was carried out at 30 m pixel size using a machine learning (Random Forests) algorithm and various configurations of the independent variables from single sensor single polarization to multi-sensor multi-polarization. The observed RelRMSE varied between 55–66% depending on the input predictor variables. For similar predictor variables, the mapping accuracy was slightly higher at L- when compared to C-band.

The availability of significantly more datasets at C-band reduced speckle as the much denser Sentinel-1 time series seemed to have compensated for the inherent limitations of a shorter wavelength. Such a finding suggests that using denser L-band time series, as those available from the soon to be launched NISAR mission, have the potential to further improve GSV estimation accuracy in high volume forests. The GSV retrieval errors decreased by 5–10% when adding temporal information (i.e., backscatter coefficient temporal standard deviation) as an independent variable eliminating the need for a second polarization. This suggests a high correlation between the information of co- and cross-polarized channels, which may be explained by the overall high GSV levels and thus the relative low correlation between GSV and backscatter. Little synergies were observed when using both C- and L-bands, as well as when jointly using C-band ascending and descending passes. While the utility of the pixel level GSV values is somewhat reduced, their aggregation at grid level decreased the estimation errors (25–35%) and provided more reliable estimates which may be useful for regional and national assessments. Future work should focus on reducing GSV errors by fusing the Lidar data acquired by NASA's Global Ecosystem Dynamics Investigation (GEDI) mission to obtain a GSV gridded product that provides more accurate estimates for stock levels at regional to national levels. In addition, dense L-band temporal series from the future NISAR mission should be tested to ascertain the potential to improve the locally derived GSV estimates, as datasets from the P-band BIOMASS mission may not be available over the Carpathians.

As for the limitations of this study, the most important is related to the design of NFIs, which are not optimized for calibrating and validating remote sensing products (Santoro et al., 2021b), the large differences between the amount of data collected by the two SAR sensors, which limited a like-for-like comparison, and the available DEM (SRTM DEM) used for terrain normalization as a more precise DEM (e.g., Lidar based or Tandem-X DEM) allows for improved scattering area estimation reducing the effect of topography on the backscatter and thus improving the retrieval of the target biophysical characteristic (Small, 2011; Borlaf-Mena et al., 2020).

6.6 Annexes

Annex 6-1 (part 1). GSV accuracy as a function of the selected independent variables for a range of configurations. Abbreviations as follows: RMSE—root mean squared error, RelRMSE—relative RMSE, r—Pearson's correlation coefficient, L—stands for L-band, C—stands for C-band, H—horizontal, V—vertical, a—ascending pass, d—descending pass, sd—standard deviation, Ft—forest type, and LIA—local incidence angle.

Independent Variables	RMSE	RelRMSE	Bias	r
Single polarized models based on L-band data				
L-HH	282.9	66.3	3.1	0.14
L-HH, L-HHsd	264.0	61.6	−1.1	0.24
L-HV, L-HVsd, Ft	244.0	57.1	0.02	0.41
L-HH, L-HHsd, Ft	244.2	57.6	4.3	0.40
L-HV, L-HVsd, LIA	246.4	57.6	1.5	0.40
L-HH, L-HHsd, LIA	250.7	58.8	0.75	0.37
L-HV, L-HVsd, LIA, Ft	240.3	56.2	−0.6	0.44
L-HH, L-HHsd, LIA, Ft	237.7	55.9	3.4	0.45

Independent Variables	RMSE	RelRMSE	Bias	r
Single polarized models based on C-band data				
Ca-VV	275.0	63.9	−2.7	0.21
Cd-VV	277.5	64.6	−2.9	0.19
Cd-VH, Cd-VHsd	265.0	62.7	−2.6	0.26
Ca-VV, Ca-VVsd	262.6	62.4	−0.5	0.27
Cd-VV, Cd-VVsd	264.6	62.8	0.36	0.26
Ca-VH, Ca-VHsd, Ft	249.0	59.2	2.1	0.38
Cd-VH, Cd-VHsd, Ft	253.7	59.8	−3.8	0.36
Ca-VV, Ca-VVsd, Ft	248.7	59.3	1.0	0.39
Cd-VV, Cd-VVsd, Ft	249.9	59.5	3.1	0.37
Ca-VH, Ca-VHsd, LIA	256.8	60.9	−2.0	0.31
Cd-VH, Cd-VHsd, LIA	260.0	61.2	−3.5	0.32
Ca-VV, Ca-VVsd, LIA	257.4	61.3	1.7	0.30
Cd-VV, Cd-VVsd, LIA	261.1	61.7	−3.5	0.30
Ca-VH, Ca-VHsd, LIA, Ft	248.4	59.3	2.4	0.38
Cd-VH, Cd-VHsd, LIA, Ft	252.5	59.7	−0.3	0.37
Ca-VV, Ca-VVsd, LIA, Ft	249.5	59.5	3.7	0.38
Cd-VV, Cd-VVsd, LIA, Ft	249.8	58.6	−5.4	0.39

Annex 6-1 (part 2). GSV accuracy as a function of the selected independent variables for a range of configurations. Abbreviations as follows: RMSE—root mean squared error, RelRMSE—relative RMSE, r—Pearson's correlation coefficient, L—stands for L-band, C—stands for C-band, H—horizontal, V—vertical, a—ascending pass, d—descending pass, sd—standard deviation, Ft—forest type, and LIA—local incidence angle.

Independent variables	RMSE	RelRMSE	Bias	r
Multi-polarized models based on L-band data				
L-HV, L-HH	253.0	58.9	0.2	0.36
L-HV, L-HH, L-HH/HV	251.9	59.1	2.5	0.39
L-HV, L-HH, L-HH/HV, Ft	249.2	58.0	0.42	0.40
L-HV, L-HH, L-HH/HV, LIA	242.7	56.3	−2.1	0.43
L-HV, L-HH, L-HH/HV, LIA, Ft	241.9	56.1	−3.4	0.46
L-HV, L-HH/HV	252.8	58.8	−0.1	0.38
L-HH, L-HH/HV	251.5	58.6	1.2	0.36
L-HV, L-HH/HV, LIA	242.9	56.9	2.6	0.42
L-HV, L-HH/HV, LIA, Ft	241.2	56.3	1.4	0.45
L-HH, L-HH/HV, LIA, Ft	239.1	55.9	2.7	0.46
L-HV, L-HH/HV, L-HVsd	247.0	58.0	1.7	0.39
L-HH, L-HH/HV, L-HHsd	248.6	58.1	−0.9	0.38
L-HV, L-HH/HV, L-HVsd, LIA	242.8	56.6	0.9	0.44
L-HV, L-HH/HV, L-HVsd, LIA, Ft	236.0	55.4	2.1	0.47
L-HH, L-HH/HV, L-HHsd, LIA, Ft	237.7	55.7	1.7	0.48
Multi-frequency models (C- and L-band data)				
L-HV, Ca-VV/VH	258.7	60.4	−0.3	0.32
L-HV, Ca-VV/VH, Ft	249.0	58.1	−1.6	0.39
L-HV, Ca-VV/VH, Cd-VV/VH	252.0	59.1	2.7	0.34
L-HV, Ca-VV/VH, Cd-VV/VH, LIA	243.2	57.2	4.9	0.41
L-HV, L-HH/HV, Ca-VV, Ca-VV/VH, LIA	239.3	55.8	2.6	0.45
L-HV, L-HH/HV, Ca-VV/VH, Cd-VV/VH, LIA	240.3	56.1	0.2	0.45
L-HV, L-HH/HV, Ca-VV/VH, Ca-VHsd, Cd-VV/VH, Cd-VHsd, LIA	242.3	57.6	−0.3	0.46
L-HV, L-HH/HV, Ca-VH, Ca-VV/VH, Cd-VH, Cd-VV/VH, LIA	240.1	57.3	1.2	0.46

Independent variables	RMSE	RelRMSE	Bias	r
Multi-polarized models based on C-band data				
Ca-VV, Ca-VH	267.0	62.4	0.7	0.25
Cd-VV, C-VH	262.0	61.1	0.2	0.27
Ca-VV, Ca-VH, Ca-VV/VH	264.8	61.8	3.3	0.24
Cd-VV, Cd-VH, Cd-VV/VH	260.6	61.2	2.6	0.28
Ca-VV, Ca-VH, Ca-VV/VH, Ft	253.1	59.0	−1.0	0.35
Cd-VV, Cd-VH, Cd-VV/VH Ft	248.8	58.0	−1.9	0.38
Ca-VV, Ca-VH, Ca-VV/VH, LIA	253.4	59.7	6.1	0.30
Cd-VV, Cd-VH, Cd-VV/VH, LIA	251.9	58.	−0.5	0.34
Ca-VV, Ca-VH, Ca-VV/VH, LIA, Ft	252.4	58.5	−3.0	0.36
Cd-VV, Cd-VH, Cd-VV/VH, LIA, Ft	245.7	57.0	−4.6	0.41
Ca-VH, Ca-VV/VH	264.2	61.5	−1.8	0.26
Cd-VH, Cd-VV/VH	263.9	61.4	−3.5	0.27
Ca-VV, Ca-VV/VH	265.3	62.0	0.4	0.25
Cd-VV, Cd-VV/VH	262.3	61.3	−0.1	0.26
Ca-VH, Ca-VV/VH, LIA	258.8	60.4	0.4	0.29
Cd-VH, Cd-VV/VH, LIA	253.8	59.2	−1.1	0.35
Ca-VV, Ca-VV/VH, LIA, Ft	249.2	58.1	1.4	0.36
Cd-VV, Cd-VV/VH, LIA, Ft	246.0	57.4	−0.5	0.41
Ca-VH, Ca-VV/VH, Ca-VHsd	259.4	61.3	−2.4	0.31
Cd-VH, Cd-VV/VH, Cd-VHsd	261.6	62.2	2.8	0.28
Ca-VH, Ca-VV/VH, Ca-VHsd, LIA	258.2	61.4	0.8	0.31
Ca-VH, Ca-VV/VH, Ca-VHsd, LIA, Ft	248.9	59.5	2.0	0.38
Cd-VH, Cd-VV/VH, Cd-VHsd, LIA, Ft	246.8	58.3	−1.3	0.42
Models based on C-band data from ascending and descending passes				
Ca-VV, Ca-VVsd, Cd-VV, Cd-VVsd	256.9	61.2	−1.3	0.32
Ca-VH, Ca-VHsd, Cd-VH, Cd-VHsd	258.3	61.2	−3.9	0.32
C-VVa, C-VVa sd, C-VVd, C-VVd sd, Ft	249.4	59.8	1.5	0.38
Ca-VH, Ca-VHsd, Cd-VH, Cd-VHsd, Ft	254.2	59.8	−3.5	0.37
C-VVa, C-VVa sd, C-VVd, C-VVd sd, Ft, LIAa, LIAd	248.6	59.0	−1.4	0.40
Ca-VH, Ca-VVVH, Ca-VVsd, Cd-VH, Cd-VVVH, Cd-VVsd	251.6	60.0	1.9	0.34
Ca-VV, Ca-VVVH, Cd-VV, Cd-VVVH, Ca-VHsd, Cd-VHsd	254.6	60.7	0.6	0.33

Conclusions

Forests are both a vital part of Earth's climate system and a source of livelihood for many people around the world. To make a sustainable use of forest resources they need to be quantified, a task often completed through statistic forest inventories based on in situ data. The main limitations of such forest inventories are the sparse sampling, as well as the time and expense required to perform them. Remote sensing can complement said inventories generalizing field samples to a complete coverage and at short repeat intervals.

This thesis has analyzed the possibility of extracting forest variables using SAR data in a mountainous area in the Romanian South-eastern Carpathians. A large portion of the work has been devoted to assessing possible estimation bias related to the influence of the terrain. The influence of the digital elevation model (DEM) over Sentinel-1 image normalization was assessed. Several DEMs were tested (SRTM, AW3D, TanDEM-X), with TanDEM-X DEM providing the largest reduction of the differences between orbits. Said reduction was particularly noticeable for steep areas or complex landforms such as valleys, where it reduced the appearance of pseudo-shadow, "dark" areas that can cause misclassification.

The rugged topography of the study area causes frequent occlusions and distortions in the SAR images. Said distortions depend on the viewing geometry, and thus, it is possible to increase coverage using data acquired from different orbits through mosaicking. Two workflows were assessed, by-orbit classification of combination of annual statistics, and classification of multi-orbit weighted statistics. Accuracy was slightly higher for the by-orbit strategy, whereas the mosaic strategy was affected by higher errors due an increased standard deviation of amplitude. Said increase was attributed to differences between the images acquired from different orbits. These could have been caused by under-corrected radiometric distortions, or directional effects associated with slope orientation, as it can alter the distance signal traverses within forest canopies. For example, if slope surface is parallel to wave propagation direction the distance traversed will be larger, whereas if it is perpendicular the distance will be shorter.

Forest mask creation was accurate when using amplitude annual statistics, albeit relevant errors could appear when including images processed with older versions of Sentinel-1 instrument processing facility. Adding long-term coherence helped separating forest from urban areas, as it is the only land cover that retains coherence for long periods. Short-term (minimum temporal baseline possible) coherence statistics were useful for separating forest from low-vegetation sub-classes. Detecting selective logging based on Sentinel-1/2 imagery proved to be challenging due saturation of the relationship between cover and sensor wavelengths, or the influence of tree phenology.

Considering the presence of directional effects, a forest classification strategy was devised to separate between main forest type taking advantage of species specific phenological cycles. An ensemble of models relating amplitude and incidence angle was employed to identify forest types and understand their phenology. Modelled results showed 1) canopy transmission varies with leaf dynamics, 2) broadleaf and needleleaf forests have distinct “phenological” signatures, and 3) it is possible to use said signature to separate said classes with high accuracy.

Estimation of above ground biomass from C-band Sentinel-1 and L-band ALOS PALSAR 2 data attained similar results, with little gain observed when both wavelengths were employed together, as they seem to convey similar information. However, training a local model for the study area did result in an increase of accuracy when compared with global biomass estimates underlining the importance of adjusting models sensitive to local conditions.

Future lines of work

The work reflected in this thesis is a relevant steppingstone for future studies. The methods used for DEM evaluation could be employed to assess new models, or to select the most adequate DEM over a given area. The fitting methodology employed for forest type classification could be extended substituting by-acquisition fitting with multi-date/multi-obit fitting. This could allow obtaining a description of phenology and spatial estimates of canopy opacity in combination with canopy height data from LiDAR sensors (i.e., GEDI). Phenology descriptors could be employed for trend removal, helping to separate selective logging or insect attacks from phenology. Canopy opacity could be used to analyze parameters such as canopy moisture or leaf area index. Other possible applications could be mosaic generation and improvement of forest presence/absence classification, or biomass estimation, reducing the influence of phenology and terrain orientation on the radar signal.

References

Aber, J.S., Marzolff, I., Ries, J.B., Aber, S.E.W., 2010. Principles of Photogrammetry, in: Small-Format Aerial Photography and UAS Imagery. Elsevier. https://doi.org/10.1016/B978-0-12-812942-5.00003-3

Achard, F., Bontemps, S., Lamarche, C., Da Maet, T., Mayaux, P., Van Bogaert, E., Defourny, P., 2017. Quality Assessment of the CCI Land Cover Maps, in: First CCI Land Cover User Workshop, Frascati, Italy, 31 August 2017. Frascati, Italy.

Agrawala, S., 1998. Context and Early Origins of the Intergovernmental Panel on Climate Change. Climatic Change 39, 605–620. https://doi.org/10.1023/A:1005315532386

Ahern, F.J., Leckie, D.J., Drieman, J.A., 1993. Seasonal changes in relative C-band backscatter of northern forest cover types. IEEE Trans. Geosci. Remote Sensing 31, 668–680. https://doi.org/10.1109/36.225533

Alberdi, I., Hernández, L., Condés, S., Vallejo, R., Cañellas, I., 2016. Spain, in: Vidal, C., Alberdi, I.A., Hernández Mateo, L., Redmond, J.J. (Eds.), National Forest Inventories. Springer International Publishing, Cham, pp. 749–767. https://doi.org/10.1007/978-3-319-44015-6_41

Anfodillo, T., Carrer, M., Valle, E.D., Giacoma, E., Lamedica, S., Pettenella, D., 2008. Activity 2.7: forestry and timber industry. Report on current state of forest resources in the Carpathians. Università Degli Studi Di Padova, Dipartimento Territorio e Sistemi Agro-Forestali Legnaro.

Askne, J.I.H., Dammert, P.B.G., Ulander, L.M.H., Smith, G., 1997. C-band repeat-pass interferometric SAR observations of the forest. IEEE Trans. Geosci. Remote Sensing 35, 25–35. https://doi.org/10.1109/36.551931

Askne, J.I.H., Fransson, J.E.S., Santoro, M., Soja, M.J., Ulander, L.M.H., 2013. Model-Based Biomass Estimation of a Hemi-Boreal Forest from Multitemporal TanDEM-X Acquisitions. Remote Sensing 5, 5574–5597. https://doi.org/10.3390/rs5115574

Attema, E.P.W., Ulaby, F.T., 1978. Vegetation modeled as a water cloud. Radio Science 13, 357–364. https://doi.org/10.1029/rs013i002p00357

Avitabile, V., Herold, M., Heuvelink, G.B.M., Lewis, S.L., Phillips, O.L., Asner, G.P., Armston, J., Ashton, P.S., Banin, L., Bayol, N., Berry, N.J., Boeckx, P., de Jong, B.H.J., DeVries, B., Girardin, C.A.J., Kearsley, E., Lindsell, J.A., Lopez-Gonzalez, G., Lucas, R., Malhi, Y., Morel, A., Mitchard, E.T.A., Nagy, L., Qie, L., Quinones, M.J., Ryan, C.M., Ferry, S.J.W.,

Sunderland, T., Laurin, G.V., Gatti, R.C., Valentini, R., Verbeeck, H., Wijaya, A., Willcock, S., 2016. An integrated pan-tropical biomass map using multiple reference datasets. Global Change Biology 22, 1406–1420. https://doi.org/10.1111/gcb.13139

Baccini, A., Laporte, N., Goetz, S.J., Sun, M., Dong, H., 2008. A first map of tropical Africa's above-ground biomass derived from satellite imagery. Environ. Res. Lett. 3, 045011. https://doi.org/10.1088/1748-9326/3/4/045011

Badea, O., Silaghi, D.M., Neagu, S., Taut, I., Leca, S., 2013. Forest Monitoring - Assessment, Analysis and Warning System for Forest Ecosystem Status. Notulae Botanicae Horti Agrobotanici Cluj-Napoca 41.

Ban, C., 2012. Sovereign Debt, Austerity, and Regime Change: The Case of Nicolae Ceausescu's Romania. East European Politics and Societies 26, 743–776. https://doi.org/10.1177/0888325412465513

Baron, D., Erasmi, S., 2017. High Resolution Forest Maps from Interferometric TanDEM-X and Multitemporal Sentinel-1 SAR Data. PFG 85, 389–405. https://doi.org/10.1007/s41064-017-0040-1

Barrett, F., McRoberts, R.E., Tomppo, E., Cienciala, E., Waser, L.T., 2016. A questionnaire-based review of the operational use of remotely sensed data by national forest inventories. REMOTE SENSING OF ENVIRONMENT. https://doi.org/10.1016/j.rse.2015.08.029

Barrick, D.E., 1970. Chapter 9: Rough surfaces, in: Ruck, G.T. (Ed.), Radar Cross Section Handbook. Plenum Press, New York.

Bartholomé, E., Belward, A.S., 2005. GLC2000: a new approach to global land cover mapping from Earth observation data. International Journal of Remote Sensing 26, 1959–1977. https://doi.org/10.1080/01431160412331291297

Baycheva, T., Sotirov, M., Winkel, G., Kleinschmit, D., Holmgren, S., 2015. List of policies relevant for sustainable multi-purpose forestry at EU level [WWW Document]. URL https://archive.org/details/diabolo-d-01.01-forest-policies (accessed 1.14.22).

Beland, M., Parker, G., Sparrow, B., Harding, D., Chasmer, L., Phinn, S., Antonarakis, A., Strahler, A., 2019. On promoting the use of lidar systems in forest ecosystem research. Forest Ecology and Management 450, 117484. https://doi.org/10.1016/j.foreco.2019.117484

Belenguer-Plomer, M.A., Tanase, M.A., Fernandez-Carrillo, A., Chuvieco, E., 2019. Burned area detection and mapping using Sentinel-1 backscatter coefficient and thermal anomalies. Remote Sensing of Environment 233, 111345. https://doi.org/10.1016/j.rse.2019.111345

Bojinski, S., Fellous, J.-L., 2013. Response by ESA to GCOS, Results of the Climate Change Initiative, Requirements Analysis [WWW Document]. URL https://climate.esa.int/media/documents/ESA_Response_to_GCOS_v3_2a.pdf

Bojinski, S., Verstraete, M., Peterson, T.C., Richter, C., Simmons, A., Zemp, M., 2014. The Concept of Essential Climate Variables in Support of Climate Research, Applications, and Policy. Bulletin of the American Meteorological Society 95, 1431–1443. https://doi.org/10.1175/BAMS-D-13-00047.1

Bonan, G.B., 2008. Forests and Climate Change: Forcings, Feedbacks, and the Climate Benefits of Forests. Science 320, 1444–1449. https://doi.org/10.1126/science.1155121

Borlaf-Mena, I., Badea, O., Tanase, M.A., 2021a. Influence of the Mosaicking Algorithm on Sentinel-1 Land Cover Classification Over Rough Terrain, in: 2021 IEEE International Geoscience and Remote Sensing Symposium IGARSS, Brussels, Belgium, 11–16 July 2021. Presented at the IGARSS 2021 - 2021 IEEE International Geoscience and Remote Sensing Symposium, Brussels, Belgium, 11–16 July 2021, IEEE, Brussels, Belgium, pp. 6646–6649. https://doi.org/10.1109/IGARSS47720.2021.9553648

Borlaf-Mena, I., Badea, O., Tanase, M.A., 2021b. Assessing the Utility of Sentinel-1 Coherence Time Series for Temperate and Tropical Forest Mapping. Remote Sensing 13, 4814. https://doi.org/10.3390/rs13234814

Borlaf-Mena, I., Santoro, M., Villard, L., Badea, O., Tanase, M.A., 2020. Investigating the Impact of Digital Elevation Models on Sentinel-1 Backscatter and Coherence Observations. Remote Sensing 12, 3016. https://doi.org/10.3390/rs12183016

Breidenbach, J., Granhus, A., Hylen, G., Eriksen, R., Astrup, R., 2020. A century of National Forest Inventory in Norway – informing past, present, and future decisions. For. Ecosyst. 7, 46. https://doi.org/10.1186/s40663-020-00261-0

Breiman, L., 2001. Random Forests. Machine Learning 45, 5–32. https://doi.org/10.1023/A:1010933404324

Breunig, M.M., Kriegel, H.-P., Ng, R.T., Sander, J., 2000. LOF: identifying density-based local outliers. SIGMOD Rec. 29, 93–104. https://doi.org/10.1145/335191.335388

Brolly, M., Woodhouse, I.H., 2013. Vertical backscatter profile of forests predicted by a macroecological plant model. International Journal of Remote Sensing 34, 1026–1040. https://doi.org/10.1080/01431161.2012.715777

Bruzzone, L., Marconcini, M., Wegmuller, U., Wiesmann, A., 2004. An advanced system for the automatic classification of multitemporal SAR images. IEEE Trans. Geosci. Remote Sensing 42, 1321–1334. https://doi.org/10.1109/TGRS.2004.826821

Buitinck, L., Louppe, G., Blondel, M., Pedregosa, F., Mueller, A., Grisel, O., Niculae, V., Prettenhofer, P., Gramfort, A., Grobler, J., Layton, R., Vanderplas, J., Joly, A., Holt, B.,

Varoquaux, G., 2013. API design for machine learning software: experiences from the scikit-learn project. arXiv:1309.0238 [cs].

Büttner, G., Kosztra, B., Soukup, T., Sousa, A., Langanke, T., 2017. CLC2018 Technical Guidelines [WWW Document]. URL https://land.copernicus.eu/user-corner/technical-library/corine-land-cover-nomenclature-guidelines/html (accessed 4.8.21).

Canadian Space Agency, 2019. Over 36,000 historical RADARSAT-1 satellite images of the Earth now available to the public [WWW Document]. Canadian Goverment. URL https://www.canada.ca/en/space-agency/news/2019/03/open-data-over-36000-historical-radarsat-1-satellite-images-of-the-earth-now-available-to-the-public.html (accessed 5.7.22).

Canty, M.J., Nielsen, A.A., Conradsen, K., Skriver, H., 2019. Statistical Analysis of Changes in Sentinel-1 Time Series on the Google Earth Engine. Remote Sensing 12, 46. https://doi.org/10.3390/rs12010046

Cartus, O., Kellndorfer, J., Walker, W., Franco, C., Bishop, J., Santos, L., Fuentes, J., 2014. A National, Detailed Map of Forest Aboveground Carbon Stocks in Mexico. Remote Sensing 6, 5559–5588. https://doi.org/10.3390/rs6065559

Cartus, O., Santoro, M., Kellndorfer, J., 2012. Mapping forest aboveground biomass in the Northeastern United States with ALOS PALSAR dual-polarization L-band. Remote Sensing of Environment 124, 466–478. https://doi.org/10.1016/j.rse.2012.05.029

Castel, T., Beaudoin, A., Stach, N., Stussi, N., Le Toan, T., Durand, P., 2001. Sensitivity of space-borne SAR data to forest parameters over sloping terrain. Theory and experiment. International Journal of Remote Sensing 22, 2351–2376. https://doi.org/10.1080/01431160121407

Catrina, I., Giurgiu, V., 1983. Semicentenarrul Institutului de cercetari si experimentate forestiera. Revista padurilor 98, 170–184.

CEOS, 2022. CEOS overview [WWW Document]. Committee on Earth Observation Satellites website. URL https://ceos.org/about-ceos/overview/ (accessed 5.7.22).

CEOS (Ed.), 2021. Product Family Specification, Normalised Radar Backscatter.

Chang, C.Y., Bräutigam, K., Hüner, N.P.A., Ensminger, I., 2021. Champions of winter survival: cold acclimation and molecular regulation of cold hardiness in evergreen conifers. New Phytol 229, 675–691. https://doi.org/10.1111/nph.16904

Chuvieco, E., 2015. Teledetección ambiental: la observación de la tierra desde el espacio, Ariel ciencia. ed. Barcelona, España.

Ciceu, A., Radu, R.G., García-Duro, J., 2019. National forestry accounting plan of Romania for the first. Voluntari, Romania.

Cimino, J., Brandani, A., Casey, D., Rabassa, J., Wall, S.D., 1986. Multiple Incidence Angle SIR-B Experiment Over Argentina: Mapping of Forest Units. IEEE Transactions on Geoscience and Remote Sensing GE-24, 498–509. https://doi.org/10.1109/TGRS.1986.289664

Clapp, R.E., 1946. A theoretical and experimental study of radar ground return. Radiation Laboratory, Massachusetts Institute of Technology.

Clerc, S., MPC Team, 2018. Sentinel-2 mission product calibration: data Quality report.

CNIG, Centro Nacional de Información Geográfica, 2019a. Centro de Descargas del CNIG (IGN) [WWW Document]. URL http://centrodedescargas.cnig.es (accessed 1.13.20).

CNIG, Centro Nacional de Información Geográfica, 2019b. Primera cobertura del plan nacional de fotografía aérea [WWW Document]. URL https://pnoa.ign.es/estado-del-proyecto-lidar/primera-cobertura (accessed 8.21.20).

CNIG, Centro Nacional de Información Geográfica, 2014. National Plan for Aerial Orthophotography [WWW Document]. URL http://pnoa.ign.es/ (accessed 5.21.19).

Cohen, J., 1960. A Coefficient of Agreement for Nominal Scales. Educational and Psychological Measurement 20, 37–46. https://doi.org/10.1177/001316446002000104

Congalton, R.G., 1991. A review of assessing the accuracy of classifications of remotely sensed data. Remote Sensing of Environment 37, 35–46. https://doi.org/10.1016/0034-4257(91)90048-B

Copernicus Land Monitoring Service, 2021. Tree-cover/forest and change 2015-2018.

Cosgriff, R.L., Peake, W.H., Taylor, R.C., 1960. Terrain Scattering Properties for Sensor System Design:(Terrain Handbook II), Bulletin of the Engineering Experiment Station. Columbus Antenna Laboratory, College of Engineering, Ohio State University, Ohio, USA.

COST action E43, 2009. Harmonising national forest inventories in Europe: Reference definitions [WWW Document]. URL https://web.archive.org/web/20220111082832/http://739uq.w4yserver.at/refdef/cost-e43-reference-definitions-tex4ht.html

Courty, L.G., Soriano-Monzalvo, J.C., Pedrozo-Acuña, A., 2019. Evaluation of open-access global digital elevation models (AW3D30, SRTM, and ASTER) for flood modelling purposes. J Flood Risk Management 12. https://doi.org/10.1111/jfr3.12550

Crippen, R., Buckley, S., Agram, P., Belz, E., Gurrola, E., Hensley, S., Kobrick, M., Lavalle, M., Martin, J., Neumann, M., Nguyen, Q., Rosen, P., Shimada, J., Simard, M., Tung, W., 2016. NASADEM global elevation model: methods and progress. The International Archives of the Photogrammetry, Remote Sensing and Spatial Information Sciences XLI-B4, 125–128. https://doi.org/10.5194/isprs-archives-XLI-B4-125-2016

Del Bosque González, I., Arozarena Villar, A., Villa Alcázar, G., Valcárcel Sanz, N., Porcuna Fernández Monasterio, A., 2005. Creación de un Sistema de Información Geográfico de Ocupación del Suelo en España. PROYECTO SIOSE, in: Teledetección: Avances En La Observación de La Tierra. Presented at the XI Congreso Nacional de Teledetección, Universidad de La Laguna.

Deletant, D., Ionescu, M., 2004. Romania and the Warsaw Pact: 1955-1989. Cold War International History Project, The Woolrow Wilson International ….

Dellwig, L.F., Burchell, C., 1972. Side-Look Radar: Its Uses and Limitations as a Reconnaissance Tool. Highway Research Record.

den Besten, N., Steele-Dunne, S., Aouizerats, B., Zajdband, A., de Jeu, R., van der Zaag, P., 2021. Observing Sucrose Accumulation With Sentinel-1 Backscatter. Front. Remote Sens. 2, 778691. https://doi.org/10.3389/frsen.2021.778691

DeVries, B., Verbesselt, J., Kooistra, L., Herold, M., 2015. Robust monitoring of small-scale forest disturbances in a tropical montane forest using Landsat time series. Remote Sensing of Environment 161, 107–121. https://doi.org/10.1016/j.rse.2015.02.012

DIABOLO, 2021. Glossary [WWW Document]. Distributed, Integrated and Harmonised Forest Information for Bioeconomy Outlooks. URL http://diabolo-project.eu/dissemination/glossary/ (accessed 12.28.21).

DIABOLO, 2019. Distributed, integrated and harmonised forest information for bioeconomy outlooks (DIABOLO) [WWW Document]. Community Research and Development Information Service. URL https://web.archive.org/web/20220114104408/https://cordis.europa.eu/project/id/633464 (accessed 1.14.22).

Diniz, J.M.F. de S., 2019. Avaliação do potencial dos dados polarimétricos Sentinel-1A para mapeamento do uso e cobertura da terra na região de Ariquemes - RO [WWW Document]. URL http://mtc-m21c.sid.inpe.br/col/sid.inpe.br/mtc-m21c/2019/01.28.12.01/doc/publicacao.pdf (accessed 11.20.21).

DLR, 2020. TanDEM-X DEM proposal submission procedure [WWW Document]. TanDEM-X Science Service System. URL https://tandemx-science.dlr.de/cgi-bin/wcm.pl?page=TDM-Proposal-Submission-Procedure (accessed 9.8.20).

DLR, 2019. EOWEB GeoPortal [WWW Document]. URL https://eoweb.dlr.de/egp/ (accessed 1.13.20).

Doblas, J., Shimabukuro, Y., Sant'Anna, S., Carneiro, A., Aragão, L., Almeida, C., 2020. Optimizing Near Real-Time Detection of Deforestation on Tropical Rainforests Using Sentinel-1 Data. Remote Sensing 12, 3922. https://doi.org/10.3390/rs12233922

Dobson, M.C., Pierce, L.E., Ulaby, F.T., 1996. Knowledge-based land-cover classification using ERS-1/JERS-1 SAR composites. IEEE Transactions on Geoscience and Remote Sensing 34, 83–99. https://doi.org/10.1109/36.481896

Dostálová, A., Hollaus, M., Milenković, M., Wagner, W., 2016. Forest area derivation from Sentinel-1 Data. ISPRS Ann. Photogramm. Remote Sens. Spatial Inf. Sci. III–7, 227–233. https://doi.org/10.5194/isprsannals-III-7-227-2016

Dostálová, A., Lang, M., Ivanovs, J., Waser, L.T., Wagner, W., 2021. European Wide Forest Classification Based on Sentinel-1 Data. Remote Sensing 13, 337. https://doi.org/10.3390/rs13030337

Dostalova, A., Milenkovic, M., Hollaus, M., Wagner, W., 2016. Influence of Forest Structure on the Sentinel-1 Backscatter Variation- Analysis with Full-Waveform LiDAR Data 740, 202.

Dostálová, A., Wagner, W., Milenković, M., Hollaus, M., 2018. Annual seasonality in Sentinel-1 signal for forest mapping and forest type classification. International Journal of Remote Sensing 39, 7738–7760. https://doi.org/10.1080/01431161.2018.1479788

Doxani, G., Vermote, E., Roger, J.-C., Gascon, F., Adriaensen, S., Frantz, D., Hagolle, O., Hollstein, A., Kirches, G., Li, F., Louis, J., Mangin, A., Pahlevan, N., Pflug, B., Vanhellemont, Q., 2018. Atmospheric Correction Inter-Comparison Exercise. Remote Sensing 10, 352. https://doi.org/10.3390/rs10020352

Dubayah, R., Blair, J.B., Goetz, S., Fatoyinbo, L., Hansen, M., Healey, S., Hofton, M., Hurtt, G., Kellner, J., Luthcke, S., Armston, J., Tang, H., Duncanson, L., Hancock, S., Jantz, P., Marselis, S., Patterson, P.L., Qi, W., Silva, C., 2020. The Global Ecosystem Dynamics Investigation: High-resolution laser ranging of the Earth's forests and topography. Science of Remote Sensing 1, 100002. https://doi.org/10.1016/j.srs.2020.100002

Dubois, C., Mueller, M.M., Pathe, C., Jagdhuber, T., Cremer, F., Thiel, C., Schmullius, C., 2020. Characterization of land cover seasonality in Sentinel-1 time series data. ISPRS Ann. Photogramm. Remote Sens. Spatial Inf. Sci. V-3–2020, 97–104. https://doi.org/10.5194/isprs-annals-V-3-2020-97-2020

Duncanson, L.I., Niemann, K.O., Wulder, M.A., 2010. Integration of GLAS and Landsat TM data for aboveground biomass estimation. Canadian Journal of Remote Sensing 36, 129–141. https://doi.org/10.5589/m10-037

Elomina, J., Pülzl, H., 2021. How are forests framed? An analysis of EU forest policy. Forest Policy and Economics 127, 102448. https://doi.org/10.1016/j.forpol.2021.102448

Enander, K.-G., 2007. Skogsbruk på samhällets villkor; Skogsskötsel och skogspolitik under 150 år.

Encyclopedia Britannica, 2022. Romania: History, Map, & Facts. Encyclopedia Britannica.

Englhart, S., Keuck, V., Siegert, F., 2011. Aboveground biomass retrieval in tropical forests — The potential of combined X- and L-band SAR data use. Remote Sensing of Environment 115, 1260–1271. https://doi.org/10.1016/j.rse.2011.01.008

EROS, 2017. Shuttle Radar Topography Mission (SRTM) 1 Arc-Second Global. https://doi.org/10.5066/f7pr7tft

ESA, 2018. Sentinel-1 new product format operational on 13 March 2018 [WWW Document]. URL https://sentinel.esa.int/web/sentinel/-/sentinel-1-new-product-format-operational-on-13-march-2018 (accessed 6.7.21).

ESA, 2010. ESA Climate Change Initiative Guidelines [WWW Document]. URL https://climate.esa.int/media/documents/ESA_CCI_Project_Guidelines_V1.pdf (accessed 6.6.22).

Esch, T., Bachofer, F., Heldens, W., Hirner, A., Marconcini, M., Palacios-Lopez, D., Roth, A., Üreyen, S., Zeidler, J., Dech, S., Gorelick, N., 2018. Where We Live—A Summary of the Achievements and Planned Evolution of the Global Urban Footprint. Remote Sensing 10, 895. https://doi.org/10.3390/rs10060895

Esch, T., Heldens, W., Hirner, A., Keil, M., Marconcini, M., Roth, A., Zeidler, J., Dech, S., Strano, E., 2017. Breaking new ground in mapping human settlements from space – The Global Urban Footprint. ISPRS Journal of Photogrammetry and Remote Sensing 134, 30–42. https://doi.org/10.1016/j.isprsjprs.2017.10.012

Esch, T., Schenk, A., Ullmann, T., Thiel, M., Roth, A., Dech, S., 2011. Characterization of Land Cover Types in TerraSAR-X Images by Combined Analysis of Speckle Statistics and Intensity Information. IEEE Trans. Geosci. Remote Sensing 49, 1911–1925. https://doi.org/10.1109/TGRS.2010.2091644

European Commission, 2021. New EU Forest Strategy for 2030, COM/2021/572 final.

European Commission, 2013. A new EU Forest Strategy: for forests and the forest-based sector, COM/2013/659/FINAL.

European Commission, 1998. A forestry strategy for the European Union, COM/1998/649/FINAL.

European Council, 1992. On the conservation of natural habitats and of wild fauna and flora, 92/43/EEC.

European Parliament, European Council, 2021. Establishing the Union Space Programme and the European Union Agency for the Space Programme and repealing Regulations (EU) No 912/2010, (EU) No 1285/2013 and (EU) No 377/2014 and Decision No 541/2014/EU, PE/21/2021/INIT.

European Parliament, European Council, 2018. On the inclusion of greenhouse gas emissions and removals from land use, land use change and forestry in the 2030 climate and energy framework, OJ L.

European Parliament, European Council, 2013. On accounting rules on greenhouse gas emissions and removals resulting from activities relating to land use, land-use change and forestry and on information concerning actions relating to those activities, 529/2013/EU.

European Parliament, European Council, 2000. Establishing a framework for Community action in the field of water policy, 2000/60/EC.

FAO, 2011. Forest inventory [WWW Document]. Sustainable Forest Management (SFM) Toolbox. URL https://www.fao.org/sustainable-forest-management/toolbox/modules/forest-inventory/basic-knowledge/en/ (accessed 12.24.21).

FAO FRA, 2000. On definitions of forest and forest change., Working Papers. Food and Agriculture Organization of the United Nations, Forest Resources Assessment, Rome.

FAO, UNEP, 2020. The State of the World's Forests 2020. FAO and UNEP. https://doi.org/10.4060/ca8642en

Farr, T.G., Rosen, P.A., Caro, E., Crippen, R., Duren, R., Hensley, S., Kobrick, M., Paller, M., Rodriguez, E., Roth, L., Seal, D., Shaffer, S., Shimada, J., Umland, J., Werner, M., Oskin, M., Burbank, D., Alsdorf, D., 2007. The Shuttle Radar Topography Mission. Reviews of Geophysics 45. https://doi.org/10.1029/2005RG000183

Fassnacht, F.E., Latifi, H., Stereńczak, K., Modzelewska, A., Lefsky, M., Waser, L.T., Straub, C., Ghosh, A., 2016. Review of studies on tree species classification from remotely sensed data. Remote Sensing of Environment 186, 64–87. https://doi.org/10.1016/j.rse.2016.08.013

Felicísimo, A.M., 1994. Modelos digitales del terreno: introducción y aplicaciones en las ciencias ambientales. Pentalfa Ediciones, Oviedo.

Feranec, J., Soukup, T., Feranec, G., Jaffrain, G. (Eds.), 2016. European Landscape Dynamics: CORINE Land Cover Data. CRC Press, Boca Raton, FL, USA. https://doi.org/10.1201/9781315372860

Flores, A., Herndon, K., Thapa, R., Cherrington, E., 2019. Synthetic Aperture Radar (SAR) Handbook: Comprehensive Methodologies for Forest Monitoring and Biomass Estimation. https://doi.org/10.25966/NR2C-S697

Florinsky, I.V., Skrypitsyna, T.N., Luschikova, O.S., 2018. Comparative accuracy of the AW3D30 DSM, ASTER GDEM, and SRTM1 DEM: A case study on the Zaoksky testing ground, Central European Russia. Remote Sensing Letters 9, 706–714. https://doi.org/10.1080/2150704X.2018.1468098

Frey, O., Santoro, M., Werner, C.L., Wegmuller, U., 2013. DEM-Based SAR Pixel-Area Estimation for Enhanced Geocoding Refinement and Radiometric Normalization. IEEE Geosci. Remote Sensing Lett. 10, 48–52. https://doi.org/10.1109/LGRS.2012.2192093

Fridman, J., Westerlund, B., 2016. Sweden, in: Vidal, C., Alberdi, I.A., Hernández Mateo, L., Redmond, J.J. (Eds.), National Forest Inventories. Springer International Publishing, Cham, pp. 769–782. https://doi.org/10.1007/978-3-319-44015-6_42

Frison, P.-L., Fruneau, B., Kmiha, S., Soudani, K., Dufrêne, E., Toan, T.L., Koleck, T., Villard, L., Mougin, E., Rudant, J.-P., 2018. Potential of Sentinel-1 Data for Monitoring Temperate Mixed Forest Phenology. Remote Sensing 10, 2049. https://doi.org/10.3390/rs10122049

Frison, P.L., Fruneau, B., Rudant, J.P., Dufrêne, E., Soudani, K., Koleck, T., Villard, L., Lepage, M., Dejoux, J.F., Toan, T.L., 2017. Contribution of radar Sentinel-1 data for vegetation seasonal monitoring, in: 2017 9th International Workshop on the Analysis of Multitemporal Remote Sensing Images (MultiTemp). IEEE.

Fung, A.K., 1994. Microwave scattering and emission models and their applications, The Artech House remote sensing library. Artech House, Boston.

Gaboardi, C., 2003. Utilização de imagem de coerência SAR para classificação do uso da terra: Floresta Nacional do Tapajós [WWW Document]. URL http://mtc-m12.sid.inpe.br/col/sid.inpe.br/marciana/2003/04.10.08.52/doc/publicacao.pdf (accessed 11.20.21).

Gao, B., 1996. NDWI—A normalized difference water index for remote sensing of vegetation liquid water from space. Remote Sensing of Environment 58, 257–266. https://doi.org/10.1016/S0034-4257(96)00067-3

García-Duro, J., Ciceu, A., Chivulescu, S., Badea, O., Tanase, M.A., Aponte, C., 2021. Shifts in Forest Species Composition and Abundance under Climate Change Scenarios in Southern Carpathian Romanian Temperate Forests. Forests 12, 1434. https://doi.org/10.3390/f12111434

Garzuglia, M., Pekkarinen, A., Jonsson, Ö., Marklund, L., Piña, L., Contessa, V., Wilkie, M.L., Lanly, J.P., Russell, S., Henderson-Howat, D., 2018. 1948-2018, seventy years of FAO's Global Forest Resources Assessment. Food and Agriculture Organization of the United Nations, Rome, Italy.

GDAL/OGR contributors, 2020. GDAL/OGR Geospatial Data Abstraction software Library. Open Source Geospatial Foundation.

GeoPandas contributors, 2020. GeoPandas: Python tools for geographic data.

Gibbs, H.K., Brown, S., Niles, J.O., Foley, J.A., 2007. Monitoring and estimating tropical forest carbon stocks: making REDD a reality. Environ. Res. Lett. 2, 045023. https://doi.org/10.1088/1748-9326/2/4/045023

Gillies, S., others, 2013. Rasterio: geospatial raster I/O for Python programmers. Mapbox.

Giurgiu, V., 2011. Revista Padurilor: 125 de ani de existenta. Revista padurilor 128, 3–7.

Giurgiu, V., Decei, I., Drăghiciu, D., 2004. Metode şi tabele dendrometrice [Forest Mensuration Methods and Tables]. Editura Ceres, Bucuresti, Romania.

Global Forest Resources Assessment, 2000. On definitions of forest and forest change.

Goetz, S.J., Hansen, M., Houghton, R.A., Walker, W., Laporte, N., Busch, J., 2015. Measurement and monitoring needs, capabilities and potential for addressing reduced emissions from deforestation and forest degradation under REDD+. Environ. Res. Lett. 10, 123001. https://doi.org/10.1088/1748-9326/10/12/123001

Gómez, C., Alejandro, P., Hermosilla, T., Montes, F., Pascual, C., Ruiz, L.A., Álvarez-Taboada, F., Tanase, M., Valbuena, R., 2019. Remote sensing for the Spanish forests in the 21st century: a review of advances, needs, and opportunities. Forest Syst 28, eR001. https://doi.org/10.5424/fs/2019281-14221

GRASS Development Team, 2017. Geographic Resources Analysis Support System (GRASS GIS) Software. Open Source Geospatial Foundation.

Griffiths, P., Kuemmerle, T., Baumann, M., Radeloff, V.C., Abrudan, I.V., Lieskovsky, J., Munteanu, C., Ostapowicz, K., Hostert, P., 2014. Forest disturbances, forest recovery, and changes in forest types across the Carpathian ecoregion from 1985 to 2010 based on Landsat image composites. Remote Sensing of Environment 151, 72–88. https://doi.org/10.1016/j.rse.2013.04.022

Griffiths, P., Kuemmerle, T., Kennedy, R.E., Abrudan, I.V., Knorn, J., Hostert, P., 2012. Using annual time-series of Landsat images to assess the effects of forest restitution in post-socialist Romania. Remote Sensing of Environment 118, 199–214. https://doi.org/10.1016/j.rse.2011.11.006

Grohmann, C.H., 2018. Evaluation of TanDEM-X DEMs on selected Brazilian sites: Comparison with SRTM, ASTER GDEM and ALOS AW3D30. Remote Sensing of Environment 212, 121–133. https://doi.org/10.1016/j.rse.2018.04.043

Grumbine, R.E., 1994. What is ecosystem management? Conservation Biology 8, 27–38. https://doi.org/10.1046/j.1523-1739.1994.08010027.x

Gschwantner, T., Alberdi, I., Bauwens, S., Bender, S., Borota, D., Bosela, M., Bouriaud, O., Breidenbach, J., Donis, J., Fischer, C., Gasparini, P., Heffernan, L., Hervé, J.-C., Kolozs,

L., Korhonen, K.T., Koutsias, N., Kovácsevics, P., Kučera, M., Kulbokas, G., Kuliešis, A., Lanz, A., Lejeune, P., Lind, T., Marin, G., Morneau, F., Nord-Larsen, T., Nunes, L., Pantić, D., Redmond, J., Rego, F.C., Riedel, T., Šebeň, V., Sims, A., Skudnik, M., Tomter, S.M., 2022. Growing stock monitoring by European National Forest Inventories: Historical origins, current methods and harmonisation. Forest Ecology and Management 505, 119868. https://doi.org/10.1016/j.foreco.2021.119868

Gschwantner, T., Berger, A., Büchsenmeister, R., Hauk, E., 2016. Austria, in: Vidal, C., Alberdi, I.A., Hernández Mateo, L., Redmond, J.J. (Eds.), National Forest Inventories. Springer International Publishing, Cham, pp. 135–157. https://doi.org/10.1007/978-3-319-44015-6_7

Guth, P.L., 2006. Geomorphometry from SRTM. photogramm eng remote sensing 72, 269–277. https://doi.org/10.14358/PERS.72.3.269

Hagolle, O., Huc, M., Villa Pascual, D., Dedieu, G., 2015. A Multi-Temporal and Multi-Spectral Method to Estimate Aerosol Optical Thickness over Land, for the Atmospheric Correction of FormoSat-2, LandSat, VENµS and Sentinel-2 Images. Remote Sensing 7, 2668–2691. https://doi.org/10.3390/rs70302668

Hall, R., Arsenault, E., Skakun, R., 2006. Remotely sensed data in the mapping of insect defoliation, in: Understanding Forest Disturbance and Spatial Pattern. CRC Press, pp. 85–111. https://doi.org/10.1201/9781420005189.ch4

Hansen, J.N., Mitchard, E.T.A., King, S., 2020. Assessing Forest/Non-Forest Separability Using Sentinel-1 C-Band Synthetic Aperture Radar. Remote Sensing 12, 1899. https://doi.org/10.3390/rs12111899

Hansen, M.C., Potapov, P.V., Moore, R., Hancher, M., Turubanova, S.A., Tyukavina, A., Thau, D., Stehman, S.V., Goetz, S.J., Loveland, T.R., Kommareddy, A., Egorov, A., Chini, L., Justice, C.O., Townshend, J.R.G., 2013. High-Resolution Global Maps of 21st-Century Forest Cover Change. Science 342, 850–853. https://doi.org/10.1126/science.1244693

Havranek, W.M., Tranquillini, W., 1995. Physiological Processes during Winter Dormancy and Their Ecological Significance, in: Ecophysiology of Coniferous Forests. Elsevier, pp. 95–124. https://doi.org/10.1016/B978-0-08-092593-6.50010-4

Henderson, F.M., Lewis, A.J. (Eds.), 1998. Principles and applications of imaging radar, 3rd. ed. ed. J. Wiley, New York.

Hirt, C., Filmer, M.S., Featherstone, W.E., 2010. Comparison and validation of the recent freely available ASTER-GDEM ver1, SRTM ver4.1 and GEODATA DEM-9S ver3 digital elevation models over Australia. Australian Journal of Earth Sciences 57, 337–347. https://doi.org/10.1080/08120091003677553

Hoekman, D.H., Reiche, J., 2015. Multi-model radiometric slope correction of SAR images of complex terrain using a two-stage semi-empirical approach. Remote Sensing of Environment 156, 1–10. https://doi.org/10.1016/j.rse.2014.08.037

Hölzl, R., 2010. Historicizing Sustainability: German Scientific Forestry in the Eighteenth and Nineteenth Centuries. Science as Culture 19, 431–460. https://doi.org/10.1080/09505431.2010.519866

Homolová, L., Malenovský, Z., Clevers, J.G.P.W., García-Santos, G., Schaepman, M.E., 2013. Review of optical-based remote sensing for plant trait mapping. Ecological Complexity 15, 1–16. https://doi.org/10.1016/j.ecocom.2013.06.003

Hsu, C.-C., 1996. Theoretical models for microwave remote sensing of forests and vegetation. Massachusetts Institute of Technology.

Hu, T., Su, Y., Xue, B., Liu, J., Zhao, X., Fang, J., Guo, Q., 2016. Mapping Global Forest Aboveground Biomass with Spaceborne LiDAR, Optical Imagery, and Forest Inventory Data. Remote Sensing 8, 565. https://doi.org/10.3390/rs8070565

Hunter, J.D., 2007. Matplotlib: A 2D graphics environment. Computing in Science & Engineering 9, 90–95. https://doi.org/10.1109/MCSE.2007.55

Hyde, P., Nelson, R., Kimes, D., Levine, E., 2007. Exploring LiDAR–RaDAR synergy—predicting aboveground biomass in a southwestern ponderosa pine forest using LiDAR, SAR and InSAR. Remote Sensing of Environment 106, 28–38. https://doi.org/10.1016/j.rse.2006.07.017

ICAS, 2017. Amenajamentul. O.S. Arpaş. Regia Naţională a pădurilor Romsilva. Institutul de Cercetări şi amenajări Silvice, Bucharest, Romania.

ICAS, 2016. Amenajamentul. O.S. Sibiu. Regia Naţională a pădurilor Romsilva. Institutul de Cercetări şi amenajări Silvice, Bucharest, Romania.

ICAS, 2015a. Amenajamentul. O.S. Topoloveni. Regia Naţională a pădurilor Romsilva. Institutul de Cercetări şi amenajări Silvice, Bucharest, Romania.

ICAS, 2015b. Amenajamentul. O.S. Vidraru. Regia Naţională a pădurilor Romsilva. Institutul de Cercetări şi amenajări Silvice, Bucharest, Romania.

ICAS, 2014a. Amenajamentul. O.S. Aninoasa. Regia Naţională a pădurilor Romsilva. Institutul de Cercetări şi amenajări Silvice, Bucharest, Romania.

ICAS, 2014b. Amenajamentul. O.S. Domnesti. Regia Naţională a pădurilor Romsilva. Institutul de Cercetări şi amenajări Silvice, Bucharest, Romania.

ICAS, 2014c. Amenajamentul. O.S. Mihăeşti. Regia Naţională a pădurilor Romsilva. Institutul de Cercetări şi amenajări Silvice, Bucharest, Romania.

ICAS, 2014d. Amenajamentul. O.S. Muşăteşti. Regia Naţională a pădurilor Romsilva. Institutul de Cercetări şi amenajări Silvice, Bucharest, Romania.

ICAS, 2013a. Amenajamentul. O.S. Cotmeana. Regia Naţională a pădurilor Romsilva. Institutul de Cercetări şi amenajări Silvice, Bucharest, Romania.

ICAS, 2013b. Amenajamentul. O.S. Piteşti. Regia Naţională a pădurilor Romsilva. Institutul de Cercetări şi amenajări Silvice, Bucharest, Romania.

ICSU, 2018. The origins of the IPCC: How the world woke up to climate change. International Science Council. URL https://council.science/current/blog/the-origins-of-the-ipcc-how-the-world-woke-up-to-climate-change/ (accessed 12.31.21).

IEEE Radar Systems Panel, 2020. IEEE Standard Letter Designations for Radar-Frequency Bands. IEEE Std 521-2019 (Revision of IEEE Std 521-2002) 1–15. https://doi.org/10.1109/IEEESTD.2020.8999849

IGN, I.G.N., 2016. Plan Nacional de Ortofotografía Aérea. Especificaciones técnicas. [WWW Document]. URL http://pnoa.ign.es/caracteristicas-tecnicas (accessed 5.21.19).

Ilie, L., 2016. Romania moves to protect some of Europe's last virgin forests.

International Union for Conservation of Nature, 2011. The Bonn Challenge [WWW Document]. URL https://www.iucn.org/theme/forests/our-work/forest-landscape-restoration/bonn-challenge (accessed 10.28.20).

Iojă, C.I., Pătroescu, M., Rozylowicz, L., Popescu, V.D., Vergheleţ, M., Zotta, M.I., Felciuc, M., 2010. The efficacy of Romania's protected areas network in conserving biodiversity. Biological Conservation 143, 2468–2476. https://doi.org/10.1016/j.biocon.2010.06.013

Ioras, F., Abrudan, I.V., Dautbasic, M., Avdibegovic, M., Gurean, D., Ratnasingam, J., 2009. Conservation gains through HCVF assessments in Bosnia-Herzegovina and Romania. Biodiversity and Conservation 18, 3395–3406. https://doi.org/10.1007/s10531-009-9649-8

IPCC, 2019. History — IPCC [WWW Document]. The Intergovernmental Panel on Climate Change. URL https://www.ipcc.ch/about/history/ (accessed 12.30.21).

IPCC, 2008. Climate Change 2007: Synthesis Report (SYR), Contribution of Working Groups I, II and III to the Fourth Assessment Report (AR4) of the Intergovernmental Panel on Climate Change (IPCC). IPCC, Geneva, Switzerland.

IPCC, 2003. Good practice guidance for land use, land-use change and forestry. Hayama, Kanagawa.

IPCC, Houghton, J.T., Jenkins, G.J., Ephraums, J.J., IPCC (Eds.), 1990. Climate change: the IPCC scientific assessment. Cambridge University Press, Cambridge ; New York.

IPCC, OECD, IEA, 1996. Revised 1996 IPCC Guidelines for National Greenhouse Gas Inventories. UK Meteorological Office, Bracknell, England.

Izzawati, Wallington, E.D., Woodhouse, I.H., 2006. Forest height retrieval from commercial X-band SAR products. IEEE Trans. Geosci. Remote Sensing 44, 863–870. https://doi.org/10.1109/TGRS.2006.870828

Jacob, A.W., Vicente-Guijalba, F., Lopez-Martinez, C., Lopez-Sanchez, J.M., Litzinger, M., Kristen, H., Mestre-Quereda, A., Ziolkowski, D., Lavalle, M., Notarnicola, C., Suresh, G., Antropov, O., Ge, S., Praks, J., Ban, Y., Pottier, E., Mallorqui Franquet, J.J., Duro, J., Engdahl, M.E., 2020. Sentinel-1 InSAR Coherence for Land Cover Mapping: A Comparison of Multiple Feature-Based Classifiers. IEEE J. Sel. Top. Appl. Earth Observations Remote Sensing 13, 535–552. https://doi.org/10.1109/JSTARS.2019.2958847

Jacquemoud, S., Verhoef, W., Baret, F., Bacour, C., Zarco-Tejada, P.J., Asner, G.P., François, C., Ustin, S.L., 2009. PROSPECT and SAIL models: a review of use for vegetation characterization. Remote Sensing of Environment 113, 56–66. https://doi.org/10.1016/j.rse.2008.01.026

Jasiewicz, J., Stepinski, T.F., 2013. Geomorphons — a pattern recognition approach to classification and mapping of landforms. Geomorphology 182, 147–156. https://doi.org/10.1016/j.geomorph.2012.11.005

JAXA, 2019. ALOS Global Digital Surface Model "ALOS World 3D - 30m" (AW3D30) [WWW Document]. URL https://www.eorc.jaxa.jp/ALOS/en/aw3d30/index.htm (accessed 1.13.20).

JAXA, NASA, 2020. PALSAR Data at NASA's Alaska Satellite Facility (ASF) [WWW Document]. Distributed Active Archive Center (DAAC). URL https://earthdata.nasa.gov/learn/articles/tools-and-technology-articles/unrestricted-palsar-asf-daac/ (accessed 5.7.22).

Joint Research Centre, 2015. Forest ecosystem services.

Jones, E., Oliphant, T., Peterson, P., 2014. SciPy: Open source scientific tools for Python.

Kennedy, R.E., Yang, Z., Cohen, W.B., 2010. Detecting trends in forest disturbance and recovery using yearly Landsat time series: 1. LandTrendr, temporal segmentation algorithms. Remote Sensing of Environment 114, 2897–2910. https://doi.org/10.1016/j.rse.2010.07.008

Kirches, G., Brockmann, C., Boettcher, M., Peters, M., Bontemps, S., Lamarche, C., Schlerf, M., Santoro, M., Defourny, P., 2017. Land cover cci-product user guide-version 2 [WWW Document]. URL http://maps.elie.ucl.ac.be/CCI/viewer/download/ESACCI-LC-Ph2-PUGv2_2.0.pdf (accessed 11.20.21).

Klawitter, N., 2015. Logging threatens one of Europe's last virgin forests.

Knorn, J., Kuemmerle, T., Radeloff, V.C., Szabo, A., Mindrescu, M., Keeton, W.S., Abrudan, I., Griffiths, P., Gancz, V., Hostert, P., 2012. Forest restitution and protected area effectiveness in post-socialist Romania. Biological Conservation 146, 204–212. https://doi.org/10.1016/j.biocon.2011.12.020

Korhonen, K.T., 2016. Finland, in: Vidal, C., Alberdi, I.A., Hernández Mateo, L., Redmond, J.J. (Eds.), National Forest Inventories. Springer International Publishing, Cham, pp. 369–384. https://doi.org/10.1007/978-3-319-44015-6_19

Kosztra, B., Büttner, G., 2019. Updated CLC illustrated nomenclature guidelines [WWW Document]. URL https://land.copernicus.eu/user-corner/technical-library/corine-land-cover-nomenclature-guidelines/docs/pdf/CLC2018_Nomenclature_illustrated_guide_20190510.pdf (accessed 4.8.21).

Krige, J., Russo, A., Sebesta, L., 2000. A history of the European Space Agency 1958-1987, SP. European Space Agency, Noordwijk.

Kweon, S.-K., Oh, Y., 2015. A Modified Water-Cloud Model With Leaf Angle Parameters for Microwave Backscattering From Agricultural Fields. IEEE Trans. Geosci. Remote Sensing 53, 2802–2809. https://doi.org/10.1109/TGRS.2014.2364914

LaBau, V.J., Bones, J.T., Kingsley, N.P., Lund, H.G., Smith, W.B., 2007. A History of the Forest Survey in the United States: 1830-2004. U. S. Department of Agriculture, Forest Service.

Landis, J.R., Koch, G.G., 1977. The Measurement of Observer Agreement for Categorical Data. Biometrics 33, 159. https://doi.org/10.2307/2529310

Langanke, T., Büttner, G., Dufourmont, H., Iasillo, D., Probeck, M., Rosengren, M., Sousa, A., Strobl, P., Weichselbaum, J., 2013. GIO land (GMES/Copernicus initial operations land) High Resolution Layers (HRLs)–summary of product specifications.

Lanz, A., Abegg, M., Braendli, U.-B., Camin, P., Cioldi, F., Ginzler, C., Fischer, C., 2016. Switzerland, in: Vidal, C., Alberdi, I.A., Hernández Mateo, L., Redmond, J.J. (Eds.), National Forest Inventories. Springer International Publishing, Cham, pp. 783–805. https://doi.org/10.1007/978-3-319-44015-6_43

Lawrence, A., 2009. Forestry in transition: Imperial legacy and negotiated expertise in Romania and Poland. Forest Policy and Economics 11, 429–436. https://doi.org/10.1016/j.forpol.2009.02.003

Le Toan, T., Quegan, S., Davidson, M.W.J., Balzter, H., Paillou, P., Papathanassiou, K., Plummer, S., Rocca, F., Saatchi, S., Shugart, H., Ulander, L., 2011. The BIOMASS mission: Mapping global forest biomass to better understand the terrestrial carbon cycle. Remote Sensing of Environment, DESDynI VEG-3D Special Issue 115, 2850–2860. https://doi.org/10.1016/j.rse.2011.03.020

Leckie, D.G., Ranson, K.J., 1998. Forestry applications using imaging radar, in: Principles and Applications of Imaging Radar. John Wiley and Sons New York, pp. 435–509.

Lefsky, M.A., Cohen, W.B., Parker, G.G., Harding, D.J., 2002. Lidar Remote Sensing for Ecosystem Studies. BioScience 52, 19. https://doi.org/10.1641/0006-3568(2002)052[0019:LRSFES]2.0.CO;2

Lewis, A., Lacey, J., Mecklenburg, S., Ross, J., Siqueira, A., Killough, B., Szantoi, Z., Tadono, T., Rosenavist, A., Goryl, P., Miranda, N., Hosford, S., 2018. CEOS Analysis Ready Data for Land (CARD4L) Overview, in: IGARSS 2018 - 2018 IEEE International Geoscience and Remote Sensing Symposium. Presented at the IGARSS 2018 - 2018 IEEE International Geoscience and Remote Sensing Symposium, pp. 7407–7410. https://doi.org/10.1109/IGARSS.2018.8519255

Lewis, J.G., 1999. The Pinchot Family and the Battle to Establish American Forestry. Pennsylvania History: A Journal of Mid-Atlantic Studies 66, 143–165.

Li, W., MacBean, N., Ciais, P., Defourny, P., Lamarche, C., Bontemps, S., Houghton, R.A., Peng, S., 2018. Gross and net land cover changes in the main plant functional types derived from the annual ESA CCI land cover maps (1992–2015). Earth Syst. Sci. Data 10, 219–234. https://doi.org/10.5194/essd-10-219-2018

Ling, Y., Teng, S., Liu, C., Dash, J., Morris, H., Pastor-Guzman, J., 2022. Assessing the Accuracy of Forest Phenological Extraction from Sentinel-1 C-Band Backscatter Measurements in Deciduous and Coniferous Forests. Remote Sensing 14, 674. https://doi.org/10.3390/rs14030674

Linser, S., 2005. The MCPFE's Work on Biodiversity, in: Marchetti, M. (Ed.), Monitoring and Indicators of Forest Biodiversity in Europe: From Ideas to Operationality. European Forest Institute, Joensuu.

Loh, W.-Y., 2002. Regression tress with unbiased variable selection and interaction detection. Statistica Sinica 12, 361–386.

Lorenz, M., 1995. International Co-operative Programme on Assessment and Monitoring of Air Pollution Effects on Forests-ICP Forests-. Water Air Soil Pollut 85, 1221–1226. https://doi.org/10.1007/BF00477148

Lorite Martínez, S., Moreno Jabato, J., Garrido Sáenz de Tejada, J.M., Rodríguez-Cuenca, B., 2019. Automatic classification of bridges and continental water bodies from 3D point clouds (aerial lidar). Int. Arch. Photogramm. Remote Sens. Spatial Inf. Sci. XLII-2/W13, 1047–1051. https://doi.org/10.5194/isprs-archives-XLII-2-W13-1047-2019

Lorite Martínez, S., Ojeda Manrique, J.C., Rodríguez-Cuenca, B., González Cristóbal, E., Muñoz, P., 2017. Procesado y distribución de nubes de puntos en el proyecto PNOA-LiDAR, in: XVII Congreso de La Asociación Española de Teledetección. Presented at the

Nuevas plataformas y sensores de teledetección, Editorial Universitat Politècnica de València, Murcia, pp. 329–332.

Lucas, R., Armston, J., Fairfax, R., Fensham, R., Accad, A., Carreiras, J., Kelley, J., Bunting, P., Clewley, D., Bray, S., Metcalfe, D., Dwyer, J., Bowen, M., Eyre, T., Laidlaw, M., Shimada, M., 2010. An Evaluation of the ALOS PALSAR L-Band Backscatter—Above Ground Biomass Relationship Queensland, Australia: Impacts of Surface Moisture Condition and Vegetation Structure. IEEE Journal of Selected Topics in Applied Earth Observations and Remote Sensing 3, 576–593. https://doi.org/10.1109/JSTARS.2010.2086436

Lucas, R.M., Cronin, N., Moghaddam, M., Lee, A., Armston, J., Bunting, P., Witte, C., 2006. Integration of radar and Landsat-derived foliage projected cover for woody regrowth mapping, Queensland, Australia. Remote Sensing of Environment 100, 388–406. https://doi.org/10.1016/j.rse.2005.09.020

Luckman, A., Baker, J., Wegmüller, U., 2000. Repeat-Pass Interferometric Coherence Measurements of Disturbed Tropical Forest from JERS and ERS Satellites. Remote Sensing of Environment 73, 350–360. https://doi.org/10.1016/S0034-4257(00)00110-3

MacMillan, R.A., Shary, P.A., 2009. Chapter 9 Landforms and Landform Elements in Geomorphometry, in: Developments in Soil Science. Elsevier, pp. 227–254. https://doi.org/10.1016/S0166-2481(08)00009-3

Maghsoudi, Y., Collins, M., Leckie, D.G., 2012. Polarimetric classification of Boreal forest using nonparametric feature selection and multiple classifiers. International Journal of Applied Earth Observation and Geoinformation 19, 139–150. https://doi.org/10.1016/j.jag.2012.04.015

Maghsoudi, Y., Collins, M.J., Leckie, D.G., 2013. Radarsat-2 Polarimetric SAR Data for Boreal Forest Classification Using SVM and a Wrapper Feature Selector. IEEE J. Sel. Top. Appl. Earth Observations Remote Sensing 6, 1531–1538. https://doi.org/10.1109/JSTARS.2013.2259219

Mantescu, L., Vasile, M., 2009. Property reforms in rural Romania and community-based forests. Romanian Sociology 7, 95–113.

Marin, G., Bouriaud, O., Dumitru, M., Nitu, D., 2010. Romania, in: Tomppo, E., Gschwantner, T., Lawrence, M., McRoberts, R.E. (Eds.), National Forest Inventories. Springer Netherlands, Dordrecht. https://doi.org/10.1007/978-90-481-3233-1

Marin, G., Bouriaud, O., Dumitru, M., Nitu, M.D., 2016. Romania, in: Vidal, C., Alberdi, I.A., Hernández Mateo, L., Redmond, J.J. (Eds.), National Forest Inventories. Springer International Publishing, Cham, pp. 683–698. https://doi.org/10.1007/978-3-319-44015-6_37

Martinez, J.M., Beaudoin, A., Wegmuller, U., Strozzi, T., 1998. Classification of land-cover and forest types using multidate ERS tandem data acquired over hilly terrain, in: IGARSS '98. Sensing and Managing the Environment. 1998 IEEE International Geoscience and Remote Sensing. Symposium Proceedings. (Cat. No.98CH36174). Presented at the IGARSS '98. Sensing and Managing the Environment. 1998 IEEE International Geoscience and Remote Sensing. Symposium Proceedings. (Cat. No.98CH36174), pp. 1809–1811 vol.4. https://doi.org/10.1109/IGARSS.1998.703659

Martone, M., Rizzoli, P., Wecklich, C., González, C., Bueso-Bello, J.-L., Valdo, P., Schulze, D., Zink, M., Krieger, G., Moreira, A., 2018. The global forest/non-forest map from TanDEM-X interferometric SAR data. Remote Sensing of Environment 205, 352–373. https://doi.org/10.1016/j.rse.2017.12.002

MCPFE, 2015. The updated pan-european indicators for sustainable forest management [WWW Document]. FOREST EUROPE. URL https://web.archive.org/web/20210726061029/https://foresteurope.org/wp-content/uploads/2016/11/III.-ELM_7MC_2_2015_MinisterialDeclaration_adopted-2.pdf (accessed 1.10.22).

MCPFE, 2002. Vienna living forest summit declaration. Improved Pan European indicators for sustainable forest management as adopted by the MCPFE Expert Level Meeting, in: Ministerial Conference on the Protection of Forests in Europe. Presented at the Fourth Ministerial Conference on the Protection of the Forests in Europe, Vienna, Austria.

McRoberts, R., Tomppo, E., 2007. Remote sensing support for national forest inventories. Remote Sensing of Environment 110, 412–419. https://doi.org/10.1016/j.rse.2006.09.034

Mermoz, S., Le Toan, T., 2016. Forest Disturbances and Regrowth Assessment Using ALOS PALSAR Data from 2007 to 2010 in Vietnam, Cambodia and Lao PDR. Remote Sensing 8, 217. https://doi.org/10.3390/rs8030217

Mermoz, S., Réjou-Méchain, M., Villard, L., Le Toan, T., Rossi, V., Gourlet-Fleury, S., 2015. Decrease of L-band SAR backscatter with biomass of dense forests. Remote Sensing of Environment 159, 307–317. https://doi.org/10.1016/j.rse.2014.12.019

Metz, B., IPCC (Eds.), 2007. Climate change 2007: mitigation of climate change: contribution of Working Group III to the Fourth assessment report of the Intergovernmental Panel on Climate Change. Cambridge University Press, Cambridge ; New York.

Michelakis, D., Stuart, N., Lopez, G., Linares, V., Woodhouse, I.H., 2014. Local-Scale Mapping of Biomass in Tropical Lowland Pine Savannas Using ALOS PALSAR. Forests 5, 2377–2399. https://doi.org/10.3390/f5092377

Michelsen, K.-E., 1995. History of forest research in Finland. Part 1. The unknown forest. Metsäntutkimuslaitos (Finnish Forest Research Institute).

Micu, D.M., Dumitrescu, A., Cheval, S., Birsan, M.-V., 2015. Climate of the Romanian Carpathians, Springer Atmospheric Sciences. Springer International Publishing, Cham. https://doi.org/10.1007/978-3-319-02886-6

Millennium Ecosystem Assessment, 2003. Ecosystems and human well-being: a framework for assessment, Millennium Ecosystem Assessment Series. Island Press.

Mitchard, E.T.A., Saatchi, S.S., Lewis, S.L., Feldpausch, T.R., Woodhouse, I.H., Sonké, B., Rowland, C., Meir, P., 2011. Measuring biomass changes due to woody encroachment and deforestation/degradation in a forest–savanna boundary region of central Africa using multi-temporal L-band radar backscatter. Remote Sensing of Environment, DESDynI VEG-3D Special Issue 115, 2861–2873. https://doi.org/10.1016/j.rse.2010.02.022

Mitchard, E.T.A., Saatchi, S.S., White, L.J.T., Abernethy, K.A., Jeffery, K.J., Lewis, S.L., Collins, M., Lefsky, M.A., Leal, M.E., Woodhouse, I.H., Meir, P., 2012. Mapping tropical forest biomass with radar and spaceborne LiDAR in Lopé National Park, Gabon: overcoming problems of high biomass and persistent cloud. Biogeosciences 9, 179–191. https://doi.org/10.5194/bg-9-179-2012

Mitchell, A.L., Tapley, I., Milne, A.K., Williams, M.L., Zhou, Z.-S., Lehmann, E., Caccetta, P., Lowell, K., Held, A., 2014. C- and L-band SAR interoperability: Filling the gaps in continuous forest cover mapping in Tasmania. Remote Sensing of Environment 155, 58–68. https://doi.org/10.1016/j.rse.2014.02.020

Moiret-Guigand, A., Jaffrain, G., Pennec, A., Dufourmont, H., 2021. CLC2018/CLCC1218 validation report [WWW Document]. URL https://land.copernicus.eu/user-corner/technical-library/clc-2018-and-clc-change-2012-2018-validation-report

Moore, G.K., 1979. What is a picture worth? A history of remote sensing / Quelle est la valeur d'une image? Un tour d'horizon de télédétection. Hydrological Sciences Bulletin 24, 477–485. https://doi.org/10.1080/02626667909491887

Morain, S.A., Simonett, D.S., 1967. K-band radar in vegetation mapping. University of Kansas, Center for Research.

Moreira, A., Prats-Iraola, P., Younis, M., Krieger, G., Hajnsek, I., Papathanassiou, K.P., 2013. A tutorial on synthetic aperture radar. IEEE Geosci. Remote Sens. Mag. 1, 6–43. https://doi.org/10.1109/MGRS.2013.2248301

Morgenstern, E.K., 2007. The origin and early application of the principle of sustainable forest management. The Forestry Chronicle 83, 485–489. https://doi.org/10.5558/tfc83485-4

Munteanu, C., Nita, M.D., Abrudan, I.V., Radeloff, V.C., 2016. Historical forest management in Romania is imposing strong legacies on contemporary forests and their management. Forest Ecology and Management 361, 179–193. https://doi.org/10.1016/j.foreco.2015.11.023

Næsset, E., McRoberts, R.E., Pekkarinen, A., Saatchi, S., Santoro, M., Trier, Ø.D., Zahabu, E., Gobakken, T., 2020. Use of local and global maps of forest canopy height and aboveground biomass to enhance local estimates of biomass in miombo woodlands in Tanzania. International Journal of Applied Earth Observation and Geoinformation 93, 102138. https://doi.org/10.1016/j.jag.2020.102138

NASA, USGS, 2020. Release of NASADEM Data Products [WWW Document]. Release of NASADEM Data Products. URL https://lpdaac.usgs.gov/news/release-nasadem-data-products/ (accessed 9.11.20).

National Aeronautics and Space Administration, 2022. Remote Sensing: An Overview [WWW Document]. Earth Data: open data for open science. URL https://earthdata.nasa.gov/learn/backgrounders/remote-sensing/ (accessed 4.13.22).

National Aeronautics and Space Administration Jet Propulsion Laboratory, 2020. NASADEM Merged DEM Global 1 arc second V001 [WWW Document]. URL https://lpdaac.usgs.gov/products/nasadem_hgtv001 (accessed 4.6.21).

National Oceanic and Atmospheric Administration, 2021. What is remote sensing? [WWW Document]. National Ocean Service. URL https://oceanservice.noaa.gov/facts/remotesensing.html (accessed 4.13.22).

Neumann, M., Saatchi, S.S., Ulander, L.M.H., Fransson, J.E.S., 2012. Assessing Performance of L- and P-Band Polarimetric Interferometric SAR Data in Estimating Boreal Forest Above-Ground Biomass. IEEE Transactions on Geoscience and Remote Sensing 50, 714–726. https://doi.org/10.1109/TGRS.2011.2176133

Newton, A.C., Hill, R.A., Echeverría, C., Golicher, D., Rey Benayas, J.M., Cayuela, L., Hinsley, S.A., 2009. Remote sensing and the future of landscape ecology. Progress in Physical Geography: Earth and Environment 33, 528–546. https://doi.org/10.1177/0309133309346882

Nilson, T., Peterson, U., 1994. Age dependence of forest reflectance: Analysis of main driving factors. Remote Sensing of Environment 48, 319–331. https://doi.org/10.1016/0034-4257(94)90006-X

Nita, M.D., Munteanu, C., Gutman, G., Abrudan, I.V., Radeloff, V.C., 2018. Widespread forest cutting in the aftermath of World War II captured by broad-scale historical Corona spy satellite photography. Remote Sensing of Environment 204, 322–332. https://doi.org/10.1016/j.rse.2017.10.021

ODP, 2019. Aerial LiDAR Scanning datasets [WWW Document]. URL http://data.opendataportal.at/dataset?tags=ALS&sort=score+desc (accessed 12.29.19).

Oh, Y., Young-Mi Jang, Sarabandi, K., 2002. Full-wave analysis of microwave scattering from short vegetation: an investigation on the effect of multiple scattering. IEEE Trans. Geosci. Remote Sensing 40, 2522–2526. https://doi.org/10.1109/TGRS.2002.805085

Olesk, A., Voormansik, K., Pohjala, M., Noorma, M., 2015. Forest change detection from Sentinel-1 and ALOS-2 satellite images, in: 2015 IEEE 5th Asia-Pacific Conference on Synthetic Aperture Radar (APSAR), Singapore, 1–4 September 2015. Presented at the 2015 IEEE 5th Asia-Pacific Conference on Synthetic Aperture Radar (APSAR), IEEE, Singapore, pp. 522–527. https://doi.org/10.1109/APSAR.2015.7306263

Ollinger, S.V., 2010. Sources of variability in canopy reflectance and the convergent properties of plants. New Phytologist 189, 375–394. https://doi.org/10.1111/j.1469-8137.2010.03536.x

Olson, D.M., Dinerstein, E., Wikramanayake, E.D., Burgess, N.D., Powell, G.V.N., Underwood, E.C., D'amico, J.A., Itoua, I., Strand, H.E., Morrison, J.C., Loucks, C.J., Allnutt, T.F., Ricketts, T.H., Kura, Y., Lamoreux, J.F., Wettengel, W.W., Hedao, P., Kassem, K.R., 2001. Terrestrial Ecoregions of the World: A New Map of Life on Earth: A new global map of terrestrial ecoregions provides an innovative tool for conserving biodiversity. BioScience 51, 933–938. https://doi.org/10.1641/0006-3568(2001)051[0933:TEOTWA]2.0.CO;2

Ouchi, K., 2013. Recent Trend and Advance of Synthetic Aperture Radar with Selected Topics. Remote Sensing 5, 716–807. https://doi.org/10.3390/rs5020716

Pandas contributors, 2020. Pandas. Zenodo. https://doi.org/10.5281/zenodo.3509134

Patel, P., Srivastava, H.S., Panigrahy, S., Parihar, J.S., 2006. Comparative evaluation of the sensitivity of multi-polarized multi-frequency SAR backscatter to plant density. International Journal of Remote Sensing 27, 293–305. https://doi.org/10.1080/01431160500214050

Peter, L., 2015. Romania acts to save forests from logging spree.

Pfeil, I., Wagner, W., Forkel, M., Dorigo, W., Vreugdenhil, M., 2020. Does ASCAT observe the spring reactivation in temperate deciduous broadleaf forests? Remote Sensing of Environment 250, 112042. https://doi.org/10.1016/j.rse.2020.112042

Potapov, P.V., Turubanova, S.A., Tyukavina, A., Krylov, A.M., McCarty, J.L., Radeloff, V.C., Hansen, M.C., 2015. Eastern Europe's forest cover dynamics from 1985 to 2012 quantified from the full Landsat archive. Remote Sensing of Environment 159, 28–43. https://doi.org/10.1016/j.rse.2014.11.027

Proietti, R., Antonucci, S., Monteverdi, M.C., Garfì, V., Marchetti, M., Plutino, M., Di Carlo, M., Germani, A., Santopuoli, G., Castaldi, C., Chiavetta, U., 2020. Monitoring spring phenology in Mediterranean beech populations through in situ observation and Synthetic Aperture Radar methods. Remote Sensing of Environment 248, 111978. https://doi.org/10.1016/j.rse.2020.111978

Proisy, C., Mougin, E., Dufrene, E., Le Dantec, V., 2000. Monitoring seasonal changes of a mixed temperate forest using ERS SAR observations. IEEE Trans. Geosci. Remote Sensing 38, 540–552. https://doi.org/10.1109/36.823949

Puhr, C.B., Donoghue, D.N.M., 2000. Remote sensing of upland conifer plantations using Landsat TM data: A case study from Galloway, south-west Scotland. International Journal of Remote Sensing 21, 633–646. https://doi.org/10.1080/014311600210470

Pulella, A., Aragão Santos, R., Sica, F., Posovszky, P., Rizzoli, P., 2020. Multi-Temporal Sentinel-1 Backscatter and Coherence for Rainforest Mapping. Remote Sensing 12, 847. https://doi.org/10.3390/rs12050847

Purinton, B., Bookhagen, B., 2017. Validation of digital elevation models (DEMs) and comparison of geomorphic metrics on the southern Central Andean Plateau. Earth Surf. Dynam. 5, 211–237. https://doi.org/10.5194/esurf-5-211-2017

Python Software Foundation, 2020. Python Language Reference, version 3.

Quegan, S., Le Toan, T., Yu, J.J., Ribbes, F., Floury, N., 2000. Multitemporal ERS SAR analysis applied to forest mapping. IEEE Trans. Geosci. Remote Sensing 38, 741–753. https://doi.org/10.1109/36.842003

Rahman, H., Dedieu, G., 1994. SMAC: a simplified method for the atmospheric correction of satellite measurements in the solar spectrum. International Journal of Remote Sensing 15, 123–143. https://doi.org/10.1080/01431169408954055

Raney, R.K., 1998. Radar fundamentals: technical perstective. Principals and Applications of Imaging Radar, Manual of Remote Sensing 2, 9–130.

Ranson, K.J., Sun, G., 2000. Effects of environmental conditions on boreal forest classification and biomass estimates with SAR. IEEE Trans. Geosci. Remote Sensing 38, 1242–1252. https://doi.org/10.1109/36.843016

Reiche, J., Leiterer, R., Cartus, O., Santoro, M., Schmullius, C., Li, Z., 2010. Forest Dragon 2: Large-Area Forest Growing Stock Volume Mapping in China, using space borne radar. https://doi.org/10.5167/UZH-77389

Riedel, T., Polley, H., Klatt, S., 2016. Germany, in: Vidal, C., Alberdi, I.A., Hernández Mateo, L., Redmond, J.J. (Eds.), National Forest Inventories. Springer International Publishing, Cham, pp. 405–421. https://doi.org/10.1007/978-3-319-44015-6_21

Rignot, E.J.M., Williams, C.L., Way, J., Viereck, L.A., 1994. Mapping of forest types in Alaskan boreal forests using SAR imagery. IEEE Trans. Geosci. Remote Sensing 32, 1051–1059. https://doi.org/10.1109/36.312893

Rizzoli, P., Martone, M., Gonzalez, C., Wecklich, C., Borla Tridon, D., Bräutigam, B., Bachmann, M., Schulze, D., Fritz, T., Huber, M., Wessel, B., Krieger, G., Zink, M., Moreira, A., 2017. Generation and performance assessment of the global TanDEM-X digital elevation model. ISPRS Journal of Photogrammetry and Remote Sensing 132, 119–139. https://doi.org/10.1016/j.isprsjprs.2017.08.008

Robinson, C., Saatchi, S., Neumann, M., Gillespie, T., 2013. Impacts of Spatial Variability on Aboveground Biomass Estimation from L-Band Radar in a Temperate Forest. Remote Sensing 5, 1001–1023. https://doi.org/10.3390/rs5031001

Rodionova, N.V., 2018. 2015–2016 Seasonal Variations of Backscattering from Natural Coverage in the Moscow Region Based on Radar Data from the Sentinel 1A Satellite. Izv. Atmos. Ocean. Phys. 54, 1272–1281. https://doi.org/10.1134/S0001433818090311

Rodríguez, E., Morris, C.S., Belz, J.E., 2006. A Global Assessment of the SRTM Performance. photogramm eng remote sensing 72, 249–260. https://doi.org/10.14358/PERS.72.3.249

Rodríguez-Veiga, P., Quegan, S., Carreiras, J., Persson, H.J., Fransson, J.E.S., Hoscilo, A., Ziółkowski, D., Stereńczak, K., Lohberger, S., Stängel, M., Berninger, A., Siegert, F., Avitabile, V., Herold, M., Mermoz, S., Bouvet, A., Le Toan, T., Carvalhais, N., Santoro, M., Cartus, O., Rauste, Y., Mathieu, R., Asner, G.P., Thiel, C., Pathe, C., Schmullius, C., Seifert, F.M., Tansey, K., Balzter, H., 2019. Forest biomass retrieval approaches from earth observation in different biomes. International Journal of Applied Earth Observation and Geoinformation 77, 53–68. https://doi.org/10.1016/j.jag.2018.12.008

Rodríguez-Veiga, P., Saatchi, S., Tansey, K., Balzter, H., 2016. Magnitude, spatial distribution and uncertainty of forest biomass stocks in Mexico. Remote Sensing of Environment 183, 265–281. https://doi.org/10.1016/j.rse.2016.06.004

Roşculeţ, G., 2011. The Forest Code of 1910 applied to the forests belonging to the compossessorates and the rural communities. Bulletin of the Transilvania University of Braşov, Series VII: Social Sciences and Law 147–154.

Rüetschi, M., Schaepman, M., Small, D., 2017. Using Multitemporal Sentinel-1 C-band Backscatter to Monitor Phenology and Classify Deciduous and Coniferous Forests in Northern Switzerland. Remote Sensing 10, 55. https://doi.org/10.3390/rs10010055

Saatchi, S.S., Harris, N.L., Brown, S., Lefsky, M., Mitchard, E.T.A., Salas, W., Zutta, B.R., Buermann, W., Lewis, S.L., Hagen, S., Petrova, S., White, L., Silman, M., Morel, A., 2011.

Benchmark map of forest carbon stocks in tropical regions across three continents. Proceedings of the National Academy of Sciences 108, 9899–9904. https://doi.org/10.1073/pnas.1019576108

Saatchi, S.S., Rignot, E., 1997. Classification of boreal forest cover types using SAR images. Remote Sensing of Environment 60, 270–281. https://doi.org/10.1016/S0034-4257(96)00181-2

Sandberg, G., Ulander, L.M.H., Fransson, J.E.S., Holmgren, J., Le Toan, T., 2011. L- and P-band backscatter intensity for biomass retrieval in hemiboreal forest. Remote Sensing of Environment, DESDynI VEG-3D Special Issue 115, 2874–2886. https://doi.org/10.1016/j.rse.2010.03.018

Santillan, J.R., Makinano-Santillan, M., 2016. Vertical accuracy assessment of 30-m resolution ALOS, ASTER, AND SRTM global DEMs over northeastern Mindanao, Philippines. Int. Arch. Photogramm. Remote Sens. Spatial Inf. Sci. XLI-B4, 149–156. https://doi.org/10.5194/isprsarchives-XLI-B4-149-2016

Santoro, M., 2003. Estimation of biophysical parameters in boreal forests from ERS and JERS SAR interferometry.

Santoro, M., Askne, J., Dammert, P.B.G., 2005. Tree height influence on ERS interferometric phase in boreal forest. IEEE Trans. Geosci. Remote Sensing 43, 207–217. https://doi.org/10.1109/TGRS.2004.841250

Santoro, M., Askne, J., Smith, G., Fransson, J.E.S., 2002. Stem volume retrieval in boreal forests from ERS-1/2 interferometry. Remote Sensing of Environment 81, 19–35. https://doi.org/10.1016/S0034-4257(01)00329-7

Santoro, M., Askne, J.I.H., Wegmuller, U., Werner, C.L., 2007a. Observations, Modeling, and Applications of ERS-ENVISAT Coherence Over Land Surfaces. IEEE Trans. Geosci. Remote Sensing 45, 2600–2611. https://doi.org/10.1109/TGRS.2007.897420

Santoro, M., Beaudoin, A., Beer, C., Cartus, O., Fransson, J.E.S., Hall, R.J., Pathe, C., Schmullius, C., Schepaschenko, D., Shvidenko, A., Thurner, M., Wegmüller, U., 2015. Forest growing stock volume of the northern hemisphere: Spatially explicit estimates for 2010 derived from Envisat ASAR. Remote Sensing of Environment 168, 316–334. https://doi.org/10.1016/j.rse.2015.07.005

Santoro, M., Beer, C., Cartus, O., Schmullius, C., Shvidenko, A., McCallum, I., Wegmüller, U., Wiesmann, A., 2011. Retrieval of growing stock volume in boreal forest using hyper-temporal series of Envisat ASAR ScanSAR backscatter measurements. Remote Sensing of Environment 115, 490–507. https://doi.org/10.1016/j.rse.2010.09.018

Santoro, M., Beer, C., Cartus, O., Schmullius, C., Shvidenko, A., McCallum, I., Wegmüller, U., Wiesmann, A., 2010. The BIOMASAR algorithm: An approach for retrieval of forest

growing stock volume using stacks of multi-temporal SAR data, in: Proceedings of ESA Living Planet Symposium.

Santoro, M., Cartus, O., 2021. ESA Biomass Climate Change Initiative (Biomass_cci): Global datasets of forest above-ground biomass for the years 2010, 2017 and 2018, v3. https://doi.org/10.5285/5F331C418E9F4935B8EB1B836F8A91B8

Santoro, M., Cartus, O., 2018. Research Pathways of Forest Above-Ground Biomass Estimation Based on SAR Backscatter and Interferometric SAR Observations. Remote Sensing 10, 608. https://doi.org/10.3390/rs10040608

Santoro, M., Cartus, O., Carvalhais, N., Rozendaal, D.M.A., Avitabile, V., Araza, A., de Bruin, S., Herold, M., Quegan, S., Rodríguez-Veiga, P., Balzter, H., Carreiras, J., Schepaschenko, D., Korets, M., Shimada, M., Itoh, T., Moreno Martínez, Á., Cavlovic, J., Cazzolla Gatti, R., da Conceição Bispo, P., Dewnath, N., Labrière, N., Liang, J., Lindsell, J., Mitchard, E.T.A., Morel, A., Pacheco Pascagaza, A.M., Ryan, C.M., Slik, F., Vaglio Laurin, G., Verbeeck, H., Wijaya, A., Willcock, S., 2021a. The global forest above-ground biomass pool for 2010 estimated from high-resolution satellite observations. Earth System Science Data 13, 3927–3950. https://doi.org/10.5194/essd-13-3927-2021

Santoro, M., Cartus, O., Fransson, J.E.S., 2021b. Integration of allometric equations in the water cloud model towards an improved retrieval of forest stem volume with L-band SAR data in Sweden. Remote Sensing of Environment 253, 112235. https://doi.org/10.1016/j.rse.2020.112235

Santoro, M., Eriksson, L., Askne, J., Schmullius, C., 2006. Assessment of stand-wise stem volume retrieval in boreal forest from JERS-1 L-band SAR backscatter. International Journal of Remote Sensing 27, 3425–3454. https://doi.org/10.1080/01431160600646037

Santoro, M., Shvidenko, A., Mccallum, I., Askne, J., Schmullius, C., 2007b. Properties of ERS-1/2 coherence in the Siberian boreal forest and implications for stem volume retrieval. Remote Sensing of Environment 106, 154–172. https://doi.org/10.1016/j.rse.2006.08.004

Schadauer, K., Barreiro, S., 2010. Cost Action FP1001 (USEWOOD). COST. URL https://www.cost.eu/actions/FP1001/ (accessed 4.30.22).

Scheller, R.M., Mladenoff, D.J., 2005. A spatially interactive simulation of climate change, harvesting, wind, and tree species migration and projected changes to forest composition and biomass in northern Wisconsin, USA. Global Change Biology 11, 307–321. https://doi.org/10.1111/j.1365-2486.2005.00906.x

Schimel, D., Melillo, J., Tian, H., McGuire, A.D., Kicklighter, D., Kittel, T., Rosenbloom, N., Running, S., Thornton, P., Ojima, D., Parton, W., Kelly, R., Sykes, M., Neilson, R., Rizzo, B., 2000. Contribution of Increasing CO2 and Climate to Carbon Storage by Ecosystems

in the United States. Science 287, 2004–2006. https://doi.org/10.1126/science.287.5460.2004

Schmullius, C., Vollrath, A., Paradzay, C., Smit, I., Lück, W., Hajnsek, I., Renaud, M., 2010. Mapping of Vegetation Structure in the African Savanna: The Sarvanna Project, in: Proceedings of ESA Living Planet Symposium. Presented at the ESA Living Planet Symposium, Bergen, Norway.

Sexton, J.O., Song, X.-P., Feng, M., Noojipady, P., Anand, A., Huang, C., Kim, D.-H., Collins, K.M., Channan, S., DiMiceli, C., Townshend, J.R., 2013. Global, 30-m resolution continuous fields of tree cover: Landsat-based rescaling of MODIS vegetation continuous fields with lidar-based estimates of error. International Journal of Digital Earth 6, 427–448. https://doi.org/10.1080/17538947.2013.786146

Sharma, R., Leckie, D., Hill, D., Crooks, B., Bhogal, A.S., Arbour, P., D'eon, S., 2005. Hypertemporal radarsat SAR data of a forested terrain, in: International Workshop on the Analysis of Multi-Temporal Remote Sensing Images, 2005, Biloxi, MS, USA, 16–18 May 2005. Presented at the International Workshop on the Analysis of Multi-Temporal Remote Sensing Images, 2005, Biloxi, MS, USA, 16–18 May 2005, IEEE, Biloxi, MS, USA, pp. 71–75. https://doi.org/10.1109/AMTRSI.2005.1469843

Shaw, J., 2008. Benefits of a strategic national forest inventory to science and society: the USDA Forest Service Forest Inventory and Analysis program. iForest 1, 81–85. https://doi.org/10.3832/ifor0345-0010081

Shimada, M., Itoh, T., Motooka, T., Watanabe, M., Shiraishi, T., Thapa, R., Lucas, R., 2014a. New global forest/non-forest maps from ALOS PALSAR data (2007–2010). Remote Sens. Environ. 155, 13–31. https://doi.org/10.1016/j.rse.2014.04.014

Shimada, M., Itoh, T., Motooka, T., Watanabe, M., Shiraishi, T., Thapa, R., Lucas, R., 2014b. New global forest/non-forest maps from ALOS PALSAR data (2007–2010). Remote Sensing of Environment 155, 13–31. https://doi.org/10.1016/j.rse.2014.04.014

Shiroma, G.H.X., Lavalle, M., Buckley, S.M., 2022. An Area-Based Projection Algorithm for SAR Radiometric Terrain Correction and Geocoding. IEEE Trans. Geosci. Remote Sensing 1–1. https://doi.org/10.1109/TGRS.2022.3147472

Shuman, C.A., Zwally, H.J., Schutz, B.E., Brenner, A.C., DiMarzio, J.P., Suchdeo, V.P., Fricker, H.A., 2006. ICESat Antarctic elevation data: Preliminary precision and accuracy assessment. Geophys. Res. Lett. 33, L07501. https://doi.org/10.1029/2005GL025227

Sica, F., Pulella, A., Nannini, M., Pinheiro, M., Rizzoli, P., 2019. Repeat-pass SAR interferometry for land cover classification: A methodology using Sentinel-1 Short-Time-Series. Remote Sensing of Environment 232, 111277. https://doi.org/10.1016/j.rse.2019.111277

Simard, M., Pinto, N., Fisher, J.B., Baccini, A., 2011. Mapping forest canopy height globally with spaceborne lidar. J. Geophys. Res. 116, G04021. https://doi.org/10.1029/2011JG001708

SIOSE, Sistema de Ocupación del Suelo de España, n.d. Especificaciones técnicas SIOSE [WWW Document]. URL https://www.siose.es/especificaciones-tecnicas (accessed 8.27.20).

Siqueira, P., 2019. Forest Stand Height Estimation. https://doi.org/10.25966/4530-7686

Skakun, S., Wevers, J., Brockmann, C., Doxani, G., Aleksandrov, M., Batič, M., Frantz, D., Gascon, F., Gómez-Chova, L., Hagolle, O., López-Puigdollers, D., Louis, J., Lubej, M., Mateo-García, G., Osman, J., Peressutti, D., Pflug, B., Puc, J., Richter, R., Roger, J.-C., Scaramuzza, P., Vermote, E., Vesel, N., Zupanc, A., Žust, L., 2022. Cloud Mask Intercomparison eXercise (CMIX): An evaluation of cloud masking algorithms for Landsat 8 and Sentinel-2. Remote Sensing of Environment 274, 112990. https://doi.org/10.1016/j.rse.2022.112990

Small, D., 2012. SAR backscatter multitemporal compositing via local resolution weighting, in: 2012 IEEE International Geoscience and Remote Sensing Symposium, Munich, Germany, 22–27 July 2012; Presented at the IGARSS 2012 - 2012 IEEE International Geoscience and Remote Sensing Symposium, IEEE, Munich, Germany, pp. 4521–4524. https://doi.org/10.1109/IGARSS.2012.6350465

Small, D., 2011. Flattening Gamma: Radiometric Terrain Correction for SAR Imagery. IEEE Trans. Geosci. Remote Sensing 49, 3081–3093. https://doi.org/10.1109/TGRS.2011.2120616

Small, D., Rohner, C., Miranda, N., Ruetschi, M., Schaepman, M.E., 2021. Wide-Area Analysis-Ready Radar Backscatter Composites. IEEE Trans. Geosci. Remote Sensing 1–14. https://doi.org/10.1109/TGRS.2021.3055562

Smith, B., 2003. Accuracy and resolution of shuttle radar topography mission data. Geophys. Res. Lett. 30, 1467. https://doi.org/10.1029/2002GL016643

Soininen, A., 2004. TerraScan user's guide.

Soudani, K., Delpierre, N., Berveiller, D., Hmimina, G., Vincent, G., Morfin, A., Dufrêne, É., 2021. Potential of C-band Synthetic Aperture Radar Sentinel-1 time-series for the monitoring of phenological cycles in a deciduous forest. International Journal of Applied Earth Observation and Geoinformation 104, 102505. https://doi.org/10.1016/j.jag.2021.102505

Spurr, S.H., 1948. Aerial Photography. UNASYLVA-FAO 2.

Stanescu, V., Negrutiu, F., 1983. aniversarea centenarului invatamintului silvic superior din Romania. Revista padurilor 98, 185–194.

Steele-Dunne, S.C., McNairn, H., Monsivais-Huertero, A., Judge, J., Liu, P.W., Papathanassiou, K., 2017. Radar remote sensing of agricultural canopies: a review. IEEE Journal of Selected Topics in Applied Earth Observations and Remote Sensing 10, 2249–2273. https://doi.org/10.1109/jstars.2016.2639043

Strozzi, T., Wegmuller, U., Luckman, A., Balzter, H., 1999. Mapping deforestation in Amazon with ERS SAR interferometry, in: 1999 IEEE International Geoscience and Remote Sensing Symposium. IGARSS'99, Hamburg, Germany, 28 June–2 July 1999. Presented at the IEEE 1999 International Geoscience and Remote Sensing Symposium. IGARSS'99, IEEE, Hamburg, Germany, pp. 767–769. https://doi.org/10.1109/IGARSS.1999.774434

Sun, Q., Jiao, Q., Dai, H., 2018. Evaluating the capabilities of vegetation spectral indices on chlorophyll content estimation at Sentinel-2 spectral resolutions, in: MIPPR 2017: Remote Sensing Image Processing, Geographic Information Systems, and Other Applications. Presented at the MIPPR 2017: Remote Sensing Image Processing, Geographic Information Systems, and Other Applications, SPIE, pp. 346–351. https://doi.org/10.1117/12.2285611

Tachikawa, T., Hato, M., Kaku, M., Iwasaki, A., 2011. Characteristics of ASTER GDEM version 2. Presented at the 2011 IEEE international geoscience and remote sensing symposium, IEEE, pp. 3657–3660.

Tadono, T., Ishida, H., Oda, F., Naito, S., Minakawa, K., Iwamoto, H., 2014. Precise Global DEM Generation by ALOS PRISM. ISPRS Ann. Photogramm. Remote Sens. Spatial Inf. Sci. II–4, 71–76. https://doi.org/10.5194/isprsannals-II-4-71-2014

Takaku, J., Tadono, T., Tsutsui, K., Ichikawa, M., 2016. VALIDATION OF "AW3D" GLOBAL DSM GENERATED FROM ALOS PRISM. ISPRS Ann. Photogramm. Remote Sens. Spatial Inf. Sci. III–4, 25–31. https://doi.org/10.5194/isprsannals-III-4-25-2016

Tanase, M., de la Riva, J., Santoro, M., Pérez-Cabello, F., Kasischke, E., 2011. Sensitivity of SAR data to post-fire forest regrowth in Mediterranean and boreal forests. Remote Sensing of Environment 115, 2075–2085. https://doi.org/10.1016/j.rse.2011.04.009

Tanase, M.A., 2010. Sar sensitivity to burn severity and forest recovery in mediterranean environments. Universidad de Zaragoza.

Tanase, M.A., Aponte, C., Mermoz, S., Bouvet, A., 2018. Detection of windthrows and insect outbreaks by L-band SAR: a case study in the Bavarian forest national park. Remote Sensing of Environment 209, 700–711. https://doi.org/10.1016/j.rse.2018.03.009

Tanase, M.A., Ismail, I., Lowell, K., Karyanto, O., Santoro, M., 2015. Detecting and Quantifying Forest Change: The Potential of Existing C- and X-Band Radar Datasets. PLOS ONE 10, e0131079. https://doi.org/10.1371/journal.pone.0131079

Tanase, M.A., Marin, G., Belenguer-Plomer, M.A., Borlaf, I., Popescu, F., Badea, O., 2020. Deep Neural Networks for Forest Growing Stock Volume Retrieval: A Comparative Analysis for L-band SAR data, in: IGARSS 2020-2020 IEEE International Geoscience and Remote Sensing Symposium. IEEE, pp. 4975–4978.

Tanase, Mihai A., Panciera, R., Lowell, K., Aponte, C., Hacker, J.M., Walker, J.P., 2014a. Forest Biomass Estimation at High Spatial Resolution: Radar Versus Lidar Sensors. IEEE Geoscience and Remote Sensing Letters 11, 711–715. https://doi.org/10.1109/LGRS.2013.2276947

Tanase, M. A., Panciera, R., Lowell, K., Tian, S., Garcia-Martin, A., Walker, J.P., 2014. Sensitivity of L-Band Radar Backscatter to Forest Biomass in Semiarid Environments: A Comparative Analysis of Parametric and Nonparametric Models. IEEE Transactions on Geoscience and Remote Sensing 52, 4671–4685. https://doi.org/10.1109/tgrs.2013.2283521

Tanase, Mihai A., Panciera, R., Lowell, K., Tian, S., Hacker, J.M., Walker, J.P., 2014b. Airborne multi-temporal L-band polarimetric SAR data for biomass estimation in semi-arid forests. Remote Sensing of Environment 145, 93–104. https://doi.org/10.1016/j.rse.2014.01.024

Tanase, M.A., Villard, L., Pitar, D., Apostol, B., Petrila, M., Chivulescu, S., Leca, S., Borlaf-Mena, I., Pascu, I.-S., Dobre, A.-C., 2019. Synthetic aperture radar sensitivity to forest changes: A simulations-based study for the Romanian forests. Science of The Total Environment 689, 1104–1114.

Thiel, C.J., Thiel, C., Schmullius, C.C., 2009. Operational Large-Area Forest Monitoring in Siberia Using ALOS PALSAR Summer Intensities and Winter Coherence. IEEE Trans. Geosci. Remote Sensing 47, 3993–4000. https://doi.org/10.1109/TGRS.2009.2021469

Thirion-Lefevre, L.., Colin-Koeniguer, E.., 2007. Investigating Attenuation, Scattering Phase Center, and Total Height Using Simulated Interferometric SAR Images of Forested Areas. IEEE Trans. Geosci. Remote Sensing 45, 3172–3179. https://doi.org/10.1109/TGRS.2007.904921

Thurner, M., Beer, C., Santoro, M., Carvalhais, N., Wutzler, T., Schepaschenko, D., Shvidenko, A., Kompter, E., Ahrens, B., Levick, S.R., Schmullius, C., 2014. Carbon stock and density of northern boreal and temperate forests. Global Ecology and Biogeography 23, 297–310. https://doi.org/10.1111/geb.12125

Tomppo, E., Schadauer, K., 2004. COST Action E43 [WWW Document]. COST. URL https://www.cost.eu/actions/E43/ (accessed 1.5.22).

Tomppo, E., Schadauer, K., McRoberts, R.E., Gschwantner, T., Gabler, K., Ståhl, G., 2010. Introduction, in: Tomppo, E., Gschwantner, T., Lawrence, M., McRoberts, R.E. (Eds.), National Forest Inventories. Springer Netherlands, Dordrecht, pp. 1–18. https://doi.org/10.1007/978-90-481-3233-1_1

Tomter, S.M. (Ed.), 2019. Landsskogtakseringen 1919–2019. NIBIO, Oslo, Norway.

Tomter, S.M., 2016. Norway, in: Vidal, C., Alberdi, I.A., Hernández Mateo, L., Redmond, J.J. (Eds.), National Forest Inventories. Springer International Publishing, Cham, pp. 601–619. https://doi.org/10.1007/978-3-319-44015-6_32

Torres, P., Rodes-Blanco, M., Viana-Soto, A., Nieto, H., García, M., 2021. The Role of Remote Sensing for the Assessment and Monitoring of Forest Health: A Systematic Evidence Synthesis. Forests 12, 1134. https://doi.org/10.3390/f12081134

Touzi, R., Lopes, A., Bruniquel, J., Vachon, P.W., 1999. Coherence estimation for SAR imagery. IEEE Trans. Geosci. Remote Sensing 37, 135–149. https://doi.org/10.1109/36.739146

Tropek, R., Sedláček, O., Beck, J., Keil, P., Musilová, Z., Šímová, I., Storch, D., 2014. Comment on "High-resolution global maps of 21st-century forest cover change." Science 344, 981–981. https://doi.org/10.1126/science.1248753

Truckenbrodt, J., Freemantle, T., Williams, C., Jones, T., Small, D., Dubois, C., Thiel, C., Rossi, C., Syriou, A., Giuliani, G., 2019. Towards Sentinel-1 SAR Analysis-Ready Data: A Best Practices Assessment on Preparing Backscatter Data for the Cube. Data 4, 93. https://doi.org/10.3390/data4030093

Tucker, C.J., 1979. Red and photographic infrared linear combinations for monitoring vegetation. Remote Sensing of Environment 8, 127–150. https://doi.org/10.1016/0034-4257(79)90013-0

Turnock, D., 1988. Woodland conservation: The emergence of rational land use policies in Romania. GeoJournal 17. https://doi.org/10.1007/BF00181052

Udali, A., Lingua, E., Persson, H.J., 2021. Assessing Forest Type and Tree Species Classification Using Sentinel-1 C-Band SAR Data in Southern Sweden. Remote Sensing 13, 3237. https://doi.org/10.3390/rs13163237

Ulaby, F.T., Long, D.G., 2014. Microwave radar and radiometric remote sensing. The University of Michigan Press, Ann Arbor, MI, USA.

Ulaby, F.T., Moore, R.K., Fung, A.K., 1982. Microwave remote sensing. 2: Radar remote sensing and surface scattering and emission theory, Remote sensing. Addison-Wesley, Reading, Mass.

United Nations, 2015a. Paris agreement. UN,.

United Nations, 2015b. Paris Agreement, FCCC/CP/2015/L.9/Rev.1. United Nations Secretariat, Paris, France.

United Nations, 2014. Forests: Action Statements and Action Plans. United Nations Secretariat, New York, NY, USA.

United Nations, 1997. Kyoto Protocol to the United Nations Framework Convention on Climate Change, FCCC/CP/1997/L.7/Add.1. United Nations Secretariat, Kyoto, Japan.

United Nations, 1992a. Convention on Biological Diversity. UN,.

United Nations, 1992b. Non-legally binding authoritative statement of principles for a global consensus on the management, conservation and sustainable development of all types of forests. Presented at the UN Conference on Environment and Development, UN, Rio de Janeiro, Brazil.

United Nations, 1992c. United Nations Framework Convention on Climate Change. UN,.

U.S. Geological Survey, 2022. What is remote sensing and what is it used for? [WWW Document]. U.S. Geological Survey. URL https://www.usgs.gov/faqs/what-remote-sensing-and-what-it-used (accessed 4.13.22).

USGS, 2019. EarthExplorer [WWW Document]. URL https://earthexplorer.usgs.gov/ (accessed 1.13.20).

van der Walt, S., Colbert, S.C., Varoquaux, G., 2011. The NumPy Array: A Structure for Efficient Numerical Computation. Computing in Science & Engineering 13, 22–30. https://doi.org/10.1109/MCSE.2011.37

van Zyl, J.J., 1989. Unsupervised classification of scattering behavior using radar polarimetry data. IEEE Transactions on Geoscience and Remote Sensing 27, 36–45. https://doi.org/10.1109/36.20273

Veen, P., Fanta, J., Raev, I., Biriş, I.A., Smidt, J. de, Maes, B., 2010. Virgin forests in Romania and Bulgaria: results of two national inventory projects and their implications for protection. Biodiversity and Conservation 19, 1805–1819. https://doi.org/10.1007/s10531-010-9804-2

Viana-Soto, A., Aguado, I., Salas, J., García, M., 2020. Identifying Post-Fire Recovery Trajectories and Driving Factors Using Landsat Time Series in Fire-Prone Mediterranean Pine Forests. Remote Sensing 12, 1499. https://doi.org/10.3390/rs12091499

Vidal, C., Alberdi, I., Redmond, J., Vestman, M., Lanz, A., Schadauer, K., 2016a. The role of European National Forest Inventories for international forestry reporting. Annals of Forest Science 73, 793–806. https://doi.org/10.1007/s13595-016-0545-6

Vidal, C., Sallnäs, O., Redmond, J., Alberdi, I., Barreiro, S., Hernández, L., Schadauer, K., 2016b. Introduction, in: Vidal, C., Alberdi, I.A., Hernández Mateo, L., Redmond, J.J. (Eds.),

National Forest Inventories. Springer International Publishing, Cham, pp. 1–23. https://doi.org/10.1007/978-3-319-44015-6_1

Villanueva, G.L., Smith, M.D., Protopapa, S., Faggi, S., Mandell, A.M., 2018. Planetary Spectrum Generator: An accurate online radiative transfer suite for atmospheres, comets, small bodies and exoplanets. Journal of Quantitative Spectroscopy and Radiative Transfer 217, 86–104. https://doi.org/10.1016/j.jqsrt.2018.05.023

Villard, L., Le Toan, T., Ho Tong Minh, D., Mermoz, S., Bouvet, A., 2016. Forest Biomass From Radar Remote Sensing, in: Land Surface Remote Sensing in Agriculture and Forest. Elsevier, pp. 363–425. https://doi.org/10.1016/B978-1-78548-103-1.50009-1

Vincent, P., Bourbigot, M., Hajduch, G., 2018. Release Note of S-1 IPF for End Users of Sentinel-1 products [WWW Document]. URL https://sentinel.esa.int/documents/247904/2142675/S-1-IPF-Sentinel-1-products-Release-Note.pdf (accessed 11.20.21).

Vincent, P., Bourbigot, M., Johnsen, H., Piantanida, R., 2020. Sentinel-1 Product Specification [WWW Document]. URL https://sentinel.esa.int/documents/247904/1877131/Sentinel-1-Product-Specification (accessed 11.20.21).

Wagner, W., 2003. Large-scale mapping of boreal forest in SIBERIA using ERS tandem coherence and JERS backscatter data. Remote Sensing of Environment 85, 125–144. https://doi.org/10.1016/S0034-4257(02)00198-0

Wakefield, A., 2014. Aerial photography in the First World War - Telegraph. The Daily Telegraph.

Walker, S., 2020. Violence escalates as Romania cracks down on illegal timber trade. The Guardian.

Watson, J.E.M., Evans, T., Venter, O., Williams, B., Tulloch, A., Stewart, C., Thompson, I., Ray, J.C., Murray, K., Salazar, A., McAlpine, C., Potapov, P., Walston, J., Robinson, J.G., Painter, M., Wilkie, D., Filardi, C., Laurance, W.F., Houghton, R.A., Maxwell, S., Grantham, H., Samper, C., Wang, S., Laestadius, L., Runting, R.K., Silva-Chávez, G.A., Ervin, J., Lindenmayer, D., 2018. The exceptional value of intact forest ecosystems. Nat Ecol Evol 2, 599–610. https://doi.org/10.1038/s41559-018-0490-x

Way, J., Rignot, E.J.M., McDonald, K.C., Oren, R., Kwok, R., Bonan, G., Dobson, M.C., Viereck, L.A., Roth, J.E., 1994. Evaluating the type and state of Alaska taiga forests with imaging radar for use in ecosystem models. IEEE Transactions on Geoscience and Remote Sensing 32, 353–370. https://doi.org/10.1109/36.295050

Way, J., Zimmermann, R., Rignot, E., McDonald, K., Oren, R., 1997. Winter and spring thaw as observed with imaging radar at BOREAS. J. Geophys. Res. 102, 29673–29684. https://doi.org/10.1029/96JD03878

Wegmüller, U., Werner, C., 1996. Land applications using ERS-1/2 tandem data, in: Fringe Workshop: ERS SAR Interferometry, Zurich, Switzerland, 30 October 1996. Presented at the Fringe Workshop: ERS SAR Interferometry, Zurich, Switzerland, 30 October 1996, European Space Agency, Zurich, Switzerland, pp. 97–112.

Wegmüller, U., Werner, C., Strozzi, T., Wiesmann, A., 2002a. Automated and precise image registration procedures, in: Analysis of Multi-Temporal Remote Sensing Images, Series in Remote Sensing. WORLD SCIENTIFIC, pp. 37–49. https://doi.org/10.1142/9789812777249_0002

Wegmüller, U., Werner, C., Strozzi, T., Wiesmann, A., 2002b. Automated and precise image registration procedures, in: Analysis of Multi-Temporal Remote Sensing Images, Ispra, Italy, 16–18 July 2002. Presented at the Proceedings of the First International Workshop on Multitemp 2001, World scientific, Trento, Italy, pp. 37–49. https://doi.org/10.1142/9789812777249_0002

Wegmuller, U., Werner, C.L., 1995. SAR interferometric signatures of forest. IEEE Trans. Geosci. Remote Sensing 33, 1153–1161. https://doi.org/10.1109/36.469479

Wegnüller, U., Werner, C., Strozzi, T., Wiesmann, A., Frey, O., Santoro, M., 2016. Sentinel-1 Support in the GAMMA Software. Procedia Computer Science 100, 1305–1312. https://doi.org/10.1016/j.procs.2016.09.246

Werner, C., Wegmuller, U., Strozzi, T., Wiesmann, A., 2005. Precision estimation of local offsets between pairs of SAR SLCs and detected SAR images, in: Proceedings. 2005 IEEE International Geoscience and Remote Sensing Symposium, 2005. IGARSS '05. Presented at the Proceedings. 2005 IEEE International Geoscience and Remote Sensing Symposium, 2005. IGARSS '05., pp. 4803–4805. https://doi.org/10.1109/IGARSS.2005.1526747

Werner, C., Wegmüller, U., Strozzi, T., Wiesmann, A., 2000. Gamma SAR and interferometric processing software, in: Proceedings of the ERS-Envisat Symposium, Gothenburg, Sweden, 15-20 October 2000. ESA Publications Division, Noordwijk, The Netherlands.

Wessel, B., 2016. TanDEM-X Ground Segment–DEM Products Specification Document.

Wilson, A.M., Jetz, W., 2016. Remotely Sensed High-Resolution Global Cloud Dynamics for Predicting Ecosystem and Biodiversity Distributions. PLOS Biology 14, e1002415. https://doi.org/10.1371/journal.pbio.1002415

WMO, UNEP, ICSU, UNESCO, IOC, UNFCCC, UNFCCC, World Meteorological Organization (WMO), 1998. Report on the Adequacy of the Global Climate Observing Systems (No. 48), GCOS. WMO, Geneva.

WMO, UNEP, IOC, ICSU, World Meteorological Organization (WMO), 1995. Plan for space-based observations (No. 15), GCOS. WMO, Geneva.

Woodhouse, I.H., 2006. Introduction to microwave remote sensing. Taylor & Francis, Boca Raton, FL, USA.

World Bank, 2020. Romania current climate [WWW Document]. URL https://climateknowledgeportal.worldbank.org/ (accessed 3.21.22).

Xu, H., 2006. Modification of normalised difference water index (NDWI) to enhance open water features in remotely sensed imagery. International Journal of Remote Sensing 27, 3025–3033. https://doi.org/10.1080/01431160600589179

Yang, H., Yang, X., Heskel, M., Sun, S., Tang, J., 2017. Seasonal variations of leaf and canopy properties tracked by ground-based NDVI imagery in a temperate forest. Sci Rep 7, 1267. https://doi.org/10.1038/s41598-017-01260-y

Yu, H., Ni, W., Zhang, Zhongjun, Sun, G., Zhang, Zhiyu, 2020. Regional Forest Mapping over Mountainous Areas in Northeast China Using Newly Identified Critical Temporal Features of Sentinel-1 Backscattering. Remote Sensing 12, 1485. https://doi.org/10.3390/rs12091485

Zhu, X., Liu, D., 2014. Accurate mapping of forest types using dense seasonal Landsat time-series. ISPRS Journal of Photogrammetry and Remote Sensing 96, 1–11. https://doi.org/10.1016/j.isprsjprs.2014.06.012

Zhu, Z., Wulder, M.A., Roy, D.P., Woodcock, C.E., Hansen, M.C., Radeloff, V.C., Healey, S.P., Schaaf, C., Hostert, P., Strobl, P., Pekel, J.-F., Lymburner, L., Pahlevan, N., Scambos, T.A., 2019. Benefits of the free and open Landsat data policy. Remote Sensing of Environment 224, 382–385. https://doi.org/10.1016/j.rse.2019.02.016

Zillman, J.W., 2009. A history of climate activities. World Meteorological Organization Bulletin 58, 141.